

The Architecture of Nanoparticle Surfaces and Interfaces

By

Elizabeth Margaret Raine

471531

University College

A dissertation submitted for the degree of Doctor of Philosophy at the

Inorganic Chemistry Laboratory, Department of Chemistry,

University of Oxford

2018

The Architecture of Nanoparticle Surfaces and Interfaces

By

Elizabeth Margaret Raine

471531

University College

Supervisor

Prof. S. C. Edman Tsang

Industrial Supervisors

Dr. Paul Collier and Dr. Mark Feaviour

Internal Assessor

Prof. John Foord

A dissertation submitted for the degree of Doctor of Philosophy at the

Inorganic Chemistry Laboratory, Department of Chemistry,

University of Oxford

2018

Table of Contents

Table of Contents i
Acknowledgements ix
Abstract xi
List of figures xiii
List of tables xx
List of abbreviations and symbols xxii
List of publications xxiv

Chapter 1: Introduction 1
1.1 Principles of catalysis 2
1.1.1 Types of catalysis 5
1.1.2 Theory of heterogeneous catalysis 6
1.2 Nanoparticle catalysis 9
1.2.1 Nanoparticle stabilisers and support effects 12
1.3 Bimetallic catalysis 14
1.3.1 Electronic effects 14
1.3.2 Geometric effects 15
1.3.3 Bimetallic morphologies 17
1.3.4 Platinum bimetallic catalysts 18
1.4 Formic acid decomposition 20
1.5 Oxygen reduction reaction 22
1.6 Aims and objectives 26
1.7 Thesis overview 27
1.8 References 28

Chapter 2: Analytical Techniques 33
2.1 Introduction 34
2.2 X-ray diffraction 34

2.2.1 Powder x-ray diffraction 35
2.2.2 Wide angle x-ray scattering 37
2.3 X-ray absorption spectroscopy 37
2.4 Transmission electron microscopy 39
2.5 Energy-dispersive x-ray spectroscopy 42
2.6 Low energy ion scattering 43
2.7 Temperature programmed reduction 44
2.8 Thermogravimetric analysis 45
2.9 Atom probe tomography 45
2.10 Magic angle spinning nuclear magnetic resonance 47
2.11 References 48

Chapter 3: Experimental Methods 50
3.1 Introduction 51
3.2 Synthesis of colloidal nanoparticles 51
3.2.1 Monometallic platinum nanoparticles 51
3.2.2 Bimetallic nanoparticles 52
3.3 Synthesis of silica supported nanoparticles 53
3.3.1 Monometallic platinum nanoparticles 53
3.3.2 Bimetallic nanoparticles 54
3.4 Synthesis of carbon supported nanoparticles 54
3.4.1 Carbon supported co-reduced platinum nickel 54
3.4.2 Stepwise nanoparticle syntheses in SBA-15 55
3.5 Catalyst Testing 55
3.5.1 Liquid phase formic acid decomposition reaction 55
3.5.2 Gas phase formic acid decomposition reaction for XAS 56
3.5.3 Electrochemical oxygen reduction reaction 56
3.6 Characterisation 58
3.6.1 X-ray diffraction (XRD) 58
3.6.2 X-ray absorption spectroscopy (XAS) 59

3.6.3 Transmission electron microscopy (TEM) and energy-dispersive x-ray spectroscopy (EDX) 59
3.6.4 Low energy ion scattering (LEIS) 60
3.6.5 Temperature programmed reduction (TPR) 60
3.6.6 Thermogravimetric analysis (TGA) 60
3.6.7 Atom probe tomography (APT) 61
3.6.8 Magic angle spinning nuclear magnetic resonance (MAS-NMR) 62
3.7 References 62

Chapter 4: Polymer stabilised nanoparticle synthesis 64
4.1 Background 65
4.2 Objectives 67
4.3 Experimental details 67
4.4 Characterisation of colloidal platinum nanoparticles 68
4.4.1 Platinum(PVP) nanoparticles 68
4.5 Characterisation of colloidal bimetallic nanoparticles 71
4.5.1 Platinum silver colloidal nanoparticles 72
4.5.2 Platinum nickel colloidal nanoparticles 82
4.5.3 Platinum zinc colloidal nanoparticles 87
4.6 Formic acid decomposition 93
4.7 Conclusions 97
4.8 References 99

Chapter 5: Silica supported nanoparticle synthesis 101
5.1 Background 102
5.2 Objectives 104
5.3 Experimental details 104
5.4 Characterisation of supported platinum nanoparticles 105
5.4.1 Platinum(SBA-15) nanoparticles 105

5.5 Characterisation of supported bimetallic nanoparticles 108
5.5.1 Platinum silver supported nanoparticles 108
5.5.2 Platinum nickel supported nanoparticles 110
5.5.3 Platinum zinc supported nanoparticles 113
5.6 Formic acid decomposition 125
5.6.1 Liquid phase formic acid decomposition 125
5.6.2 *In-situ* XAS with gas phase formic acid decomposition 131
5.7 Conclusion 135
5.8 References 138

Chapter 6: Tailored platinum nickel nanoparticle catalysts 140
6.1 Background 141
6.2 Objectives 143
6.3 Experimental details 143
6.4 Characterisation of platinum nickel nanoparticles 144
6.4.1 Pt_1Ni_3 catalysts 144
6.4.2 Pt_1Ni_1 catalysts 156
6.5 SBA-15 wall effect 159
6.6 Oxygen reduction reaction 164
6.7 Conclusion 171
6.8 References 174

Chapter 7: Conclusions and Future Perspectives 176
7.1 Conclusions 177
7.2 Future Perspectives 178

Appendix 1 180
Appendix 2 185

DECLARATION

I confirm that this is my own work and the use of all materials from other sources has been properly and fully acknowledged.

Elizabeth Raine

DEDICATION

To my family, in particular my grandparents.

Acknowledgements

Firstly I would like to thank my supervisor Professor Edman Tsang for his guidance and support throughout the course of my DPhil project. I would also like to Johnson Matthey and the Engineering and Physical Sciences Research Council for providing the funding for this research, without which this project would not have been possible. I would also like to express my gratitude to my industrial supervisors Dr Paul Collier and Dr Mark Feaviour from Johnson Matthey. In addition I would like to thank Oxford University, Johnson Matthey and the Research Complex at Harwell for providing the research equipment and facilities needed in order to complete this project.

I would like to thank Professor Gopinathan Sankar and Adam Clark for their collaboration with the XAS experiments and analysis, as well as Dr Simantini Nayak for her assistance with the ORR experiments. In addition, I would like to thank Dr Neil Young for training and assistance with TEM and Dr Amy Kolpin and Dr Hanif Mahadi for their introduction to synthetic techniques, as well as training for use of the characterisation equipment in the lab including TGA, TPR, XRD and TEM.

I would like to thank Dr Tong Li for help with the APT measurements and Simson Wu for help with XAS fittings. In addition, thanks go to Dr Emily Brooke and Dr Tuğce Eralp Erden at Johnson Matthey for their help with Cryo-TEM/HRTEM and XPS respectively. I would also like to thank Diamond Light Source for the beamtimes which allowed XAS and WAXS/SAXS analysis, along with the beamline scientists Dr Diego Gianolio, Dr Giannantonio Cibin and Dr Glenn Smales.

I would like to thank all the members of the Tsang group, both past and present, for their discussions, support and entertainment throughout my time in the group. In particular, I would like to thank Dr Amy Kolpin and Dr Simon Jones for their previous work as well as Dr Hanif Mahadi, Dr Simon Fairclough, Dr Tugce Ayvali, Dr Hannah Kriessl, Dr Bin Yu, Dr Ian McPherson, Jiri

Kulhavy, Tim Sudmeier, Josh Fellowes and Kirsty Purchase for discussion and friendship throughout the course of this project. I would also like to thank all those in University College MCR who have ensured my free time has been busy, entertaining and unforgettable.

A significant thanks goes to James Moran, who spent many hours attempting to understand chemistry to help with proofreading. Finally and perhaps most importantly, I would like to thank my parents, my family and James for their continual support, motivation and encouragement, without which it would not have been possible for me to complete this project.

The Architecture of Nanoparticle Surfaces and Interfaces

A thesis submitted for the degree of Doctor of Philosophy
Elizabeth Raine, University College, Trinity Term 2018

Abstract

Heterogeneous catalysts are vital for many industrial processes, however the high compositions of platinum group metals mean that the catalysts are often expensive and are not always cost efficient. In many cases, although platinum is a good catalyst, an enhancement in activity can be seen when alloying with a secondary metal. In order to increase the cost efficiency of these catalysts, an improvement in activity and reduction in expensive metal mass is needed. One method of combining these factors is the production of core-shell nanoparticles, removing the highly expensive metal from the inactive particle core while maintaining the close contact of the active metal with the secondary metal.

This thesis provides an insight into two synthetic methods to produce designed bimetallic nanoparticles with tailored active sites for improving catalysis. The first method explored uses the polymer polyvinylpyrrolidone as a capping agent while subsequent deposition techniques are employed to tailor the surface layer. The second method uses a mesoporous silica (SBA-15) which induces the surface segregation of some secondary metals. These two synthetic methods are evaluated through extensive characterisation to better understand the metallic interfaces and through the use of the formic acid decomposition reaction to understand the changes in the active sites at the surfaces. The SBA-15 method was also used to produce a series of catalysts with enhanced activity for the oxygen reduction reaction. The research presented is a step towards highly designed nanoparticle catalysts, with the tailoring of active sites made possible through degree of interaction of a secondary metal.

Keywords: Heterogeneous catalyst, Geometric modification, Electronic modification, Formic acid dehydrogenation, Oxygen reduction reaction.

List of figures

Figure 1.1. A simplified schematic energy profile for an exothermic reaction, with the catalysed route in blue and the uncatalysed route in red. 4

Figure 1.2. Schematic comparison of a catalysed reaction and a uncatalysed reaction. Reprinted with permission from J. Heveling, J. Chem. Educ., 2012, 89, 1530–1536. Copyright 2012 American Chemical Society.[23] 7

Figure 1.3. Volcano plot representing the adsorption of formate onto a metal surface and the temperature required for the dehydrogenation reaction to occur. Reproduced from reference[23]. 8

Figure 1.4. Schematic band structure diagrams, a) showing the broad half-filled s-band and narrow d-band. b) shows the splitting of the narrow d-band into bonding and antibonding states, with the Fermi level shown in red. Images reproduced and modified from reference[32]. 9

Figure 1.5. Number of publications related to nanoparticle catalysts each year from 1990 to 2017. Collated through searching "nanoparticle catalyst" in SciFinder. 10

Figure 1.6. Schematic showing change of band structure from bulk metals to nanoparticles and the orbitals of isolated molecules. Reproduced from reference[38] 12

Figure 1.7. Schematic to show the addition of a secondary metal (purple) donating electrons to the PGM (blue), leading to increased filling of the d-band and a down-shift of the d-band centre. Reproduced from Ref. 70 with permission from the PCCP Owner Societies. 15

Figure 1.8. Schematic showing the variation in d-band under tensile and compressive strain. Reproduced from Ref. 70 with permission from the PCCP Owner Societies. 16

Figure 1.9. Schematic diagrams showing the steric effect of strain on a bidentate binding adsorbate. a) shows the surface layer under compressive strain, with the surface atoms contracted in lattice. b) shows the original mono-metallic sample. c) shows the surface layer under tensile strain with the surface atoms expanded in lattice. Each sample shows both the side on view (top) and top down view (bottom), with the formate ion binding to adjacent surface atoms. Models were produced in CrystalMaker with the surface atoms in all diagrams having the parameters of platinum (blue), and the subsurface atoms in a) having the metal parameters of nickel (pale grey) and in c) having the metal parameters of silver (dark grey). 17

Figure 1.10. Schematic diagrams of a selection of morphologies of bimetallic nanoparticles. Morphologies mentioned in this thesis include a) mixed alloy, b) island clusters, c) core-shell nanoparticles and d) multiple small core material coated in single shell material. Republished with permission of Royal Society of Chemistry, from A. Zaleska-Medynska, et.al, Adv. Colloid Interface Sci., 2016, 229, 80–107; permission conveyed through Copyright Clearance Center, Inc.[73] 18

Figure 1.11. Schematic of a PEM fuel cell, reproduced from reference[89]. 21

Figure 1.12. ORR mechanism schematic for a full 4-electron reduction. Republished with permission of Elsevier, from J. Stacy, et.al, Renew. Sustain. Energy Rev., 2017, 69, 401–414; permission conveyed through Copyright Clearance Center, Inc[101] 23

Figure 1.13. Volcano plot showing the relationship between the energy of adsorption of O_2 and catalytic activity for a selection of metals. Reprinted with permission from J. K. Nørskov, J. Rossmeisl, A. Logadottir, L. Lindqvist, J. R. Kitchin, T. Bligaard and H. Jónsson, J. Phys. Chem. B, 2004, 108, 17886–17892. Copyright 2004 American Chemical Society. 24

Figure 1.14. Activity of core-shell nanoparticles for ORR. Higher activity corresponds to darker colour. Nanoparticles that did not converge are shown in white. Republished with permission of AIP Publishing, from J. B. Corona, et.al, J. Chem. Phys., 2016, 145; permission conveyed through Copyright Clearance Center, Inc [111]. 26

Figure 2.1. Schematic diagram showing destructive interference produced from two planes in a crystal. Image modified from reference.[5] 36

Figure 2.3. An image showing a typical XAS spectrum. The blue area shows the XANES region and the red area shows the EXAFS region. 38

Figure 2.4. Image showing both bright field (left) and dark field (right) microscope set up. In the bright field set-up, the objective aperture is opened to allow the transmitted electrons (highlighted in yellow) to pass through. In the dark field set-up the objective aperture is opened to allow one set of diffracted electrons (highlighted in green) to pass through. Image modified from reference.[13] 41

Figure 2.5. Image showing the range of interactions which can occur after the primary electron beam meets the sample. Transmitted electrons, scattered electrons and x-rays are commonly used in this thesis for various techniques. Image reproduced from reference.[14] 42

Figure 2.6. LEIS process. a) Ne+ ions are scattered by surface atoms causing a change in energy. b) Higher energy Ne+ ions are used to sputter the surface atoms off the particles. c) Ne+ ions are scattered by the new surface of the particle, showing particle composition at a specific depth. ..44

Figure 2.7. Schematic showing the process of atom probe tomography. Atoms on the sample tip are ionised and accelerated towards the detector, where their position and type are recorded. Image modified from reference.[22] 46

Figure 4.1. Representation of a PVP polymer bound to a metal particle of unspecified shape. Reproduced from literature.[15] 70

Figure 4.2. XRD profile showing Pt(PVP) nanoparticles. Observed intensity is shown in red, fitted intensity is shown in blue. Pt reference (00-004-0802) positions are shown in yellow. 73

Figure 4.3. STEM and TEM images of Pt(PVP) particles taken at Johnson Matthey. a) STEM image of many particles showing homogeneity. b) Size distribution graph. c) HR-TEM image showing the lattices of various particles. d) HR-TEM image showing the intensity profile used to calculate lattice parameter. 74

Figure 4.4. XRD profile showing PtAg(PVP) nanoparticles. Observed intensity is shown in red, fitted intensity is shown in blue. Pt reference (00-004-0802) positions are shown in yellow and Ag reference (00-004-0783) positions are shown in green. 76

Figure 4.5. STEM and TEM images of PtAg(PVP) particles taken at Johnson Matthey. a) STEM image of many particles showing homogeneity. b) Size distribution graph. c) HR-TEM image showing lattices and intensity profile used to calculate lattice parameter for edges. d) HR-TEM image showing lattices and intensity profile used to calculate lattice parameter for centre.....78

Figure 4.6. STEM EDX images of PtAg(PVP) particles taken at Johnson Matthey. a) EDX profile showing atomic compositions, with Ag reference stick pattern in black. b&c) STEM EDX maps of PtAg(PVP) sample in different regions, with Pt in green and Ag in pink. 80

Figure 4.7. Schematic to show stepwise synthesis method and cryo-TEM sampling points. 81

Figure 4.8. Dark field STEM images showing sample at different points in the synthesis. a) Sample point A, Ag 1 hour. b) Sample point B, Ag 2 hours. c) Sample point C, Ag H_2, and d) Secondary electron image showing sample point D, PtAg 1 hour. 82

Figure 4.9. STEM EDX images of PtAg(PVP) larger particles. a) Secondary electron image, b) Pt map (red), c) Ag map (blue). 84

Figure 4.10. XRD profile showing PtNi(PVP) nanoparticles. Observed intensity is shown in red, fitted intensity is shown in blue. Pt reference (00-004-0802) positions are shown in yellow and Ni reference (00-004-0850) positions are shown in green. 86

Figure 4.11. STEM and TEM images of PtNi(PVP) particles taken at Johnson Matthey. a) STEM image of many particles showing homogeneity. b) Size distribution graph. c) HR-TEM image showing lattices of various particles. d) HR-TEM image showing intensity profile used to calculate lattice parameter. 87

Figure 4.12. STEM and EDX images of PtNi(PVP) particles taken at Johnson Matthey. a) STEM image showing the region mapped. b) EDX map showing Ni in blue and Pt in red. 88

Figure 4.13. EDX point analysis. a) STEM image showing analysis points. b) EDX profile from area 1. c) EDX profile from area 3. 89

Figure 4.14. a) STEM and b) Secondary electron image showing area of the PtNi(PVP) sample which was analysed with EDX point analysis. The blue circle represents area 3 which contained Ni species. 90

Figure 4.15. XRD profile showing PtZn(PVP) nanoparticles. Observed intensity is shown in red, fitted intensity is shown in blue. Pt reference (00-004-0802) positions are shown in yellow, Zn reference (00-004-0831) positions are shown in green and ZnO reference (00-001-1136) positions are shown in purple. 92

Figure 4.16. STEM and TEM images of PtZn(PVP) particles taken at Johnson Matthey. a) STEM image of many particles showing homogeneity. b) Size distribution graph. c) HR-TEM image showing the intensity profile used to calculate the lattice parameter. d) HR-TEM image showing lattices of various particles on the surface of a larger ZnO particle. 93

Figure 4.17. SEI and EDX images of PtZn(PVP) particles taken at Johnson Matthey. Images show areas of sample with large ZnO particles. a) SEI showing large particles around 400 nm decorated with nanoparticles. b) EDX overlay of Zn (pink) and Pt (green). c) EDX map of Zn (pink). d) EDX map of O (red). 95

Figure 4.18. Investigation into areas of small PVP supported particles. a) STEM image of an area of smaller particles, and an enlarged section showing the corresponding EDX map, with Pt shown in green. b) EDX profile of the same area, indicating high Pt content and minimal Zn content. .96

Figure 4.19. A TGA profile for Pt(PVP) on heating from room temperature to 1000 °C while monitoring weight change. 98

Figure 4.20. Conversion rates of the polymer supported catalysts for the liquid phase formic acid decomposition reaction in the first 20 minutes.....99

Figure 5.1. Schematic showing the SBA-15 structure and the impregnation and reduction method of nanoparticle depositions. Image modified from reference[11]. 109

Figure 5.2. XRD profile showing Pt(SBA-15) nanoparticles. Observed intensity is shown in red, fitted intensity is shown in blue. Pt reference (00-004-0802) positions are shown in yellow.....112

Figure 5.3. STEM images and EDX mapping of Pt(SBA-15) sample. a) STEM image of representative area of Pt(SBA-15), and b) size distribution histogram from this area. c) STEM image and EDX maps showing distribution of Pt in red, Si in blue and O in green. 113

Figure 5.4. XRD profile showing PtAg(SBA-15) nanoparticles. Observed intensity is shown in red, fitted intensity is shown in blue. Pt reference (00-004-0802) positions are shown in yellow and Ag reference (00-004-0783) positions are shown in green.....114

Figure 5.5. STEM images and EDX mapping of PtAg(SBA-15) sample. a) STEM image of representative area of PtAg(SBA-15), and b) size distribution histogram from this area. c) STEM image and EDX maps showing Pt distribution (red) and Ag distribution (pink). 115

Figure 5.6. XRD profile showing PtNi(SBA-15) nanoparticles. Observed intensity is shown in red, fitted intensity is shown in blue. Pt reference (00-004-0802) positions are shown in yellow, Ni reference (00-004-0850) positions are shown in green and NiPt reference (03-065-2797) positions are shown in purple.....116

Figure 5.7. STEM images and EDX mapping of PtNi(SBA-15) sample. a) STEM image of representative area of PtNi(SBA-15), and b) size distribution histogram from this area. c) STEM image and EDX maps showing Pt distribution (red) and Ni distribution (blue). 117

Figure 5.8. STEM/EDX point analysis. a) STEM image showing the points analysed with EDX. b) EDX profile of point 1, an area with nanoparticles and c) EDX profile of point 2, an area where no nanoparticles are visible. 118

Figure 5.9. XRD profile showing PtZn(SBA-15) nanoparticles. Observed intensity is shown in red, fitted intensity is shown in blue. Pt reference (00-004-0802) positions are shown in yellow and Zn reference (00-004-0831) positions are shown in green. 119

Figure 5.10. STEM images and EDX mapping of PtZn(SBA-15) sample. a) STEM image of representative area of PtZn(SBA-15), and b) size distribution histogram from this area. c) STEM image and EDX maps showing Pt distribution (red) and Zn distribution (yellow).....120

Figure 5.11. a) STEM image with b) corresponding secondary electron image investigating the particle deposition.....121

Figure 5.12. APT diagram of the PtZn(SBA-15) sample with Pt plotted in red and Zn plotted in yellow. 122

Figure 5.13. Low energy ion scattering spectrum of PtZn(SBA-15), with the black line showing the composition at 0.06 nm and the red line showing the composition at 3.9 nm.....122

Figure 5.14. TPR showing the reduction behaviour of the monometallic samples, Pt in yellow, Zn in blue, and the PtZn(SBA-15) sample in red. 123

Figure 5.15. Wide angle x-ray scattering profiles obtained from each sample, with the metallic Pt phase shown in red below for comparison. 124

Figure 5.16. a) A comparison of measured Zn standard materials, and the isolated tetrahedron result of the FDMNES calculations. b) Zn K-edge XANES plot of the series of catalysts. c) A direct comparion of the Zn(SBA-15) Zn K-edge spectrum and the calculated result for a Zn isolated tetrahedron. Spectra prepared by Adam Clark. 125

Figure 5.17. a) Pt L_3-edge XANES profiles of two standard materials, platinic acid (PtO) and metallic Pt. b) Measured spectrum of Pt(SBA-15) and the three PtZn(SBA-15) samples.....126

Figure 5.18. Schematic to show the Si speciation and corresponding chemical shift values. Increasing the coordination to R (Zn or H) leads to a decrease in chemical shift value. 127

Figure 5.19. ^{29}Si and ^{1}H NMR deconvoluted and simulated spectra for the pure SBA-15 support and each PtZn(SBA-15) catalyst. 129

Figure 5.20. ^{195}Pt NMR spectra for Pt_8Zn_2(SBA-15) sample at the top. Deconvoluted and simulated reference spectra of Pt (middle) and PtO_2 (bottom). 131

Figure 5.21. Conversion rates of the silica supported catalysts for the liquid phase formic acid decomposition reaction in the first 20 minutes.....132

Figure 5.22. Conversion rates of the liquid phase formic acid decomposition reaction with the PtZn series of catalysts after reaction for 20 minutes. 135

Figure 5.23. Conversion rates of liquid phase formic acid decomposition reaction with three catalysts after 20 minutes (red) and 60 minutes (blue).....136

Figure 5.24. Conversion rates of liquid phase formic acid decomposition reaction with two PtNi(SBA-15) catalysts, one prepared with combined impregnation and reduction of both metals and the other with a two-stage impregnation and reduction of the metals. 137

Figure 5.25. Reaction cell used for in-situ XAS with the gas phase formic acid decomposition reaction at Diamond Light Source beamline B18. 137

Figure 5.26. Pt L_3-edge XANES spectra. a) Reference patterns for PtO (platinic acid) and Pt metal. b) Initial XANES spectra of PtZn(SBA-15) series. c) Final XANES spectra of PtZn(SBA-15) series after exposure to formic acid vapour. 138

Figure 5.27. Graph showing the extracted nanoparticle diameter (black) and Pt-Pt bond distance (blue), compared to the relative metallic Pt fraction (as shown in the inset plot). 139

Figure 5.28. Zn K-edge XANES spectra. a) Comparison of initial and final states for Zn(SBA-15). b) Reference Zn formate dihydrate spectrum(black) and initial calculate isolated tetrahedron (red). c) Final XANES spectra of PtZn(SBA-15) series. 140

Figure 5.29. Conversion profile of Zn silicate to Zn formate phase for each sample. 141

Figure 6.1. XRD profile for the Pt_1Ni_3 stepwise catalyst with the observed profile shown in red and the fitted profile in blue. Reference stick patterns are shown at the bottom for Pt (yellow), Ni (green) and NiPt alloy (purple). 150

Figure 6.2. XRD profile for the Pt_1Ni_3 co-reduction catalyst with the observed profile shown in red and the fitted profile in blue. Reference stick patterns are shown at the bottom for Pt (yellow), Ni (green) and NiPt alloy (purple). 151

Figure 6.3. TEM images showing homogeneity across the support and size distribution of both a) Pt_1Ni_3 stepwise and b) Pt_1Ni_3 co-reduction samples. 152

Figure 6.4. Size distribution histogram showing Pt_1Ni_3 stepwise (red) and Pt_1Ni_3 co-reduction (black) samples. 153

Figure 6.5. STEM & EDX images showing Pt_1Ni_3 stepwise samples. Pt is shown in red, Ni in green and O in purple. Figures a&b show an area of alloyed PtNi and figures c-f show an area of NiO_x coating the carbon support with Pt particles on the surface. 154

Figure 6.6. STEM/EDX images showing Pt_1Ni_3 co-reduction samples. Pt is shown in red, Ni in green and O in blue. a) HAADF STEM image, b-d) EDX maps of the same area, with Pt shown in red, Ni shown in green and O shown in blue. Note that c) shows an overlay of both Pt and Ni. 155

Figure 6.7. APT reconstruction of the Pt_1Ni_3/C stepwise sample showing Pt in red and Ni (or C) in green. 156

Figure 6.8. APT reconstruction of Pt_1Ni_3/C co-reduction sample showing Pt in red and Ni (or C) in green. a) shows areas of PtNi alloy and b&c) show areas of core-shell particles. 157

Figure 6.9. EXAFS fitting spectra for both Pt_1Ni_3 co-reduction and stepwise samples. a) Ni K-edge for co-reduction sample. b) Pt L_3-edge for co-reduction sample. c) Ni K-edge for stepwise sample. d) Pt L_3-edge for stepwise sample. 159

Figure 6.10. XRD profile for the Pt_1Ni_3 reverse-stepwise catalyst with the observed profile shown in red and the fitted profile in blue. Reference stick patterns are shown at the bottom for Pt (yellow), Ni (green) and NiPt alloy (purple).....160

Figure 6.11. a) TEM image showing homogeneity across the support and b) size distribution histogram of the Pt_1Ni_3/C reverse-stepwise sample. 161

Figure 6.12. XRD profile for the Pt_1Ni_1 stepwise catalyst with the observed profile shown in red and the fitted profile in blue. Reference stick patterns are shown at the bottom for Pt (yellow), Ni (green) and NiPt alloy (purple).....162

Figure 6.13. XRD profile for the Pt_1Ni_1 co-reduction catalyst with the observed profile shown in red and the fitted profile in blue. Reference stick patterns are shown at the bottom for Pt (yellow), Ni (green) and NiPt alloy (purple).....163

Figure 6.14. TEM images showing size distribution and homogeneity across the support of Pt_1Ni_1/C both a) stepwise and b) co-reduction samples. 164

Figure 6.15. Size distribution histogram showing Pt_1Ni_1 both stepwise (red) and co-reduction (black). Samples size of 160 particles for both samples. Note that 6 outliers were observed for the co-reduction sample with diameters of 15-40 nm. 165

Figure 6.16. TEM image showing the Ni(SBA-15) sample prior to impregnation of Pt. SBA-15 channels do not appear to contain large Ni particles. 166

Figure 6.17. TPR profile of 10 wt.% Ni(SBA-15) in red and 2 wt.% Ni(SBA-15) in blue. 167

Figure 6.18. TPR profile showing the reduction of 10 wt.% PtNi(SBA-15). 168

Figure 6.19. Schematic proposal of the synthesis mechanism when utilising the SBA-15 wall effect and varying the synthesis route. 170

Figure 6.20. Cyclic voltammograms of the four catalyst species along with the commercial Pt reference sample. Electrochemical surface area was calculated from the area of the H desorption peak.....172

Figure 6.21. LSV plots of the whole series of catalysts as well as the Pt commercial catalyst. .174

Figure 6.22. a) Mass activity and b) Surface area activity bar charts for four synthesised catalyst samples and the commercial Pt reference catalyst. 175

Figure A1.1. Dark field time-lapse of PtAg(PVP) at sample point A, with one image taken every 5 seconds for 45 seconds. Ag seeds can be seen to aggregate and move towards the larger Ag particles.....188

Figure A1.2. Three dark field images of PtAg(PVP) at sample point A. The first shows the beam damage to the sample after the time-lapse above, the empty area around the large particles shows the areas which the seed particles have moved from. The middle image shows the frequent large Ag particles across the sample. The final image shows the smaller seed particles of around 5 nm dominating the reaction mixture.....189

Figure A1.3. Three dark field images of PtAg(PVP) at sample point B. The image on the left shows the large particles around 50 nm remain in the sample, with the smaller seed particles throughout the sample. The middle image shows the seed particles are still throughout the PVP, although some are more agglomerated as seen in the third image. 189

Figure A1.4. Three dark field images of PtAg(PVP) at sample point C. The first image shows that the particle sizes have remained the same after H_2 bubbling, with some large particles and many smaller seeds. The middle image shows that the seeds are well dispersed throughout the sample and the agglomeration has diminished. The final image shows the increase in seed size after the electron beam was held on the area for 30 seconds. The seed particles are fluidized and grow, likely through an Ostwald ripening process. 190

Figure A1.5. SEI images showing PtAg(PVP) at sample point D. The first image shows that the particle sizes have remained the same, with some large particles and many smaller seeds. The middle image shows chain-like structures of the smaller particles. The final image shows the decoration of smaller particles on the surface of the larger particles. ……... 191

Figure A2.1. Blank SBA-15 XRD profile showing high background between 20-35 °2θ 193

Figure A2.2 a&b) TEM images showing Pt_5Zn_5(SBA-15). Average diameter of the particles was measured to be 3.2 nm (± 2.3 nm, n=105). 194

Figure A2.3. a) TEM image of Pt_8Zn_2(SBA-15). b) EDX maps indicating Pt in red and Zn in yellow, along with C (bright yellow), O (green) and Si (blue). The mean diameter of the particles is 3.1 nm (± 1.5 nm, n=150). 194

Figure A2.4. a) TEM image of Pt(SBA-15). b) EDX maps indicating Pt in red, along with C (yellow), O (green) and Si (blue). The mean particle diameter is 3.2 nm (± 2.2 nm, n=101). 195

Figure A2.5. TEM and EDX mapping of Zn(SBA-15) showing Zn in green, along with O in red and Si in orange. 195

List of tables

Table 3.1 EXAFS fitting results for the PtAg(PVP) sample. The Ag-Ag scattering path was fitted from the Ag K-edge data, and the Pt-Pt and Pt-Ag scattering paths were fitted from the Pt L_3-edge data.....85

Table 3.2. EXAFS fitting results for the PtNi(PVP) sample. Ni-O and Ni-Ni scattering paths were fitted from the Ni K-edge data and the Pt-Ni and Pt-Pt scattering paths were fitted from the Pt L_3-edge data. 91

Table 3.3. EXAFS fitting results for the PtZn(PVP) sample. Zn-O and Zn-Zn scattering paths were fitted from the Zn K-edge data and the Pt-Pt scattering path was fitted from the Pt L_3-edge data. 97

Table 3.4. Summary table of sample particle sizes and lattice parameters. 101

Table 3.1. Table showing the refined Pt lattice parameter for the samples obtained through peak fitting of the (111) reflection. 124

Table 3.2. ^{29}Si MAS NMR data with speciation percentage identified for each sample and for the pure SBA-15 support. 130

Table 3.3. Summary of catalyst conversion rate, lattice parameter (as calculated from XRD) and the difference in work function of Pt and the secondary metal. 134

Table 3.4. Summary table of sample particle sizes and lattice parameters. 142

Table 6.1. Table showing the EXAFS scattering paths and the corresponding distance, coordination number, Debye-Waller factor and energy difference for both Pt_1Ni_3 co-reduction and stepwise samples. Error is given in brackets as distance $x10^{-2}$ and Debye-Waller factor $x10^{-3}$..158

Table 6.2. Table showing ICP results for each catalyst compared to calculated stoichiometries. 171

Table 63. Catalytic mass and electrochemical surface area of each sample. Pt_1Ni_1 co-reduction mass value is estimated from the ICP results of the Pt_1Ni_1 stepwise sample and so is shown in italic in this table.....173

Table 6.4. Summary table of sample particle sizes and lattice parameters. 176

List of abbreviations and symbols

ALD	Atomic layer deposition
APT	Atom probe tomography
CPMAS	Cross-polarisation magic angle spinning
CV	Cyclic voltammetry
DFT	Density functional theorem
ECSA	Electrochemical surface area
EDX	Energy-dispersive x-ray spectroscopy
EXAFS	Extended x-ray absorption fine structure
FWHM	Full width half maximum
HAADF	High-angle annular dark field
HR-TEM	High resolution transmission electron microscopy
(HS)-LEIS	(High Sensitivity) Low energy ion scattering
LSV	Linear sweep voltammetry
MAS	Magic angle spinning
MW	molecular weight
NMR	Nuclear magnetic resonance
ORR	Oxygen reduction reaction
PEM	Polymer exchange membrane
PGM	Platinum group metal
PVP	polyvinylpyrrolidone
RDE	Rotating disk electrode
RF	Radio frequency
SBA-15	Santa Barbara amorphous - 15
STEM	Scanning transmission electron microscopy

TEM	Transmission electron microscopy
TGA	Thermogravimetric analysis
TPR	Temperature programmed reduction
UHV	Ultra-high vacuum
XANES	X-ray near edge structure
XAS	X-ray absorption spectroscopy
XPS	X-ray photoelectron spectroscopy
XRD	X-ray diffraction

List of publications

1. M. M.-J. Li, J. Zheng, J. Qu, F. Liao, E. Raine, W. C. H. Kuo, S. S. Su, P. Po, Y. Yuan and S. C. E. Tsang, *Sci. Rep.*, 2016, **6**, 20527.

2. Y.-K. Peng, C. N. P. Lui, Y.-W. Chen, S.-W. Chou, E. Raine, P.-T. Chou, K. K. L. Yung and S. C. E. Tsang, *Chem. Mater.*, 2017, **29**, 4411–4417.

3. B. Yu, T. Ayvali, E. Raine, T. Li, M. M-J. Li, J. Zheng, S. Wu, A. A. Bagabas and S. C. E. Tsang, Chemical Science, 2018, Submitted.

4. E. Raine, A. Clark, G. Smales, A. Smith, D. Gianolio, T. Li, J. Zheng, T. Hyde, M. Feaviour, P. Collier, G. Sankar and S. C. E. Tsang, ACS Catalysis, 2018, Submitted.

5. S. Nayak, E. Raine, F. Niu, S. Fairclough, T. Li, S. Wu, A. Erbe, K. Vincent and S. C. E. Tsang, 2018, In preparation

Chapter 1

Introduction

1.1 Principles of catalysis 2
1.1.1 Types of catalysis 5
1.1.2 Theory of heterogeneous catalysis 6
1.2 Nanoparticle catalysis 9
1.2.1 Nanoparticle stabilisers and support effects 12
1.3 Bimetallic catalysis 14
1.3.1 Electronic effects 14
1.3.2 Geometric effects 15
1.3.3 Bimetallic morphologies 17
1.3.4 Platinum bimetallic catalysts 18
1.4 Formic acid decomposition 20
1.5 Oxygen reduction reaction 22
1.6 Aims and objectives 26
1.7 Thesis overview 27
1.8 References 28

1.1 Principles of catalysis

It is a widely accepted fact that the global environment is changing, with a rise in mean global temperatures, an increase in extreme weather events and widespread changes in weather patterns.[1] The rapid increase in temperature is highlighted by the fact that each of the last 17 years has been included in the top 18 warmest years, as recorded by the American National Oceanic and Atmospheric Association.[2] With temperatures rising with increasing rate since the 1900s, this rapid rise in temperature has been correlated to the rise in global industrialisation which has enhanced the greenhouse effect.[3] This is the effect by which gases in the atmosphere trap the solar radiation reflected by the Earth, causing a heating effect of the atmosphere. Common greenhouse gases include CO_2, CH_4 and N_2O. As a result of population and economic growth, as well as the increasing global industrialisation, the anthropogenic emissions of these gases has rapidly increased.[4,5]

There is a serious need for more environmentally friendly chemical processes as over 21% greenhouse gas emissions are produced by industry, 25% from electricity and heat production and 14% from transport,[6]. In 1998, the United States Environmental Protection Agency set guidelines on how to increase the sustainability of the chemical industry. One of their 12 principles of Green Chemistry is to use catalysts rather than stoichiometric reagents in order to minimise waste. Catalysts can be used to reduce harsh reaction conditions and minimise unwanted side products, leading to more environmentally friendly reactions in industry, transportation and electricity production.

In the early 1800s, scientists began to notice that chemical reactions could be affected by trace amounts of a substance which was not consumed in the reaction. One of the first observations of catalysis was by Davy, when researching miners safety lamps. On the addition of a platinum spiral near an ignited wick in the presence of coal gas (methane), he found that the platinum would continue to glow white hot even after the wick was extinguished.[7] The hot platinum wire would

continue to catalyse the oxygen and methane without the flame, keeping the platinum wire incandescent. He described this in a letter as "*more like magic than anything else I have seen*".[8] One of the most important investigations leading to the discovery of catalysis was by Johan Döbereiner in 1823, when he found that platinum could be used to ignite a stream of hydrogen.[9] This ultimately led to the production of the first lighter and by 1828 over 20,000 Döbereiner lighters were used in England and Germany.[10]

Attempts were made to rationalise these phenomena, however it was not until 1836 when Berzelius first coined the term catalysis when writing in a review "*Catalytic power actually means that substances are able to awake affinities which are asleep at this temperature by their mere presence and not by their own affinity… to which they remain indifferent*".[11] After over 180 years of studying catalysts, it is now possible to improve the definition of catalysis. A catalyst is now defined as a "*substance which when present in small amounts increases the rate of a chemical reaction or process but which is chemically unchanged by the reaction*". Catalysis is "*the phenomenon of a catalyst in action*".[12,13]

It is now known that a catalyst works by creating an alternative path for the reaction with a lower activation energy barrier. For all processes, the reaction rate is governed by the Arrhenius Equation (Equation 1).

$$k = A\, e^{-\frac{E_a}{RT}} \qquad \textit{(Equation 1)}$$

Where k is the rate constant for the chemical reaction, A is the pre-exponential factor, E_a is the activation energy, R is the universal gas constant and T is the temperature in Kelvin.

In the absence of a catalyst, the activation energy remains constant and so the rate is dependent on temperature, with an increase in temperature leading to an increase in rate. In some cases, the activation energy is so high that it is not industrially viable to simply increase the temperature.[14]

However, in many systems it is possible to use a catalyst to decrease the activation energy, which leads to an increase in the rate without increasing the temperature.

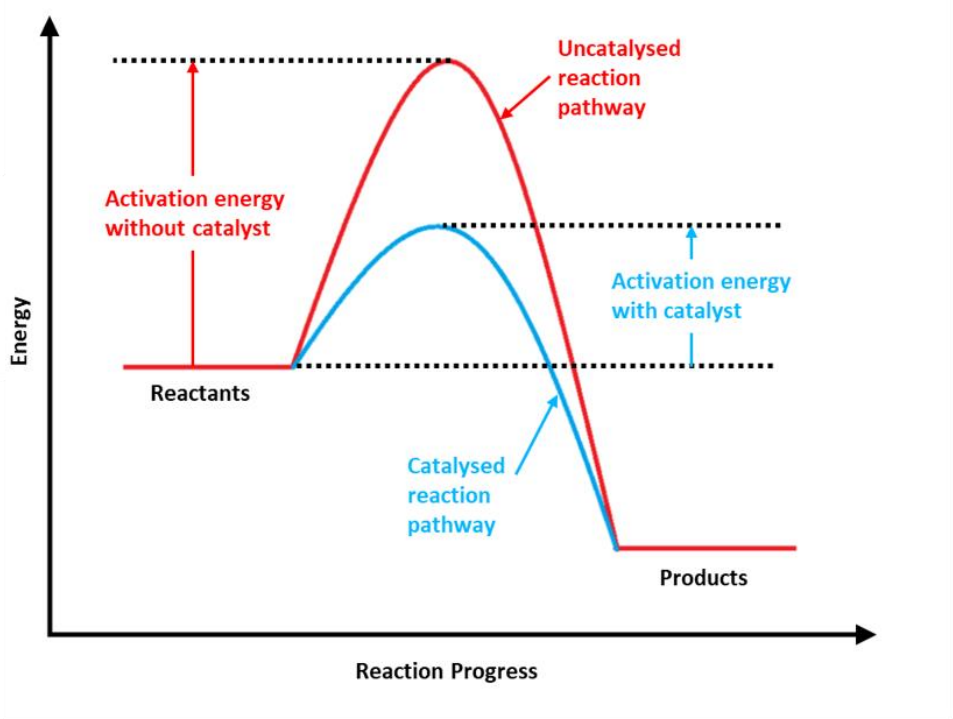


Figure 1.1. A simplified schematic energy profile for an exothermic reaction, with the catalysed route in blue and the uncatalysed route in red.

Figure 1.1 shows a simplified diagram of the two reaction pathways for a catalysed and uncatalysed reaction. The decrease in the transition state energy of the catalysed reaction is shown to decrease the activation energy and thus would increase the rate of the reaction. Although the decrease in transition state causes a change in kinetics between the two routes, the unaltered energy levels of the reactants and products mean that the thermodynamics of the reaction remain unchanged.[13] The equilibrium position of the reaction is always governed by the Gibb's Free Energy, Equation 2, where for the reaction to proceed spontaneously $\Delta G < 0$. Where $\Delta G > 0$, the equilibrium position will lie towards the reactants and the product yield will be very low. Thus, a catalyst cannot speed up a thermodynamically unfavourable reaction.

$$\Delta G = \Delta H - T\Delta S \qquad \textit{(Equation 2)}$$

Where ΔG is the Gibb's free energy for a reaction, ΔH is the enthalpy change, T is the reaction temperature and ΔS is the entropy change.

1.1.1 Types of catalysis

All catalysts share the same principle in that they decrease the activation energy of the reaction, however with each reaction thermodynamically different, the best catalysts are often highly specific and tailored to the reaction. Although there are many different catalysts, they can all be assigned to one of 3 categories: homogeneous catalysts, biocatalysts and heterogeneous catalysts.

A homogeneous catalyst is one which is in the same phase as the reactants used, which is often the liquid phase. Homogeneous catalysts most commonly take the form of organometallic complexes, where a metal centre is stabilised with the surrounding ligands. It is possible to achieve a high level of control over the metal complex through modification of the ligands, leading to electronic and steric changes at the metal centre active site.[15,16] This means that these catalysts are often used either in industries which require specific products with few impurities or those where product chirality is important, such as the pharmaceutical industry.[17] However, as the catalyst is in the same phase as the reaction, separation is more difficult and can be costly.

Biocatalysis is the process of using biologically occurring enzymes as catalysts. These cannot be classified as either heterogeneous or homogeneous catalysts as, although they operate in the same phase as the reaction, the organic framework is considerably larger than traditional homogeneous catalysts. Enzyme catalytic activities can be very high[18] and, with the complex protein structure leading to defined active sites, increased selectivities are very common.[19] These catalysts perform well under mild conditions, however they are highly sensitive to temperature, pressure and pH, therefore are unsuitable for most industrial processes.[20]

Heterogeneous catalysts are those which are found in a different phase to the reactant, most commonly as solids, with the reactants in the liquid or gas phase. Solid catalysts are most common

because of their durability under high temperatures and pressures and because of the relative ease of catalyst separation from the reaction.[21] Often high throughput flow reactors are used, with solid heterogenous catalysts packed into a fixed bed and the liquid or gas reactants passed across the catalyst.[22] One example of this type of catalyst is in the catalytic converter of an exhaust, where the exhaust gases are passed through a monolith coated in catalyst material.[23] The ease of separation is seen as a vital benefit, with traditional heterogeneous catalysts making up 85-90% of the market share for all catalysts sold.[24,25]

Both homogeneous catalysts and biocatalysts use a single metal atom centre for catalysis, however heterogeneous catalysts often use the solid metal surface. This allows reactants to adsorb on neighbouring surface metal atoms to stabilise the transition state.[26]

1.1.2 Theory of heterogeneous catalysis

In Figure 1.1, the catalytic pathway had a lower transition state energy than the uncatalysed reaction. However this model is simplified down to one step, where in reality the catalysed pathway will consist of multiple stages in the reaction. When using a heterogeneous catalyst, the reaction occurs on the catalyst surface and so the complete catalytic reaction will consist of at least an adsorption, reaction and desorption step. Each step in the reaction will have its own activation energy but none will be higher than that of the uncatalysed reaction, as shown in Figure 1.2. The catalysed reaction will also have many intermediates, which must all be less stable than the final product. This is because the reaction will stop at the most stable species, as shown by the dotted line in Figure 1.2.

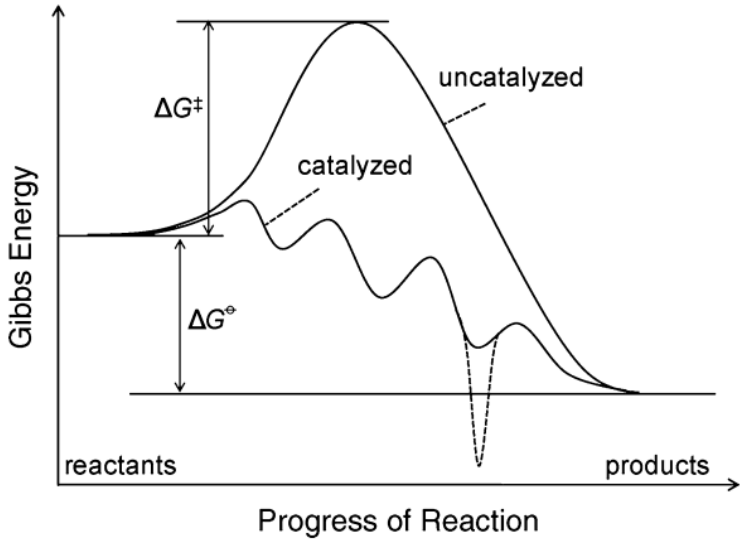


Figure 1.2. Schematic comparison of a catalysed reaction and an uncatalysed reaction. Reprinted with permission from J. Heveling, J. Chem. Educ., 2012, 89, 1530–1536. Copyright 2012 American Chemical Society.[23]

There can be many steps in a catalytic reaction, in addition to adsorption and desorption including the dissociation, activation and reaction of adsorbates. The process with the highest activation energy is the catalytic rate determining step, assuming the reaction is not operating under diffusion control.[27] Often the step with the highest activation energy is the chemisorption of the reagent onto the surface of the catalyst, and so one would expect that the catalyst activity would be enhanced by a strong catalyst-reagent bond. However, in order for the catalyst to be recycled, the products must dissociate from the surface and so the product-catalyst bond must be weak. Sabatier's Principle suggests that there must be a medium bond strength between reactants, intermediates and the products for a highly active catalyst.[28,29] This concept was represented visually by Balandin when he plotted the enthalpy of adsorption of formate onto a metal surface against the temperature at which the reaction proceeded. This formed a volcano plot,[30] as shown in Figure 1.3.

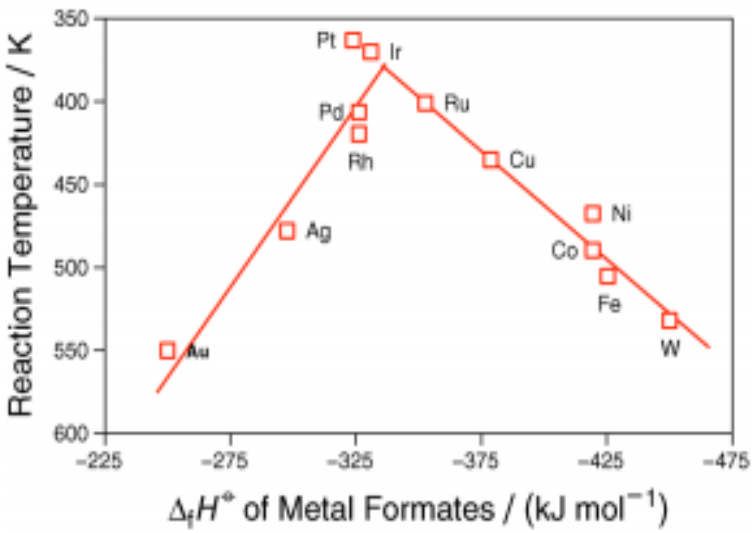


Figure 1.3. Volcano plot representing the adsorption of formate onto a metal surface and the temperature required for the dehydrogenation reaction to occur. Reproduced from reference[23].

The catalysts with the optimum activity are shown at the peak of the volcano with the lowest reaction temperatures. These metals have intermediate enthalpies of adsorption, whereas the metals to the left bind too weakly to reactants which results in high activation energies and metals to the right bind too strongly which leads to catalyst surface coverage and high dissociation energies. This leaves a small selection of metals which are deemed appropriate for each reaction, however further tailoring of activity can be done by using modifiers, by alloying, or by forming specific surface structures.[31] Catalytic activity and selectivity can be refined by controlling the surface active sites of heterogeneous catalysts.[26]

The use of the d-band model is widely accepted to explain perturbations in binding strengths of adsorbates to surfaces.[32] The one-electron state in the adsorbate will interact with the valence states of the surface atoms. These transition metal surface atoms have both s- and d-states which combine to form the s- and d-band. The s-band is half filled for all transition metals and the d-band is much more varied across the periodic table, although all the d-bands are much narrower than the broad s-bands, as shown in Figure 1.4a. The narrow d-bands often diverge to form a bonding and antibonding band upon interaction with the adsorbate, as shown in Figure 1.4b.

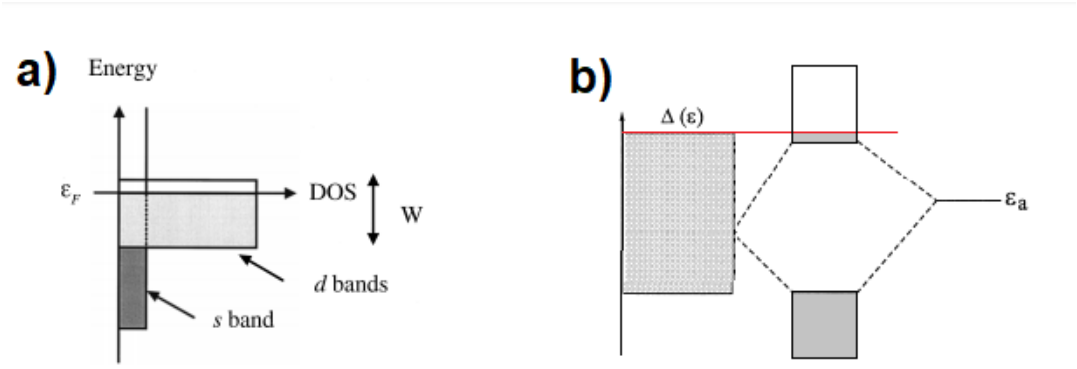


Figure 1.4. Schematic band structure diagrams, a) showing the broad half-filled s-band and narrow d-band. b) shows the splitting of the narrow d-band into bonding and antibonding states, with the Fermi level shown in red. Images reproduced and modified from reference[32].

Often for noble metals the Fermi level is at an energy similar to the antibonding bands, and the bonding is strongest when these are empty. As the transition metals are crossed to the right of the periodic table, the number of d-electrons increases, the antibonding band becomes more filled, and the metal-adsorbate bond weakens. An additional method to change the filling of the antibonding band is to change the metal d-band centre, which leads to a change in energy of the bonding and antibonding bands with respect to the Fermi level. On increasing the d-band centre, the antibonding band becomes higher in energy. This means fewer states in the antibonding band are filled and the adsorbate-surface bond is stronger. The opposite effect is seen when the d-band centre is lowered in energy.[33] Thus, where the metal binds too strongly with the adsorbate, alloying with another metal can be used to decrease the d-band centre which weakens the adsorbate-surface binding.

1.2 Nanoparticle catalysis

Heterogeneous catalysis has been used for over 100 years in industry, with the most common catalysts being composed of highly dispersed metal nanoparticles supported on a support of high surface area.[31] However, until recently, the means of characterising these particles were minimal. Advances in characterisation methods over the last 20 years have led to a substantial increase in the amount of research done on these systems, as can be shown by the increase in publications in

this area, Figure 1.5. With this dramatic increase in nanoparticle characterisation research, the nanoparticle market was worth $12 billion in 2017 and is expected to continue growing to $25 billion by 2022.[34]

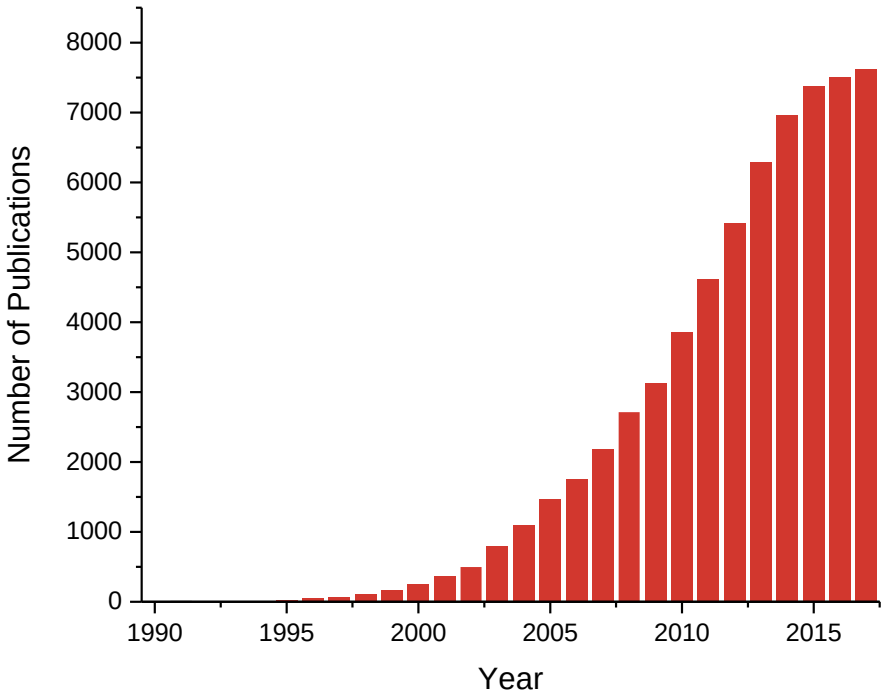


Figure 1.5. Number of publications related to nanoparticle catalysts each year from 1990 to 2017. Collated through searching "nanoparticle catalyst" in SciFinder.

The volcano plot in Figure 1.3 highlighted that the most highly active catalysts for formic acid decomposition were platinum, iridium, palladium, rhodium and rhenium, all of which are expensive metals. In addition, unlike homogeneous catalysts or biocatalysts with one active metal centre, heterogeneous catalysts only have active metal atoms at the surface of the particle for heterogeneous catalysts. At the time of preparation of this thesis, the price of platinum was $942 /oz[35] which makes bulk metal heterogeneous catalysts economically infeasible.

One of the reasons why nanoparticle catalysis has become increasingly popular with industry is due to the high activity of the platinum group metals (PGMs). Through decreasing the particle size, a greater proportion of the atoms become surface atoms which leads to a higher surface area to volume ratio for smaller particles. In the case of heterogeneous catalysis, where the catalytic

reaction occurs on the catalyst particle surface, fewer ineffective core atoms increases cost efficiency.

In addition to the increase in proportion of surface atoms, nanoparticles can show changes in reactivity due to their electronic structure. The most obvious example of this is the case of nanogold, which has been studied for many years. When gold is in its bulk state, its reactivity is very low and it is said to be inert. However as the gold particles transition to nanoparticles changes to the d-band structure lead to considerably enhanced catalytic properties. Gold nanoparticles of 5 nm are highly active catalysts for many reactions, including CO oxidation and the hydrochlorination of acetylene.[36,37]

In the bulk metal the d-orbitals from an extremely large number of metal atoms overlap to form a complete and continuous band structure, where the spacing between energy levels (δ) is calculated by Equation 3:

$$\delta = \frac{E_f}{n} \qquad \textit{(Equation 3)}$$

Where n is the number of atoms in the particle and E_f is the energy of the Fermi level for the metal.[38]

In the bulk metal the number of atoms is sufficiently large that the spacing between the energy levels is negligible. Figure 1.6 shows the transition from bulk metals through nanoparticles to single molecules, as well as their corresponding band structures and molecular orbital energies. As the number of atoms in the system decreases, an increase in space between the energy levels and between the bands is observed. As this number continues to decrease, so that the system resembles an individual molecule, the band structure devolves and the discrete molecular orbitals are formed. The unusual properties of nanoparticles arise from the gradual changes in the d-band structure, where the electrons become more localised to the individual atoms whilst maintaining some aspects of the band structure.[39]

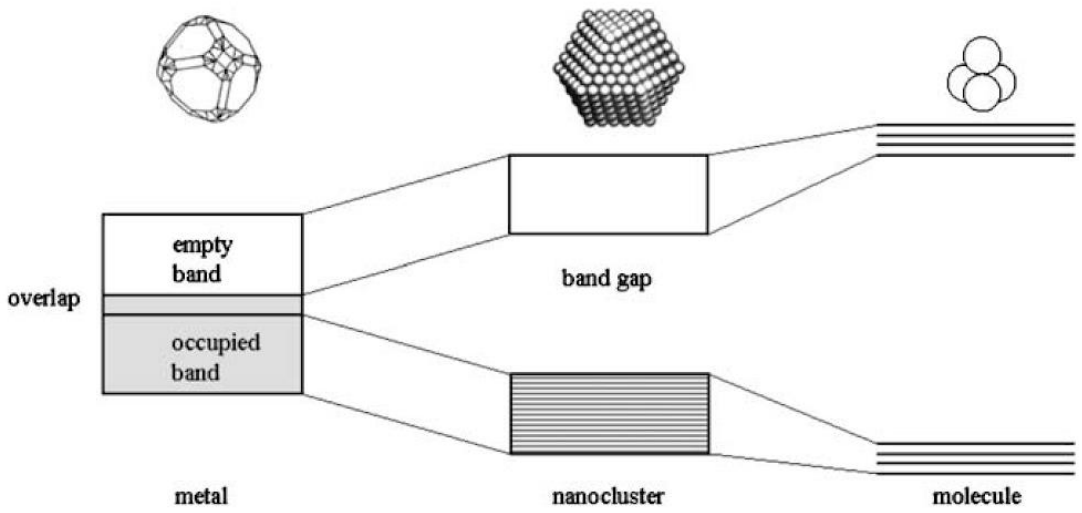


Figure 1.6. Schematic showing change of band structure from bulk metals to nanoparticles and the orbitals of isolated molecules. Reproduced from reference[38].

Decreasing the particle size leads to increased activity for heterogeneous catalysts, as a larger proportion of the atoms are surface atoms.[39,40] However these surface atoms are not fully coordinated and so have a higher surface energy, leading to particle instability. The high surface energy leads to particle aggregation, decreasing the particle size and increasing stability.[41] Techniques such as steric blocking with stabilisers and the tethering of nanoparticles to supports can be used to reduce surface energy and abate particle aggregation.[42,43]

1.2.1 Nanoparticle stabilisers and support effects

There are two main methods of nanoparticles stabilisation: encapsulation in a polymer stabiliser and deposition of nanoparticles onto a high surface area support. One polymeric stabiliser commonly used is polyvinylpyrrolidone (PVP), which is a long aliphatic chain with repeating hydrophilic pyrrolidone ring units attached.[44] The pyrrolidone ring can bind to the metal nanoparticle surface through the carbonyl oxygen, while the long hydrophobic alkyl chain wraps around the particle and creates a repulsive interaction with other encapsulated particles.[45,46] There are many factors which can affect the success of a polymer as a stabiliser, including its chain length, the functional groups of the repeating unit and the ratio of polymer to metal.[47,48] Usually

these surfactants are successful stabilisers for stopping aggregation, but occasionally the polymer chain can attach to more than one metal particle and cause a "beads on a string" morphology, where multiple particles are touching.[49]

An alternative method to prevent agglomeration is to tether the nanoparticles to a support of high surface area, which leads to reduced mobility and an increase in particle stability.[50] Common supports include metal oxides, silica, alumina and activated carbon, and require a high surface area to maintain high particle dispersion.[43] Supported nanoparticles can be synthesised in many ways and can form specific morphologies, however control is challenging and is often dependent on the binding strength of the metal to the support.[51] Sintering and deactivation can still occur under reaction conditions if the particles are not strongly bound to the support,[52] although this is greatly decreased compared to an unsupported material. Porous support materials can also be used to control the size of the particle growth, ensuring that the particles do not grow to larger than the channel diameter. Microporous materials can be used to support small metal clusters whereas mesoporous materials can promote the formation of nanoparticles. SBA-15 is a well ordered hexagonal mesoporous silica structure of two-dimensional channels.[53] It has been investigated recently as a support material and has been shown to yield greater catalytic activity than other supports.[54–56]

One interesting postulation behind this enhanced activity could be that the interaction between the metal and the support channels is particularly strong in the SBA-15 system, which may lead to bimetallic segregation and differing reactivities. The metal-support interaction is a well-researched occurrence, with the support often causing a perturbation in the catalyst activity.[57,58] This was first reported when it was noticed that PGM nanoparticles which are supported on titania lose their ability for H_2 and CO chemisorption. This was attributed to the change in metal charge as a result of the interaction between the metal and the electrons of the titania.[58] The interaction of platinum

with silica and carbon has been shown to be minimal, but the effect with transition metals can be much larger.[59,60]

1.3 Bimetallic catalysis

Combining a metal near the top of Sabatier's volcano plot with a secondary transition metal can increase the cost efficiency, as the highly active metals are often very expensive, and also enhance the activity of the initial metal. When combining PGMs with these secondary metals, it is usual for the PGM to be the active site for the catalysis, with the secondary metal in close contact.[61,62] Adding a secondary metal to a system has also been shown to decrease nanoparticle aggregation.[63] Many of these bimetallic catalysts have been seen to show superior activity or selectivity compared with their monometallic counterparts,[64,65] with most explanations for this focusing on site blocking and favourable electronic changes. In Section 1.1.2, the balance of adsorbate binding strength needed for optimum catalytic ability and how the d-band theory model showed that decreasing the d-band centre led to a decrease in metal-adsorbate bonding was discussed.[32,33] The d-band centre can be modified through both electronic and structural effects of alloying the catalyst material.

1.3.1 Electronic effects

The most common explanation for the increase in catalytic activity in bimetallic catalysts is due to the electronic effect introduced by the secondary metal.[66,67] Jones *et al.* studied the effect of PdAg on the formic acid decomposition reaction and concluded that the decoration of palladium with silver increases the electron density on the palladium, which increases the activity of the reaction.[68] This was attributed to the silver donating electron density to the palladium, because the silver has a lower work function.[69] When electrons are added to the platinum d-band, the energy of the d-band centre is reduced which causes the antibonding band to also decrease in energy.[70] This leads to filled states in the antibonding region and therefore weakening of the metal-adsorbate bond.[33] The volcano plot in Section 1.1.2 showed that palladium had stronger binding with formate

than the expected optimum conditions[23] and so alloying with silver could lead to the weakening of this bond and an increase in the catalytic ability.

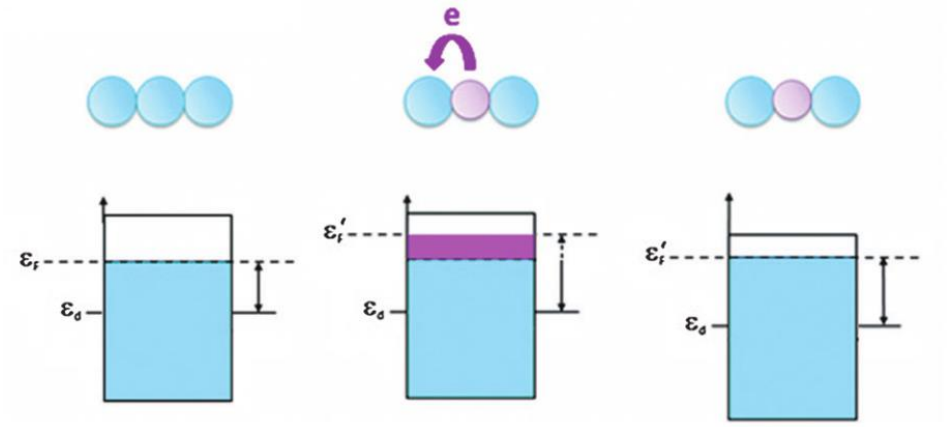


Figure 1.7. Schematic to show the addition of a secondary metal (purple) donating electrons to the PGM (blue), leading to increased filling of the d-band and a down-shift of the d-band centre. Reproduced from Ref. 70 with permission from the PCCP Owner Societies.

Figure 1.7 is a schematic showing the increase in electron density in the d-band after addition of the electron-donating secondary metal. In order to maintain the Fermi level, the d-band centre is lowered which leads to more anti-bonding states being filled and hence the weakening of the adsorbate bond. On addition of a metal with a higher work function, electron density is transferred to the secondary metal which leads to a reverse of this process and hence a stronger metal-adsorbate bond. This perturbation can also be termed the "ligand effect", in order to distinguish between the effects of geometric strain on the electronics of the material.

1.3.2 Geometric effects

In addition to the ligand effect changing the position of the d-band centre, an additional perturbation in shape and centre of the d-band is caused by strain effects in bimetallic particles. As shown in Figure 1.8, depositing a thin layer of active metal on the surface of a secondary metal can change the active metal interatomic distance. In cases where the secondary metal has a smaller lattice, the active metal is subject to compressive strain and a contraction in the surface lattice can be observed. Similarly, where the secondary metal has a larger lattice, the active metal undergoes

tensile strain and there is an expansion in the surface lattice. This modification of lattice parameter leads to a change in the d-band shape. In cases where the atoms are further apart, the d-orbitals overlap less and the d-band narrows which leads to an up-shift of the d-band centre. Likewise, in cases where the atoms are closer together, the d-orbital overlap increases and the d-band becomes broader, causing a down-shift in d-band centre.

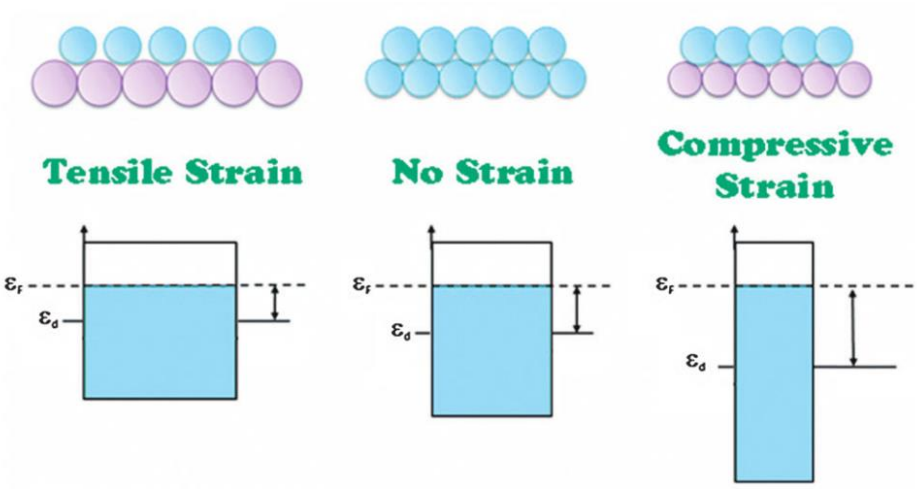


Figure 1.8. Schematic showing the variation in d-band under tensile and compressive strain. Reproduced from Ref. 70 with permission from the PCCP Owner Societies.

It is noted that the impacts of the ligand effect and the geometric strain effect on the change in d-band centre are hard to separate and so the overall impact on the d-band centre is more widely used to predict catalytic behaviour than either one individually.

In addition to the effect on the d-band centre, the geometric strain effect can also cause a steric effect on the binding of bidentate materials. When a bidentate adsorbate binds to two adjacent surface atoms, the distance between these atoms is important to the binding strength of the adsorbate, as well as to any adsorbate dissociation steps along the reaction pathway. Figure 1.9 shows three models with various types of geometric strain and the impact of this on formate binding. Figure 1.9a shows the surface layer under compressive strain, with a contraction in the surface atoms allowing a direct overlap of formate and the surface atoms. Figure 1.9c shows the surface layer under tensile strain with an expansion of the surface lattice causing a worse overlap

with the formate molecule. Figure 1.9b shows the monometallic metal with no surface perturbation, where the formate binds moderately well with the adjacent atoms.

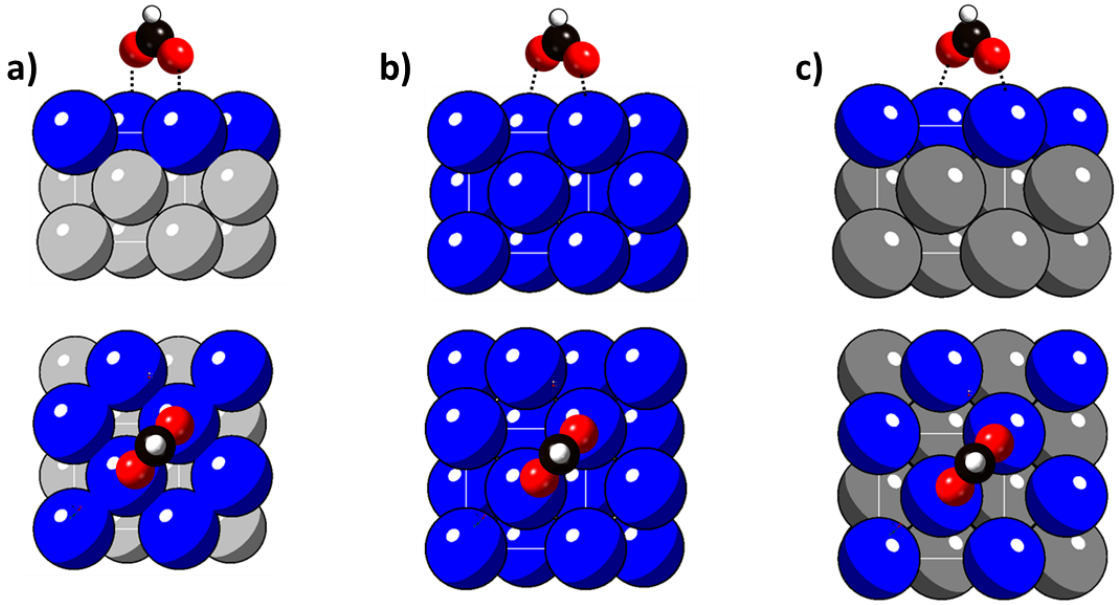


Figure 1.9. Schematic diagrams showing the steric effect of strain on a bidentate binding adsorbate. a) shows the surface layer under compressive strain, with the surface atoms contracted in lattice. b) shows the original mono-metallic sample. c) shows the surface layer under tensile strain with the surface atoms expanded in lattice. Each sample shows both the side on view (top) and top down view (bottom), with the formate ion binding to adjacent surface atoms. Models were produced in CrystalMaker with the surface atoms in all diagrams having the parameters of platinum (blue), and the subsurface atoms in a) having the metal parameters of nickel (pale grey) and in c) having the metal parameters of silver (dark grey).

1.3.3 Bimetallic morphologies

Nanoparticle alloys can form many morphologies including core-shell, hetero-junction and homogeneous, as shown in Figure 1.10. Core-shell and hetero-junction particles are often synthesised by the formation of a host particle with the subsequent deposition of a decorating metal to the surface, whereas homogeneous mixed alloys are more commonly formed from co-precipitation.[71] Alloy mixing is not only dependent on synthesis methods but also on surface segregation energies, with segregation more commonly giving an island or core-shell type nanoparticle and anti-segregation more commonly giving homogeneously mixed alloys. Nørskov *et al.* calculated segregation energies of transition metal alloys and showed that platinum has anti-segregation with most transition metals.[72]

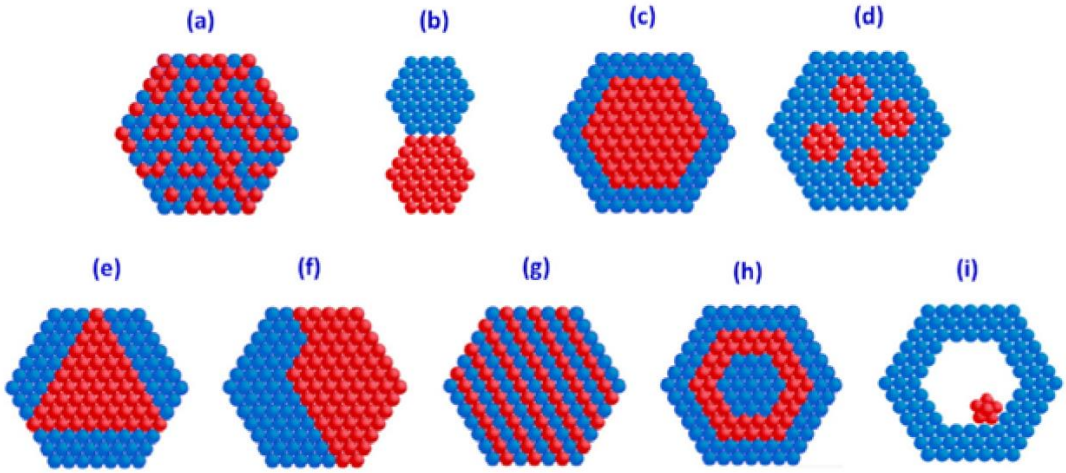


Figure 1.10. Schematic diagrams of a selection of morphologies of bimetallic nanoparticles. Morphologies mentioned in this thesis include a) mixed alloy, b) island clusters, c) core-shell nanoparticles and d) multiple small core material coated in single shell material. Republished with permission of Royal Society of Chemistry, from A. Zaleska-Medynska, et.al, Adv. Colloid Interface Sci.*, 2016, 229, 80–107; permission conveyed through Copyright Clearance Center, Inc.*[73]

Core-shell particles are ideal for improving the number of PGM surface sites, whilst maintaining close contact with the secondary metal.[74] In addition to the enhancement in catalytic behaviour, a core-shell geometry minimises the percentage of PGM in the particle core and is therefore also cost efficient. Although core-shell particles are often formed through preparation of a core particle followed by deposition of the shell overlayer, in order to form the morphology desired, the particles are known to relax to their thermodynamically favoured morphology. The overall particle with the lowest energy will be formed when the metal with the lower surface energy is at the shell and the one with the higher surface energy at the core.[75,76] Additionally, atomic size may also affect the morphology, with the smaller atoms being present in the core and the larger atoms often found in the shell.[75,77] This minimises the steric hinderance of the core-shell formation.

1.3.4 Platinum bimetallic catalysts

The volcano plot in Section 1.1.2 showed that the metal catalyst with the lowest reaction temperature for formic acid dehydrogenation was platinum. However, the high cost of platinum means that it is often important for industrial catalysts to contain a mixture of a high performance expensive PGM and a cheaper metal. It is often found that the platinum-adsorbate bond is slightly

stronger than the optimal value, which means that on decreasing the bond strength the catalyst activity will improve. Thus, through the use of a secondary metal to lower the energy of the d-band centre, as discussed in Sections 1.3.1 and 1.3.2, it is possible to improve the cost efficiency and activity of the highly active platinum catalyst.

Platinum has the highest work function of the transition metals and so addition of any other metal will lead to a transfer of electron density from the secondary metal to the platinum. This increases the electron count in the platinum d-band and lowers the d-band centre. As a result of this, it might be thought that alloying platinum with any other transition metal would lead to increased activity, but the geometric effect also plays a vital role. It was discussed in Section 1.3.2 that, on forming an overlayer of the PGM on a secondary metal, an expansion or contraction of the PGM lattice can lead to change in shape of the d-band and hence a change in position of the d-band centre. Compressive strain leads to greater orbital overlap and a lowering of the d-band centre, which increases catalytic activity for platinum on the decomposition of formic acid. The introduction of a metal with a larger lattice parameter than platinum causes a tensile strain in the surface, a smaller orbital overlap and a higher d-band centre. Therefore, to lower the d-band centre and form a more active catalyst, a secondary metal with a smaller lattice parameter than platinum (3.9242 Å) can be used. Most transition metals have a smaller lattice parameter than platinum, with key exceptions being silver, manganese and gold. These metallic perturbations were confirmed when Bligaard and Nørskov calculated the d-band changes for a platinum surface with various underlying metals.[78] It was seen that where the secondary metal used is iron, cobalt, nickel or copper the d-band centre is shifted down, whereas when platinum is on the surface of silver or gold there is an increase in energy of the d-band centre.[78]

In order to achieve these highly active and cost-effective catalytic alloys, it is expected that the platinum must be present at the surface and in close contact with the secondary metal. Thus, the most logical bimetallic morphology to form is a core-shell structure with a platinum shell, however

this is not a facile synthesis. As discussed in Section 1.3.3, when forming a core-shell particle it is common for the metal with the lower surface energy to migrate to the shell of the system. Platinum has a high surface energy of 2.48 J/m^2,[79] indicating that platinum is commonly found at the core in a material. However, platinum's atomic radius of 177 pm is particularly large compared to most other late transition metals, which indicates that it would form on the shell of metal with a considerably smaller atomic radius. In the PtNi system the surface energies are similar (nickel surface energy = 2.45 J/m^2)[79] but the nickel is smaller in radius (149 pm), which indicates that a platinum shell on nickel core could be thermodynamically more stable than the reverse. In the PtAg system, the silver has a considerably smaller surface energy (1.25 J/m^2)[79] and a similar atomic radius (165 pm) which results in a silver shell on a platinum core morphology being more stable.

In order to achieve the high contact between the platinum shell and the transition metal core, and to maintain the distortions from this interaction, a very thin layer of platinum needs to be deposited on the core material. The formation of a thin layer of platinum on the surface of various substrates has been investigated using Atomic Layer Deposition (ALD), although this technique has been shown to form platinum nanoparticles rather than a thin uniform layer due to the island growth mechanism.[80–82]

1.4 Formic acid decomposition

Hydrogen is widely accepted as the future of renewable energy with fuel cells emerging into the consumer markets rapidly,[83,84] however supply and storage of the hydrogen fuel remains an issue.[85] In recent years, the development of proton exchange membrane (PEM) fuel cells as a source of electricity has been widespread.[86,87] Hydrogen PEM fuel cells consist of a proton exchange membrane separating an anode and a cathode as shown in Figure 1.11. At the anode, hydrogen is split into two protons which travel through the membrane as the electrons pass around an external

circuit to the cathode producing a current. At the cathode the electrons, protons and oxygen from the air combine to form water.[88,89]

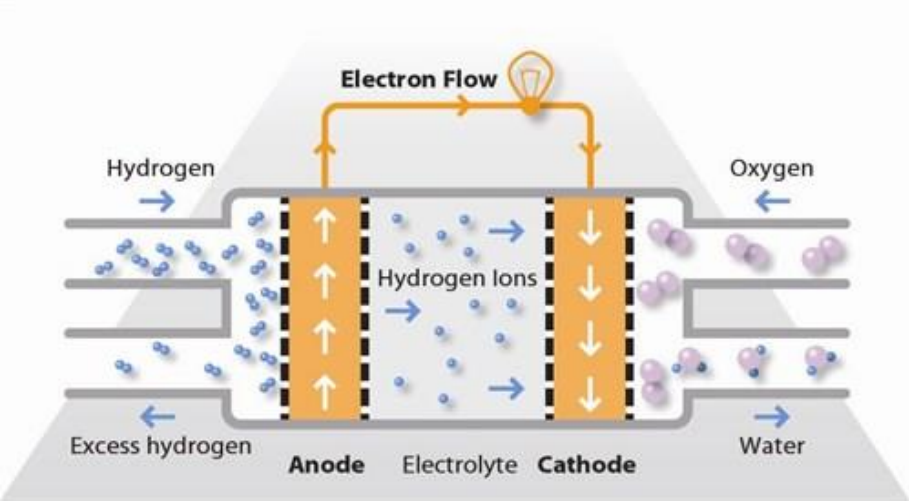


Figure 1.11. Schematic of a PEM fuel cell, reproduced from reference[89].

With only hydrogen and oxygen as reactants and the only waste product being water, fuel cells are a practical solution to the energy problem and can already be seen in the UK market with the Toyota Mirai, a fuel cell hybrid car.[90,91] However, there are two main problems with the current process. The catalyst at the anode is currently platinum based which, at very low concentrations of carbon monoxide, can become poisoned leading to drastically reduced activity.[92] The other major issue is the supply and storage of hydrogen, which is currently liquefied or stored under high pressure, both of which are costly processes.[93] Recent research has been focused on storing hydrogen in small molecules, such as formic acid, hydrazine or borohydrides.[94–96] Formic acid is of particular interest as a hydrogen storage material, as it is easily cycled with carbon dioxide.[97] Through the use of a catalyst, carbon dioxide can be used to store hydrogen as formic acid which can then be used to supply hydrogen and be converted back to carbon dioxide. This means that the net carbon output of the system is zero.[98]

Formic acid can decompose at room temperature through two pathways: the dehydrogenation pathway, producing carbon dioxide and hydrogen (Equation 4), which is useful for the hydrogen

storage capability and the dehydration pathway, producing carbon monoxide and water (Equation 5).[99] The dehydration pathway is undesirable when using formic acid as a hydrogen carrier, as it not only wastes fuel but also produces carbon monoxide which is known to poison both fuel cell catalysts and the dehydrogenation catalyst.

$$HCOOH \rightarrow H_2 + CO_2 \qquad \Delta G = -48.4\ kJ\ mol^{-1} \qquad \textit{(Equation 4)}$$

$$HCOOH \rightarrow H_2O + CO \qquad \Delta G = -28.5\ kJ\ mol^{-1} \qquad \textit{(Equation 5)}$$

The reaction mechanisms for each pathway have been highly studied and it has been found that formic acid binds dissociatively to form a bound formate species and a hydrogen atom on the surface. There are two common binding modes: a bidentate bridging mode through the two carboxylic oxygen atoms, which has been identified as the intermediate for the dehydrogenation reaction, and a monodentate binding mode through one carboxylic oxygen, which decomposes through the dehydration route.[99] Through tailoring the catalyst surface, the bridging mode can be stabilised and the dehydrogenation pathway enhanced.

The formic acid decomposition reaction is well known to be susceptible to structural and electronic changes for both the activity and selectivity of products, which makes it a good probe reaction for studying these changes at the surface active sites of the catalyst.[68,99] The first experimental proof of Sabatier's principle used formate binding to produce the volcano plot discussed in Section 1.1.2 and this reaction is still used today as a model system for probing adsorption effects.[100]

1.5 Oxygen reduction reaction

The use of formic acid as a hydrogen storage material for PEM fuel cells helps to resolve one of the main problems with the development of fuel cells. However, one of the other reasons why fuel cells are economically inviable is the slow oxygen reduction reaction (ORR) which occurs at the cathode. Although this reaction is catalysed by platinum, it remains slow and the high cost of

platinum in the cell means that further development of economically viable cells has been slow.[101,102] Research has been focused on finding an alternative to the platinum catalyst currently used. However, as platinum-based catalysts still prove to be the most active for this reaction, efforts to improve cost efficiency rely on alloying platinum with alternative cheaper metals.[103,104] These ORR catalysts are often deposited on a carbon support in order to maintain their small size and high surface areas. The carbon supports often have high surface area, high electronic conductivity and good chemical stability.[105,106]

The ORR can proceed through one of two pathways: the partial reduction to hydrogen peroxide, which is a two-electron process, and the full reduction to water, a 4-electron pathway and the desirable pathway for the use in PEM fuel cells. The full reduction process mechanism, as shown in Figure 1.12, proceeds by the adsorption of O_2 on the catalyst surface followed by the first electron transfer and the addition of H to form *OOH species adsorbed onto the surface. This is then followed by a second electron transfer, again with H addition, to the *OOH intermediate which results in the formation of two OH species on the surface. The full reduction is then completed by a further two one-electron reduction stages leading to the protonation of each OH species and the desorption of two water molecules.[101]

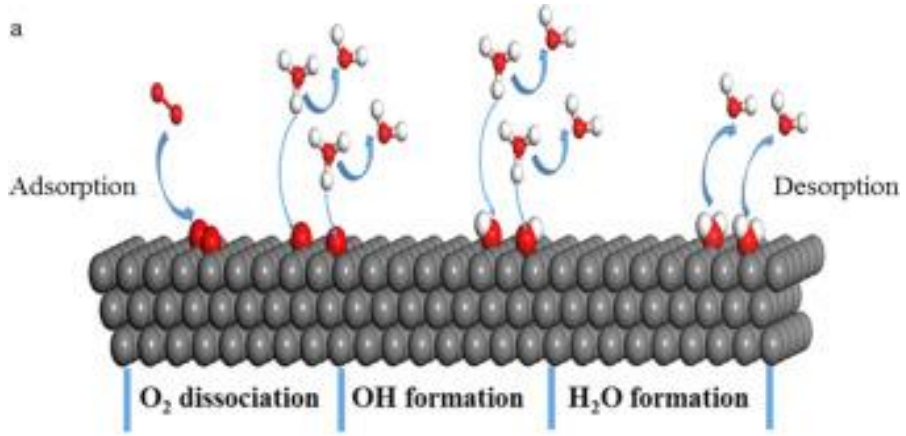


Figure 1.12. ORR mechanism schematic for a full 4-electron reduction. Republished with permission of Elsevier, from J. Stacy, et.al, Renew. Sustain. Energy Rev., *2017, 69, 401–414; permission conveyed through Copyright Clearance Center, Inc*[101]

The Sabatier Principle discussed in Section 1.1.2, where the adsorbates need to bind with optimal strength to the surface, can be used in order to improve the catalytic activity of the platinum cathode for ORR. Density Functional Theory (DFT) has been performed by Nørskov *et al*. to produce a theoretical volcano plot comparing the energy of adsorption of oxygen on the surfaces and the catalytic activity, as shown in Figure 1.13.[107] It can be seen that whilst platinum and palladium are the best catalysts for ORR, there is room for improvement as platinum is not at the peak of the volcano. In order to increase the platinum activity further, a less negative heat of adsorption (lower binding energy) is needed. Calculations have shown that alloying platinum with nickel, cobalt and iron, where platinum segregates to the surface, lowers the d-band centre thus lowering binding energy and enhancing the activity.[107] It should also be noted that the oxygen binding energy is not the only factor relating to the activity, with the hydroxide binding energy also important. The binding energies of these two species are roughly linearly correlated with each other for metal surfaces, with some exceptions such as silver which has a stronger hydroxide adsorption energy than expected.[107]

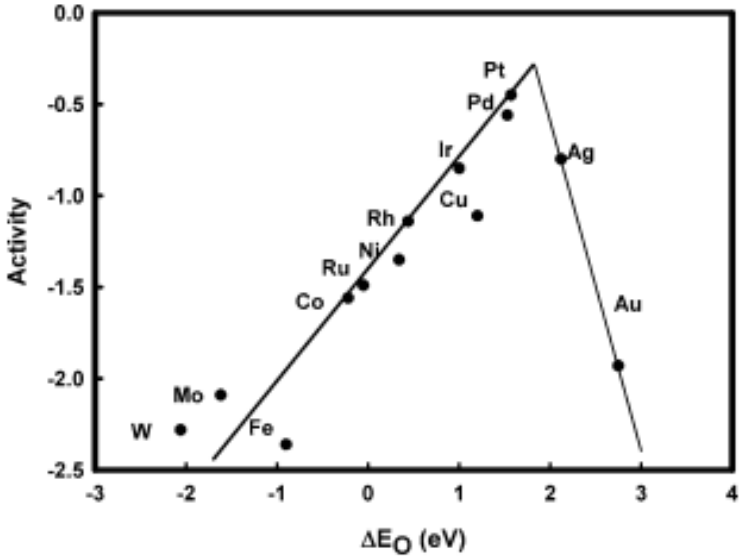


Figure 1.13. Volcano plot showing the relationship between the energy of adsorption of O_2 and catalytic activity for a selection of metals. Reprinted with permission from J. K. Nørskov, J. Rossmeisl, A. Logadottir, L. Lindqvist, J. R. Kitchin, T. Bligaard and H. Jónsson, J. Phys. Chem. B*, 2004, 108, 17886–17892. Copyright 2004 American Chemical Society.*

One method to reduce the cost of the catalyst while improving the activity is to alloy platinum with a transition metal, which reduces the d-band centre and improves the activity while using a lower proportion of PGM. Since the discovery of platinum alloys as ORR catalysts in the 1980s, research into these systems has grown and they are now widely thought of as the next generation of fuel cell catalysts. PtNi and PtCo catalysts are currently in use in the Toyota Mirai and in hydrogen powered London buses.[102] Currently the most active platinum-transition metal alloy is the $Pt_{2.5}Ni$ nano-octahedra, which has a mass activity of 3.3 Amg^{-1}(Pt) compared to 0.2 Amg^{-1}(Pt) for a pure platinum catalyst.[108] However because of the high platinum composition of 75% these catalysts do not significantly reduce platinum loading. This alloying enhancement is thought to be due to compressive strains, down-shifting of the d-band centre and morphology effects which leave more active sites exposed.[101,102]

Particle size can also affect the binding strength and the activity of the catalysts. For pure platinum species it has been seen that, on decreasing the particle size, a higher proportion of low coordinate edge sites are present which have higher oxygen binding energies and thus the activity decreases.[109] However for alloyed particles the system is a little more complex, due to factors such as degree of alloying, composition and particle shape. The effect of particle size on Pt_3Co alloys have been investigated and it was found that specific activity increased with increasing particle size to around 6 nm, as smaller nanoparticles were oxidised at a lower potential.[110]

An enhancement in the concentration of platinum on the surface can lead to greater catalytic activity in the alloys, as the surface atoms are the only atoms involved in the catalytic process. Therefore, there has been some investigation into core-shell particles with platinum shells for ORR. A theoretical study has been produced which details the ORR activity for a matrix of combinations of materials,[111] as shown in Figure 1.14.

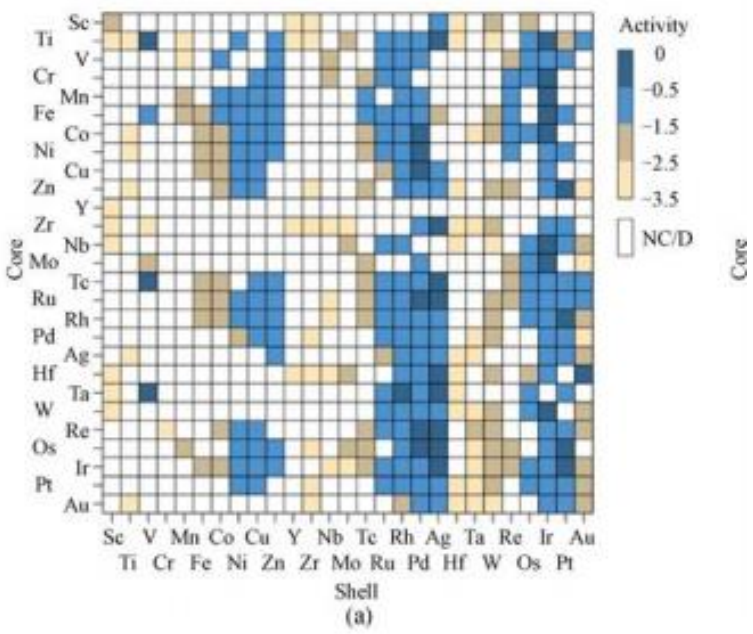


Figure 1.14. Activity of core-shell nanoparticles for ORR. Higher activity corresponds to darker colour. Nanoparticles that did not converge are shown in white. Republished with permission of AIP Publishing, from J. B. Corona, et.al, J. Chem. Phys.*, 2016, 145; permission conveyed through Copyright Clearance Center, Inc* [111].

As expected platinum and palladium show the most highly active shell materials, with silver and iridium shells also forming highly active alternatives. The high activity of silver is particularly interesting as it has a much lower cost than the other active metals, but oxygen binding to its surface is slightly weaker unless combined with other metals. These silver shell materials are also known to dissolve in acidic environments used in fuel cells.[111]

1.6 Aims and objectives

As discussed in the previous sections of this introduction, heterogeneous catalysis is a field extensively used in industry in order to ensure cheaper and "greener" processes. However, these catalysts are not necessarily at their most efficient. By understanding catalyst structures and surfaces it is possible to tailor catalyst syntheses to specific reactions and therefore improve catalytic efficiency. In this thesis various techniques are used in order to progress the field of designing and forming nanoparticles with specific surfaces and metal interfaces.

The modification of the nanoparticle surfaces is primarily achieved through introducing a secondary metal into the system, with this thesis presenting an investigation into how this creates an electronic and structural effect on the catalytic active sites. The synthesis of these structures is not highly reported and so a primary aim of this thesis is to investigate both polymer supported and silica supported synthesis routes to these highly directed structures.

The various structures formed were extensively characterised and the surface features were investigated through catalytic testing. The liquid phase formic acid decomposition reaction was used as the probe reaction, as it is known to be susceptible to structural and electronic changes at the binding sites and therefore gives vital information about the catalyst surface and tailoring impact.

A final aim of this thesis was to improve the catalysts used for the oxygen reduction reaction (ORR) in fuel cells. With the ORR reaction currently one of the least efficient processes in fuel cells, improving these catalysts could significantly progress this technology. In order to accomplish these aims, the methodology used for this thesis is a combination of synthesis method development and catalyst testing to further correlate synthesis with catalyst tailoring.

1.7 Thesis overview

This thesis consists of seven chapters, with Chapters 4-6 detailing the experimental work undertaken over the course of my DPhil degree.

Chapter 1 introduces the principles of catalysis, with an emphasis on heterogeneous catalysis and nanoparticulate catalysts. Focus is directed towards the modification of catalysts through the use of bimetallic systems, including electronic and geometric effects. The formic acid decomposition reaction and the oxygen reduction reaction are also introduced.

Chapter 2 summarises the background and theory of the most common analytical techniques used within this thesis for the characterisation of nanoparticle catalysts.

Chapter 3 provides detailed descriptions of the experimental techniques used within the thesis to synthesise, characterise and test the catalysts.

Chapter 4 investigates the use of polyvinylpyrrolidone (PVP) as a nanoparticle stabiliser for the synthesis of bimetallic nanoparticles with well-defined structures and metal interfaces.

Chapter 5 explores the use of a mesoporous silica support (SBA-15) for the synthesis of bimetallic nanoparticles with well-defined structures and metal interfaces.

Chapter 6 further explores the structurally directing effect of SBA-15 walls. This is used to enhance the catalytic behaviour of PtNi bimetallic systems for the oxygen reduction reaction (ORR).

Chapter 7 summaries the findings presented throughout the previous three chapters and concludes with a brief discussion of future perspectives for this research.

1.8 References

1 *GISTEMP Team, 2018: GISS Surface Temperature Analysis (GISTEMP) by NASA Goddard Institute for Space Studies from https://data.giss.nasa.gov/gistemp/,* 2018.

2 *NOAA National Centers for Environmental Information, State of the Climate: Global Climate Report for Annual 2016*, 2016.

3 *U.S Environmental Protection Agency. 2016. Climate change indicators in the United States, 2016. Fourth Edition, EPA 430-R-16-004*, 2016.

4 *IPCC, Climate Change 2014 Synthesis Report, Summary for Policymakers*, 2014.

5 R. Heede, *Clim. Change*, 2014, **122**, 229–241.

6 *IPCC, Climate Change 2014 Mitigation of Climate Change, 2014*, 2014.

7 H. Davy, *Philos. Trans. R. Soc. London* , 1817, **107**, 77–85.

8 *Letter from Davy to John Buddle, British Museum Add. MSS 33963 f. 114*.

9 J. W. Döbereiner, *J. für Chem*, 1823, **38**, 321–326.

10 J. M. Thomas, J. M. Thomas and W. J. Thomas, *Principles and Practice of Heterogeneous*

Catalysis, Wiley, 2015.

11 J. J. Berzelius, *Annls. Chim. Phys*, 1836, **61**, 146.

12 *OED Online*, Oxford University Press, 2018.

13 G. C. Bond, *Heterogeneous catalysis : principles and applications*, Oxford : Clarendon Press, Oxford, 2nd ed., 1987.

14 C. A. Lewis and R. Wolfenden, *Proc. Natl. Acad. Sci.*, 2008, **105**, 17328 LP-17333.

15 M. Picquet, *Platin. Met. Rev.*, 2013, **57**, 272–280.

16 L. Resconi, L. Cavallo, A. Fait and F. Piemontesi, *Chem. Rev.*, 2000, **100**, 1253–1346.

17 C. A. Busacca, D. R. Fandrick, J. J. Song and C. H. Senanayake, *Adv. Synth. Catal.*, 2011, **353**, 1825–1864.

18 J. Berg, J. Tymoczko and L. Stryer, *Biochemistry. 5th edition*, New York, 5th edn., 2002.

19 A. Illanes, *Enzyme Biocatalysis: Principles and Applications*, Springer Netherlands, 2008.

20 F. Cavani, G. Centi, S. Perathoner and F. Trifirò, *Sustainable Industrial Chamistry: Principles, Tools and Industrial Examples*, Wiley, 2009.

21 H. Mao, Y. Shen, Q. Zhang, M. Ulaganathan, S. Zhao, Y. Yang and H. H. Hng, *Carbon N. Y.*, 2016, **96**, 75–82.

22 R. Munirathinam, J. Huskens and W. Verboom, *Adv. Synth. Catal.*, 2015, **357**, 1093–1123.

23 J. Heveling, *J. Chem. Educ.*, 2012, **89**, 1530–1536.

24 J. M. Thomas, *Philos. Trans. R. Soc. A Math. Phys. Eng. Sci.*

25 J. Hagen, *Industrial Catalysis: A Practical Approach*, Wiley-VCH Verlag GmbH & Co. KGaA, 2006.

26 F. Zaera, *Chem. Rec.*, 2005, **5**, 133–144.

27 G. Ertl and G. Ertl, Eds., *Handbook of Heterogeneous Catalysis*, Weinheim : Wiley-VCH, Weinheim, 2nd, compl edn., 2008.

28 G. Rothenberg, *Catalysis : Concepts and Green Applications*, Wiley-VCH, Weinheim, 2015.

29 P. Sabatier and J. B. Senderens, *R Acad. Sci.*, 1902, **134**, 514–516.

30 A. A. Balandin, *Adv. Catal.*, 1958, **10**, 96–129.

31 G. C. Bond, *Metal-Catalysed Reactions of Hydrocarbons*, Springer US, 2005.

32 B. Hammer and J. K. Norskov, *Adv. Catal.*, 2000, **45**, 71–129.

33 B. Hammer and J. K. Norskov, *Nature*, 1995, 376, 238–240.

34 MarketsandMarkets™, *Metal Nanoparticles Market by metal (Platinum, Gold, Silver, Iron, Titanium, Copper, Nickel), End-use industry (Pharmaceutical & healthcare, Electrical & electronics, Catalyst, Personal care & cosmetics), and Region - Global Forecast to 2022*, 2017.

35 JM Bullion Platinum Price, https://www.jmbullion.com/charts/platinum-price/.

36 M. Haruta, T. Kobayashi, H. Sano and N. Yamada, *Chem. Lett.*, 1987, **16**, 405–408.

37 G. J. Hutchings, *Gold Bull.*, 1996, **29**, 123–130.

38 B. Corain, G. Schmid and N. Toshima, *Metal nanoclusters in catalysis and materials science : the issue of size control*, Elsevier, Amsterdam , 2008.

39 K. Kolasinski, *Surface Science: Foundations of Catalysis and Nanoscience*, John Wiley and Sons, 2012.

40 R. Van Hardeveld and F. Hartog, *Surf. Sci.*, 1969, **15**, 189–230.

41 A. Tsuda and N. V. Konduru, *NanoImpact*, 2016, **2**, 38–44.

42 K. M. Koczkur, S. Mourdikoudis, L. Polavarapu and S. E. Skrabalak, *Dalt. Trans.*, 2015, **44**, 17883–17905.

43 J. Gabaldon, M. Bore and A. Datye, *Top. Catal.*, 2007, **44**, 253–262.

44 G. Cao, *Nanostructures & Nanomaterials: Synthesis, Properties & Applications*, Imperial College Press, 2004.

45 Y. Borodko, S. E. Habas, M. Koebel, P. D. Yang, H. Frei and G. a Somorjai, *J. Phys. Chem. B*, 2006, **110**, 23052–23059.

46 R. Si, Y. W. Zhang, L. P. You and C. H. Yan, *J. Phys. Chem. B*, 2006, **110**, 5994–6000.

47 H. S. Shin, H. J. Yang, S. Bin Kim and M. S. Lee, *J. Colloid Interface Sci.*, 2004, **274**, 89–94.

48 A. Kyrychenko, O. M. Korsun, I. I. Gubin, S. M. Kovalenko and O. N. Kalugin, *J. Phys. Chem. C*, 2015, **119**, 7888–7899.

49 E. P. Boonekamp, J. J. Kelly and L. G. J. Fokkink, *Langmuir*, 1994, **10**, 4089–4094.

50 A. Cao, R. Lu and G. Veser, *Phys. Chem. Chem. Phys.*, 2010, **12**, 13499–13510.

51 C. R. Henry, *Prog. Surf. Sci.*, 2005, **80**, 92–116.

52 C. T. Campbell, *Acc. Chem. Res.*, 2013, **46**, 1712–1719.

53 D. Zhao, Q. Huo, J. Feng, B. F. Chmelka and G. D. Stucky, *J. Am. Chem. Soc.*, 1998, **120**, 6024–6036.

54 A. J. Vizcaíno, A. Carrero and J. A. Calles, 2006, 1–12.

55 M. Zhao, T. L. Church and A. T. Harris, *Appl. Catal. B Environ.*, 2011, **101**, 522–530.

56 Y. Kathiraser, J. Ashok and S. Kawi, *Catal. Sci. Technol.*, 2016, **6**, 4327–4336.

57 U. Diebold, *Surf. Sci. Rep.*, 2003, **48**, 53–229.

58 S. J. Tauster, S. C. Fung and R. L. Garten, *J. Am. Chem. Soc.*, 1978, **100**, 170–175.

59 R. J. Isaifan, H. A. E. Dole, E. Obeid, L. Lizarraga, P. Vernoux and E. A. Baranova, *Electrochem. Solid-State Lett.* , 2012, **15**, E14–E17.

60 H. Wang, K. An, A. Sapi, F. Liu and G. Somorjai, *Catal. Letters*, 2014, **144**, 1930–1938.

61 S. P. Lin, K. W. Wang, C. W. Liu, H. S. Chen and J. H. Wang, *J. Phys. Chem. C*, 2015, **119**, 15224–15231.

62 F. R. Lucci, J. Liu, M. D. Marcinkowski, M. Yang, L. F. Allard, M. Flytzani-Stephanopoulos and E. C. H. Sykes, *Nat. Commun.*, 2015, **6**, 8550.

63 J. Czaplinska, I. Sobczak and M. Ziolek, *J. Phys. Chem. C*, 2014, **118**, 12796–12810.

64 S. Alayoglu, A. U. Nilekar, M. Mavrikakis and B. Eichhorn, *Nat. Mater.*, 2008, **7**, 333–338.

65 S. Zhang, Ö. Metin, D. Su and S. Sun, *Angew. Chemie - Int. Ed.*, 2013, **52**, 3681–3684.

66 P. S. Kumbhar, R. Kharkar, D. Yadav and T. L. R. A. Rajadhyaksha, 1992, 584–586.

67 W. Yu, M. D. Poroso and J. G. Chen, , DOI:10.1021/cr300096b.

68 S. Jones, S. Fairclough, M. Gordon-Brown, W. Zheng, A. Kolpin, B. Pang, W. Kuo, J. Smith and E. Tsang, *Chem. Commun.*, 2015, **51**, 46–49.

69 Weast, *CRC handbook of chemistry and physics*, Cleveland, Ohio : CRC Press, Cleveland, Ohio, 52nd edn., 1972.

70 K. Jiang, H.-X. Zhang, S. Zou and W.-B. Cai, *Phys. Chem. Chem. Phys.*, 2014, **16**, 20360–20376.

71 D. Wang and Y. Li, *Adv. Mater.*, 2011, **23**, 1044–60.

72 A. Ruban, H. Skriver and J. Nørskov, *Phys. Rev. B*, 1999, **59**, 15990–16000.

73 A. Zaleska-Medynska, M. Marchelek, M. Diak and E. Grabowska, *Adv. Colloid Interface Sci.*, 2016, **229**, 80–107.

74 X. Liu, D. Wang and Y. Li, *Nano Today*, 2012, **7**, 448–466.

75 R. Ferrando, J. Jellinek and R. L. Johnston, *Chem. Rev.*, 2008, **108**, 845–910.

76 J. Yang, W. Hu, Y. Wu and X. Dai, *Surf. Sci.*, 2012, **606**, 971–980.

77 A. Rapallo, G. Rossi, R. Ferrando, A. Fortunelli, B. C. Curley, L. D. Lloyd, G. M. Tarbuck and R. L. Johnston, *J. Chem. Phys.*, , DOI:10.1063/1.1898223.

78 T. Bligaard and J. K. Nørskov, *Electrochim. Acta*, 2007, **52**, 5512–5516.

79 H. L. Skriver and N. M. Rosengaard, *Phys. Rev. B*, 1992, **46**, 7157–7168.

80 T. Aaltonen, M. Ritala, T. Sajavaara, J. Keinonen and M. Leskelä, *Chem. Mater.*, 2003, **15**, 1924–1928.

81 J. W. Clancey, A. S. Cavanagh, R. S. Kukreja, A. Kongkanand and S. M. George, *J. Vac. Sci. Technol. A*, 2014, **33**, 01A130.

82 L. Baker, A. S. Cavanagh, D. Seghete, S. M. George, A. J. M. Mackus, W. M. M. Kessels, Z. Y. Liu and F. T. Wagner, *J. Appl. Phys.*, 2011, **109**, 84333.

83 W. G. Colella, M. Z. Jacobson and D. M. Golden, *J. Power Sources*, 2005, **150**, 150–181.

84 J.-H. Wee, *Renew. Sustain. Energy Rev.*, 2007, **11**, 1720–1738.

85 D. Mori and K. Hirose, *Int. J. Hydrogen Energy*, 2009, **34**, 4569–4574.

86 B. Millington, S. Du and B. G. Pollet, *J. Power Sources*, 2011, **196**, 9013–9017.

87 S. J. Peighambardoust, S. Rowshanzamir and M. Amjadi, *Int. J. Hydrogen Energy*, 2010, **35**, 9349–9384.

88 X. Cheng, Z. Shi, N. Glass, L. Zhang, J. Zhang, D. Song, Z.-S. Liu, H. Wang and J. Shen, *J. Power Sources*, 2007, **165**, 739–756.

89 Fuel Cell Today Technologies PEMFC, http://www.fuelcelltoday.com/technologies/pemfc.

90 L. Ulrich, *Spectr. IEEE*, 2015, **52**, 46–55.

91 U. Eberle, B. Müller and R. von Helmolt, *Energy Environ. Sci.*, 2012, **5**, 8780.

92 J. J. Baschuk and X. Li, *Int. J. Energy Res.*, 2003, **27**, 1095–1116.

93 L. Zhou, *Renew. Sustain. Energy Rev.*, 2005, **9**, 395–408.

94 A. Boddien and H. Junge, *Nat. Nanotechnol.*, 2011, **6**, 265–266.

95 L. He, Y. Huang, A. Wang, X. Wang and T. Zhang, *AIChE J.*, 2013, **59**, 4297–4302.

96 M. L. Christian and K.-F. Aguey-Zinsou, *ACS Nano*, 2012, **6**, 7739–7751.

97 S. Enthaler, J. von Langermann and T. Schmidt, *Energy Environ. Sci.*, 2010, **3**, 1207.

98 S. Moret, P. J. Dyson and G. Laurenczy, *Nat. Commun.*, 2014, **5**, 4017.

99 K. Tedsree, T. Li, S. Jones, C. W. A. Chan, K. M. K. Yu, P. a J. Bagot, E. a Marquis, G. D. W. Smith and S. C. E. Tsang, *Nat. Nanotechnol.*, 2011, **6**, 302–307.

100 M. Bowker, P. Stone, R. Bennett and N. Perkins, *Surf. Sci.*, 2002, **511**, 435–448.

101 J. Stacy, Y. N. Regmi, B. Leonard and M. Fan, *Renew. Sustain. Energy Rev.*, 2017, **69**, 401–414.

102 M. Shao, Q. Chang, J.-P. Dodelet and R. Chenitz, *Chem. Rev.*, 2016, **116**, 3594–3657.

103 C. Zhang, X. Shen, Y. Pan and Z. Peng, *Front. Energy*, 2017, **11**, 268–285.

104 C. Song and J. Zhang, ed. J. Zhang, Springer London, London, 2008, pp. 89–134.

105 S. C. Roy, A. W. Harding, A. E. Russell and K. M. Thomas, *J. Electrochem. Soc.* , 1997, **144**, 2323–2328.

106 E. Auer, A. Freund, J. Pietsch and T. Tacke, *Appl. Catal. A Gen.*, 1998, **173**, 259–271.

107 J. K. Nørskov, J. Rossmeisl, A. Logadottir, L. Lindqvist, J. R. Kitchin, T. Bligaard and H. Jónsson, *J. Phys. Chem. B*, 2004, **108**, 17886–17892.

108 S.-I. Choi, S. Xie, M. Shao, J. H. Odell, N. Lu, H.-C. Peng, L. Protsailo, S. Guerrero, J. Park, X. Xia, J. Wang, M. J. Kim and Y. Xia, *Nano Lett.*, 2013, **13**, 3420–3425.

109 D. Y. Chung, Y.-H. Chung, N. Jung, K.-H. Choi and Y.-E. Sung, *Phys. Chem. Chem. Phys.*, 2013, **15**, 13658–13663.

110 C. Wang, D. van der Vliet, K.-C. Chang, H. You, D. Strmcnik, J. A. Schlueter, N. M. Markovic and V. R. Stamenkovic, *J. Phys. Chem. C*, 2009, **113**, 19365–19368.

111 B. Corona, M. Howard, L. Zhang and G. Henkelman, *J. Chem. Phys.*, 2016, **145**, 244708.

Chapter 2

Analytical Techniques

2.1 Introduction 34
2.2 X-ray diffraction 34
2.2.1 Powder x-ray diffraction 35
2.2.2 Wide angle x-ray scattering 37
2.3 X-ray absorption spectroscopy 37
2.4 Transmission electron microscopy 39
2.5 Energy-dispersive x-ray spectroscopy 42
2.6 Low energy ion scattering 43
2.7 Temperature programmed reduction 44
2.8 Thermogravimetric analysis 45
2.9 Atom probe tomography 45
2.10 Magic angle spinning nuclear magnetic resonance 47
2.11 References 48

2.1 Introduction

Analytical techniques are widely used in catalyst development, as characterising materials is of great importance in understanding how catalytic properties affect performance.[1] From microscopy, which allows insight into metal particle size, shape and dispersion, to spectroscopy, which probes electronic properties of the material and the adsorbates at the surface, there is no single analytical technique which is the most powerful. A combination of various complimentary methods is the most valuable way to truly understand the properties of the catalyst materials.

Characterisation techniques include diffraction, microscopy, spectroscopy, thermal methods and probing adsorbed molecules, which all give information on the electronic, geometric and compositional properties of a catalyst material. Most catalyst characterisation methods either probe the surface of a material (0-3 nm) or the whole material as bulk. However, for nanoparticle characterisation, particle sizes are often sufficiently small (0-6 nm) to be probed entirely by surface techniques. Both bulk and surface techniques have their advantages, as bulk techniques allow investigation into the whole catalyst, whereas surface techniques yield specific information on the surface active sites. For heterogeneous catalysts, all the active sites are found on the surface so characterisation of this region is particularly important.

Most analytical methods for material characterisation are performed *ex-situ*, often before and after a reaction. However, the material properties can often be highly dependent on the reaction environment and so it is possible to obtain *in-situ* measurements using many of these techniques.

2.2 X-ray diffraction

X-ray diffraction (XRD) is a commonly used analytical technique for understanding the crystal lattice structures of heterogeneous materials. The high-energy incident x-rays are scattered elastically by the crystal lattice. These x-rays have a wavelength of around 1 Å, similar to the

interlayer spacing of the crystal, which means that the scattered x-rays are subject to diffraction. The x-rays are deeply penetrating into the solid and so this is a bulk technique which provides information about the relative positions of the atoms in the unit cell.[2]

2.2.1 Powder x-ray diffraction

In a typical laboratory scale diffractometer, x-rays are generated through bombarding a Cu source with high energy electrons. This results in the ejection of electrons from the core levels (usually K) of the Cu. The higher energy electrons then drop down into the core holes of the Cu releasing x-rays with a wide spectrum of wavelengths. These x-rays are then passed through a collimator and monochromator, producing a beam of x-rays with one wavelength. When these x-rays hit a crystalline sample, they are scattered elastically by the electrons in the atoms. These scattered x-rays diffract and undergo constructive interference. The angles at which this occurs are specific for each material and are defined by Braggs Law:

$$2d \sin\theta = n\lambda \qquad \textit{(Equation 1)}$$

where d is the interlayer spacing of the crystallographic planes, θ is the angle of incident x-rays to the crystal planes, λ is the x-ray wavelength and n is any integer.

Where the angle is such that the interference is constructive and Braggs law is satisfied, a reflection peak in the profile is seen. The positions of these reflections depend on the unit cell parameters, the crystal lattice type and the wavelength of the incident x-rays. The reflection intensity depends on the type of atoms scattering the x-ray beam and their relative locations.[3] The measured patterns can be compared with a pre-compiled database containing over 50,000 unique powder x-ray diffraction patterns.[4]

Where the angle is such that the interference is destructive, reflections are cancelled out and no peak is shown in the profile. Figure 2.1 shows how the wavelength is adjusted following reflection

from different planes of the crystal. Here there is destructive interference, however constructive interference can occur at other angles.

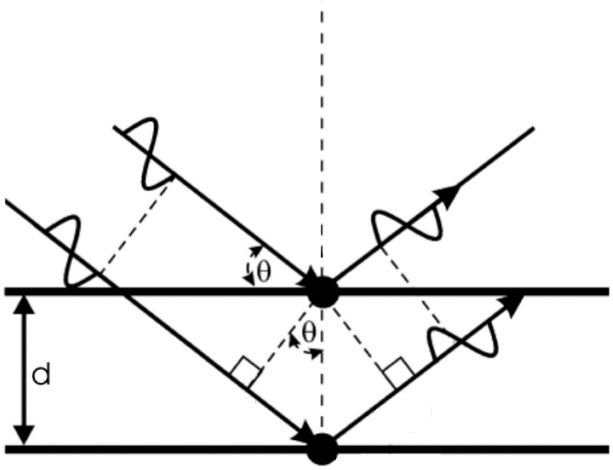


Figure 2.1. Schematic diagram showing destructive interference produced from two planes in a crystal. Image modified from reference.[5]

From the angle at which constructive interference was observed, Braggs Law gives the interlayer spacing of the crystal. Equation 2 can then be used to calculate the lattice parameter for any metal with a cubic lattice, such as Pt.[6]

$$\frac{1}{d^2} = \frac{h^2+k^2+l^2}{a^2} \qquad \textit{(Equation 2)}$$

where d is the interlayer spacing, h, k and l are the Miller indices and a is the lattice parameter. A change in the lattice parameter, due to the a compression or expansion of the lattice or the formation of an alloy, can be observed through slight shifts in the diffraction angle.

For extended crystals with long-range order, reflections are only seen at the diffraction angle as destructive interference inhibits the signal produced at all other angles. This results in sharp peaks at the diffraction angle only. However, in the case of nanoparticles, there is no long-range order and so the difference in constructive and destructive interference is less pronounced, leading to peak broadening. The Scherrer equation, Equation 3, can be used to correlate this peak broadening with the mean crystallite size.

$$L = \frac{K\,\lambda}{\beta \cos\theta} \qquad \textit{(Equation 3)}$$

where L is the average crystallite size, K is the shape factor (usually 1), λ is the wavelength of the incident x-rays, β is the full width half maximum and θ is the diffraction angle. The full width half maximum (FWHM) is used as a measure of peak broadening and is calculated as the width of a peak at half of its maximum height.

The Scherrer equation is often used to provide an estimate of particle size, although there are uncertainties with this method. Often the Scherrer equation provides a lower bound for the particle size as there are other factors which can introduce peak broadening, such as the strains and imperfections of lattices, the twinning of particles and instrumental effects.[7] Thus, the most reliable particulate size determination is obtained using a combination of XRD and alternative methods such as microscopy.

2.2.2 Wide angle x-ray scattering

Some x-rays which are scattered at wide angles, and these are monitored with wide angle x-ray scattering (WAXS) experiments. The wide angle of diffraction indicates that they have been scattered by sub-nanosized particles. WAXS profiles are produced in a similar way to powder XRD patterns, but they are more sensitive to smaller particles.

2.3 X-ray absorption spectroscopy

Another useful x-ray characterisation technique is x-ray absorption spectroscopy (XAS), which is mainly used for determining the oxidation state and local environment of an element in a sample. XAS does not need long-range order for data collection and so the structural information gained for nanoparticles can be much greater in variety and quality than that gained from XRD. XAS is also element specific, making it possible to measure very dilute species in a sample. An XAS spectrum can be broken down into two parts, as shown in Figure 2.2, which are called the XANES

and EXAFS regions. The XANES region around the white line intensity gives information about the oxidation state of the material, as well as simple geometric information. The EXAFS region gives information about neighbouring atoms, including their type, number and distance from the probed atom.

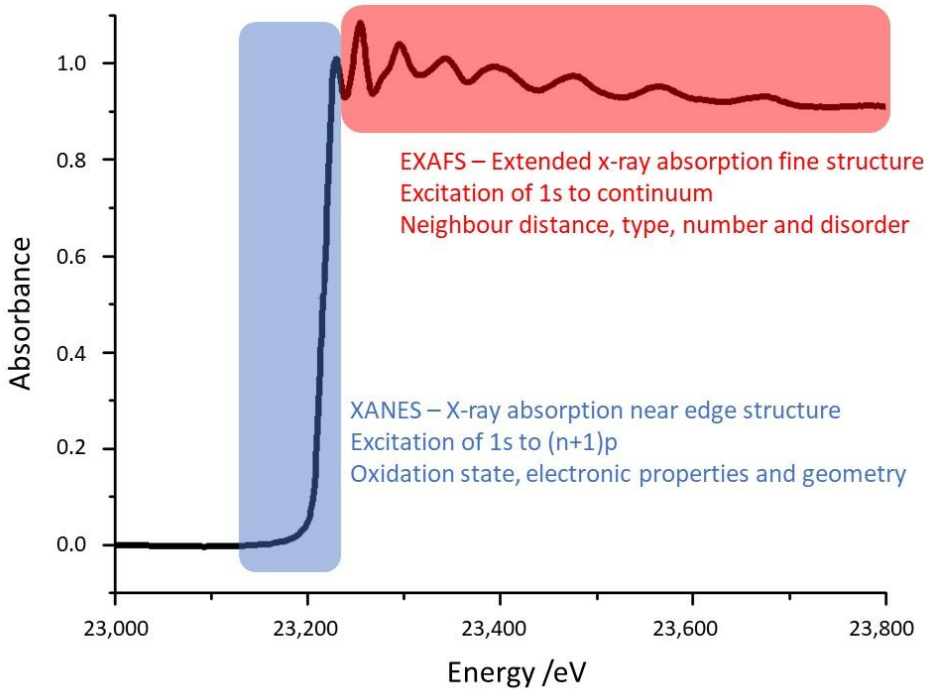


Figure 2.2. An image showing a typical XAS spectrum. The blue area shows the XANES region and the red area shows the EXAFS region.

XAS is typically performed in a synchrotron, in order to reach x-rays with high enough energy ranges. Typically, the x-ray absorption is measured with respect to the incident x-ray energy. The x-rays are passed through a monochromator and towards the sample, then the energy of the x-ray is scanned across the region of interest. Similarly to XPS, the atoms can absorb the photons, causing a decrease in the amount of energy passed through the sample and into the detector. At specific energies there are large jumps in the absorption of the x-rays, specifically where the energy is optimal for the ejection of an electron from the atom and become a photoelectron. This leads to the "edge-jump" in the "x-ray absorption near edge structure" (XANES) region. Similarly to XPS,

this can detect the oxidation state of the element and can often be used to determine coordination geometry.

After the photoelectron has been emitted, it can interact with neighbouring atoms and be scattered back towards the original atom. Here it can interfere with the outgoing photoelectron, which causes either constructive or destructive interference and leads to the oscillations termed as "extended x-ray absorption fine structure" (EXAFS). These variations can give information on the nature and number of the neighbouring atoms of the absorbing atom as well as the distance between the two atoms.[11] Due to the short mean free path of an electron, the photoelectron can probe a distance of around 6 Å from the absorbing atom.[12]

XAS is a useful technique for following a reaction *in-situ* under reaction conditions because of the large penetration depth and the short nature of each measurement. Measurements in the new "quick EXAFS" scanning modes can be as low as seconds for XANES regions and a couple of minutes for EXAFS regions.[12]

2.4 Transmission electron microscopy

Transmission electron microscopy (TEM) has become one of the most valuable characterisation tools for understanding the microstructure of materials. Typical optical microscopes using visible light have a resolution of 1 μm, which is insufficiently small for investigating the structures of nanoscale catalysts. Electron microscopes, which use an electron beam with a wavelength below 1 Å, can have a resolution down to 0.1 nm. This allows the observation of particle morphologies, dispersion across supports and structural features. The power to focus electron beams allows diffraction and imaging of electron density in a sample, producing qualitative information of only the small area probed. This is in contrast with the x-ray methods discussed in the previous sections which extract quantitative information from the whole sample. There are many techniques of

electron microscopy, however for this thesis the focus will be on conventional TEM in both bright field and dark field imaging modes.

An incident electron beam is produced by a high current, higher than the work function of the material, passing through a cathode filament (LaB_6) which allows the emission of electrons. These are then focussed, through the use of lenses, to the sample. In order to form an image using TEM, it is required to focus the electron beam through the use of many magnetic lenses. Figure 2.3 shows the ray diagram for both bright field TEM (left) and dark field TEM (right). In the top section of the diagram shows that each point in the back focal plane contains of electrons from all parts of the specimen. If there were no objective aperture here, the image would contain very little contrast.

The point at which the objective aperture is opened on the back focal plane determines whether the diffracted or non-diffracted electrons will pass. In bright field TEM, the objective aperture allows the non-diffracted electrons though and creates a bright field image where the atoms show as shadows. In dark field TEM, the objective aperture allows the diffracted electrons though and creates a dark field image where the electrons focus to show the atom positions. In most images the main crystalline features originate from this diffraction contrast. The fluorescent viewing screen at the bottom of the column projects a two-dimensional image which is often linked to a charge-coupled device (CCD) camera.

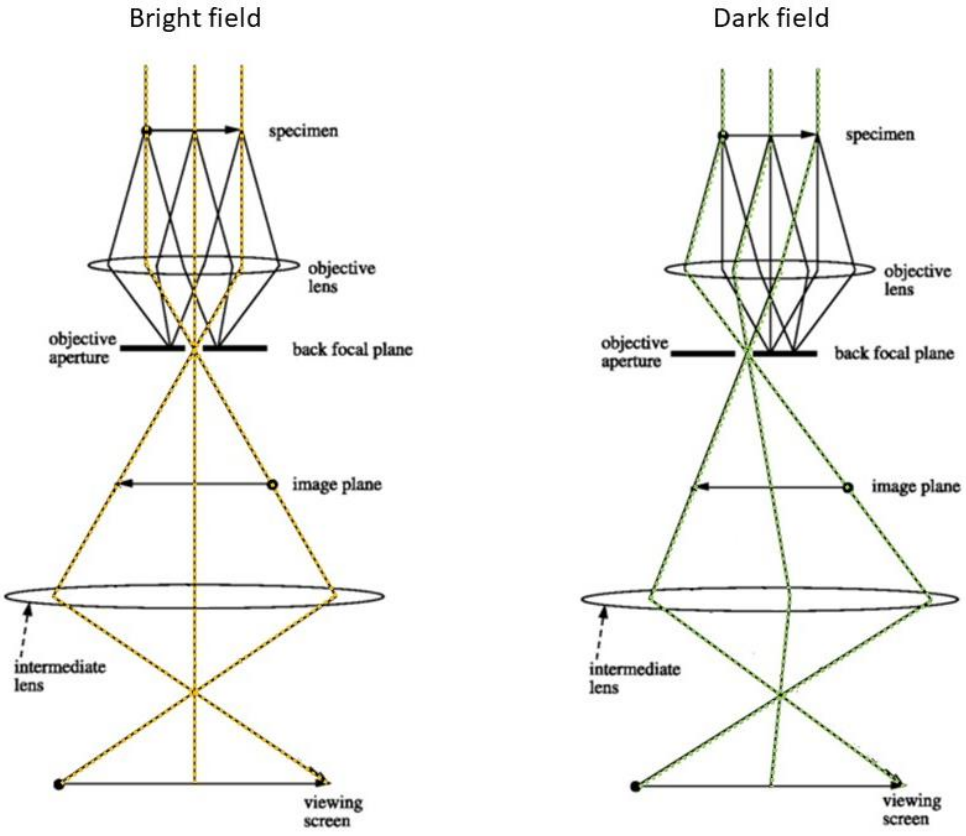


Figure 2.3. Image showing both bright field (left) and dark field (right) microscope set up. In the bright field set-up, the objective aperture is opened to allow the transmitted electrons (highlighted in yellow) to pass through. In the dark field set-up the objective aperture is opened to allow one set of diffracted electrons (highlighted in green) to pass through. Image modified from reference.[13]

There are many possible interactions of the electron beam and the sample which are summarised in Figure 2.4. The transmitted and diffracted electrons are used for bright field and dark field imaging respectively, as discussed above. The secondary electrons can also be collected by microscopes fitted with a separate secondary electron imaging detector. These electrons are deflected off the edge of the sample and so can be used to build up an image of the sample surface, rather than an image scanning the whole depth of the sample.

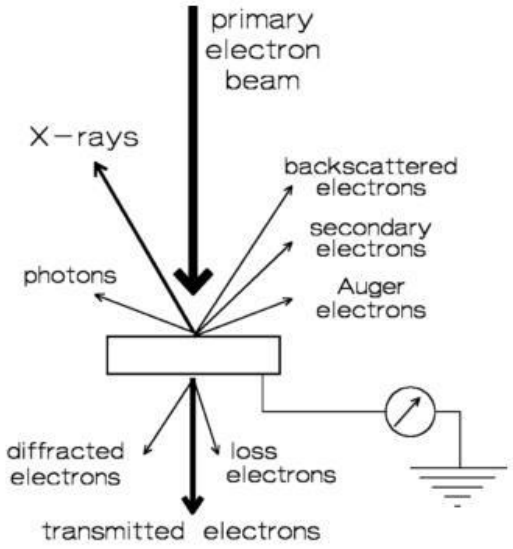


Figure 2.4. Image showing the range of interactions which can occur after the primary electron beam meets the sample. Transmitted electrons, scattered electrons and x-rays are commonly used in this thesis for various techniques. Image reproduced from reference.[14]

Cryogenic TEM allows continuous cooling of a liquid sample with liquid nitrogen while imaging takes place. This technique has gained a high interest in biochemical disciplines since the 2017 Nobel Prize in Chemistry was awarded to Jacques Dubochet, Joachim Frank and Richard Henderson for their development of cryo-electron microscopy for the imaging of biomolecules.[15] However, other areas can also benefit from cryo-TEM. Analysis of colloidal or liquid catalysts can be performed using this technique, in order to image the catalyst in its reactive state rather than through conventional TEM which shows the sample after the solvent is evaporated. The sample is plunge frozen in liquid nitrogen before a continuously cooled microtome is used to cut a thin slice of the sample. This is quickly loaded into a cryogenically cooled sample holder and inserted into a microscope. Low doses of radiation are needed to minimise specimen damage, so the resolution can often be lower than that of conventional TEM.[16]

2.5 Energy-dispersive x-ray spectroscopy

A useful technique for identifying the elemental composition of a sample is energy dispersive x-ray spectroscopy (EDX). As EDX is usually coupled with TEM, the elemental composition is

investigated in a localised manner across the microscopy image[17]. The high-energy electron beam used in TEM can be used to probe electronic states in the atoms through a similar process to XPS. XPS probes the whole sample surface, up to a depth of 3 nm, whereas TEM only analyses the composition of a small segment.

The incoming electron beam causes an excitation of a core electron, leaving a core hole which is filled by a higher energy electron undergoing relaxation and emitting an x-ray. The emitted x-rays are characteristic to specific elements and are detected to determine the concentrations of these elements in the illuminated region of the sample. Through scanning the sample, two-dimensional descriptive maps of elemental composition can be produced, as well as one-dimensional line scans of specific regions and individual point analysis.

2.6 Low energy ion scattering

Low energy ion scattering (LEIS) is used to quantitatively determine the composition of the outermost atomic layer of a sample. The superior surface sensitivity of the technique and the systematic removal of the surface layers means that a depth profile of the top 10 nm can be studied.[18] This means it is a useful technique for investigating wetting, layer deposition and thin film growth on a particle surface.[19]

The sample is loaded onto a plate in the machine under an ultra-high vacuum and undergoes sputtering to remove any air contamination on the surface. Once prepared for the measurement, the sample is bombarded by a stream of noble gas cations which can have energies in the range of 500 – 10 000 eV depending on the accelerating voltage. The ions hit the sample and undergo many interactions, including scattering, neutralisation and deposition. The angle and energy of the scattered ions is dependent on the target atom with which they interacted on the surface, so collecting these scattered ions can give information about the composition of the surface layer, as shown in Figure 2.5a. The energy of a scattered ion depends on the mass of the target atom, with

lighter atoms causing ions of lower energy and heavier atoms causing ions of higher energy. An electrostatic analyser is used to measure the velocities and energies of these scattered ions.

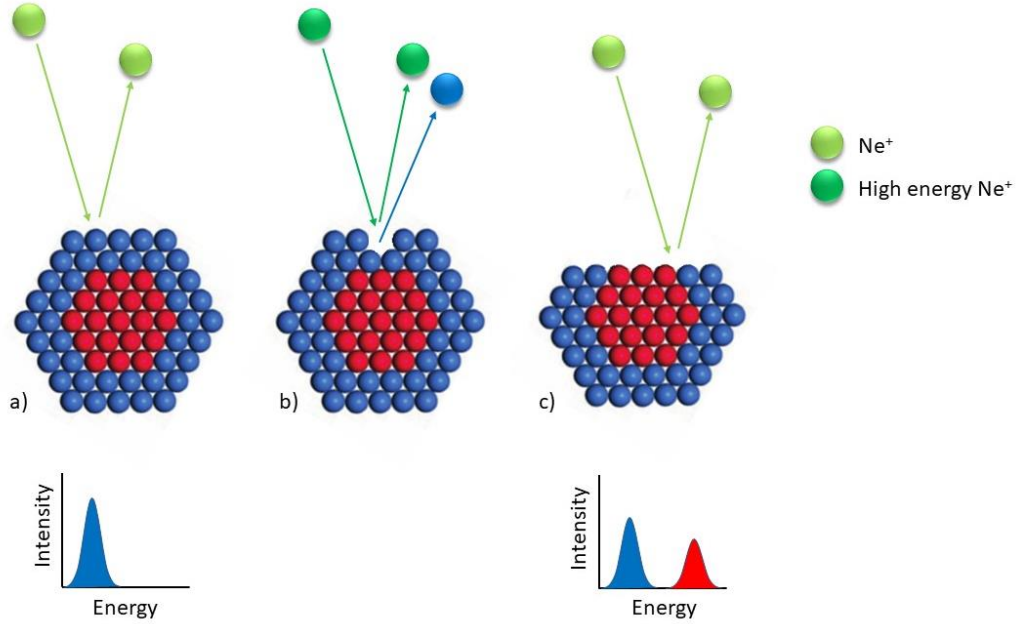


Figure 2.5. LEIS process. a) Ne+ ions are scattered by surface atoms causing a change in energy. b) Higher energy Ne+ ions are used to sputter the surface atoms off the particles. c) Ne+ ions are scattered by the new surface of the particle, showing particle composition at a specific depth.

After measurement of the outer layer surface, a higher energy Ne^+ ion beam can be used to sputter the sample and remove the top layers of atoms, as shown in Figure 2.5b. This results in the next layer being clean for a second LEIS measurement, as shown in Figure 2.5c. Through alternating measurement and sputtering, a depth profile of the sample can be accumulated.

2.7 Temperature programmed reduction

Temperature programmed reduction (TPR) is a technique used to determine the quantity of reducible species in a sample and the temperature at which they reduce. TPR can also be used to detect the induced reduction of a secondary metal, at the temperature where the primary metal is reduced. When the reduction temperature of the primary metal is reached it can undergo a coupled reduction with adjacent metals to form reduced metal species on its surface.

TPR is performed by passing hydrogen gas through a fixed bed of the sample, packed into a quartz reactor tube. The output gas is then passed through a TCD detector, which monitors the change in hydrogen concentration relative to the input gas. A lower concentration of hydrogen, due to reduction occurring in the sample, shows a positive peak. Whereas a higher concentration of hydrogen, due to expulsion of hydrogen from the sample, shows a negative peak. The quartz reactor tube is fitted inside a temperature programmed furnace, allowing the reduction to be studied across a programmed temperature ramp. To improve accuracy, the samples are pre-treated by heating them to a specific temperature under an inert gas to remove any surface contaminants.

2.8 Thermogravimetric analysis

Thermogravimetric analysis (TGA) is a useful gravimetric analysis technique which measures the change in sample mass as a function of temperature or time. A material's physical and chemical properties can be studied by monitoring its weight change when heated or cooled in a controlled manner or when held at a defined temperature over time. Changes in mass can be indicative of many chemical changes such as solvent loss, desorption, vaporization, oxidation and decomposition.[20]

Typically a small mass of sample (1-50 mg) is loaded into a Pt pan and sealed in the measurement furnace. The environment is purged with an inert or reactive gas and the weight of the pan is monitored constantly by a microbalance throughout the temperature ramp or isothermal time and compared with a tare pan. Small changes in mass can often be attributed to volatile solvents, desorption of adsorbates, or decomposition of polymers and supports.

2.9 Atom probe tomography

Atom probe tomography (APT) is a sample imaging technique that can provide a three-dimensional image of the atoms in a sample, allowing reconstruction of the alloys at an atomic

level. The samples are sharpened into nanoscale needle shaped tips, either through electrochemical polishing or focussed ion beam milling, to form a tip diameter of under 100 nm.[21] The sample is then loaded into the machine, placed under a high vacuum to allow for the travel of ions, and cooled cryogenically to remove the thermal energy of the sample and maximise the atomic structure sensitivity. Pulses of laser light of high voltage are directed to the sample, putting the atoms under a strong electric field which stimulates them to ionise one at a time and leave the sample. At a specific pulse energy, one atom can be removed from the surface at a time and accelerated through a local electrode towards a detector. A time of flight mass spectrometer is used to determine the type of atom ejected from the surface and a position sensitive detector allows atom location to be measured. Figure 2.6 shows the emission and detection process, with the laser pulse (green) causing atom ionisation and emission through the local electrode to the detector (red).

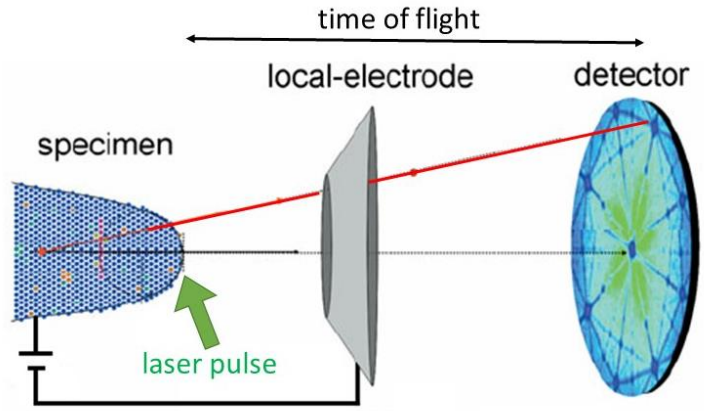


Figure 2.6. Schematic showing the process of atom probe tomography. Atoms on the sample tip are ionised and accelerated towards the detector, where their position and type are recorded. Image modified from reference.[22]

Through building up the position and type of ejected atoms individually, it is possible to form a three-dimensional image of the elemental distribution.[23] Typical detection efficiency is between 50 and 60 %, as some of the ejected atoms hit the inter-channel regions of the detector and so are not registered.[24]

2.10 Magic angle spinning nuclear magnetic resonance

Nuclear Magnetic Resonance (NMR) spectroscopy is a process used to obtain chemical, physical, electronic and structural information about molecules through measuring their chemical shifts. NMR is a bulk technique, meaning sampling is not restricted to the surface as it is in XPS. It can also be used to probe individual elements in the sample with a high degree of resolution, as it is highly element specific.

When an NMR active nucleus with a permanent magnetic dipole (i.e. a non-zero nuclear spin) is placed in an external magnetic field, its spin will align in a direction which is either parallel or anti-parallel to the external field. The sample is then subject to a radio frequency (RF) pulse and absorbs radiation at the frequency required to reverse the alignment of the spins in the external field.[25]

Each NMR active nucleus will resonate at a different RF value, allowing chemical determination of the sample to be assessed. Small changes in the electronic environment of each nucleus will shift the resonance frequency slightly. If the environment around the nucleus is more electron rich, the nucleus is shielded from the magnetic field and less energy is required to reverse the spin. This means a lower RF value is needed for the transition and the peak will have a lower chemical shift value. In contrast, if the environment around the nucleus is less electron rich, the nucleus is deshielded and more energy is required to reverse the spin, leading to a higher chemical shift.[26]

Many of the spin interactions affecting the RF value of the transition are anisotropic and so, without the continuous movement of the solution, extensive atomic-level molecular structural information is difficult to obtain. In the solid state, due to limited vibrational and rotational movement of the molecules, each atom is in a slightly different electronic environment which causes broad peaks in an NMR spectrum. One method to reduce the peak broadening effect is Magic Angle Spinning (MAS), where the sample is spun at an angle of 54°74’ reducing the

interaction of adjacent molecules and minimising peak broadening,[27] however this can still occur due to restrictions in mobility in the molecule.

2.11 References

1 R. Richards, *Surface and nanomolecular catalysis*, CRC/Taylor & Francis, Boca Raton, FL ; London, 2006.

2 J. Vickerman and I. Gilmore, *Surface Analysis – The Principal Techniques*, John Wiley & Sons, Ltd, 2009.

3 P. Atkins and D. Shriver, *Inorganic Chemistry*, Oxford University Press, Oxford, 5th ed., 2010.

4 J. W. Niemantsverdriet, *Spectroscopy in Catalysis*, Wiley-VCH Verlag GmbH & Co. KGaA, 2007.

5 R. E. Dinnebier, S. J. L. Billinge, A. Le Bail, A. Le Bail, L. M. D. Cranswick, J. K. Cockcroft, P. Norby and A. D. Zuev, *Powder Diffraction : Theory and Practice*, Royal Society of Chemistry, Cambridge, 2008.

6 B. B. He, *Two-dimensional X-Ray Diffraction*, Wiley, Hoboken, United States, 2009.

7 D. A. K. Singh, *Advanced X-ray Techniques in Research and Industry*, 2005.

8 S. Suga and A. Sekiyama, *Photoelectron Spectroscopy: Bulk and Surface Electronic Structures*, Springer Berlin Heidelberg, 2013.

9 J. M. Wagner, *X-ray Photoelectron Spectroscopy*, Nova Science Publishers, 2011.

10 P. van der Heide, *X-ray Photoelectron Spectroscopy. An Introduction to Principles and Practices*, John Wiley & Sons, Inc., 2011.

11 G. Bunker, *Introduction to XAFS : A Practical Guide to X-ray Absorption Fine Structure Spectroscopy*, Cambridge University Press, Cambridge, 2010.

12 J. Rodriguez, J. C. Hanson, P. J. Chupas, J. a Rodriguez and J. a Rodriguez, *In-situ Characterization of Heterogeneous Catalysts*, Wiley, Oxford, United States, 2013.

13 B. Fultz and J. M. Howe, *Transmission electron microscopy and diffractometry of materials*, 2008.

14 J. W. Niemantsverdriet, *Spectroscopy in Catalysis: An Introduction: Third Edition*, 2007.

15 Press Release: The Nobel Prize in Chemistry 2017, https://www.nobelprize.org/nobel_prizes/chemistry/laureates/2017/press.html.

16 R. F. Thompson, M. Walker, C. A. Siebert, S. P. Muench and N. A. Ranson, *Methods*, 2016, **100**, 3–15.

17 D. Brune, *Surface characterization : a user's sourcebook*, Scandinavian Science Publisher ; Wiley-VCH, Oslo, 1997.

18 C. V Cushman, P. Bruner, J. Zakel, G. H. Major, B. M. Lunt, N. J. Smith, T. Grehl and M. R. Linford, *Anal. Methods*, 2016, **8**, 3419–3439.

19 A. Rafati, R. ter Veen and D. G. Castner, *Surf. interface Anal.*, 2013, **45**, 11–12.

20 S. Vyazovkin, in *Characterization of Materials*, John Wiley & Sons, Inc., 2002.

21 A. Cerezo, P. H. Clifton, M. J. Galtrey, C. J. Humphreys, T. F. Kelly, D. J. Larson, S. Lozano-Perez, E. A. Marquis, R. A. Oliver, G. Sha, K. Thompson, M. Zandbergen and R. L. Alvis, *Mater. Today*, 2007, **10**, 36–42.

22 B. Gault, M. P. Moody, F. De Geuser, A. La Fontaine, L. T. Stephenson, D. Haley and S. P. Ringer, *Microsc. Microanal.*, 2010, **16**, 99–110.

23 G. Van Tendeloo, D. Van Dyck and S. J. Pennycook, *Handbook of Nanoscopy*, 2012, vol. 1–2.

24 M. K. Miller and R. G. Forbes, *Mater. Charact.*, 2009, **60**, 461–469.

25 J. A. Iggo, *NMR spectroscopy in inorganic chemistry*, Oxford University Press, Oxford, 1999.

26 J. W. Akitt, *NMR and chemistry : an introduction to modern NMR spectroscopy*, Chapman & Hall, London, 3rd edn., 1992.

27 M. Duer, *Solid-State NMR Spectroscopy Principles and Applications*, 2007.

Chapter 3

Experimental Methods

3.1 Introduction 51
3.2 Synthesis of colloidal nanoparticles 51
3.2.1 Monometallic platinum nanoparticles 51
3.2.2 Bimetallic nanoparticles 52
3.3 Synthesis of silica supported nanoparticles 53
3.3.1 Monometallic platinum nanoparticles 53
3.3.2 Bimetallic nanoparticles 54
3.4 Synthesis of carbon supported nanoparticles 54
3.4.1 Carbon supported co-reduced platinum nickel 54
3.4.2 Stepwise nanoparticle syntheses in SBA-15 55
3.5 Catalyst Testing 55
3.5.1 Liquid phase formic acid decomposition reaction 55
3.5.2 Gas phase formic acid decomposition reaction for XAS 56
3.5.3 Electrochemical oxygen reduction reaction 56
3.6 Characterisation 58
3.6.1 X-ray diffraction (XRD) 58
3.6.2 X-ray absorption spectroscopy (XAS) 59
3.6.3 Transmission electron microscopy (TEM) and energy-dispersive x-ray spectroscopy (EDX) 59
3.6.4 Low energy ion scattering (LEIS) 60
3.6.5 Temperature programmed reduction (TPR) 60
3.6.6 Thermogravimetric analysis (TGA) 60
3.6.7 Atom probe tomography (APT) 61
3.6.8 Magic angle spinning nuclear magnetic resonance (MAS-NMR) 61
3.7 References 62

3.1 Introduction

Two series of catalysts were synthesized, one stabilised with polyvinylpyrrolidone (PVP) and the other synthesised inside the channels of a mesoporous silica (SBA-15). Both series included 3 bimetallic combinations: PtAg, PtZn and PtNi, all produced at a stoichiometry of Pt_2X_8. In some cases, where described, deviations on this stoichiometry were synthesised. The activity of both series was investigated with the liquid phase formic acid decomposition reaction. A third series of PtNi(SBA-15) catalysts were synthesised using a variation of methods in order to further investigate the wall effect. These were used for ORR and compared to the commercial Pt catalyst. All samples were extensively characterised using the techniques discussed in Chapter 2.

The synthesis, activity testing and characterisation methods are discussed in this chapter. All chemicals and solvents were sourced from Sigma Aldrich, except Pt containing precursors which were supplied from Alfa Aesar.

3.2 Synthesis of colloidal nanoparticles

3.2.1 Monometallic platinum nanoparticles

PVP stabilised Pt nanoparticles, Pt(PVP), were synthesised using a modified polyol method similar to that used by Bonet *et al.*[1] In a typical synthesis, 18 μL (0.02 mmol) of $Pt(NO_3)_4$ solution was injected rapidly into a preheated solution of 11 mg (0.1 mmol) PVP (MW 40,000) in 30 mL anhydrous ethylene glycol at 120 °C. The solution was stirred under N_2 for 2 hours at 120 °C to allow reduction of Pt to form dark brown-black nanoparticles. Once the reaction was complete, the solution was cooled to room temperature and the nanoparticles were precipitated using cold acetone and centrifugation (5000 rpm, 5 min). The nanoparticles were then washed 3 times by alternating sonication in acetone and centrifugation, to remove excess PVP. The clean nanoparticles were dispersed in ethanol at a 10 mg/mL concentration.

3.2.2 Bimetallic nanoparticles

3.2.2.1 PtZn(PVP)

PtZn(PVP) nanoparticles were synthesised using a decoration redox method, similar to the method used by Gauthard *et al*.[2] with an additional reduction step. Zn reduction is aided by the presence of Pt, so the PtZn(PVP) sample was synthesised through the initial reduction of Pt, forming small seed particles, before facilitating the reduction of Zn. The Pt seed particles were synthesised as in Section 3.2.1 above. Once the reduction was complete and the solution was cooled to room temperature, the flow of N_2 was stopped and H_2 was bubbled through the solution, producing a Pt-H surface species. After 30 minutes of H_2 flow, the N_2 was replaced and a given amount of $Zn(NO_3)_2$ solution was added to the mixture and stirred for 2 hours, in order to allow Zn reduction adjacent to the Pt nanoparticles. The Zn was initially partially reduced, depositing onto the surface of the Pt by undergoing a redox reaction with the Pt-H species. Further Zn reduction was performed through adding 2 molar equivalents of $NaBH_4$ and the solution was stirred for 1 hour to allow total reduction of Zn. The nanoparticles were precipitated and washed 3 times to remove excess PVP, using cold acetone and centrifugation (5000 rpm, 5 min). The clean nanoparticles were dispersed in ethanol at a 10 mg/mL concentration.

3.2.2.2 PtAg(PVP)

PtAg(PVP) nanoparticles were also synthesised using a similar decoration redox method to that used by Gauthard *et al*.[2] Ag(PVP) particles were synthesised using a similar method to that used for Pt(PVP) described in 3.2.1. 13.6 mg (0.08 mmol) of $AgNO_3$ was added rapidly into a preheated solution of 11 mg (0.1 mmol) PVP (MW 40,000) in 30 mL anhydrous ethylene glycol at 120 °C. The solution was stirred under N_2 for 2 hours at 120 °C to allow reduction of Ag nitrate forming yellow-brown nanoparticles. After the reaction was complete and allowed to cool to room temperature, the flow of N_2 was stopped and H_2 was bubbled through the solution, producing an Ag-H surface species. After 30 minutes of H_2 flow, the N_2 was replaced and the mixture was

ramped back up to 120 °C. A given amount of $Pt(NO_3)_4$ solution was added to the mixture and stirred for 2 hours to allow Pt reduction onto the Ag surface. The Pt was initially partially reduced, depositing onto the surface of the Ag through undergoing a redox reaction with the Ag-H species. The elevated temperature of the ethylene glycol solvent was used to perform total reduction of the Pt species. Once this second reduction step was complete, the solution was allowed to cool and the nanoparticles were precipitated and washed 3 times to remove excess PVP, using cold acetone and centrifugation (5000 rpm, 5 min). The clean nanoparticles were dispersed in ethanol at a 10 mg/mL concentration.

3.2.2.3 PtNi(PVP)

PtNi(PVP) nanoparticles were synthesised using a very similar method to that used for the PtAg(PVP) in Section 3.2.2.2 above, through the decoration of Ni seed particles with Pt. The Ni seed nanoparticles were formed by using the same style polyol synthesis, with 14.6 mg (0.08 mmol) $Ni(NO_3)_2$ added rapidly to a preheated solution of 11 mg (0.1 mmol) PVP (MW 40,000) in 30 mL anhydrous ethylene glycol at 120 °C. The resultant seed solution was pale brown upon completion of the reduction. The Pt decoration process was as described in Section 3.2.2.2 above.

3.3 Synthesis of silica supported nanoparticles

3.3.1 Monometallic platinum nanoparticles

A Pt monometallic nanoparticle sample was synthesised in SBA-15, using an incipient wetness technique. 113 μL (0.128 mmol) of $Pt(NO_3)_4$ was fully dispersed in 2 mL of ethanol solution through sonication. This impregnation solution was then ground into 500 mg of SBA-15 using a pestle and mortar. After 10 minutes of grinding, the powder was left to fully dry in air for at least 5 hours. The fully dried powder was then transferred to a tube furnace and heated under N_2, using a ramp rate of 2 °C/min up to 400 °C. This was followed by a reduction at this temperature under 5% H_2 in Ar for 4 hours.

3.3.2 Bimetallic nanoparticles

Bimetallic nanoparticles supported in silica were synthesised in a similar way to the monometallic samples described in 3.3.1 above. The initial impregnation solution for the bimetallic samples was prepared with both precursors in the sample solution, leading to co-precipitation and co-reduction of the two metals in the reduction step. A typical impregnation solution was prepared through dispersing 35.2 μL (0.04 mmol) of Pt(NO3)4 solution and 30.2 mg (0.16 mmol) of Zn(NO3)2 solution in 2 mL ethanol. Total dissolution and mixing of the precursors was ensured through sonication for 5 minutes, prior to the impregnation into the SBA-15. As for the monometallic, samples the fully dried powder was then calcined and reduced under 5% H_2 in Ar at 400 °C for 4 hours.

3.4 Synthesis of carbon supported nanoparticles

3.4.1 Carbon supported co-reduced platinum nickel

PtNi nanoparticles were synthesised in SBA-15, as described in Section 3.3.2 above, allowing controlled reduction and formation inside the SBA-15 channel. For electrochemical testing, particles were transferred from the silica channels onto Vulcan carbon. The nanoparticles synthesised inside the SBA-15 were combined with Vulcan carbon (VXC72R) at an appropriate weight percentage, usually 20 wt.% metal on carbon. This powder mixture was soaked in 50 mL of distilled water and subject to continuous agitation for 3 hours, allowing for complete mixing of the carbon and silica and for the nanoparticles to migrate from the silica channels onto the carbon surface. The water was then removed from the sample through centrifugation (5000 rpm, 10 min) and the powder was soaked in 80 mL of NaOH solution (4 M) for 3 days under continuous agitation. This allowed for slow dissolution of the silica and final migration of the nanoparticles across to the carbon surface. The NaOH was removed with centrifugation (5000 rpm, 10 min) and

the particles were washed 6 times, alternating dispersion in ultrapure water and centrifugation. The catalyst was allowed to dry in air overnight.

3.4.2 Stepwise nanoparticle syntheses in SBA-15

Alternative methods were employed for nanoparticle formation in SBA-15 for varied catalytic effect, prior to deposition on carbon. The co-reduction method of nanoparticle formation inside SBA-15, described in 3.3.2 above, was adjusted to allow for stepwise reduction of the two metals. In short, the initial impregnation solution was prepared in two batches, each with only one metal dissolved inside. The first metal solution was ground into the silica and the powder was dried in air, calcined and reduced as normal. After this single metal nanoparticle deposition was complete, the second metal impregnation solution was ground into the powder and the drying, calcining and reduction process was repeated. This stepwise synthesis was performed with Ni deposition followed by Pt and also in reverse, with Pt deposition followed by Ni.

3.5 Catalyst Testing

3.5.1 Liquid phase formic acid decomposition reaction

The activities of both the colloidal and supported catalysts were tested using the liquid phase formic acid decomposition reaction. Formic acid consumption was monitored through the titration of the reaction solution with NaOH. Samples containing 0.5 mg of metal were dispersed in 25 mL of formic acid (0.1 M) and stirred at 6000 rpm at 25 °C for the timespan of the reaction, which was either 20 or 60 minutes. The reaction is stopped by filtration through a 0.4 μm polycarbonate membrane under a mild vacuum. 10 mL of reaction solution is titrated with NaOH to calculate the quantity of formic acid consumed in the time period. Two control reactions, one containing SBA-15 and the other containing PVP, were performed for comparison. Average rate of formic acid conversion normalised to Pt mass was calculated over the time of the reaction.

3.5.2 Gas phase formic acid decomposition reaction for XAS

In order to complete the *in-situ* x-ray absorption spectroscopy, it was necessary to perform the formic acid decomposition in gas phase. The silica supported samples were pressed into a pellet, loaded into an *in-situ* gas cell and purged with N_2 for initial measurement. The formic acid vapour was then supplied to the cell by passing 30 mL/min N_2 though liquid formic acid (99 %) in a bubbler at room temperature. The resultant formic acid flow was calculated to be 29.6 µL/min through the cell. The sample was held at room temperature and at this flow rate for the duration of the testing. The resultant gas was analysed with a mass spectrometer to understand the selectivity of the catalyst for the two decomposition routes.

3.5.3 Electrochemical oxygen reduction reaction

Electrochemical oxygen reduction reaction (ORR) testing was performed by Simantini Nayak and Fang Niu of the Vincent Group, Oxford and followed the below procedure. All experiments were performed at room temperature using a three-electrode system with a Metrohm Autolab, PGSTAT128N potentiostat. A Ag/AgCl (saturated KCl) reference electrode in a luggin capillary was placed near the working electrode and the Pt wire counter electrode. The ORR activities were measured under O_2 and Ar in a 0.1 M $HClO_4$ solution. Before each experiment the gas was bubbled through the electrolyte until saturation and during the measurements the gas was flowed over the solution.

The working electrode was selected to be a glassy carbon rotating disk electrode, with a geometric area of 0.385 cm^2. This was polished prior to each experiment with aqueous Al_2O_3 slurries, before being sonicated and washed in deionised water. The catalyst was prepared into an aqueous ink, through dispersion of the catalyst powder in 1 mL 2-propanol solution (20 % in H_2O) along with 4 µL of 10 wt.% Nafion, to produce a solution with catalyst concentrations of 10 mg mL^{-1}. The

catalyst ink was sonicated for 1 hour before being drop-cast onto the glassy carbon working electrode and allowed to dry for 20 minutes at room temperature prior to testing.

Cyclic voltammetry (CV) was performed in an Ar atmosphere with a sweep rate of 50 mV s^{-1}. The electrochemically active surface area (ECSA) was calculated by estimating the charge resulting from the H_{upd} adsorption (Q_H) shown by the CV measurement between 0.05 and 0.37 V. The specific ECSA was calculated using the following equation:

$$ECSA = \frac{Q_H}{M_{Pt} \times q_H} \qquad \textit{(Equation 1)}$$

where Q_H is the charge for H_{upd} adsorption, M_{Pt} is the Pt mass in each catalyst calculated based on the ICP-MS measurements and q_H is the charge required for monolayer adsorption of H_2 on Pt surfaces (210 µC cm^{-2}).

The ORR activities of each catalyst were measured in an O_2 saturated solution of 0.1 M $HClO_4$ with an O_2 atmosphere during measurement. Linear sweep voltammetry (LSV) measurements were taken for each catalyst, with different rotation speeds of 400, 800, 1200, 1600 and 2000 rpm and a sweep rate of 5 mV s^{-1}. The measurement with a rotation speed of 1600 rpm was used for calculation of the mass activity and specific activity. The current at 0.9 V was divided by the Pt loading and the ECSA for determination of the mass activity and specific activity respectively,

For the calculation of the number of electrons in the process and determination of partial or full reduction, the Levich equation (Equation 2) was used with measurements from all 5 rotation rates.

$$\frac{1}{i_m} = \frac{1}{i_K} + \frac{1}{B_L.\omega^{0.5}} \qquad \textit{(Equation 2)}$$

where i_m is the mass transport current, i_K is the kinetic current, B_L is the Levich constant and ω is the angular rotation rate of the electrode (rad/s).

3.6 Characterisation

3.6.1 X-ray diffraction (XRD)

3.6.1.1 Powder XRD

Colloidal and supported catalysts were prepared with different methods in order to achieve the best results. The colloidal samples were dispersed in a small amount of ethanol and drop-cast onto a thin glass slide before being allowed to dry in air to form a thin film of the sample with an even thickness and a smooth surface. The supported powder samples were pressed into a fixed depth well on a glass slide, using a flat glass slide to form an even thickness and smooth surface. Both types of sample were loaded onto a plastic sample holder for characterisation. The powder x-ray diffraction was performed using a Bruker Eco diffractometer, with the generator operating at 40 kV and 40 mA. The samples were rotated at 50 rpm and the scans were collected with angles between 20 and 90°, an opening degree of 1, a step size of 0.0217° and a step time of 1 second.

3.6.1.2 Wide angle x-ray scattering (WAXS)

WAXS was collected at beamline I22 of the Diamond Light Source in collaboration with Adam Clark, UCL. Data collection was performed at 18 KeV using the Pilatus 3-2M-DLS-L detector with a refined sample detector distance of 177 mm, calibrated using the NIST 640c silicon standard reference material. Scans were performed *ex-situ* within 2 mm polycarbonate capillaries with a total data acquisition time per sample of 1 s. The collected 2-dimensional images were corrected for incident flux, transmission and collection time, before being reduced to 1-dimenstional patterns using the DAWN software package.[3,4] An empty capillary was used to subtract the background from the data and a control SBA-15 sample was also collected for comparative purposes. Data was processed with baseline subtraction to allow for direct comparison and peak fitting.

3.6.2 X-ray absorption spectroscopy (XAS)

XAS was collected at beamline B18 of the Diamond Light Source in collaboration with Adam Clark, UCL. Samples were ground in a pestle and mortar and were pressed into a 13 mm pellet, with fumed silica used as an additional binder where required. The pellets were loaded into a sample rack for *ex-situ* measurements or a gas tight cell for *in-situ* measurements. The XAS measurements were conducted in the transmission geometry, in a step scan mode and using a silicon 311 double crystal monochromator. The Pt L_3 edge was measured between 11,336 and 12,364 eV, the Zn K edge was measured between 9,462 and 10,512 eV, the Ag K edge was measured between 25,314 and 26,363 eV and the Ni K edge was measured between 8,133 and 9,182 eV. The *in-situ* experiment was conducted by passing N_2 through a formic acid bubbler at room temperature, resulting in 29.6 µL/min formic acid. The gas was passed over the pellet in the cell for 1.5 hours and the XAS spectrum was recorded every 3 minutes.

XANES and EXAFS fitting was performed by Adam Clark through comparing data collected to the calculated data from modelling, using the FDMNES program.[7]

3.6.3 Transmission electron microscopy (TEM) and energy-dispersive x-ray spectroscopy (EDX)

TEM and energy dispersive spectroscopy (EDX) were performed using a number of instruments. Lower resolution imaging was performed on a JEOL 3000F microscope, which was operated at 300 kV. Higher resolution TEM was performed at Johnson Matthey on a JEM 2800 microscope operated at 200 kV, with dark field imaging in scanning mode using an off-axis annular detector and EDX analysis also in scanning mode. Sample inks were prepared by dispersing approximately 1 mg of sample in approximately 1 mL of ethanol and sonicating for 30 minutes. One drop of this dispersion was cast onto a holey carbon copper grid (400 mesh) and the solvent was allowed to evaporate in air before analysis. Average particle sizes were calculated from at least 100 particles.

3.6.4 Low energy ion scattering (LEIS)

High sensitivity-low energy ion scattering (HS-LEIS) was used to probe the change in composition at different particle depth. The data was collected at Xiamen University by Jianwei Zheng. The experiments were performed in a combined elevated pressure reaction cell using an ultrahigh vacuum (UHV) system. Sample preparation and characterisation were conducted in the primary UHV chamber (base pressure, 2×10^{-9} Torr). HS-LEIS was measured by IONTOF Qtac100 using $20Ne^{+}$ (5 keV) as ion source with a scattering angle of 145°.

3.6.5 Temperature programmed reduction (TPR)

TPR measurements were taken using a Quantachrome Instruments ChemBET Pulsar TPR/TPD Automated Chemisorption Analyser. Standard analysis was performed by packing 20 mg of sample inside the quartz reactor U-tube, fixed with quartz wool at either end of the bed. Each sample was pre-treated in helium for 30 minutes at 100 °C and cooled to room temperature before analysis. TPR was performed in a H_2 flow of 100 mL/min, with a temperature programme from 40 °C to 800 °C and a ramp rate of 10 °C/min. The TCD detector was set at 150 mA with an attenuation of 2.

3.6.6 Thermogravimetric analysis (TGA)

TGA measurements were taken using a TA instruments TGA 50, with a gas flow of air at 10 mL/min inside the furnace. 10 mg of sample powder was placed in a sample pan which was loaded into the furnace. The sample pan mass was accurately measured using a microbalance and compared to a tare pan. The sample was held at isothermal conditions for 5 minutes, then the temperature was ramped at 10 °C/min to 800 °C. The sample mass was measured over time throughout the temperature ramp.

3.6.7 Atom probe tomography (APT)

The APT experiment was performed by Tong Li at the Institute for Materials & ZGH at Ruhr-Universität Bochum. The APT specimens were prepared by drop-casting the SBA-15 particle dispersion onto a flat Si wafer, which was covered by a 200 nm thick protective Cr layer.[8] Needle shaped APT specimens were prepared from the flat Si sample by a site-specific lift-out procedure using a FEI Helios G4 CX focused ion beam (FIB) or scanning electron microscope. The APT experiments were conducted in a CAMECA LEAP 5000 XR instrument, equipped with an ultraviolet laser with a spot size of 2 µm and a wavelength of 355 nm. The detection efficiency of this state of the art microscope is ~52%. Data was acquired with equipment in the laser pulsing mode with a specimen temperature of 60 K, a target evaporation rate of 3 ions per 1000 pulses, a pulsing rate of 125 kHz and a laser pulse energy of 70 pJ. The APT data were reconstructed and analysed using the commercial IVAS 3.6.14™ software.

3.6.8 Magic angle spinning nuclear magnetic resonance (MAS-NMR)

MAS-NMR measurements were taken by Ben Griffith and John Hanna at Warwick University. ^{29}Si MAS NMR single pulse measurements were performed at a magnetic flux of 7.05 T using a Varian/Chemagnetics InfinityPlus spectrometer operating at a Larmor frequency (ν_o) of 59.6 MHz. These experiments were performed using a Bruker 7 mm HX probe which enabled a MAS frequency of 5 kHz to be implemented. Pulse length calibration was performed on solid kaolinite from which a $\pi/2$ pulse time of 4.5 µs was measured. Quantitative measurements were achieved with a $\pi/3$ pulse of 3.0 µs angle, together with a recycle delay of 240 s. To aid the simulation and deconvolution through accurate identification of the speciation in the MAS NMR data, analogous ^{1}H-^{29}Si cross-polarisation MAS (CP MAS) measurements were undertaken. These used a 4 µs ^{1}H $\pi/2$ pulse (ν_o=300.1 MHz), a 4 ms contact time, a CP ramp between 75 % and 100 % and a 5 s recycle delay. For both single pulsed and CP MAS experiments, heteronuclear ^{1}H decoupling was applied during collection. All ^{29}Si chemical shifts are reported against the IUPAC recommended

primary ^{29}Si reference of Me_4Si (δ_{iso}=0.0 ppm), with a solid kaolinite secondary reference at δ_{iso}= -92 ppm.[9]

Single pulse ^{1}H MAS measurements were performed at 9.45 T using a Bruker Avance HD spectrometer, operating at a ^{1}H ν_o of 398.8 MHz and a MAS frequency of 12 kHz. These experiments were performed using a Bruker 4 mm HX probe which enabled a MAS frequency of 12 kHz to be achieved. A ^{1}H $\pi/2$ pulse time of 2.50 μs was calibrated with solid α-alanine using a $\pi/4$ pulse of 1.25 μs, together with a recycle delay was 5 s. All ^{1}H chemical shifts are reported against the IUPAC recommended primary ^{1}H reference of Me_4Si (δ_{iso}=0.0 ppm) and a solid α-alanine secondary reference (CH_3 resonance) at δ_{iso}=1.1 ppm.[9]

All ^{195}Pt solid state NMR measurements were conducted on a Bruker Avance HD 7.05 T spectrometer (ν_o=64.5 MHz) using a novel Bruker 7 mm static solids auto-tuning (ATMA) probe. The ATMA probe allows consistent automated tuning across the 3.6 MHz Pt Knight/chemical shift range, giving highly reproducible Variable Offset Cumulative Spectroscopy (VOCS)[10–12] data which are comparable to our previous Field Sweep Fourier Transform (FSFT) method.[12] The VOCS method with automatic probe tuning stepped through the ^{195}Pt spectral range at 50 kHz frequency intervals and applied a Hahn echo ($\pi/2$ - π - acquire) experiment which employed 4/8 μs, $\pi/2/\pi$ pulse durations for data acquisition at each frequency step. A total of 250,000 transients were acquired per slice, with a recycle delay of 0.1 s used for the fast relaxing Pt metal (Knight shifted) region. The more diamagnetic PtO_2 region used a longer recycle delay of 7 s, with only 5000 transients being acquired at this higher frequency (downfield) region. Pulse time calibration and the ^{195}Pt shift referencing was performed on a Pt metal sample which served as secondary reference (δ_{iso}=-35,350 ppm) against the IUPAC reference of 1.2 M Na_2PtCl_6 (δ_{iso}=0.0 ppm).[12]

3.7 References

1 F. Bonet, V. Delmas, S. Grugeon, R. H. Urbina and P. Silvert, *NanoStructured Mater.*,

1999, **11**, 1277–1284.

2 F. Gauthard, F. Epron and J. Barbier, *J. Catal.*, 2003, **220**, 182–191.

3 M. Basham, J. Filik, M. T. Wharmby, P. C. Y. Chang, B. El Kassaby, M. Gerring, J. Aishima, K. Levik, B. C. A. Pulford, I. Sikharulidze, D. Sneddon, M. Webber, S. S. Dhesi, F. Maccherozzi, O. Svensson, S. Brockhauser, G. Náray and A. W. Ashton, *J. Synchrotron Radiat.*, 2015, **22**, 853–858.

4 J. Filik, A. W. Ashton, P. C. Y. Chang, P. A. Chater, S. J. Day, M. Drakopoulos, M. W. Gerring, M. L. Hart, O. V Magdysyuk, S. Michalik, A. Smith, C. C. Tang, N. J. Terrill, M. T. Wharmby and H. Wilhelm, *J. Appl. Crystallogr.*, 2017, **50**, 959–966.

5 J. H. Scofield, *J. Electron Spectros. Relat. Phenomena*, 1976, **8**, 129–137.

6 A. V. Naumkin, A. Kraut-Vass, S. W. Gaarenstroom and C. J. Powell, NIST X-ray Photoelectron Spectroscopy Database, https://srdata.nist.gov/xps/.

7 Y. Joly, O. Bunău, J. E. Lorenzo, R. M. Galéra, S. Grenier and B. Thompson, *J. Phys. Conf. Ser.*, 2009, **190**, 12007.

8 P. Felfer, T. Li, K. Eder, H. Galinski, A. P. Magyar, D. C. Bell, G. D. W. Smith, N. Kruse, S. P. Ringer and J. M. Cairney, *Ultramicroscopy*, 2015, **159**, 413–419.

9 R. K. Harris, E. D. Becker, S. M. Cabral de Menezes, R. Goodfellow and P. Granger, *Solid State Nucl. Magn. Reson.*, 2002, **22**, 458–483.

10 D. Massiot, I. Farnan, N. Gautier, D. Trumeau, A. Trokiner and J. P. Coutures, *Solid State Nucl. Magn. Reson.*, 1995, **4**, 241–248.

11 J. V. Hanna, K. J. Pike, T. Charpentier, T. F. Kemp, M. E. Smith, B. E. G. Lucier, R. W. Schurko and L. S. Cahill, *Chem. - A Eur. J.*, 2010, **16**, 3222–3239.

12 G. J. Rees, S. T. Orr, L. O. Barrett, J. M. Fisher, J. Houghton, G. H. Spikes, B. R. C. Theobald, D. Thompsett, M. E. Smith and J. V Hanna, *Phys. Chem. Chem. Phys.*, 2013, **15**, 17195–17207.

Chapter 4

Polymer stabilised nanoparticle synthesis

4.1 Background 65
4.2 Objectives 67
4.3 Experimental details 67
4.4 Characterisation of colloidal platinum nanoparticles 68
4.4.1 Platinum(PVP) nanoparticles 68
4.5 Characterisation of colloidal bimetallic nanoparticles 71
4.5.1 Platinum silver colloidal nanoparticles 72
4.5.2 Platinum nickel colloidal nanoparticles 82
4.5.3 Platinum zinc colloidal nanoparticles 87
4.6 Formic acid decomposition 93
4.7 Conclusions 97
4.8 References 99

4.1 Background

Over 90% of the world's chemical production processes now use at least one catalytic step[1] so the need for catalyst optimisation has never been greater. The use of bimetallic nanoparticles as catalysts is very common: Pt-Rh alloys are used in the oxidation of ammonia for nitric acid production,[2] Pt-Pd alloys are used in catalytic converters for the conversion of harmful CO and NO_x emissions,[3] and Pt based alloys are used for oxygen reduction in fuel cells[4] to name a few universal processes. Bimetallic nanoparticles are utilised so often for catalysis due to their unique structural and electronic properties, as well as their cost-efficiency compared to monometallic noble metals.[5,6] In platinum group metal (PGM) - transition metal alloys, it is usual for the PGM to be the active site for catalysis and the secondary metal to be in close contact with the PGM surface.[7,8]

Core-shell particles are an ideal step to improving the number of surface sites of the PGM, while maintaining the close contact needed with the secondary metal in order to benefit from the enhancements. In addition to enhancements in catalytic activity and selectivity, a core-shell geometry minimises the percentage of PGM in the not catalytically active particle core which makes it cost efficient. As of May 2018, the price of Pt was $942 /oz,[9] so minimising the amount of this in the catalytically inactive core is necessary for cost efficiency.

In addition to alloying PGMs with a secondary metal, it is important to use nanoparticulate catalysts to maximise the surface area to volume ratio. On decreasing the particle diameter, a greater proportion of atoms become active surface sites.[10,11] However atoms on the particle surface are not fully coordinated and so have a high surface energy, which leads to particle agglomeration. One method to maintain the nanoparticulate size is to use a polymer as a surface stabiliser, which reduces the surface energy as well as forming a steric barrier to agglomeration.[12] Polyvinylpyrrolidone (PVP) is composed of a hydrophobic long chain aliphatic backbone which

supports the repeating hydrophilic pyrrolidone ring unit. The pyrrolidone ring can bind to the metal surfaces through the carbonyl oxygen, while the hydrophobic alkyl chain creates repulsive interactions with other encapsulated particles, as described by the schematic in Figure 4.1.[13,14]

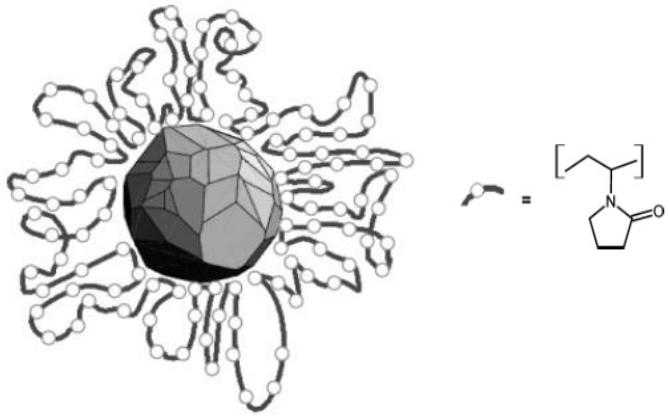


Figure 4.1. Representation of a PVP polymer bound to a metal particle of unspecified shape. Reproduced from literature.[15]

A large amount of literature investigates the performance of PVP as a stabiliser, a shape modifier and a reducing agent for monometallic particles. Various morphologies of Ag nanoparticles have been developed through controlling compositions of polymer and capping ions.[16–19] However, as a structural directing agent, PVP is too large for the control of intricately shaped nanoparticles below 10 nm.[20] In previous Pt nanoparticle syntheses, unless combined with further shape directing ions, PVP has been effectively used as a stabilising agent.[21]

There are many factors that can affect the success of PVP as a stabiliser. For example, it has been reported that the ratio of metal to polymer is vital for well distributed nucleation and for small particle growth, with common PVP to metal ratios are around 10:1. The polymer chain length can also affect the particle agglomeration. For example, smaller chain lengths (MW~10,000) interact with fewer metal ions per chain than longer chain lengths (MW~1,300,000). This leads to smaller sized metal particles when using shorter chain polymers.[22,23]

Recent work on bimetallic nanoparticles supported with PVP has been plentiful, with common alloys including Au-Ag and Pt-Pd.[24–26] Core-shell morphologies have been synthesised for Pt-Pd systems, however work on PGM - transition metal alloys with defined metal interfaces is less well documented. Further investigation into transition metal core - PGM shell PVP supported nanoparticles would benefit many catalytic processes, through increased active surface sites and improved cost-efficiency.

4.2 Objectives

The primary aim of this chapter is to investigate the synthesis of structurally directed Pt bimetallic nanoparticles. The aims of the synthetic investigation are to produce small (3-5 nm) bimetallic particles with a narrow size distribution. The secondary transition metal will ideally form a core particle and Pt will be deposited as a thin layer (2-3 atomic layers) across the surface of the secondary metal. There should be a defined interface between the secondary metal and the Pt surface with as few defects as possible. The secondary metals investigated to alloy with Pt are Ag, Ni and Zn. The use of PVP as a stabiliser is intended to allow the formation of small particles without significant aggregation. The characterisation focusses on the structural and electronic changes of the Pt surface, however the investigation into distortions in the secondary metal is also of interest. The liquid phase formic acid decomposition reaction is utilised as a probe reaction to understand the Pt surface in more detail. Changes in the decomposition activity can be correlated to the structural and electronic changes on the Pt surface active sites.

4.3 Experimental details

A detailed discussion of both the nanoparticle synthesis and the test reactions performed with the formic acid decomposition reaction can be found in Chapter 3. In summary, secondary metal seed particles were formed with a polyol method modified from Bonet *et al*.[27] This was followed by the

deposition of a Pt layer onto the seed surface through a redox mechanism modified from Gauthard *et al*.[28] Initial seed particles are formed through the addition of the stabiliser, PVP, to the reducing agent and solvent, ethylene glycol, then heating the mixture to 120 °C. Once at the reducing temperature, the metal precursor is added to the solvent mixture and stirred for 2 hours to allow metal reduction. The reaction mixture is then cooled and H_2 is bubbled through the solvent for 30 minutes, forming M-H surface species. Afterwards, the reaction mixture temperature is raised to 110 °C and the Pt precursor is injected. The reaction is stirred for 1 hour and then cooled to room temperature. The particles are washed with acetone 3 times and then re-dispersed in ethanol for storage at room temperature.

The catalytic activity of the synthesised samples is tested with the liquid phase formic acid decomposition reaction, as a probe into structural and electronic changes at the active surfaces. In brief, 0.1 mL sample is dispersed in 25 mL 0.1M formic acid and stirred at room temperature for 20 minutes. The resulting solution is filtered to remove the catalyst and then titrated against 0.1M NaOH to ascertain the amount of formic acid reacted and hence, the activity of the catalyst.

4.4 Characterisation of colloidal platinum nanoparticles

Monometallic nanoparticles stabilised by PVP were prepared in order to compare the bimetallic structural parameters to a reference Pt particle of a similar size and under similar environmental conditions. The very small particle size and the interaction with the stabiliser can affect both the lattice parameter and the electronic environment of a nanoparticle surface.

4.4.1 Platinum(PVP) nanoparticles

The nanoparticles were characterised with X-ray diffraction (XRD) and Transmission Electron Microscopy (TEM) in order to understand their sample composition, crystallinity, lattice parameter and crystallite size and shape. The XRD profile, shown in Figure 4.2, shows the measured profile in red and the fitted profile in blue. The reference Pt stick pattern is also shown

at the bottom in yellow. The reflections (111), (200), (220) and (311) can clearly be seen, as well as the (222) reflection which has a lower intensity. The lattice parameter was calculated to be 3.916 Å, which is very similar to the bulk Pt lattice of 3.924 Å. The small contraction in lattice compared to the bulk reference material may be due to the nanoparticulate size, which has been previously seen and modelled in literature.[29,30] The fitting of the first four peaks was used to obtain the full peak width at half the maximum height (FWHM) and calculate the particle size through use of the Scherrer equation, as described in Chapter 3. This resulted in a particle size of 4.4 nm.

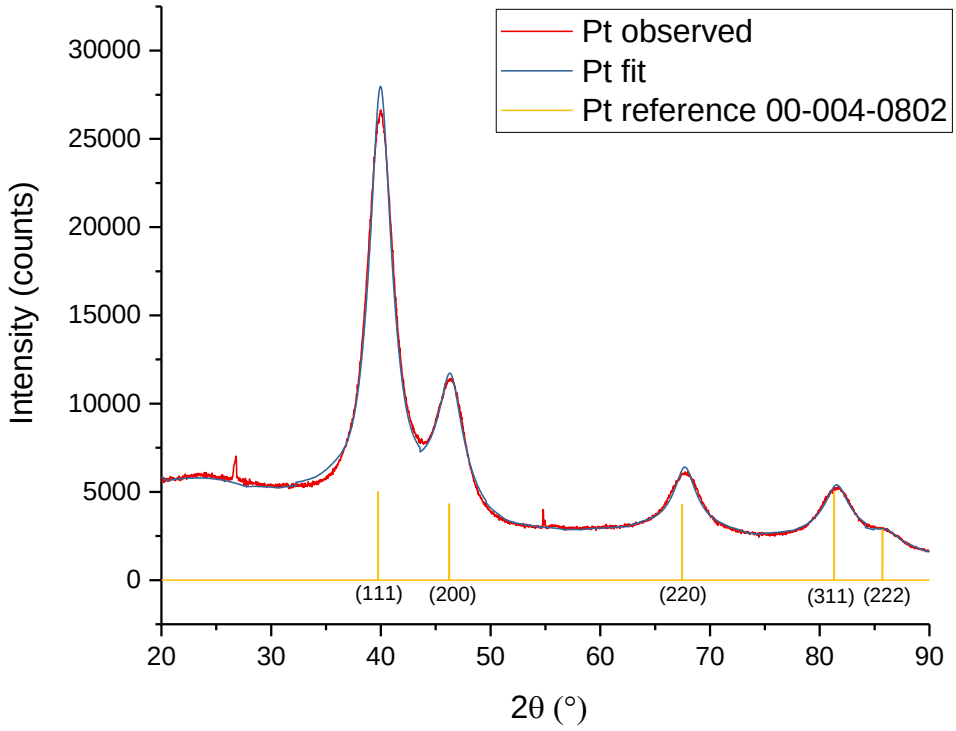


Figure 4.2. XRD profile showing Pt(PVP) nanoparticles. Observed intensity is shown in red, fitted intensity is shown in blue. Pt reference (00-004-0802) positions are shown in yellow.

TEM was further used to understand particle size, shape and agglomeration. Figure 4.3 shows that the particles are mainly spherical, but some aggregation is also visible. This is commonly seen in polymer supported samples and is known as "beads on a string" aggregation.[31] Aggregation in this manner is often due to the deposition of more than one particle on a single polymer chain.

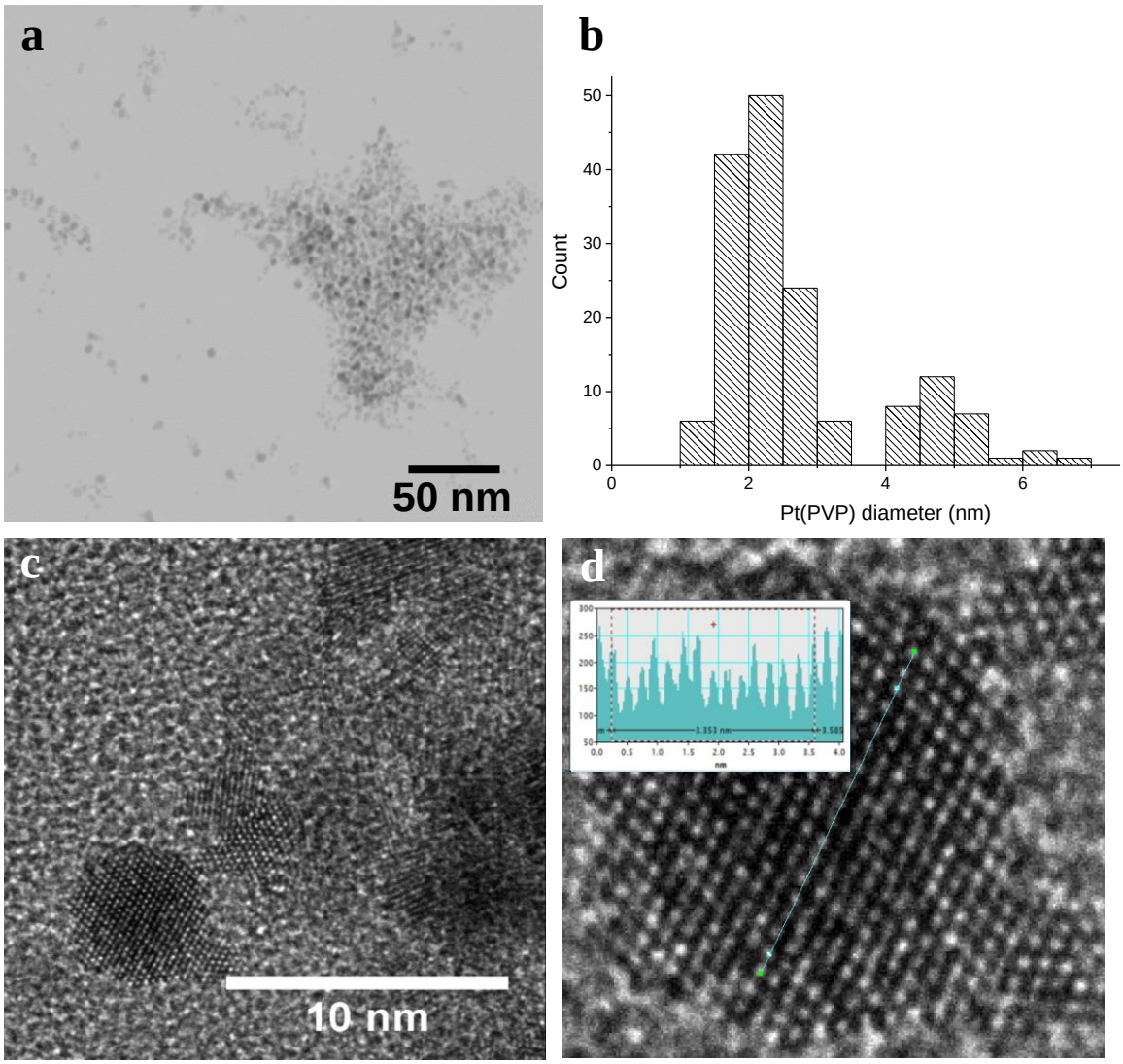


Figure 4.3. STEM and TEM images of Pt(PVP) particles taken at Johnson Matthey. a) STEM image of many particles showing homogeneity. b) Size distribution graph. c) HR-TEM image showing the lattices of various particles. d) HR-TEM image showing the intensity profile used to calculate lattice parameter.

In addition to the particle shape, a representative image was selected for particle size analysis and the diameters of 160 particles were measured. It was found that the average particle size is 3.0 nm (standard deviation of 1 nm). This is slightly lower than the crystallite size found in XRD but, as the Scherrer equation is merely an estimate of particle size, the measurements are within the bounds of uncertainty. The bimodal size distribution histogram shows that there are two differently sized particle regimes, this could be due to a variation in the number of particles surrounded by one PVP molecule. The particles around 2 nm are likely single particles, whereas the particles at 5 nm could be small aggregates due to multiple particles on one PVP chain.

Both high resolution TEM and electron diffraction were also used to obtain lattice information. Crystals were imaged along the zone-axis plane of view, with the space lattice measured and diffraction pattern obtained in the (111) orientation. The space lattice measurement gave a distance of 2.380 Å which was the same as the electron diffraction measurement. These were used to calculate the lattice parameter of 3.999 Å. This is lower than the expected measurement from XRD, although TEM gives a less accurate measurement due to the orientation of the particle and the low sampling values.

4.5 Characterisation of colloidal bimetallic nanoparticles

When a secondary metal is introduced to the system, it is expected that there will be an interaction with the Pt. Thermodynamically the metal with the lowest surface energy will be favoured as the shell of a core-shell bimetallic particle.[32,33] Ag has the lowest surface energy in our series and so is expected to form a shell around Pt, while Zn and Ni have higher surface energies than Pt and so are expected to form a core with a Pt shell. During a redox process, as in this bimetallic synthesis, a co-reduction would favour the metal with the highest redox potential precipitating first and forming the core of a core-shell particle.[34] This would lead to the initial reduction of Pt, forming a core, and the secondary metal depositing on the surface. In order to combat this, the PtAg and PtNi bimetallic colloidal PVP stabilised nanoparticles were formed in a two-step reduction, in order to encourage formation of a Pt shell on the pre-synthesised Ni or Ag core. A Zn core was not successfully synthesised and so the PtZn system was synthesised from initial reduction of a Pt core and then further addition of Zn. The colloidal sample is suspended in ethanol, so the movement of Zn from the shell towards the core to form the thermodynamically favoured product is possible.

All three samples were characterised with XRD and TEM to compare composition, crystallinity, lattice parameter and particle size and shape with the monometallic Pt counterpart. All three samples were also analysed with XAS, in order to understand more about the local environment

of the metal atoms. Cryo-TEM was also used to monitor the reaction progression for the PtAg sample, as well as to ensure that the ambient TEM was representative of the colloidal sample.

4.5.1 Platinum silver colloidal nanoparticles

The PtAg(PVP) sample was characterised with XRD. A typical profile is shown in Figure 4.4 with the observed profile in red, the fitted profile in blue and the reference stick patterns at the bottom with Pt in yellow and Ag in green. Despite the sample containing two metals, only one series of peaks is seen in the profile which are at angles similar to the Ag reference pattern. These reflections are attributed to the Ag core particle, with the Pt deposition on the Ag core assumed to be too small to show reflections. The measured Ag reflection peaks are visible at slightly higher angles than the reference would suggest, which indicates that the Pt causes a contraction in the Ag lattice due to the close contact of the two metals at the interface. There is also thought to be an expansion in the Pt lattice.

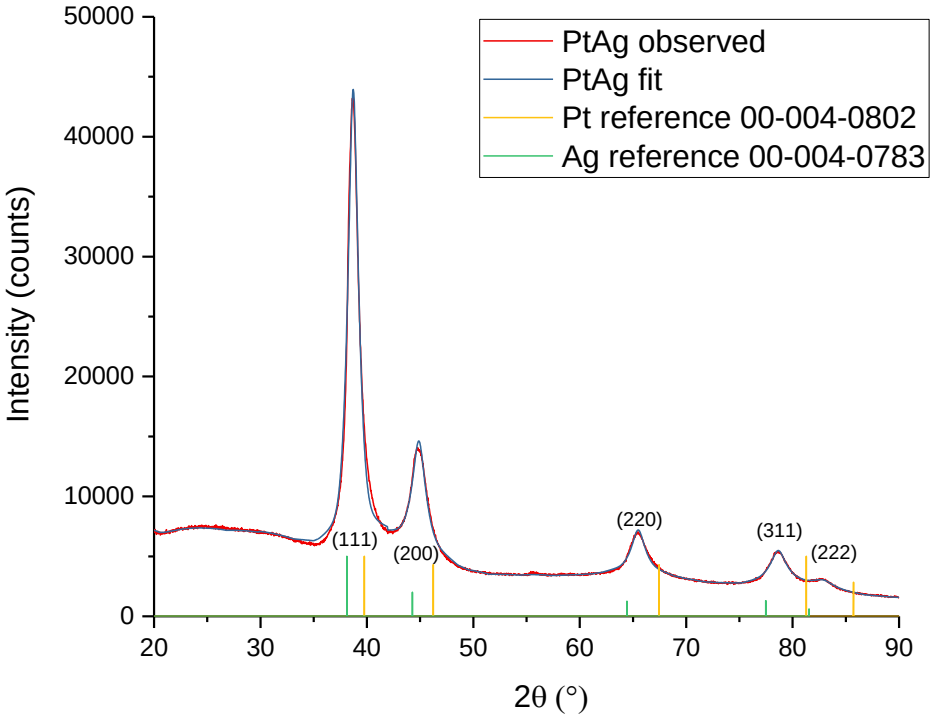


Figure 4.4. XRD profile showing PtAg(PVP) nanoparticles. Observed intensity is shown in red, fitted intensity is shown in blue. Pt reference (00-004-0802) positions are shown in yellow and Ag reference (00-004-0783) positions are shown in green.

The Ag lattice parameter was calculated to be 4.032 Å which is lower than the bulk Ag lattice of 4.085 Å. The Scherrer Equation was used to calculate the crystallite size from the (111), (200), (220) and (311) peaks and resulted in a crystallite size of 6.5 nm.

As shown in Figure 4.5, TEM was used to further investigate the size, shape and alloy morphology of the particles. Particle size analysis was performed on a representative image to calculate an average particle size of 47 nm, although a wide distribution of sizes was observed. This average particle size is much higher than the crystallite size found in XRD, which indicates that there is severe aggregation of each crystallite, also evident in the HR-TEM images.

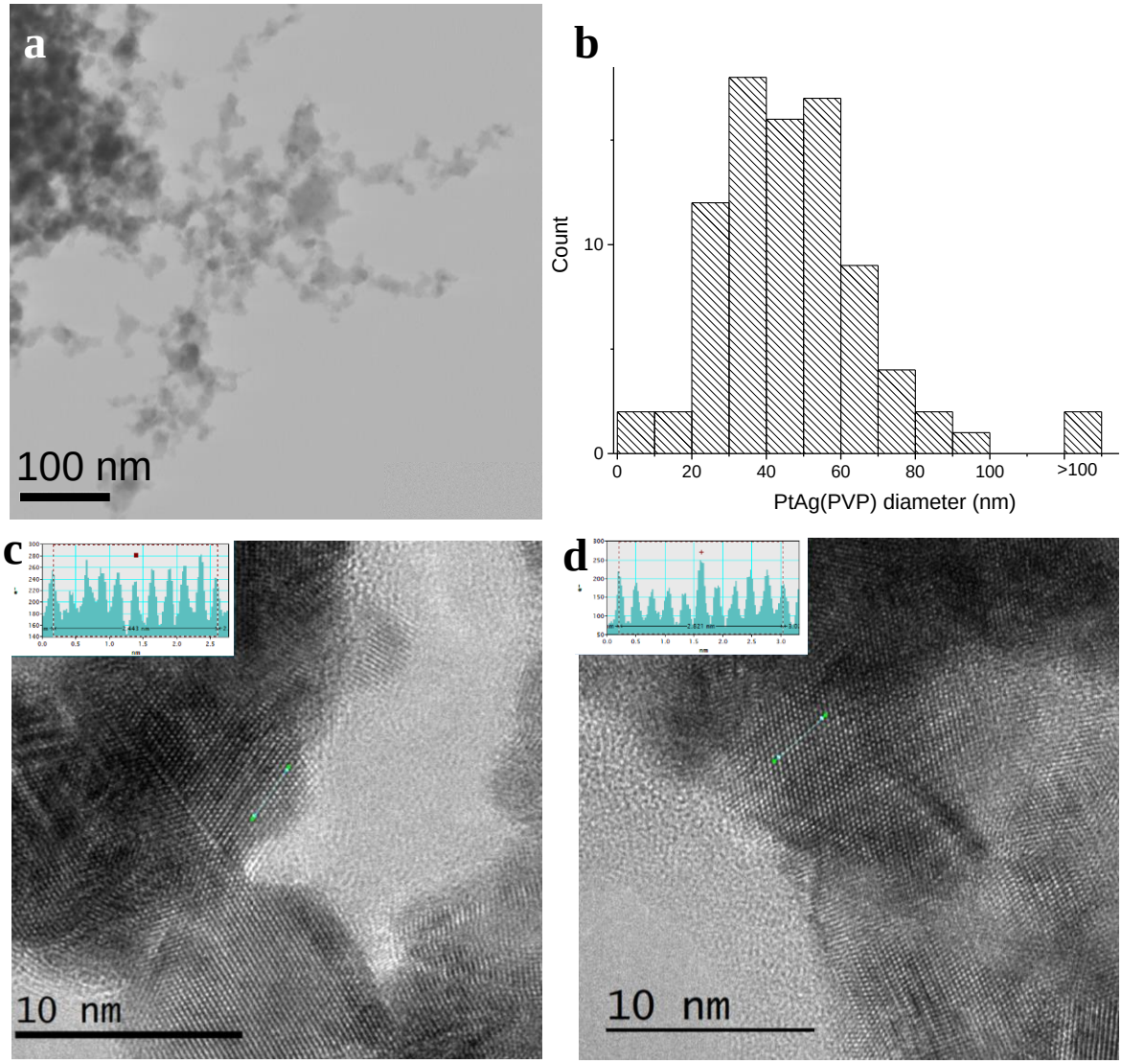


Figure 4.5. STEM and TEM images of PtAg(PVP) particles taken at Johnson Matthey. a) STEM image of many particles showing homogeneity. b) Size distribution graph. c) HR-TEM image showing lattices and intensity profile used to calculate lattice parameter for edges. d) HR-TEM image showing lattices and intensity profile used to calculate lattice parameter for centre.

Both high resolution TEM and electron diffraction were also used to obtain lattice information. Crystals were imaged along the zone-axis plane of view, with the space lattice measured and diffraction pattern obtained in the (111) orientation. The space lattice measurement gave two distances, 2.443 Å near the edges and 2.821 Å in the particle centres. This could indicate that the smaller lattice Pt is nearer the edges of the species and the larger lattice Ag is in the core. The smaller of these measurements is similar to the diffraction measurement of 2.449 Å. This was used to calculate the lattice parameter of 3.887 Å. This is lower than the expected measurement from

XRD, although TEM gives a less accurate measurement due to the orientation of the particle and the low sampling values.

As with the Pt(PVP) sample discussed in 4.4.1, it is possible to again see the particle aggregation into a “beads on a string” formation which is common in polymer supported nanoparticles. EDX mapping was used to distinguish the two metals in the particles and further understand the alloy morphology. Figure 4.6a shows an EDX profile which indicates the presence of both Pt and Ag in the sample. As expected there is a higher proportion of Ag than Pt due to the sample stoichiometry. The other high intensity assigned peaks are caused by the Cu TEM grid and possible Cd contamination, although this is in the same region as the weaker L lines produced from the Ag emission, as shown by the reference stick pattern for Ag on the x-axis. The lower intensity assigned peaks, such as Cu, Si, Fe and Cr are caused by the interaction of the x-rays with the sample holder and instrument parts.

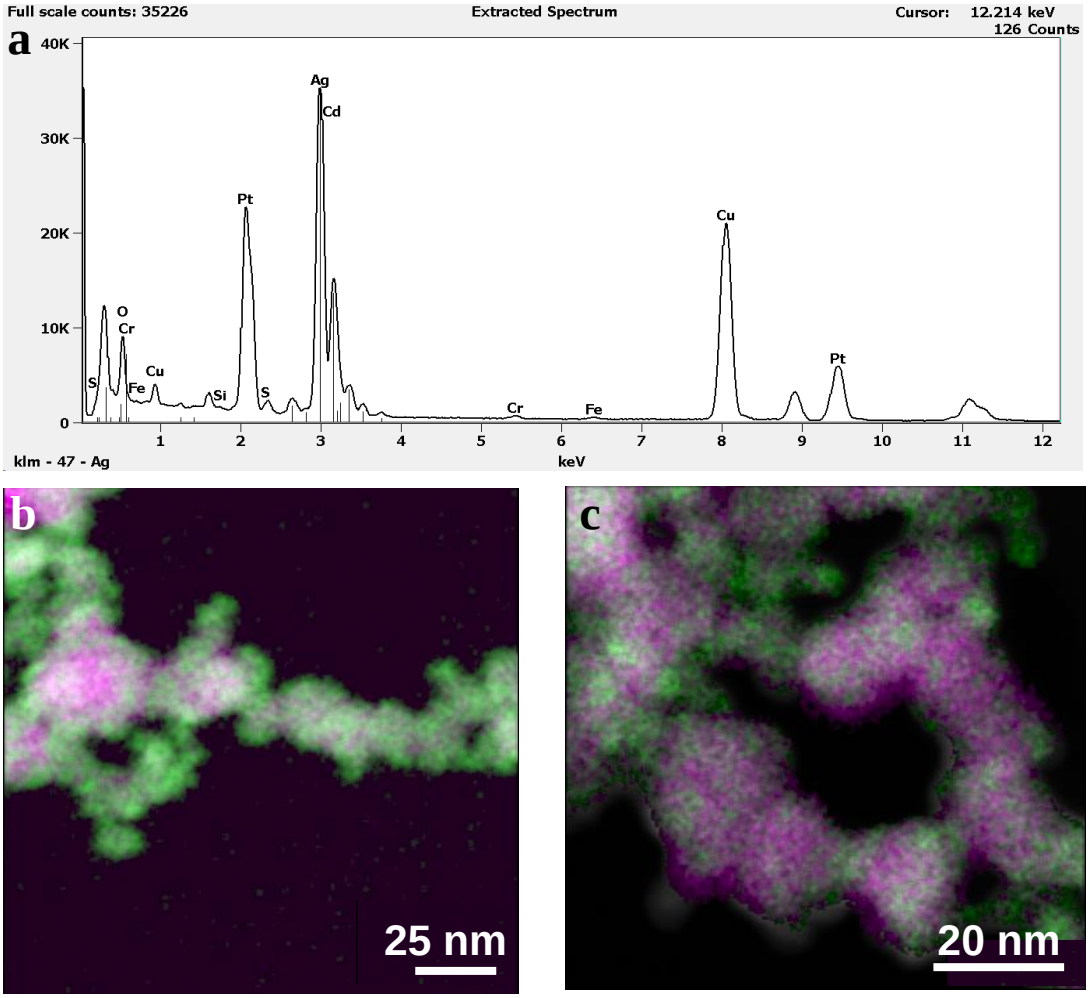


Figure 4.6. STEM EDX images of PtAg(PVP) particles taken at Johnson Matthey. a) EDX profile showing atomic compositions, with Ag reference stick pattern in black. b&c) STEM EDX maps of PtAg(PVP) sample in different regions, with Pt in green and Ag in pink.

Figure 4.6b&c show energy-dispersive x-ray spectroscopy (EDX) maps of the sample, with Ag shown in pink and Pt shown in green. In both images the Ag particles form the "beads on a string" morphology in the centre of the particles, with the Pt forming a coating of smaller nanoparticles on the Ag surface. Ag is seen to form the aggregated core particles, as a result of the initial formation of the Ag seed in the sample as with the Pt(PVP) particles in Section 4.4.1. The Pt coating on the Ag nanoparticles does not appear to be a thin and even layer, with Figure 4.6c showing many areas of the Ag surface which aren't covered by Pt.

4.5.1.1 Monitoring the synthesis

In order to understand the final catalyst morphology, various points along the synthesis were inspected. The colloidal reaction mixture has the particles suspended in a solvent and thus cryogenic-TEM was used to ensure that no change in the sample occurred between the reaction and the analysis. All previous analysis samples were prepared by drying prior to measurement, however cryo-TEM utilises the freeze-drying of the solvent and immobilises the particles during the reaction. Four sampling points were selected in order to monitor the reaction, as shown in Figure 4.7. Sampling points A and B show the formation and development of the Ag seed particles, sample point C studies the effect of the H_2 bubbling through the mixture and Sample point D studies the sample after Pt addition, prior to washing away the ethylene glycol.

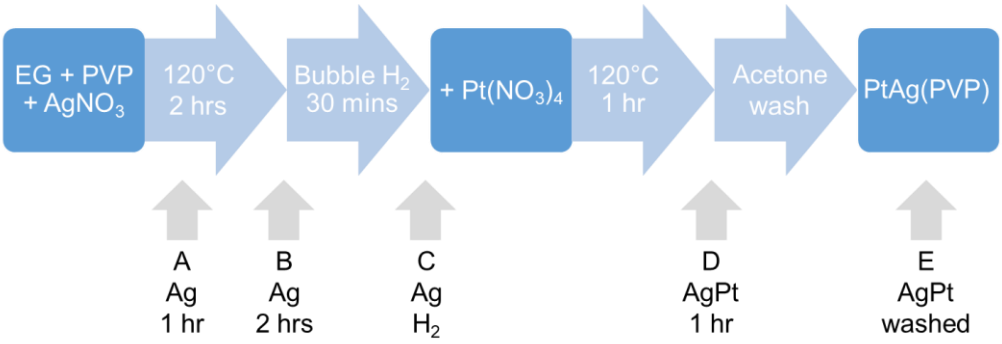


Figure 4.7. Schematic to show stepwise synthesis method and cryo-TEM sampling points.

Figure 4.8 shows dark field STEM images from sampling points A, B and C and a secondary electron image from sample point D. Figure 4.8a shows the Ag seed particles, 1 hour after Ag addition into the hot ethylene glycol and PVP mixture. After just 1 hour of growth, many small seed particles (~ 4 nm diameter) surrounding some large particles (~ 30 nm diameter) were visible. As the electron beam was focussed on the sample and the ethylene glycol began to melt, the movement of the particles could be observed. In just a few seconds, the smaller seed particles were attracted towards the larger particles and began to aggregate further. The smaller particles themselves also underwent aggregation to form larger or more aggregated seed particles. This

aggregation is expected to occur in the liquid state of the reaction, although it is feasibly accelerated by the TEM electron beam in this analysis. Further images of the Ag seed movement and aggregation are shown in Appendix 1. Figure 4.8b shows the Ag seed particles after 2 hours of growth and it can be seen that the smaller seed particles have formed extensive networks in the polymer and are aggregated together. The larger Ag particles can also still be seen, with a typical larger particle size of around 100 nm.

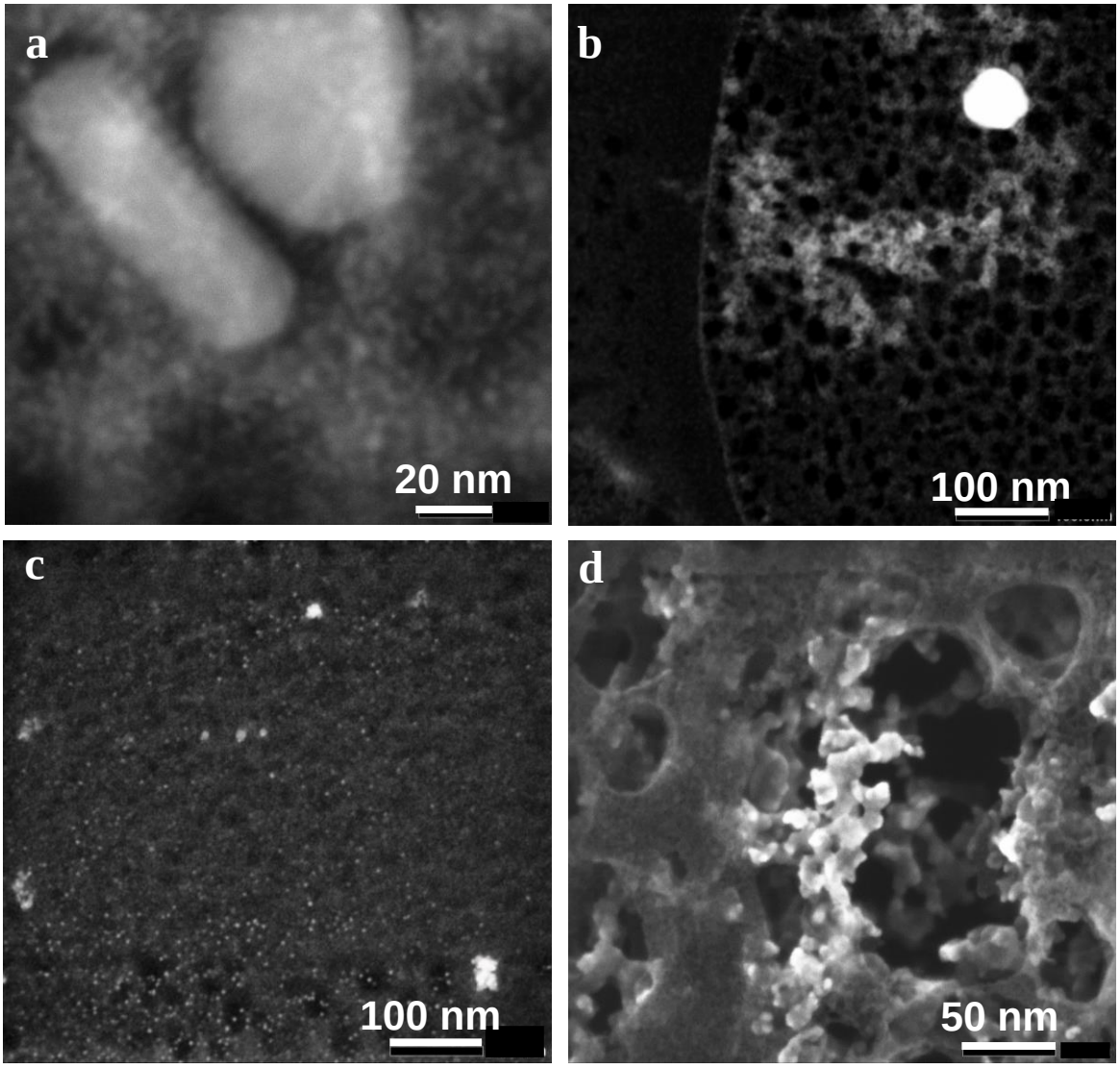


Figure 4.8. Dark field STEM images showing sample at different points in the synthesis. a) Sample point A, Ag 1 hour. b) Sample point B, Ag 2 hours. c) Sample point C, Ag H_2, and d) Secondary electron image showing sample point D, PtAg 1 hour.

Figure 4.8c shows sampling point C, which was taken after bubbling H_2 through the mixture for 30 minutes. It can be seen that the previously formed aggregates have expanded to form more evenly distributed samples. This could be due to the formation of hydride on the metal support enabling the polymer chain to become less tangled, or the bubbling of the H_2 causing more vibrational disturbances in the mixture and shaking the chains open. The larger Ag particles still remain evident in the sample, along with some more irregular aggregates.

Figure 4.8d shows a secondary electron image of the sample after Pt addition and growth for 1 hour. It shows the Ag particles in a chain morphology with Pt deposits on the surface, as observed in the ambient final product TEM images shown in Figure 4.5 & Figure 4.6. Any movement of the particles towards one another or towards the larger Ag particles was quenched after Pt addition, which is attributed to the lower Tamman temperature of Ag (344 °C) than Pt (748 °C)[35]. The Tamman temperature is the temperature at which the atoms have enough energy to allow bulk mobility and sintering and is half the melting point. Thus, for Ag seed particles, sintering can occur at much lower temperatures than the PtAg bimetallic system. The Tamman temperature applies to bulk solids, but the melting temperatures for nanoparticles below 10 nm is lower,[36,37] indicating that temperatures at which Ag can become fluidised would be reached in the microscope.

Not only is the reaction mixture colloidal, but so is the final polymer supported catalyst. The final PtAg(PVP) catalyst, supported in ethanol, was also studied with cryo-TEM to ensure that the sample had not undergone any noticeable changes whilst being dried for ambient condition TEM and for XRD. The cryo-TEM images showed no changes from the ambient condition measurements shown in Figures 4.4 & 4.5. Further cryo-TEM images of the final product are shown in Appendix 1. The similarity of the sample from point D with the ambient TEM of the final product suggests that the material does not change upon washing, suspension in ethanol, or drying. Thus, characterisation of the further bimetallic samples was studied under ambient conditions only.

Further investigation into the larger Ag particles was performed; Figure 4.9 shows a secondary electron image of a large Ag particle from sample point D (~ 300 nm diameter), and the corresponding EDX maps of the particle with Pt shown in red and Ag in blue. It can be seen that no alloying is occurring, with the larger Ag particle containing no Pt, but the deposits seen on the surface in the secondary electron image appear to be Pt. Further out from the large Ag particle, the secondary electron image shows more polymer deposits, which the EDX maps show to contain the PtAg bimetallic chains shown previously.

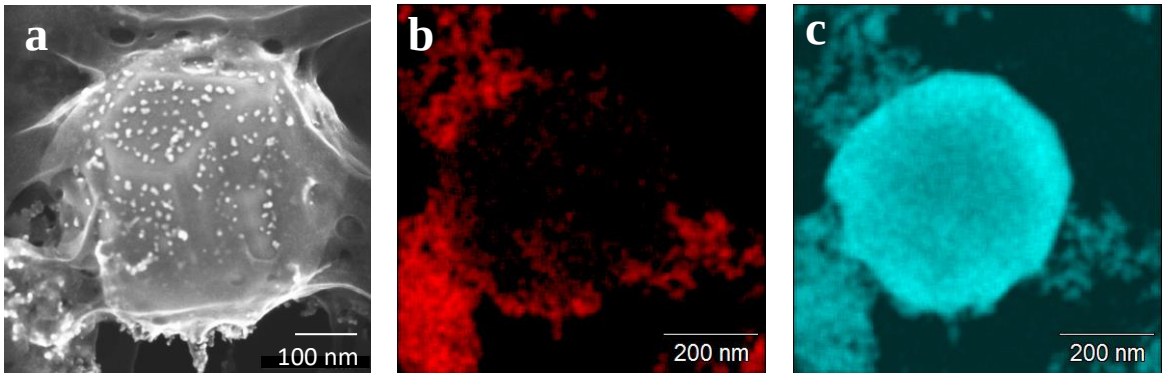


Figure 4.9. STEM EDX images of PtAg(PVP) larger particles. a) Secondary electron image, b) Pt map (red), c) Ag map (blue).

X-ray Absorption Spectroscopy (XAS) was used to further investigate the local structure at the interface and confirmed the presence of Pt deposits on the Ag surface. Data was collected at Diamond Light Source, on beamline B18, and the data was analysed in collaboration with Simson Wu. The EXAFS was fitted and the results shown in Table 4.1 indicate that the Ag forms large core particles, with a Pt decoration at the surface. The high coordination number for the Ag-Ag scattering path indicates the formation of the Ag core, with no visible alternate path from a Ag probed atom. Any surface contributions for core materials are negligible due to the high number of core atoms. The Pt scattering paths show a coordination number of 6.1 for Pt-Pt and 5.6 for Pt-Ag, indicating that the Pt forms some small particles with a high degree of contact to the Ag core. An indication of particle size can also be found from EXAFS fitting, with the coordination number

relating to the particle diameter. The Ag-Ag coordination number of 8 indicates a Ag diameter of 1 nm and the Pt-Pt coordination number of 6 indicates a Pt diameter of 0.5 nm,[38] both of which are considerably lower than the XRD and TEM measurements discussed earlier in this section. This is likely to be due to a combination of the influence of the Pt-Ag interaction and the fact that the particles at the lower end of the size distribution have diameters below the TEM detection limit. This considerably smaller particle size, compared to the value from TEM, may indicate that many particles are agglomerated with small amounts of polymer between them. This would lead to a high TEM size but a lower size from the EXAFS, as this is measured from the 1st coordination shell only.

Table 4.1 EXAFS fitting results for the PtAg(PVP) sample. The Ag-Ag scattering path was fitted from the Ag K-edge data, and the Pt-Pt and Pt-Ag scattering paths were fitted from the Pt L_3-edge data.

Scattering path	Radial distance (Å)	Coordination Number	Debye-Waller Factor
Ag-Ag	2.86 ± 0.01	8.0 ± 0.6	0.011 ± 0.001
Pt-Pt	2.77 ± 0.01	6.1 ± 0.3	0.008 ± 0.001
Pt-Ag	2.82 ± 0.01	5.6 ± 0.2	0.007 ± 0.001

The radial distances between the neighbouring atoms were also fitted, with the calculated Pt-Pt distance (2.77 Å) similar to that of the smallest radial distance of pure Pt (2.78 Å). The lattice parameter of Pt is expected to increase on alloying with Ag, however here no change is observed. This is thought to the offsetting impact of the lattice contraction resulting from the nanoparticulate size effect[39] and the lattice expansion caused by alloying. The measured Ag-Ag radial distance (2.86 Å) is smaller than that of the pure Ag (2.89 Å) due to the combination of alloying and the nanoparticulate size effect.

4.5.2 Platinum nickel colloidal nanoparticles

PtNi(PVP) samples were characterised using XRD, as shown in Figure 4.10. The measured profile is shown in red, the fitted profile in blue and the reference stick patterns at the bottom with Pt in yellow and Ni in green. The profile shows four clear peaks representing the Pt metal in the species. The Ni is not seen in the profile, indicating that the crystallite size of Ni is too small to be measured with XRD. There is also a small reflection at 55 °2θ, which is most closely related to a Pt_3O_4 species (reference 01-074-1870), although the other reflections of this phase are not clearly seen because they mostly occur at similar positions to the Pt reflections.

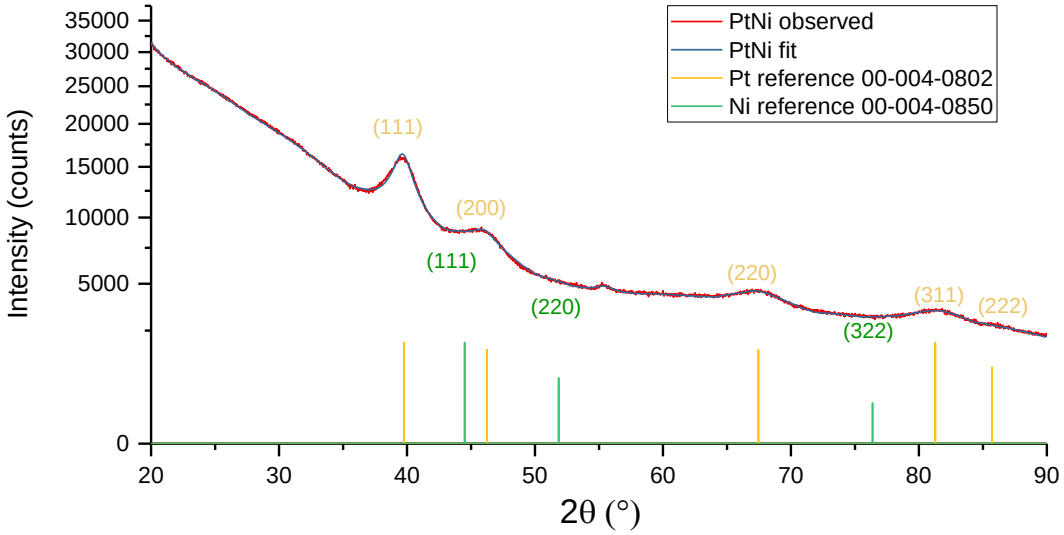


Figure 4.10. XRD profile showing PtNi(PVP) nanoparticles. Observed intensity is shown in red, fitted intensity is shown in blue. Pt reference (00-004-0802) positions are shown in yellow and Ni reference (00-004-0850) positions are shown in green.

The Pt lattice parameter was calculated to be 3.922 Å, which is slightly smaller than the bulk Pt lattice of 3.924 Å and larger than the bulk Ni lattice of 3.524 Å. The Scherrer Equation was used to calculate the crystallite size from the (111), (200), (220) and (311) peaks and resulted in a crystallite size of 3.6 nm. The small Pt_3O_4 reflection at 55 °2θ was calculated to have a crystallite size of 5.7 nm and it is thought that a small proportion of the particles could be oxidised due to interactions of the metal with PVP. TEM shows an excess of PVP in this sample compared with the other metallic systems, as discussed in Figure 4.14 later.

As shown in Figure 4.11, TEM was used to further investigate the size, shape and alloy morphology of the particles. Particle size analysis was performed on a representative area to calculate an average particle size of 3.0 nm (standard deviation of 0.6 nm), similar to the crystallite size obtained through XRD, which indicates there was no particle aggregation.

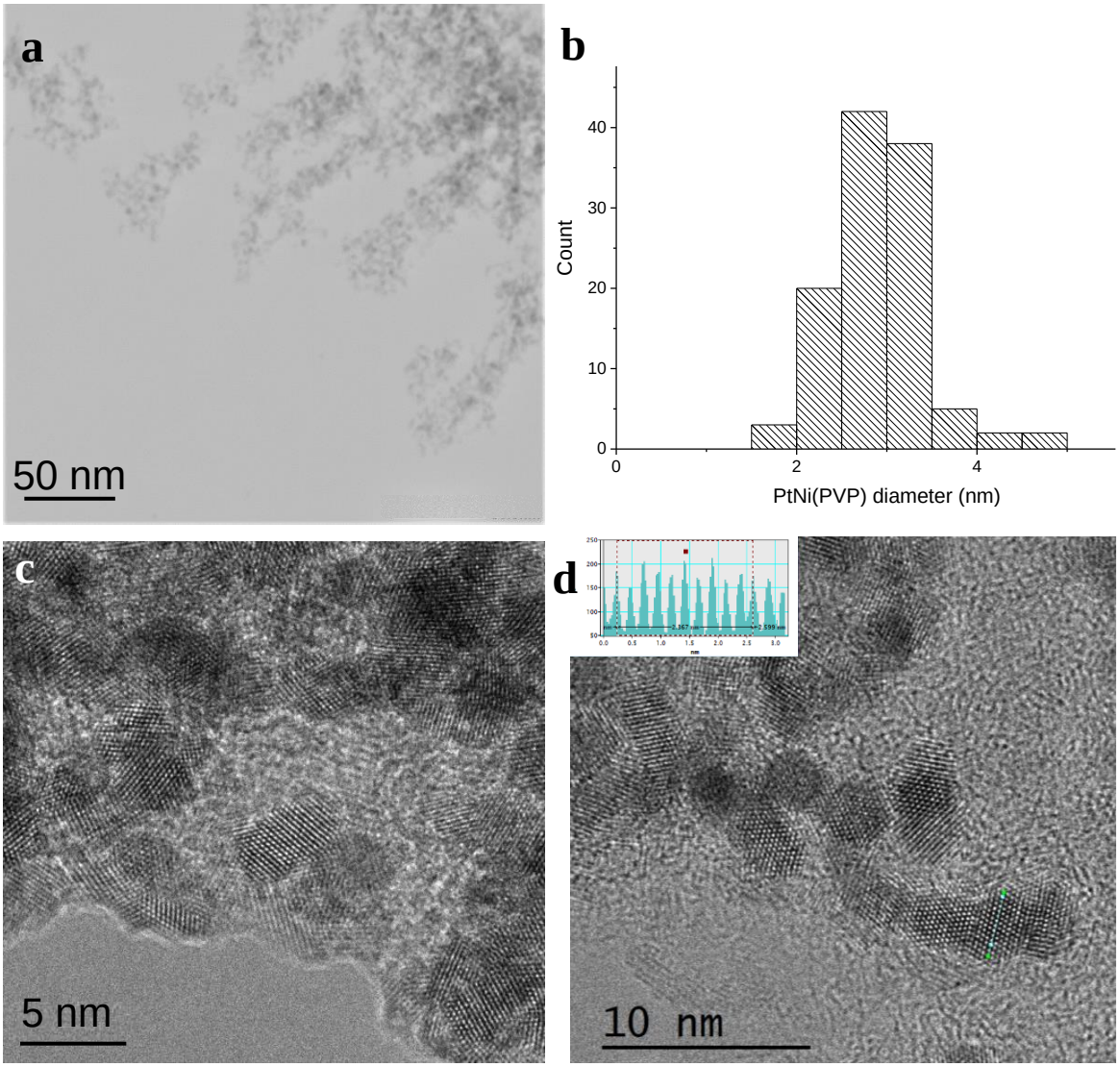


Figure 4.11. STEM and TEM images of PtNi(PVP) particles taken at Johnson Matthey. a) STEM image of many particles showing homogeneity. b) Size distribution graph. c) HR-TEM image showing lattices of various particles. d) HR-TEM image showing intensity profile used to calculate lattice parameter.

Both high resolution TEM and electron diffraction were also used to obtain lattice information. Crystals were imaged along the zone axis plane of view, with the space lattice measured and diffraction pattern obtained in the (111) orientation. The space lattice measurement gave a distance

of 2.367 Å which is similar to the diffraction measurement of 2.361 Å. This was used to calculate the lattice parameter of 3.853 Å. This is lower than the expected measurement from XRD, although TEM gives a less accurate measurement due to the orientation of the particle and the low sampling values.

TEM was also used to understand the sample morphology and it can be seen that the particles cluster together to form the chain-like aggregates, as with the Pt(PVP) and PtAg(PVP). EDX mapping shown in Figure 4.12 with Pt in red and Ni in blue, reveals the Pt is situated in the core of these particles with the Ni decorating the surface. The particles would be expected to form a Ni core - Pt shell type structure as the Ni seed particles have been formed prior to Pt addition and Pt has a lower surface energy so would be thermodynamically more favourable to be the surface component. However, the small Ni seed particles appear to cluster around the slightly larger Pt particles. It is thought that the Ni particles are particularly small and so undergo Ostwald ripening, after the introduction of the Pt nanoparticles. This is where the Ni seeds dissolve and re-deposit on the Pt surface in order to reduce overall excess surface energy.

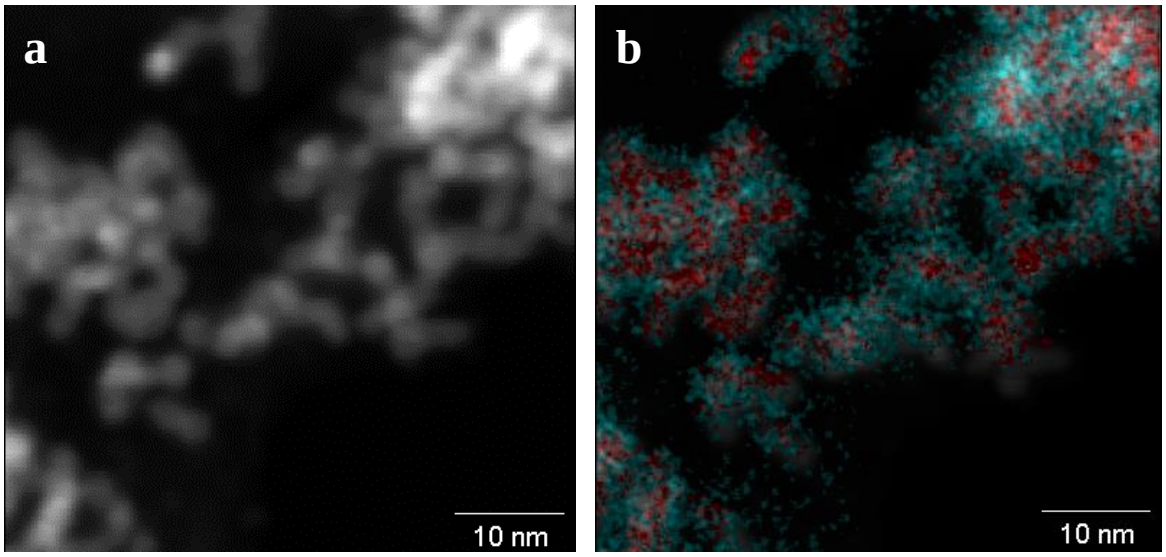


Figure 4.12. STEM and EDX images of PtNi(PVP) particles taken at Johnson Matthey. a) STEM image showing the region mapped. b) EDX map showing Ni in blue and Pt in red.

EDX point analysis was performed to investigate the Ni surface cluster formation and the inversion of the predicted structure. Figure 4.13a shows the STEM image of the areas in which point analysis was performed. Two areas (labelled 1 & 2) of visible particles were selected along with two areas (labelled 3 & 4) which visibly contained no particles. Figure 4.13b shows the EDX profile for the orange area 1, which suggests there are similar quantities of Pt and Ni in this region. The Cu is attributed to the TEM grid and low intensity background peaks of S, Ca and Cr are picked up from the sample holder and instrument. Figure 4.13c shows the EDX profile for area 3, which shows a small quantity of Ni but no Pt. Again, Cu appears from the TEM grid and low intensity Si, Cl, Cr and Fe occur from interactions with the sample holder. This indicates that there are Ni species not only clustered around the Pt but also in the areas with no Pt. Areas 2 & 4 show similar results to areas 1 & 3 respectively.

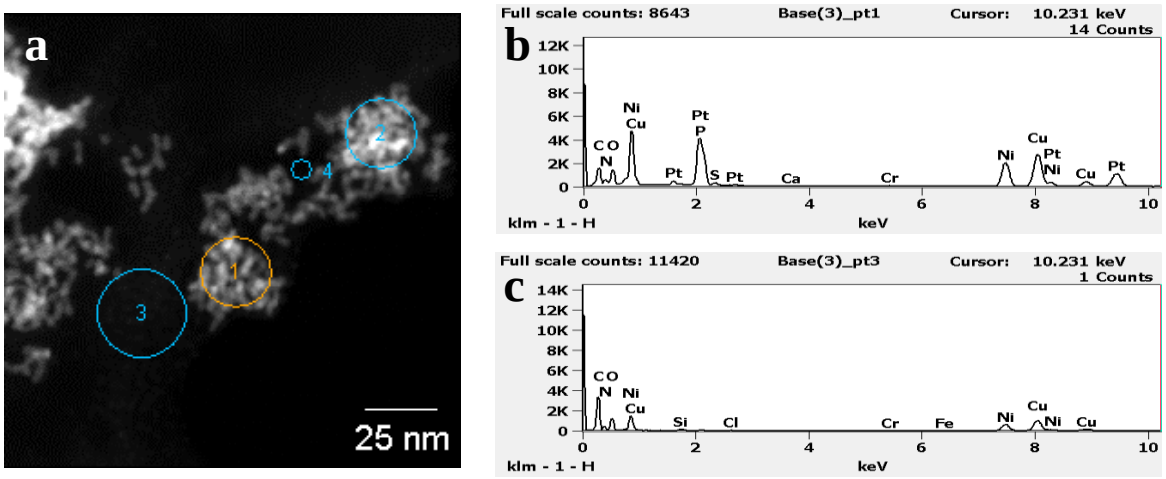


Figure 4.13. EDX point analysis. a) STEM image showing analysis points. b) EDX profile from area 1. c) EDX profile from area 3.

The same area was studied with both STEM and the secondary electron detector, in order to understand the Ni species in the "empty" regions, as shown in Figure 4.14. The secondary electron image showed that the "empty" regions often contained a large quantity of polymer and that there are very small metal clusters stuck to the polymer. This is consistent with both the EDX data, which suggests that there are metal species in the "empty" regions, and the XRD data, which

indicates that there are no large Ni metal species. This indicates that large quantities of PVP are able to stabilise the very small Ni clusters present in these "empty regions".

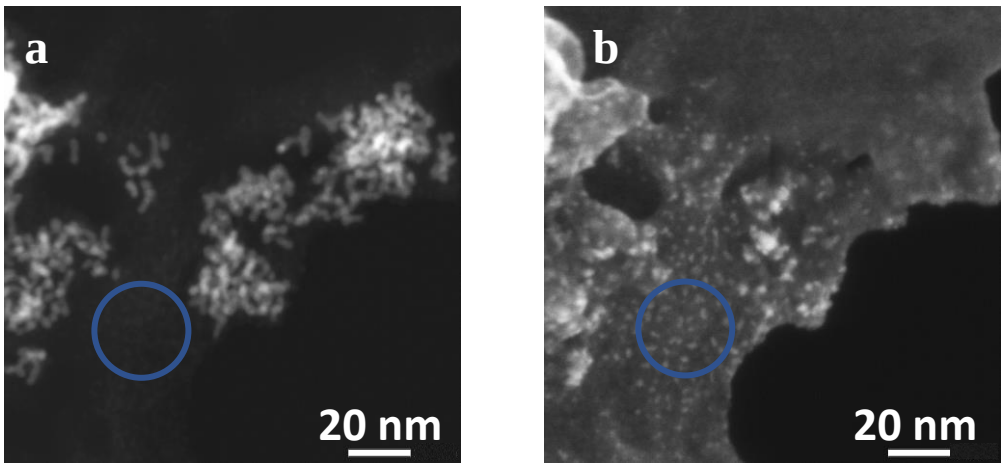


Figure 4.14. a) STEM and b) Secondary electron image showing area of the PtNi(PVP) sample which was analysed with EDX point analysis. The blue circle represents area 3 which contained Ni species.

It is thought that the excess of PVP is greater in this sample than in the PtAg(PVP) or PtZn(PVP) samples. This could be due to the polymer containing higher amounts of seed Ni meaning smaller quantities are washed out. Ni has the highest surface energy of our metals and so would need to be stabilised by the PVP. This can be achieved by covering the small seed clusters in a thick coating of PVP. However this means that they are not accessible when the Pt is added, so Pt forms surrounded by clusters of Ni, rather than on the Ni surface. The slightly larger Ni particles have more facets which are not covered by the PVP and so can cluster on the Pt surfaces.

XAS was again used to further investigate the local structure at the interface and it confirmed the presence of Ni clusters both near the Pt and in the PVP, as shown in Table 4.2. The high coordination number for Pt-Pt bonding (9.5), indicates that there are small Pt nanoparticle core structures. However the Pt-Ni scattering path is also visible, with a coordination number of 1.5, indicating that there is a large proportion of Pt surface atoms interacting with Ni. The absence of the Ni-Pt scattering pathway indicates that there is a large proportion of Ni clusters which are not adjacent to Pt. The Ni-Ni pathway's coordination number of 4.4 suggests the formation of small

Ni clusters, whilst the Ni-O coordination number of 4.5 indicates that these clusters are small and interact with surface O or the PVP. The Ni-Ni coordination number of 4 indicates a mean Ni diameter of less than 0.5 nm and the Pt-Pt coordination number of 9.5 indicates a Pt diameter of 2 nm,[38] both of which are slightly lower than the XRD and TEM measurements previously discussed. This is likely because the particles at the lower end of the size distribution have diameters below the TEM detection limit.

Table 4.2. EXAFS fitting results for the PtNi(PVP) sample. Ni-O and Ni-Ni scattering paths were fitted from the Ni K-edge data and the Pt-Ni and Pt-Pt scattering paths were fitted from the Pt L_3-edge data.

Scattering path	Radial distance (Å)	Coordination Number	Debye-Waller Factor
Ni-O	2.05 ± 0.01	4.5 ± 0.2	0.006 ± 0.001
Ni-Ni	3.01 ± 0.02	4.4 ± 0.4	0.014 ± 0.003
Pt-Ni	2.60 ± 0.01	1.5 ± 0.2	0.012 ± 0.003
Pt-Pt	2.75 ± 0.01	9.5 ± 0.2	0.006 ± 0.001

The radial distances between the neighbouring atoms were also fitted, with the calculated Pt-Pt distance (2.75 Å) smaller than the radial distance of pure Pt (2.78 Å). This slight decrease is due to the combination of the nanoparticulate size effect[39] and the expected contraction due to alloying Pt with Ni. The Ni-Ni radial distribution (3.01 Å) is larger than that of the pure Ni (2.49 Å) which is due to its alloying with Pt, which creates an expansion in the Ni lattice.

4.5.3 Platinum zinc colloidal nanoparticles

The PtZn(PVP) synthesis route was slightly modified in comparison to the PtAg(PVP) and PtNi(PVP) counterparts, as a Zn core was not successfully synthesized. Thus, the PtZn system was

synthesised from initial reduction of a Pt core and then further addition and reduction of Zn with $NaBH_4$. The sample was characterised using XRD and TEM for comparison with the other bimetallic samples.

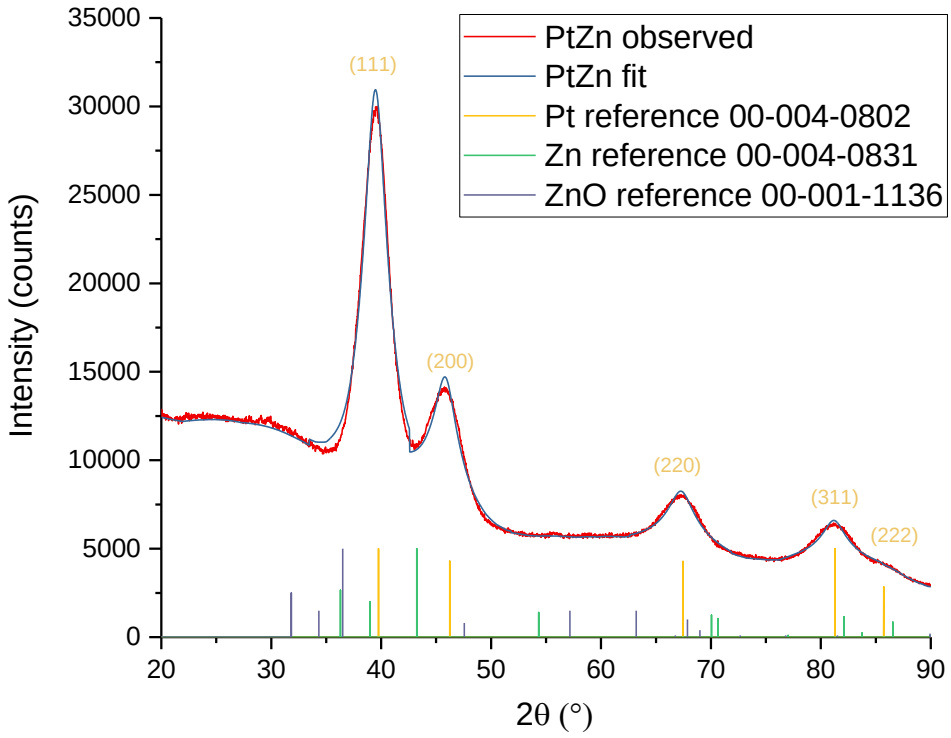


Figure 4.15. XRD profile showing PtZn(PVP) nanoparticles. Observed intensity is shown in red, fitted intensity is shown in blue. Pt reference (00-004-0802) positions are shown in yellow, Zn reference (00-004-0831) positions are shown in green and ZnO reference (00-001-1136) positions are shown in purple.

Figure 4.15 shows a typical XRD profile observed from the PtZn(PVP) sample in red, the fitted profile in blue, and the reference stick patterns at the bottom with Pt in yellow, Zn in green and ZnO in purple. The observed profile shows four clear peaks representing Pt, (111), (200), (220) and (311), with no peaks representing the Zn containing species. This could be due to the uncontrolled or incomplete reduction of the Zn species leading to non-crystalline Zn containing deposits. The Pt lattice parameter was calculated to be 3.934 Å, similar to the bulk Pt lattice of 3.924 Å with any deviance likely to be due to the nanoparticulate size, as with the Pt(PVP) sample discussed in 4.4.1. The peaks were fitted and the Scherrer equation was used to obtain a crystallite size of 3.7 nm.

TEM was used to further investigate the particle size, shape and alloy morphology. Particle size analysis was used on a representative image, as shown in Figure 4.16, to calculate an average particle size of 3.0 nm (standard deviation of 0.6 nm). This is also similar to that calculated from XRD.

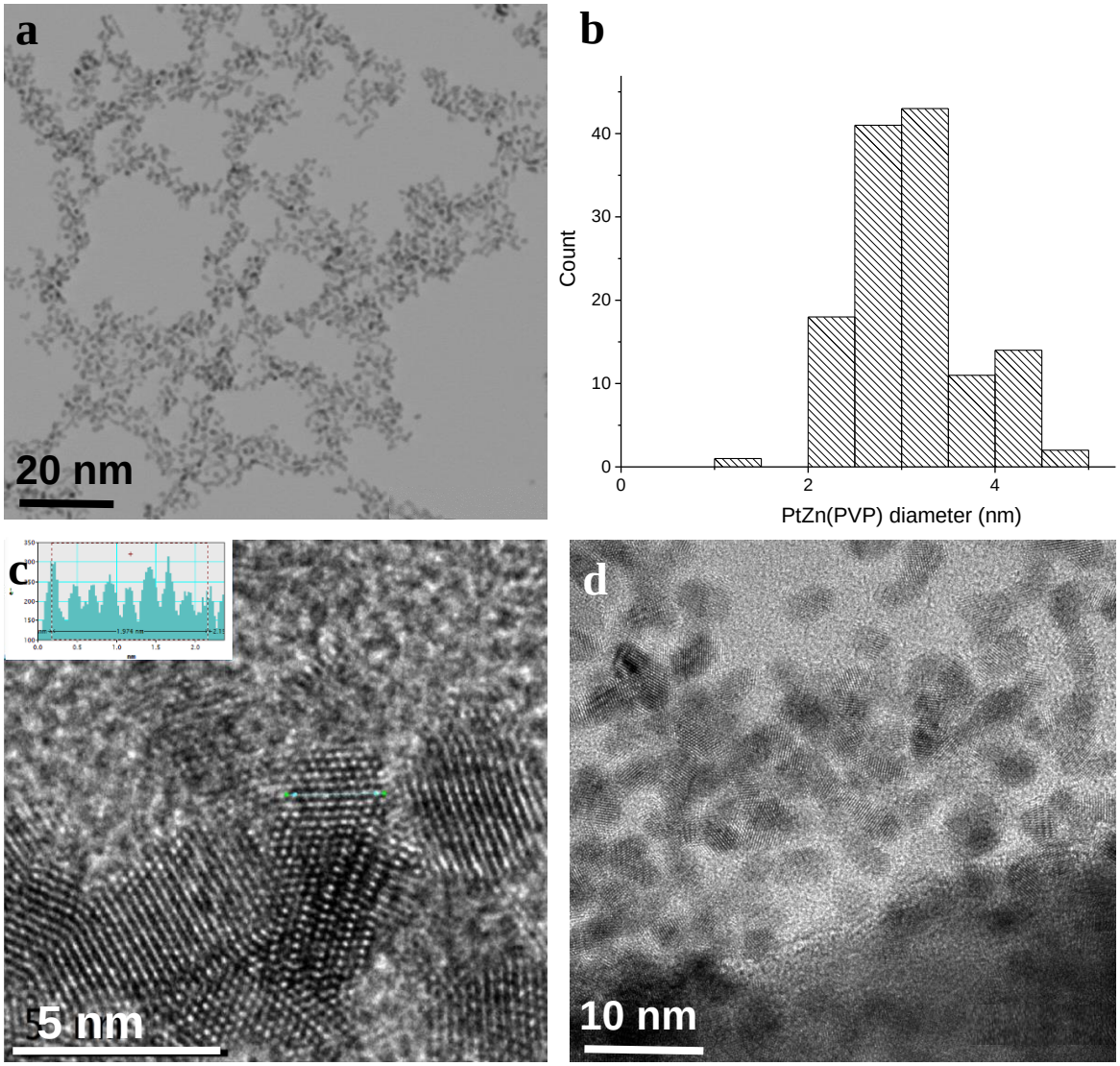


Figure 4.16. STEM and TEM images of PtZn(PVP) particles taken at Johnson Matthey. a) STEM image of many particles showing homogeneity. b) Size distribution graph. c) HR-TEM image showing the intensity profile used to calculate the lattice parameter. d) HR-TEM image showing lattices of various particles on the surface of a larger ZnO particle.

Both high resolution TEM and electron diffraction were also used to obtain lattice information. Crystals were imaged along the zone axis plane of view, with the space lattice measured and diffraction pattern obtained in the (111) orientation. The space lattice measurement gave a distance

of 2.465 Å which is similar to the diffraction measurement of 2.347 Å. This was used to calculate the lattice parameter of 3.929 Å. This is lower than the expected measurement from XRD, although TEM gives a less accurate measurement due to the orientation of the particle and the low sampling values.

Figure 4.17 shows TEM and EDX images of the PtZn(PVP) sample. These show that there are large areas of Zn containing material, likely non-crystalline ZnO, decorated with the small Pt particles. No lattice planes or diffraction rings were seen for the ZnO material, which confirms the poorly crystalline nature of the ZnO support. EDX mapping can show that the larger particles contain both Zn shown in pink and O shown in red and the overlay indicates that the Pt shown in green is decorating the surface of the ZnO in a traditional support-like manner.

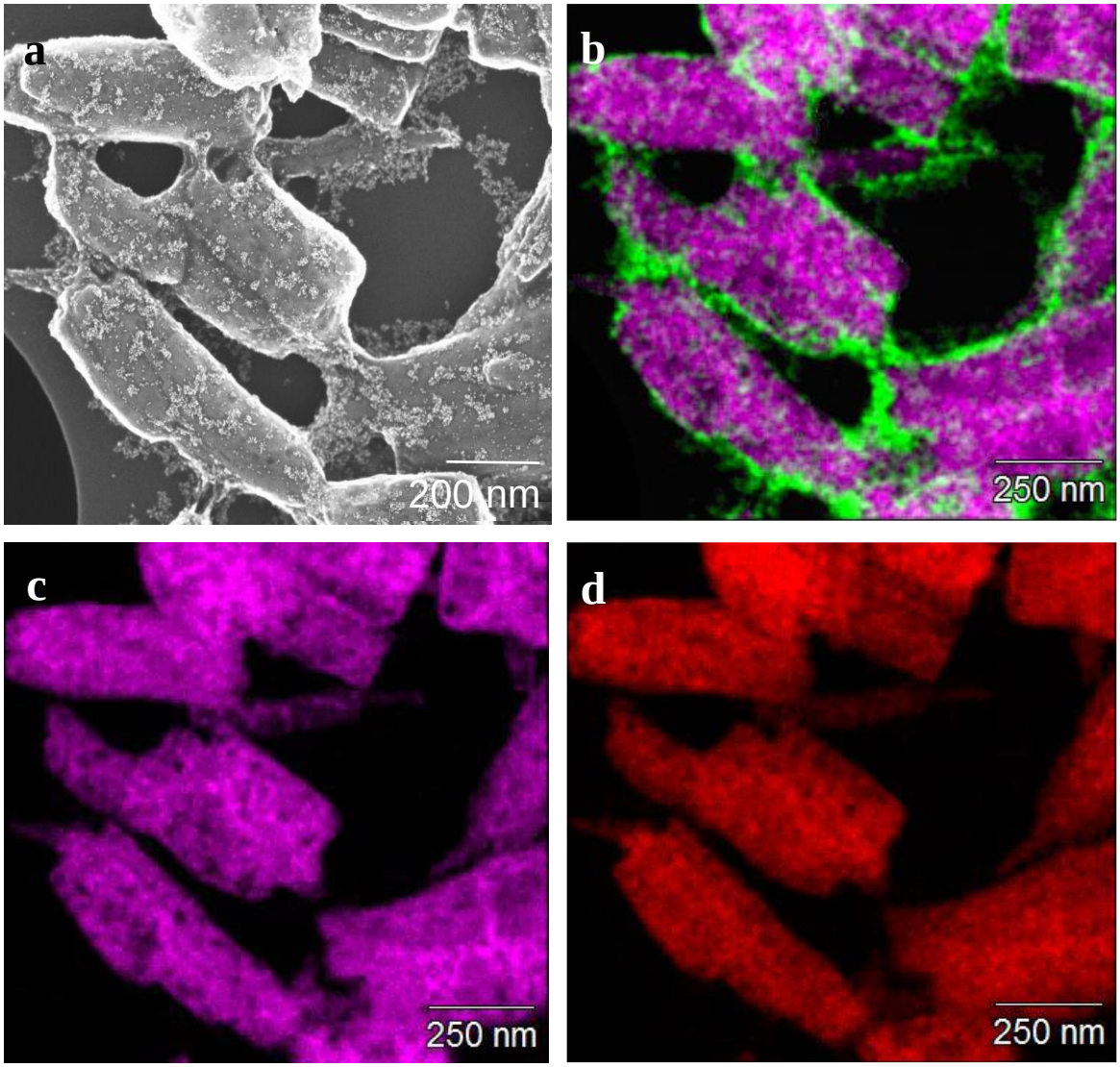


Figure 4.17. SEI and EDX images of PtZn(PVP) particles taken at Johnson Matthey. Images show areas of sample with large ZnO particles. a) SEI showing large particles around 400 nm decorated with nanoparticles. b) EDX overlay of Zn (pink) and Pt (green). c) EDX map of Zn (pink). d) EDX map of O (red).

In addition to the ZnO particles supporting Pt nanoparticles, there are also areas of PVP supported nanoparticles, as shown in Figure 4.18. This sample shows less of a "beads on a string" morphology, with small spherical Pt particles instead distributed across the sample. It is possible that due to the support-like nature of the large ZnO particles, the ratio of nanoparticles to support in these areas is lower and so the smaller Pt particles are less aggregated in the polymer. This leads to fewer occurrences of multiple particles on one chain.

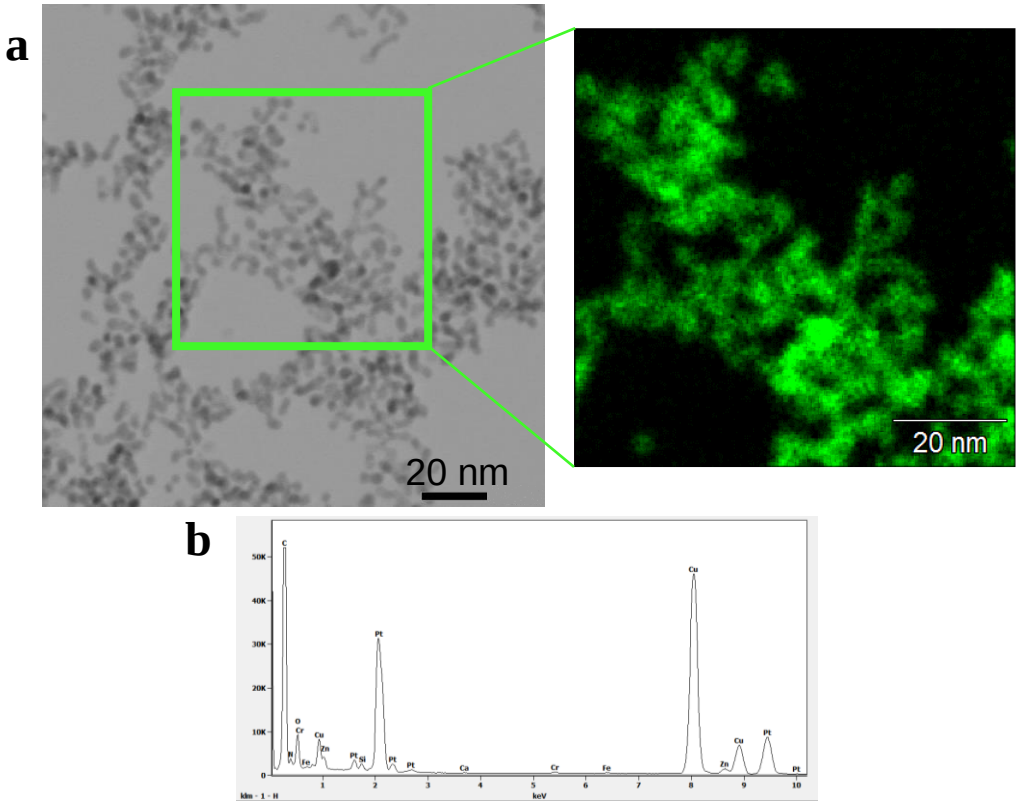


Figure 4.18. Investigation into areas of small PVP supported particles. a) STEM image of an area of smaller particles, and an enlarged section showing the corresponding EDX map, with Pt shown in green. b) EDX profile of the same area, indicating high Pt content and minimal Zn content.

XAS was again used to further investigate the local structure at the interface and it confirmed the presence of large ZnO particles with no visible interaction with the Pt, as shown in Table 4.3. The Zn K-edge data shows the high coordination number of the Zn-O scattering pathway (5.2) indicating a large ZnO component, and the presence of the Zn-Zn pathway (1.3), indicating some small areas of Zn metal. The Pt L_3-edge data shows the Pt-Pt pathway only, which indicates there is no Pt-Zn interaction. The high coordination number of Pt-Pt (10.7) indicates Pt particles, which have a size of around 3 nm,[38] and therefore supports the measurements from TEM and XRD.

Table 4.3. EXAFS fitting results for the PtZn(PVP) sample. Zn-O and Zn-Zn scattering paths were fitted from the Zn K-edge data and the Pt-Pt scattering path was fitted from the Pt L_3-edge data.

Scattering path	Radial distance (Å)	Coordination Number	Debye-Waller Factor
Zn-O	2.08 ± 0.01	5.2 ± 0.1	0.008 ± 0.001
Zn-Zn	2.89 ± 0.02	1.3 ± 0.2	0.011 ± 0.003
Pt-Pt	2.76 ± 0.01	10.7 ± 0.5	0.006 ± 0.001

The radial distances between the neighbouring atoms were also fitted, with the calculated Pt-Pt distance (2.76 Å) similar to the radial distance of pure Pt (2.775 Å). There is no significant variation in the measured value beyond the fitting error (0.01 Å), however any decrease in lattice could also be attributed to the nanoparticulate size effect.[39]

The partial reduction of the surface ZnO to metallic Zn is anticipated to occur under highly reducing conditions in this material. These catalysts were all tested with the liquid phase formic acid decomposition reaction and so, as formic acid is very reducing, the large ZnO particles are expected to undergo some surface reduction to form Pt-Zn interactions.

4.6 Formic acid decomposition

The liquid phase formic acid decomposition reaction was selected as a probe reaction for the investigation into the effect of introducing the secondary metal on the surface active site and the catalytic activity. The liquid phase formic acid decomposition is known to be particularly susceptible to electronic and geometric changes in the Pt surface and activity can be quickly measured through assessment of residual acid strength using acid-base titrations. Reaction conditions were modified from those reported in literature[40] in order to ascertain formic acid conversion at atmospheric pressure.

In order to ensure each sample catalyst measured contained the same quantity of metal, the samples were subject to thermogravimetric analysis (TGA) in order to monitor mass change before and after the polymer was burnt away at high temperatures. The remaining mass is due only to the metals and not the polymer. A typical TGA profile is shown in Figure 4.19, where the PVP is burnt off by 400 °C leaving 43% of the initial mass. The catalyst solution (approximately 0.1 mL, dependent on the polymer content) was injected into the 0.1 M formic acid and the mixture was stirred at 25 °C for 20 minutes.

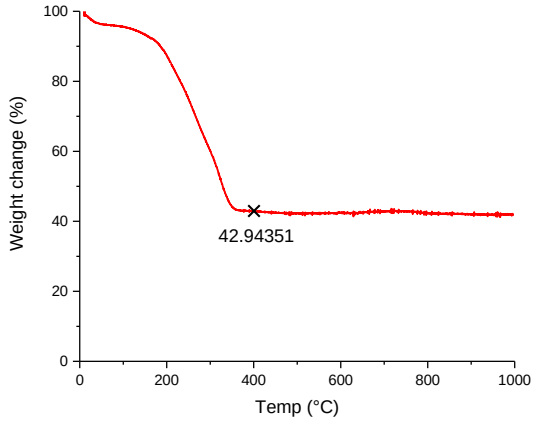


Figure 4.19. A TGA profile for Pt(PVP) on heating from room temperature to 1000 °C while monitoring weight change.

Figure 4.20 shows the conversion rates of the liquid phase formic acid decomposition reaction for each catalyst in the first 20 minutes. The monometallic Pt shows the lowest conversion, with the three bimetallic systems showing higher reactivity. This can be attributed to the electronic promotion effect that the secondary metal has on the Pt. The work functions for each of Ag (4.26 eV), Zn (4.33 eV) and Ni (5.01 eV) all have lower work functions than Pt (6.35 eV), which means that the secondary metals all donate electron density towards the Pt. This leads to a down-shift in the d-band and therefore a weaker binding of adsorbates to the metal surface, as discussed in Section 1.3.1. All three samples with a secondary metal show this ligand effect, causing weakening of the reactant-surface bond and increased reactivity. Pt has a close to optimal binding strength

and so the rate limiting step can depend on the reaction conditions. These tests were performed under conditions with a very high concentration of formic acid, which means adsorption is facile. In this case desorption is likely to be the rate limiting step and so, when adding a secondary metal, weakening of the product binding increases the overall reactivity.

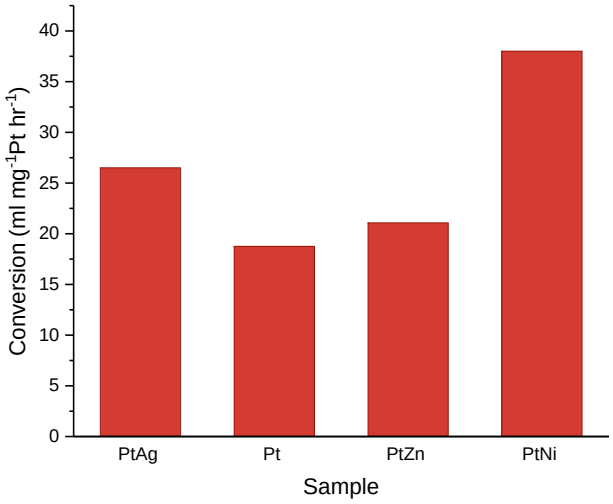


Figure 4.20. Conversion rates of the polymer supported catalysts for the liquid phase formic acid decomposition reaction in the first 20 minutes.

Ag has a lower work function than Zn and so the PtAg is more active than the PtZn. Ni has the highest work function of the three secondary metals and so electronically it would be expected that PtNi would show the smallest increase in conversion. However, Ni (3.524 Å) has a smaller lattice parameter than Pt (3.924 Å), whereas Ag (4.085) Å has a larger lattice parameter. Where there is a close interface between the Pt and the secondary metal, such as in the PtAg(PVP) and the PtNi(PVP), the two lattices can become under strain at the interface. This means that the Ni causes a contraction in the Pt lattice, whereas the Ag causes an expansion. Where the lattice is contracted, the d-orbitals overlap more and there is a broadening of the d-band. This leads to a down-shift in d-band centre and thus weaker adsorbate-surface binding and so enhanced catalytic activity when introducing Ni into the system. In contrast, when the lattice is expanded, the d-orbitals will have a decreased overlap and so the d-band will become narrower. This leads to an up-shift in the d-band

centre and stronger adsorbate-surface binding. This results in an inhibited catalytic activity when introducing Ag into the system.

Thus, the contraction in the PtNi(PVP) system is an additional factor for the enhanced conversion. The PtAg(PVP) would be expected to undergo a slight negative structural influence from the secondary metal. However this is not greatly presented in the reactivity change indicating that the lattice strain is minimal, which is likely to be due to the small lattice mismatch between Pt and Ag. Like Ni, Zn (2.664 Å) also has a lower lattice parameter than Pt (3.924 Å), however the poor crystallinity of the Zn means the structural enhancement is not manifested.

It is expected that all bimetallic species show the ligand effect, leading to a lower d-band centre, weaker binding and enhanced reactivity from an increase in electron density on the Pt. In addition to this ligand effect, a structural effect on the d-band centre is also seen with the PtNi and slightly with the PtAg systems. The PtAg is under a small amount of tensile strain, leading to a higher d-band centre and worse reactivity than the electron donation ligand effect would suggest. Whereas the PtNi is under compressive strain, with a higher d-band centre and higher reactivity.

The unexpectedly large conversion for PtAg(PVP) is thought to be attributed to the large positive electronic effect and the weaker negative structural effect. It is expected that the large Ag particles have sufficient contact for electronic promotion, but do not have a well-defined Pt-Ag interface and so do not exhibit the structural influence on the Pt. It is thought that the PtAg(PVP) would have a lower conversion, expected from the structural effect of tensile strain, had the sample been purely the small chain-like bimetallic species.

The PtZn(PVP) sample conversion was also lower than expected. It had been predicted that a structural and electronic influence would enhance the activity of this sample. The TEM and EDX mapping showed large ZnO species supporting the Pt particles, which suggests that the structural enhancement was not well implemented. In addition to the poor contact between the metals, the

XRD suggested that the ZnO material was non-crystalline, which further means the structural compressive strain effect did not materialise. The TEM also shows large areas of Pt particles supported entirely by PVP, with no interaction with Zn. The large areas of monometallic nanoparticles indicate that no electronic effect would be seen in a large proportion of the sample.

4.7 Conclusions

This chapter focused on the synthesis and characterisation of polymer supported bimetallic nanoparticles. The emphasis was to synthesise Pt bimetallic nanoparticles with a large metal-metal interface, in order to utilise the structural and electronic effects which the secondary metal can exhibit on the Pt. The liquid phase formic acid decomposition reaction was used as a probe reaction to investigate the changes at the catalytically active surfaces, due to the high susceptibility of this reaction to structural and electronic changes.

A Pt(PVP) and three bimetallic supported samples were synthesised and thoroughly characterised with XRD, TEM and XAS. A summary of the particle sizes and lattice parameters can be seen in Table 4.4.

Table 4.4. Summary table of sample particle sizes and lattice parameters.

Sample	**Particle size (nm)**		**Lattice parameter (Å)**	
	XRD	TEM	XRD	TEM
Pt(PVP)	4.4	3.0	3.916	3.887
PtAg(PVP)	6.5	47.0	4.032	3.999
PtNi(PVP)	3.6	3.0	3.922	3.853
PtZn(PVP)	3.7	3.0	3.934	3.929

It was found that, as mentioned in literature,[31] nanoparticles stabilised by a polymer often form a “beads on a string” chain aggregate. This was prominent in the seed metal particle formation for

both Pt and Ag particles. It was found that, on addition of a secondary metal to this chain-like aggregate, the secondary metal is deposited on the surface of the chain of particles. For example, in the PtAg(PVP) sample the Pt was found to be deposited as small nanoparticles on the surface of the Ag chain. The effect of the polymer on the particle size was shown to be varied, with large particles forming in the Ag seed synthesis, and very small seed clusters of Ni forming in the polymer. The smaller seed clusters of Ni did not appear as chain-like aggregates, although the thick polymer coating did inhibit further deposition of the Pt.

Through the use of cryo-TEM, it was confirmed that the Ag seed particles were very susceptible to aggregation in the reaction mixture at low temperatures. It was also shown that bubbling H_2 through the reaction mixture led to increased dispersion of the bulky areas of the polymer supported seed particles, although the mechanism of this was not further explored. Finally, the cryo-TEM showed that these polymer stabilised particles were stable when dried and characterised under ambient conditions.

The PtAg(PVP) sample mainly showed chains of Ag particles with Pt decoration on the surface, although some very large Ag particles with partial Pt surface decoration were also present. The PtNi(PVP) sample showed Ni particles aggregating around the Pt, with many small Ni clusters held in the surrounding polymer. The PtZn(PVP) sample was prepared slightly differently and was not shown to form a good Pt-Zn contact. Small Pt particles, similar in nature to the monometallic system, were stabilised by the PVP. These Pt particles are often positioned near the edges of the large non-crystalline ZnO particles.

All samples showed increased activity for the formic acid decomposition reaction in comparison with Pt, which confirmed that all three secondary metals cause an electronic donation to the Pt. This effect was particularly large in the PtAg(PVP) sample, which is attributed to the high level of Pt-Ag contact. The PtNi species were highly active and this is attributed to the structural effect

which the Ni introduces to the Pt. Ni causes a contraction in the Pt lattice leading to a broadening of the d-band, a down-shift in the d-band centre and weaker metal-adsorbate binding. It is thought that through an increased Pt-Ni and Pt-Zn interface, a further enhancement of activity could be seen. For the PtAg sample, through enhanced control of the particle size, there will be fewer contributions from large anomalous particles which could further deconvolute activity changes.

4.8 References

1 C. A. Busacca, D. R. Fandrick, J. J. Song and C. H. Senanayake, *Adv. Synth. Catal.*, 2011, **353**, 1825–1864.

2 G. Ertl and G. Ertl, Eds., *Handbook of Heterogeneous Catalysis*, Weinheim : Wiley-VCH, Weinheim, 2nd, compl edn., 2008.

3 J. Cooper and J. Beecham, *Platin. Met. Rev.*, 2013, **57**, 281–288.

4 K. Jiang, H.-X. Zhang, S. Zou and W.-B. Cai, *Phys. Chem. Chem. Phys.*, 2014, **16**, 20360–20376.

5 H. Liu, F. Nosheen and X. Wang, *Chem. Soc. Rev.*, 2015, **44**, 3056–3078.

6 H. Zhang, M. Jin and Y. Xia, *Chem. Soc. Rev.*, 2012, **41**, 8035.

7 S. P. Lin, K. W. Wang, C. W. Liu, H. S. Chen and J. H. Wang, *J. Phys. Chem. C*, 2015, **119**, 15224–15231.

8 F. R. Lucci, J. Liu, M. D. Marcinkowski, M. Yang, L. F. Allard, M. Flytzani-Stephanopoulos and E. C. H. Sykes, *Nat. Commun.*, 2015, **6**, 8550.

9 JM Bullion Platinum Price, https://www.jmbullion.com/charts/platinum-price/.

10 R. Van Hardeveld and F. Hartog, *Surf. Sci.*, 1969, **15**, 189–230.

11 K. Kolasinski, *Surface Science: Foundations of Catalysis and Nanoscience*, John Wiley and Sons, 2012.

12 G. Cao, *Nanostructures & Nanomaterials: Synthesis, Properties & Applications*, Imperial College Press, 2004.

13 Y. Borodko, S. E. Habas, M. Koebel, P. D. Yang, H. Frei and G. a Somorjai, *J. Phys. Chem. B*, 2006, **110**, 23052–23059.

14 R. Si, Y. W. Zhang, L. P. You and C. H. Yan, *J. Phys. Chem. B*, 2006, **110**, 5994–6000.

15 Y. Borodko, S. M. Humphrey, T. D. Tilley, H. Frei and G. A. Somorjai, *J. Phys. Chem. C*, 2007, **111**, 6288–6295.

16 K. M. Koczkur, S. Mourdikoudis, L. Polavarapu and S. E. Skrabalak, *Dalt. Trans.*, 2015, **44**, 17883–17905.

17 T. A. R., H. Susan and Y. Peidong, *Small*, 2008, **4**, 310–325.

18 X. Xia, J. Zeng, L. K. Oetjen, Q. Li and Y. Xia, *J. Am. Chem. Soc.*, 2012, **134**, 1793–1801.

19 Y. Sun and Y. Xia, *Science*, 2002, **298**, 2176–2179.

20 M. Crespo-Quesada, A. Yarulin, M. Jin, Y. Xia and L. Kiwi-Minsker, *J. Am. Chem. Soc.*, 2011, **133**, 12787–12794.

21 R. M. Rioux, H. Song, M. Grass, S. Habas, K. Niesz, J. D. Hoefelmeyer, P. Yang and G. A. Somorjai, *Top. Catal.*, 2006, **39**, 167–174.

22 H. S. Shin, H. J. Yang, S. Bin Kim and M. S. Lee, *J. Colloid Interface Sci.*, 2004, **274**, 89–94.

23 A. Kyrychenko, O. M. Korsun, I. I. Gubin, S. M. Kovalenko and O. N. Kalugin, *J. Phys. Chem. C*, 2015, **119**, 7888–7899.

24 W. Hou, N. A. Dehm and R. W. J. Scott, *J. Catal.*, 2008, **253**, 22–27.

25 H. U. I. Zhang, M. Jin, Y. Xiong, B. Lim and Y. Xia, 2013, **46**, 1783–1794.

26 S. Alayoglu, A. U. Nilekar, M. Mavrikakis and B. Eichhorn, *Nat. Mater.*, 2008, **7**, 333–338.

27 F. Bonet, V. Delmas, S. Grugeon, R. H. Urbina and P. Silvert, *NanoStructured Mater.*, 1999, **11**, 1277–1284.

28 F. Gauthard, F. Epron and J. Barbier, *J. Catal.*, 2003, **220**, 182–191.

29 E. Pippel, S. A. Nepijko and J. Woltersdorf, *Phys. Status Solidi*, 1980, **61**, 469.

30 W. H. Qi and M. P. Wang, *J. Nanoparticle Res.*, 2005, **7**, 51–57.

31 E. P. Boonekamp, J. J. Kelly and L. G. J. Fokkink, *Langmuir*, 1994, **10**, 4089–4094.

32 J. Yang, W. Hu, Y. Wu and X. Dai, *Surf. Sci.*, 2012, **606**, 971–980.

33 R. Ferrando, J. Jellinek and R. L. Johnston, *Chem. Rev.*, 2008, **108**, 845–910.

34 D. V. Goia and E. Matijević, *New J. Chem.*, 1998, **22**, 1203–1215.

35 Weast, *CRC handbook of chemistry and physics*, Cleveland, Ohio : CRC Press, Cleveland, Ohio, 52nd edn., 1972.

36 H. Li, P. D. Han, X. B. Zhang and M. Li, *Mater. Chem. Phys.*, 2013, **137**, 1007–1011.

37 M. Attarian Shandiz, A. Safaei, S. Sanjabi and Z. H. Barber, *J. Phys. Chem. Solids*, 2007, **68**, 1396–1399.

38 A. M. Beale and B. M. Weckhuysen, *Phys. Chem. Chem. Phys.*, 2010, **12**, 5562–74.

39 W. Qi and M. P. Wang, *Size and shape dependent lattice parameters of metallic nanoparticles*, 2005, vol. 7.

40 S. Jones, S. Fairclough, M. Gordon-Brown, W. Zheng, A. Kolpin, B. Pang, W. Kuo, J. h and E. Tsang, *Chem. Commun.*, 2015, **51**, 46–49.

Chapter 5

Silica supported nanoparticle synthesis

5.1 Background 102
5.2 Objectives 104
5.3 Experimental details 104
5.4 Characterisation of supported platinum nanoparticles 105
5.4.1 Platinum(SBA-15) nanoparticles 105
5.5 Characterisation of supported bimetallic nanoparticles 107
5.5.1 Platinum silver supported nanoparticles 108
5.5.2 Platinum nickel supported nanoparticles 110
5.5.3 Platinum zinc supported nanoparticles 113
5.6 Formic acid decomposition 125
5.6.1 Liquid phase formic acid decomposition 125
5.6.2 *In-situ* XAS with gas phase formic acid decomposition 131
5.7 Conclusion 135
5.8 References 138

5.1 Background

As discussed in the introduction to Chapter 4, the use of nanoparticles as catalysts is important for cost efficient industrial processes. As many catalysts are composed of expensive platinum group metals (PGMs), maximising the metal surface area and therefore reducing the amount of metal required is vital. It was also discussed previously that the use of bimetallic materials is another important way to maximise catalytic activity whilst decreasing the PGM composition. However, the controlled synthesis of well-defined bimetallic nanoparticles with specific metal interfaces is not facile and this chapter continues to investigate alternative methods to achieve this.

Polyvinylpyrrolidone (PVP) stabilised bimetallic nanoparticles were investigated in Chapter 4, however large particle size distributions and agglomeration led to poorly defined Pt coatings on the secondary metal cores. Additionally, manipulating the colloidal catalyst product to form an industrial catalyst is challenging. In order to combat these problems, an alternative method to stabilise nanoparticles from agglomeration is through the tethering to a solid support. A great deal of research has been performed into solid supported nanoparticles and the metal-support interaction which can have a significant effect on the reactivity. Common solid supports include silica, alumina, metal organic frameworks, zeolites and metal oxides.[1]

One method to control particle growth while using a solid support is to use a mesoporous material and impregnate the metal precursor into the channels. This ensures that, as the metal particles grow, they cannot exceed the channel width in diameter. Various porous materials are currently utilised, ranging from microporous zeolites with pores of < 2 nm to macroporous materials such as titania, with pores larger than 50 nm.[2] One interesting material in the middle of this range is SBA-15 (Santa Barbara Amorphous-15), a well ordered hexagonal mesoporous silica structure with tuneable pore sizes from 46 to 300 Å. This material, initially synthesised by Zhao *et al*.[3,4] in 1998, has since been extensively studied and modified with functional groups,[5,6] as well as being

used as a support for various metal nanoparticle catalysts.[7–10] The most common method of nanoparticle deposition inside the channels of SBA-15 is through an impregnation/reduction method shown in the schematic in Figure 5.1. The internal walls of the SBA-15 have hydroxyl surface units available to tether the formed nanoparticles, creating resistance to nanoparticle agglomeration.

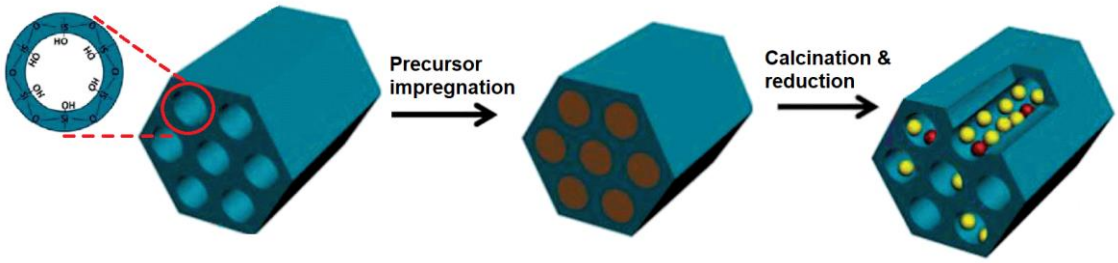


Figure 5.1. Schematic showing the SBA-15 structure and the impregnation and reduction method of nanoparticle depositions. Image modified from reference[11].

Bimetallic nanoparticles supported on SBA-15 often yield a greater catalytic activity than counterparts, although this phenomena is not well explained.[7,10,12,13] Recently, work into the NiAg bimetallic SBA-15 system has shown that a co-impregnation reduction method leads to synthesis of a Ni core - Ag shell structure.[14] This catalyst has shown an enhanced selectivity for the hydrogenation of dimethyl oxalate, which is thought to be due to the strong AgNi interaction creating geometric and electronic changes to improve the catalytic performance. The synthesis of the core-shell structure is thought to be due to the high dispersion of the Ni species and their strong interaction with Ag.[14,15]

The metal support interaction is highly studied for metal oxide supports, however there is no clear research as to how the interaction manifests in SBA-15. There is also limited research into the metal dispersion on the silica channels and how this affects the bimetallic structural growth or the catalytic activity. High resolution characterisation of bimetallic particles inside the channels is not facile, which is perhaps the reason why this synthesis method has not been further researched. The current literature would benefit from additional research into PGM bimetallic nanoparticle

synthesis and characterisation, in order to further understand the effect of the SBA-15 walls on the metal particles.

5.2 Objectives

The research in this chapter aims to investigate the use of the mesoporous silica, SBA-15, as a support for bimetallic nanoparticles with a defined metal interface. Pt is chosen as the catalytically active surface metal and Zn, Ag and Ni are the secondary metals. SBA-15 is chosen as a silica variant in order to restrict particle size to the pore diameter and also as it has been shown to have a templating effect, allowing the production of core-shell materials. Numerous characterisation techniques are employed to determine the bimetallic structure, along with the structural and electronic influence of the secondary metal on the Pt. The liquid phase formic acid decomposition reaction is again used as a probe to identify these surface binding site changes. The results are expected to complement those of the polymer stabilised nanoparticle synthesis of Chapter 4, as well as inspire the work of Chapter 6 in which this method is used for the commercial oxygen reduction reaction.

5.3 Experimental details

A detailed discussion of both the synthesis and details of the formic acid decomposition reaction is provided in Chapter 3. In summary, the nanoparticles were formed through the incipient wetness co-impregnation of both metal nitrate precursors, which were then ground and dried at room temperature. The powders were then transferred to a tube furnace and heated to 400 °C under N_2, followed by a 4 hour reduction under 5% H_2/Ar at this elevated temperature. The samples were cooled to room temperature under this H_2 atmosphere then stored in air at room temperature. One sample was synthesized in a two-step reduction with Ni impregnation and reduction, followed by Pt impregnation and further reduction in order to compare the two synthesis techniques. All

samples for PtAg and PtNi have a Pt to secondary metal atomic ratio of 20:80. PtZn was synthesised in ratios of 20:80, 50:50 and 80:20. All samples discussed in this chapter are in the 20:80 ratio unless otherwise mentioned.

The catalytic activity of the samples was tested using the liquid phase decomposition reaction as a probe reaction to investigate the structural and electronic changes at the active surfaces. In brief, 10 mg sample was dispersed in 25 mL 0.1M formic acid and stirred at room temperature for 20 or 60 minutes. The resulting solution was filtered to remove the catalyst and then titrated against 0.1M NaOH to ascertain the amount of formic acid reacted and, hence, the activity of the catalyst.

5.4 Characterisation of supported platinum nanoparticles

Monometallic nanoparticles supported in the channels of the SBA-15 silica were prepared in order to compare the bimetallic structural parameters to a reference Pt particle of a similar size and under similar environmental conditions. The very small nature of nanoparticles and their interaction with the support can affect both the lattice parameter and the electronic environment of a nanoparticle surface.

5.4.1 Platinum(SBA-15) nanoparticles

The nanoparticles were characterised using XRD and TEM to understand sample composition, crystallinity, changes in lattice parameter and crystallite size and shape. The XRD profile, Figure 5.2, shows the measured profile in red, the fitted profile in blue and the Pt reference stick pattern at the bottom in yellow. The first four reflections, (111), (200), (220) and (311), can be seen clearly along with the (222) peak which has a lower intensity. The high background at lower angles is due to the silica support, which has a broad reflection around 22 °2θ. A pure SBA-15 sample profile was acquired as a reference and is shown in Appendix 2. The first four Pt reflections were used to calculate the lattice parameter of 3.919 Å, which is similar to the bulk Pt lattice of 3.924 Å. Compared to the bulk reference material, the small contraction in lattice parameter may be due to

the nanoparticulate size, which has previously been seen and modelled in literature.[16,17] An average crystallite size of 4.9 nm was calculated from the "full peak width at half the maximum height" (FWHM) of the first four peaks, using the Scherrer Equation as described in Chapter 3.

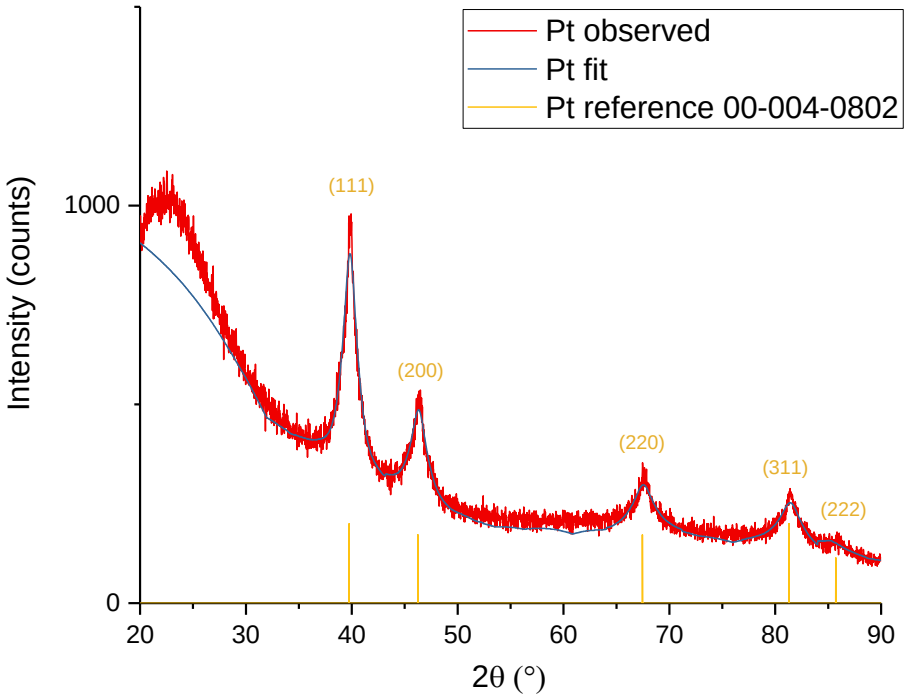


Figure 5.2. XRD profile showing Pt(SBA-15) nanoparticles. Observed intensity is shown in red, fitted intensity is shown in blue. Pt reference (00-004-0802) positions are shown in yellow.

TEM was used to further probe the particle size, shape and distribution across the support. Figure 5.3a shows a STEM image of a representative area of the sample, indicating that the particles appear to be within the SBA-15 channels and to be well distributed inside the support. Particle size analysis was performed on this image, resulting in the histogram in Figure 5.3b and an average particle diameter of 3.2 nm (standard deviation 2.2 nm). The crystallite size found in XRD is within these bounds of uncertainty. Figure 5.3c shows the EDX maps of the sample, with Pt in red, Si in blue and O in green. This shows that the Pt particles are distributed within the silica, rather than being formed on the external surfaces of the support.

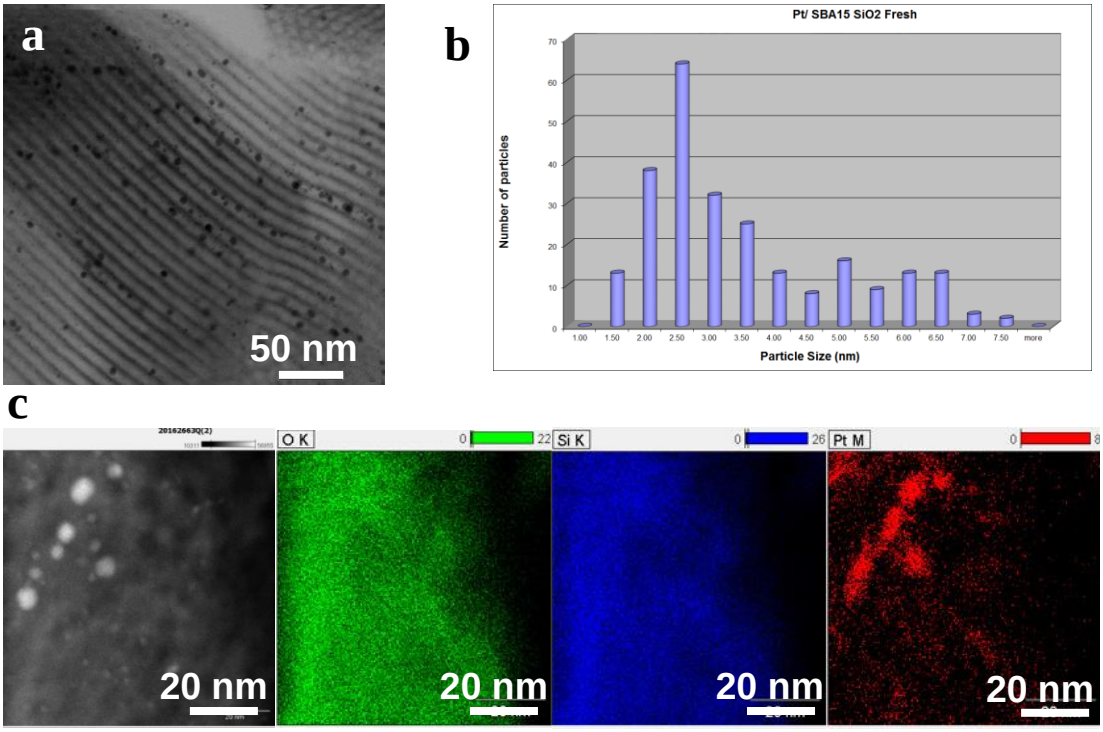


Figure 5.3. STEM images and EDX mapping of Pt(SBA-15) sample. a) STEM image of representative area of Pt(SBA-15), and b) size distribution histogram from this area. c) STEM image and EDX maps showing distribution of Pt in red, Si in blue and O in green.

Lattice fringes are not seen for the metal particles within the SBA-support, due to the depth of the support and interference of the electron beam with the silica.

5.5 Characterisation of supported bimetallic nanoparticles

The series of supported bimetallic nanoparticle samples were prepared through simultaneous co-impregnation of the two metal nitrate precursors. The precursors are thoroughly mixed before impregnation into the channels. The mild reduction temperatures mean that the thermodynamically favoured core-shell geometry is usually expected to form, with the lowest surface energy metal as the shell. This is often the case, however it is seen in these results that silica occasionally plays an important role in reversing this structure. All three bimetallic nanoparticle samples were characterised using XRD and TEM to understand sample composition, crystallinity, changes in lattice parameter and crystallite size and shape.

5.5.1 Platinum silver supported nanoparticles

XRD was used to calculate the composition, size and lattice parameter of particles inside the SBA-15 support. The PtAg(SBA-15) XRD profile is shown in Figure 5.4, with the observed profile in red, the fitted profile in blue and the reference stick patterns at the bottom for Pt in yellow and Ag in green. The first four PtAg reflections, (111), (200), (220) and (311), are clearly visible. Similar to the monometallic Pt(SBA-15) sample, the high background at low angles is because of the silica support. The lattice parameter was calculated to be 4.006 Å, which is larger than the bulk Pt lattice of 3.924 Å and lower than the bulk Ag lattice of 4.085 Å. It is likely that the two metals in this sample are in close contact, causing the Pt to undergo an expansion and the Ag a contraction. The first four peaks were fitted and the Scherrer Equation was used to calculate a crystallite size of 3.2 nm.

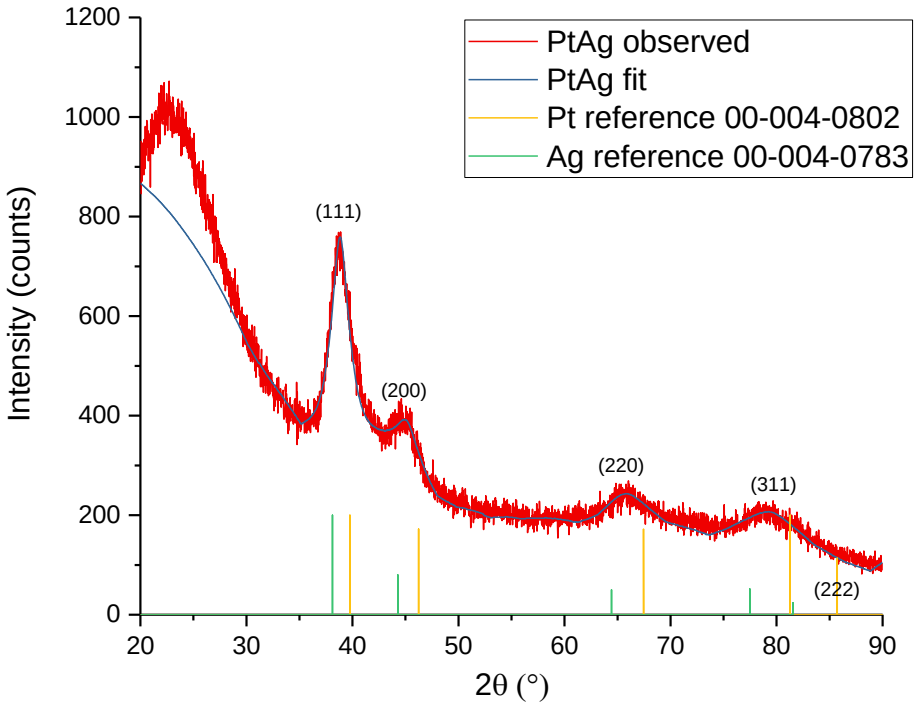


Figure 5.4. XRD profile showing PtAg(SBA-15) nanoparticles. Observed intensity is shown in red, fitted intensity is shown in blue. Pt reference (00-004-0802) positions are shown in yellow and Ag reference (00-004-0783) positions are shown in green.

TEM was also used to calculate the size of the particles, as well as their distribution across the support and the interaction of the metals. Figure 5.5a shows a STEM image of a representative area of the sample, with many small particles inside the channels and some larger particles filling the pores. This area was used for particle size analysis, producing the size distribution histogram shown in Figure 5.5b and resulting in an average particle size of 2.5 nm (standard deviation of 2 nm). The crystallite size found in XRD is within these bounds of uncertainty. Figure 5.5c shows a STEM image and the corresponding EDX maps, with Pt shown in red and Ag in pink. These confirm the proposal from the XRD, that the metals are located in close contact with each other. It is difficult to tell whether the particles are homogeneous alloys or whether they have a segregated metal shell, although it is likely that there is a mixture of metal atoms on the surface.

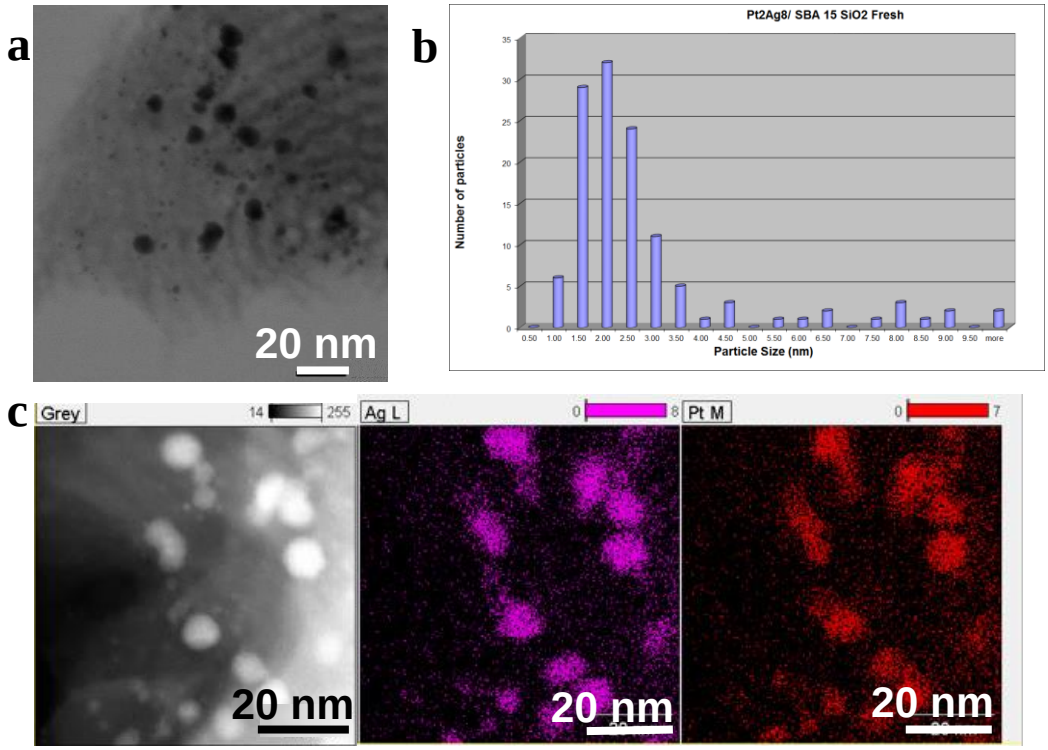


Figure 5.5. STEM images and EDX mapping of PtAg(SBA-15) sample. a) STEM image of representative area of PtAg(SBA-15), and b) size distribution histogram from this area. c) STEM image and EDX maps showing Pt distribution (red) and Ag distribution (pink).

5.5.2 Platinum nickel supported nanoparticles

The XRD profile for the PtNi(SBA-15) catalyst is shown in Figure 5.6, with the observed profile in red, the fitted profile in blue and the reference stick patterns at the bottom. Due to the small nanoparticulate size, the peak broadening is dramatic and the resolution is low. This, in addition to the high silica background at low angles, leads to poor quality reflections. Nevertheless, the reflections seen are attributed to Pt and PtNi, with the Pt (111), (200), (220), (311) and (222) and the PtNi (111), (200) and (202) reflections visible. The Pt lattice parameter of 3.916 Å was calculated, although there is likely to be some uncertainty in this value due to the overlap of peaks. The calculated value is slightly smaller than the bulk Pt lattice of 3.924 Å and larger than the bulk Ni lattice of 3.524 Å, so there is a small contraction in Pt lattice. The first two Pt reflections were fitted and the Scherrer Equation was used to calculate an average crystallite size of 5.0 nm.

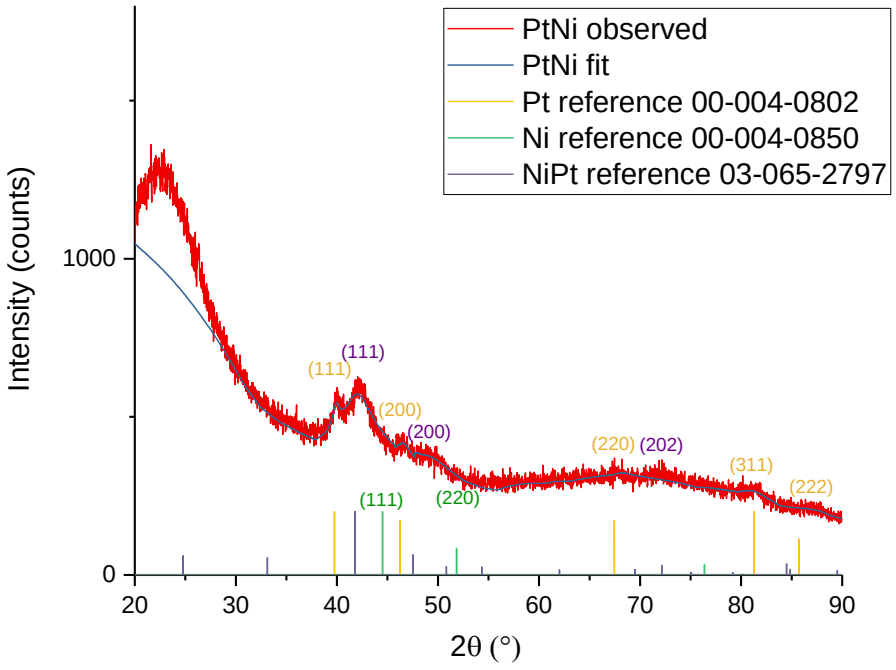


Figure 5.6. XRD profile showing PtNi(SBA-15) nanoparticles. Observed intensity is shown in red, fitted intensity is shown in blue. Pt reference (00-004-0802) positions are shown in yellow, Ni reference (00-004-0850) positions are shown in green and NiPt reference (03-065-2797) positions are shown in purple.

TEM was also used to calculate the size of the particles, as well as their distribution across the support and the interaction of the metals. It revealed the presence of particles inside the SBA-15

channels. Figure 5.7a shows a STEM image of a representative area of the sample, where the small particles appear inside the channels. This area was used for particle size analysis producing the size distribution histogram shown in Figure 5.7b. The mean particle diameter was calculated to be 2.1 nm (standard deviation of 1.0 nm). This measurement is lower than the crystallite size found in XRD, which indicates that there could be small areas of larger particles that are not seen in TEM. Although the suspension prepared for TEM was sonicated to disperse the particles evenly, it is possible that the aliquot used for drop-casting was collected from the top of the vial and therefore did not capture any anomalous larger particles from the lower regions of the solution. Figure 5.7c shows a STEM image and the corresponding EDX maps, with the Ni shown in blue and the Pt shown in red. It is thought that the Pt is predominantly concentrated inside the particles, whereas the Ni is both inside the particles and spread across the support.

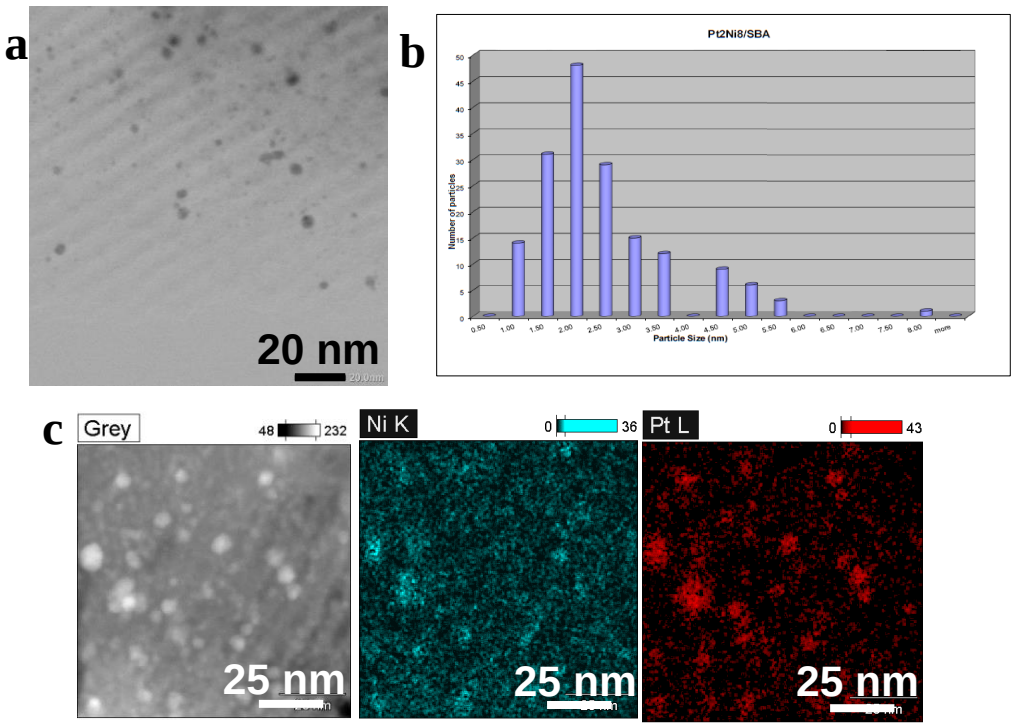


Figure 5.7. STEM images and EDX mapping of PtNi(SBA-15) sample. a) STEM image of representative area of PtNi(SBA-15), and b) size distribution histogram from this area. c) STEM image and EDX maps showing Pt distribution (red) and Ni distribution (blue).

EDX point analysis was performed in order to assess further whether Ni is spread across the support or only appears in the particles. Figure 5.8a shows the STEM image of the areas in which the point analysis was performed. Two areas (labelled 1 & 3) containing particles were selected, along with two areas (labelled 2 & 4) which appeared to be empty support in the STEM images. Figure 5.8a shows the EDX profile for area 1, which suggests a high Pt and Ni content. There is a higher proportion of Pt in these particles than would be expected from the stoichiometry, which indicates that the Ni is also found elsewhere. Figure 5.8b shows the EDX profile for area 2, which shows small amounts of Ni and insignificant amounts of Pt. This confirms that the Pt is localised in the particles whereas the Ni is distributed across the support. This point analysis was performed in two different regions of the sample, with four areas measured in each region. All eight sampling points confirmed the higher proportion of Pt to Ni in the particles and the presence of Ni on the support where no particles are visible.

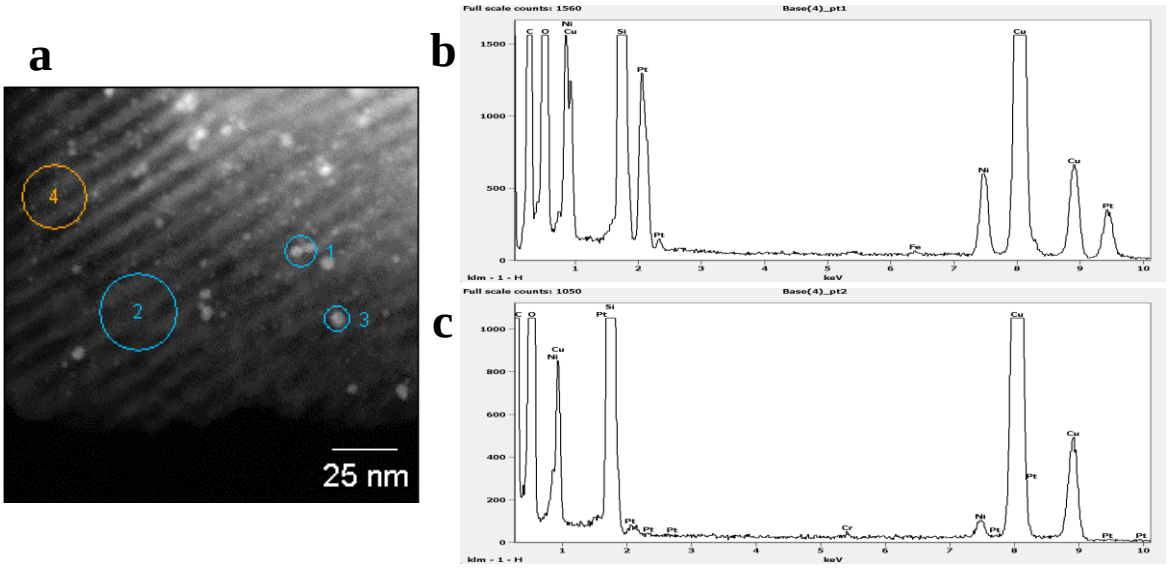


Figure 5.8. STEM/EDX point analysis. a) STEM image showing the points analysed with EDX. b) EDX profile of point 1, an area with nanoparticles and c) EDX profile of point 2, an area where no nanoparticles are visible.

5.5.3 Platinum zinc supported nanoparticles

XRD was used to calculate the composition, size and lattice parameter of particles inside the SBA-15 support. Figure 5.9 shows the XRD profile for a PtZn(SBA-15) sample, with the observed profile in red, the fitted profile in blue and the reference stick patterns at the bottom for Pt in yellow and Zn in green. Similar to the PtNi(SBA-15) samples, the intensity of the reflections is low due to the small nanoparticle size and high SBA-15 background. The first four Pt reflections, (111), (200), (220) and (311), can be seen but peak fitting is only possible for the first two reflections. The lattice parameter was calculated to be 3.898 Å, which is slightly smaller than the bulk Pt lattice of 3.924 Å, indicating a contraction in the Pt lattice. Although Zn has a hexagonal structure, it has a smaller lattice parameter (2.665 Å) than Pt and so induces a contraction in the Pt when a close metal interface was formed. The (111) and (200) peaks were fitted and the Scherrer equation was used to calculate a mean crystallite size of 2.6 nm.

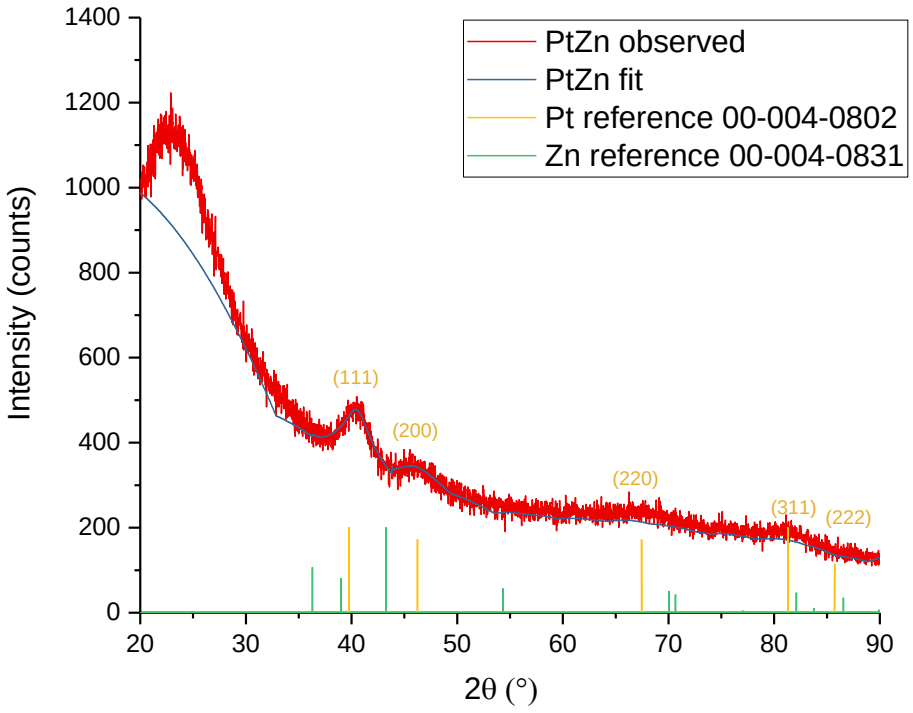


Figure 5.9. XRD profile showing PtZn(SBA-15) nanoparticles. Observed intensity is shown in red, fitted intensity is shown in blue. Pt reference (00-004-0802) positions are shown in yellow and Zn reference (00-004-0831) positions are shown in green.

TEM was also used to calculate the size of the particles, as well as their distribution across the support and the interaction of the metals. Figure 5.10a shows a STEM image of a representative area of the PtZn(SBA-15) sample, where the small nanoparticles appear inside the SBA-15 channels. TEM images for samples with alternative Pt:Zn ratios are shown in Appendix 2. The image shown here was used for particle size analysis producing the size distribution histogram shown in Figure 5.10b. The mean particle diameter was calculated to be 4.2 nm (standard deviation of 1.9 nm) which is slightly larger than the crystallite size from XRD. The crystallite size found in XRD is within these bounds of uncertainty. Figure 5.10c shows a STEM image and the corresponding EDX maps, with Zn distribution shown in yellow and Pt in red. Similar to the PtNi(SBA-15) sample discussed in Section 5.5.2, the Pt is predominantly concentrated inside the particles whilst the Ni is found both inside the particles and spread across the support.

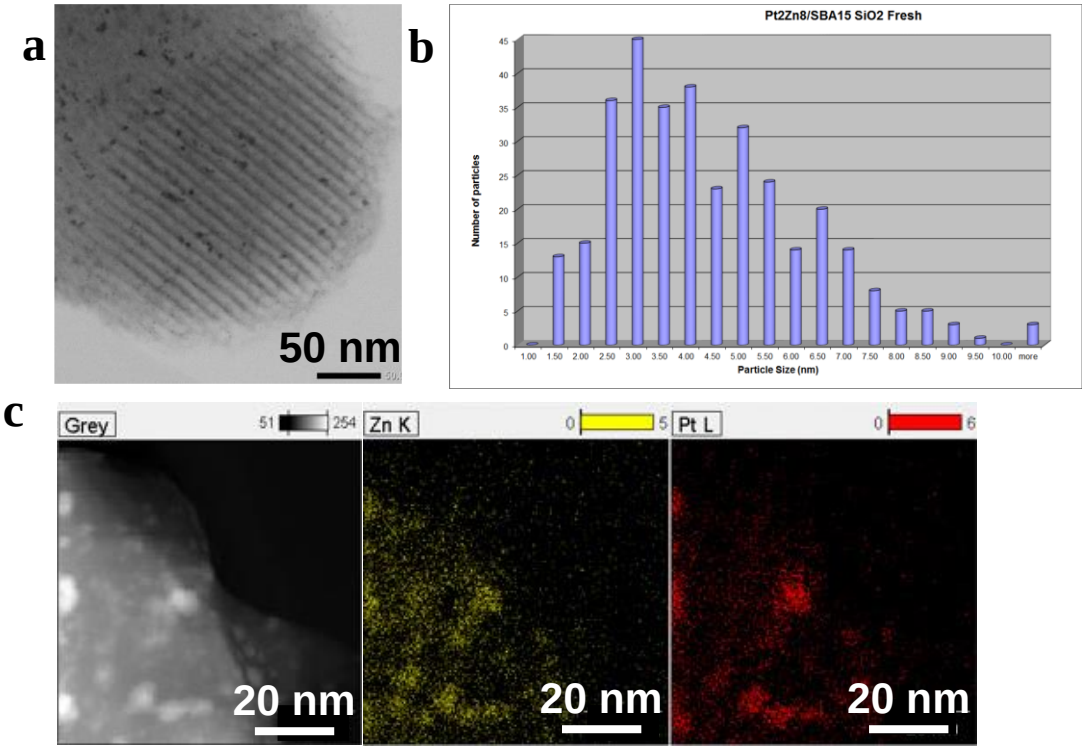


Figure 5.10. STEM images and EDX mapping of PtZn(SBA-15) sample. a) STEM image of representative area of PtZn(SBA-15), and b) size distribution histogram from this area. c) STEM image and EDX maps showing Pt distribution (red) and Zn distribution (yellow).

It is unclear from STEM and EDX mapping whether these particles are impregnated inside the channels or bound on the silica particle surface, so further TEM was used. Figure 5.11 shows a STEM image and corresponding secondary electron image (SEI) of the PtZn(SBA-15) sample. The STEM image clearly shows particles in the support while the SEI shows there are no particles on the surface, giving clarification that the particles are indeed impregnated into the channels.

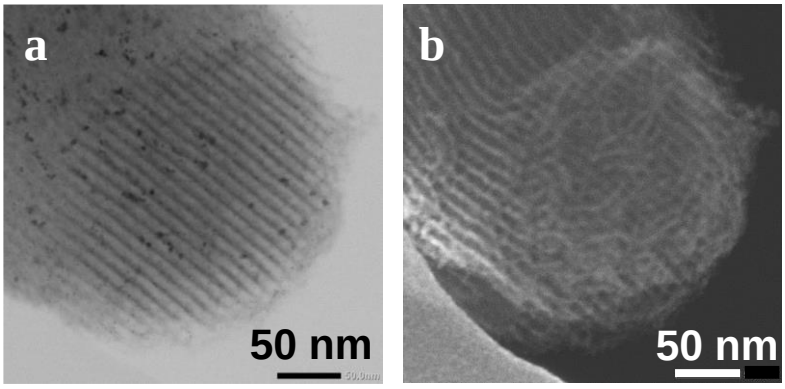


Figure 5.11. a) STEM image with b) corresponding secondary electron image investigating the particle deposition.

Further characterisation was performed to investigate the Zn dispersion across the SBA-15 surfaces and channels. As shown in section 5.6.1 below, the PtZn catalyst has a remarkably higher activity when supported in SBA-15, thus further information regarding the structure was collected to understand this enhancement. Atom probe tomography (APT) was performed by Tong Li at the Institute for Materials & ZGH, Ruhr-Universität Bochum and was used to visualise the location of each metal species within the channels. Figure 5.12 shows three end-on cross-sections, and one side-on cross-section, of channels in the SBA-15, with Pt shown in red and Zn shown in yellow. The end on images (green) show many small Pt particles of around 2-3 nm in diameter and the Zn atoms highly dispersed across the sample. The side-on image (blue) shows slightly elongated Pt particles inside the channels, indicating that there may be some preferential growth along the channel direction. In all areas the Zn is highly dispersed across the sample.

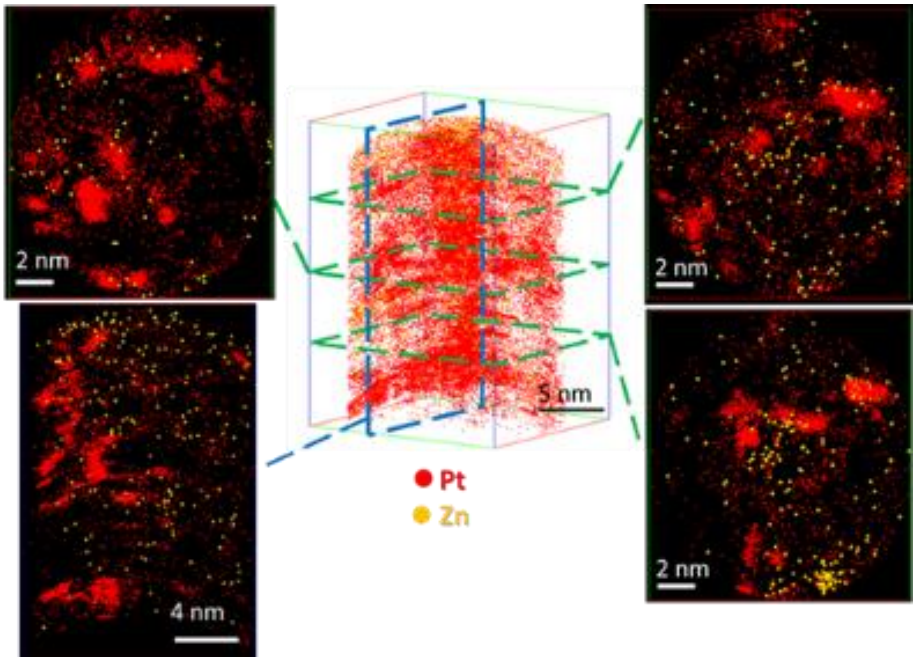


Figure 5.12. APT diagram of the PtZn(SBA-15) sample with Pt plotted in red and Zn plotted in yellow.

Low energy ion scattering was performed at Xiamen University, China as another method to probe the composition at various depths of the particles. Figure 5.13 shows the surface composition at 0.06 nm in black and the composition at 3.9 nm into the particles in red. At the surface the predominant species is Zn but, after probing into the particle to a depth of 3.9 nm, the Pt signal appears much more strongly indicating a Pt dominant core in the particle.

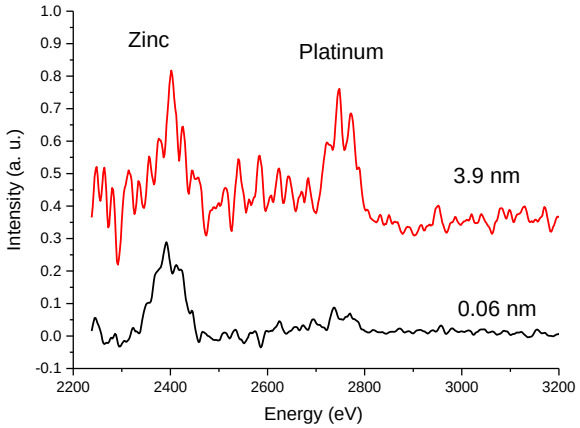


Figure 5.13. Low energy ion scattering spectrum of PtZn(SBA-15), with the black line showing the composition at 0.06 nm and the red line showing the composition at 3.9 nm.

Temperature programmed reduction was used to investigate the interaction of Pt and Zn in the reduction process, as is shown in Figure 5.14. The H_2 uptake at 400 °C indicates the reduction of the Pt nitrate precursor to the metal particles. The Pt sample shows a small reduction peak which increases in size on addition of Zn in the PtZn(SBA-15) sample. This indicates that the Pt promotes the reduction of Zn due to the hydrogen spillover effect. Therefore, where Zn is in close contact with Pt, it can be reduced to metal atoms on the surface of the Pt nanoparticles.

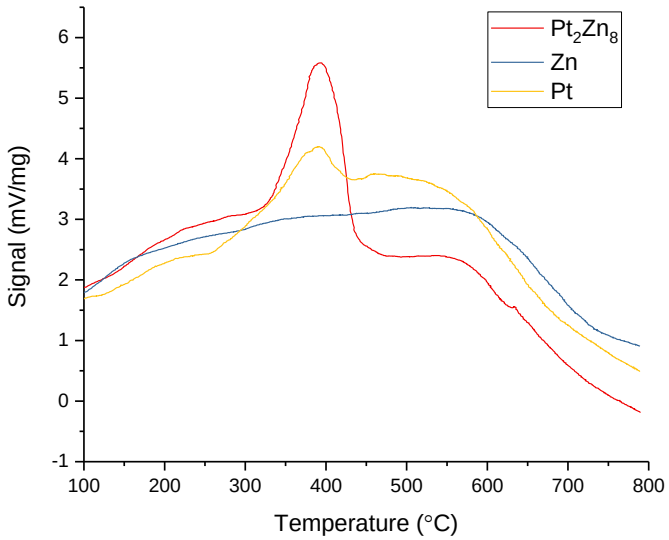


Figure 5.14. TPR showing the reduction behaviour of the monometallic samples, Pt in yellow, Zn in blue, and the PtZn(SBA-15) sample in red.

Wide angle x-ray scattering (WAXS) was also used to probe the particle composition and crystalline components in the samples. The data was collected at Diamond Light Source on beamline I11 and was processed by Glen Smales, University College London. The peak intensity in WAXS is much greater than in XRD, which enables further investigation into the lattice distortion of a sample. This technique was performed on the whole series of Zn containing PtZn(SBA-15) samples, with increasing Zn content down the series of profiles shown in Figure 5.15. It can be seen that the Pt containing species have reflections corresponding to the values expected for a reference metallic Pt crystal structure, shown in red. This confirms that there is an extended crystalline Pt metallic structural phase in the samples and that no oxidic Pt phases are

present. However, on increasing the Zn content, no Zn reflections arise. This is due to the highly dispersed non-crystalline nature of the Zn species in the sample, which appear to form as single isolated atoms across the support and Pt particles.

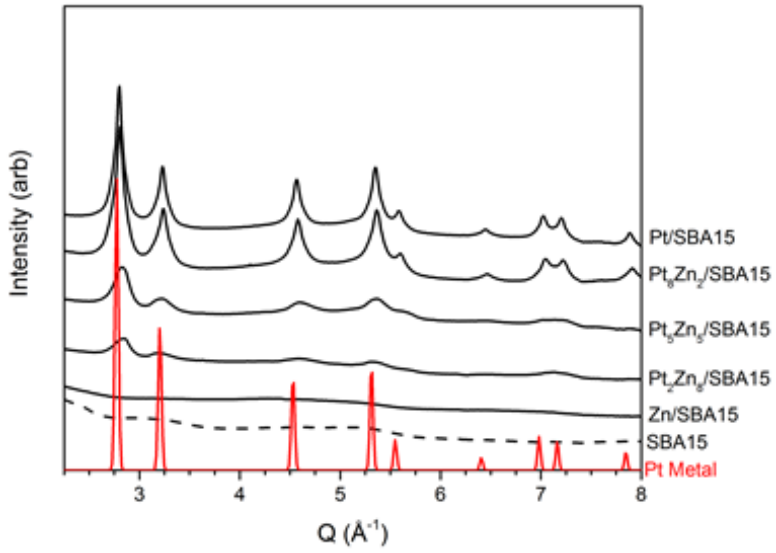


Figure 5.15. Wide angle x-ray scattering profiles obtained from each sample, with the metallic Pt phase shown in red below for comparison.

In addition, on increasing the Zn content there is a small but progressive shift in the Pt peaks to higher Q, indicating a lattice contraction. Table 5.1 shows the refined Pt lattice parameter for each sample. A 1.5% decrease in lattice parameter is seen from 3.890 Å for Pt(SBA-15) to 3.830 Å for Pt_2Zn_8(SBA-15). This contraction is attributed to the inclusion of Zn in the sample and the increased decoration of the Zn atoms on the Pt particle surface.

Table 5.1. Table showing the refined Pt lattice parameter for the samples obtained through peak fitting of the (111) reflection.

Sample	Lattice Parameter (Å)
Pt(SBA-15)	3.890 ± 0.001
Pt_8Zn_2(SBA-15)	3.879 ± 0.001
Pt_5Zn_5(SBA-15)	3.843 ± 0.001
Pt_2Zn_8(SBA-15)	3.830 ± 0.001

X-ray absorption near edge spectroscopy (XANES) was used to further characterise the local environment of the Pt and Zn species in the sample. Data was collected at Diamond Light Source, on beamline B18, and the data was analysed in collaboration with Adam Clark, University College London. The Zn K-edge data was used to investigate the structure of the Zn in the silica walls, while the Pt L_3-edge was used for probing the structure and electronic properties of the Pt nanoparticles. The Zn K-edge XANES shows a different profile to many standard Zn salts tested, as shown in Figure 5.16a&b. Figure 5.16a shows the profiles of various Zn standard materials collected and the Zn isolated silicate tetrahedron profile result from FDMNES modelling. Figure 5.16b shows the collected spectra from the series of PtZn(SBA-15) and Zn(SBA-15) samples. It can be seen that none of the standard materials tested show a synonymous profile to the samples, but the modelled isolated tetrahedron shows the closest similarity. Figure 5.16c shows a direct comparison of the modelled isolated silicate tetrahedron and the Zn(SBA-15) result. This suggests that the Zn is bonded to the silica walls, forming isolated tetrahedrally-coordinated oxidic species. No extended tetrahedral sharing units of ZnO, $Zn(OH)_2$ or other related bulk structures are seen.

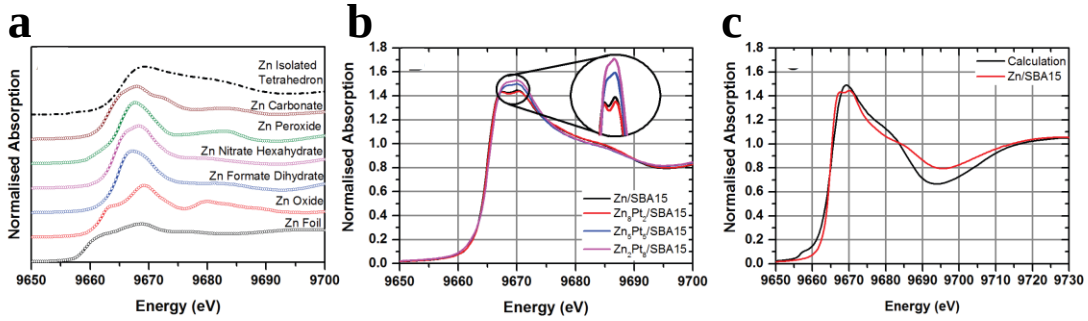


Figure 5.16. a) A comparison of measured Zn standard materials, and the isolated tetrahedron result of the FDMNES calculations. b) Zn K-edge XANES plot of the series of catalysts. c) A direct comparion of the Zn(SBA-15) Zn K-edge spectrum and the calculated result for a Zn isolated tetrahedron. Spectra prepared by Adam Clark.

Figure 5.16b also shows that, on increasing the Zn content in the PtZn(SBA-15) series, the white line intensity decreases and the peak splits into a strong doublet. This agrees with the results

reported by Mei *et al*., who attributed this change to the formation of $[ZnO_4]^{6-}$ on the silica surface.[18]

The Pt L_3-edge was also probed to investigate the structural and electronic properties of the Pt nanoparticles. Figure 5.17a shows the reference patterns of Pt metal and of PtO_2, while Figure 5.17b shows the XANES spectrum of the Pt containing samples. The collected XANES profiles show that both the metallic species and a small oxidic component are present in the structures. The Pt(SBA-15) sample has the most metallic nature, showing that the oxidic component is more prominent after addition of Zn. However, the oxidic component does not noticeably increase with a further increase Zn content. The exact fraction of the oxidic component is not yet known, as the particle size effects of metal clusters on the XANES spectrum make linear combination fitting difficult.[19–22] As there was no crystalline oxidic Pt seen in the WAXS, the oxidic Pt phase is particularly small or non-crystalline. It is thought that the Pt-O component is likely to be forming a shell across the Pt nanoparticle surface, through binding to the silica surface oxygen moieties or atmospheric surface oxidation.

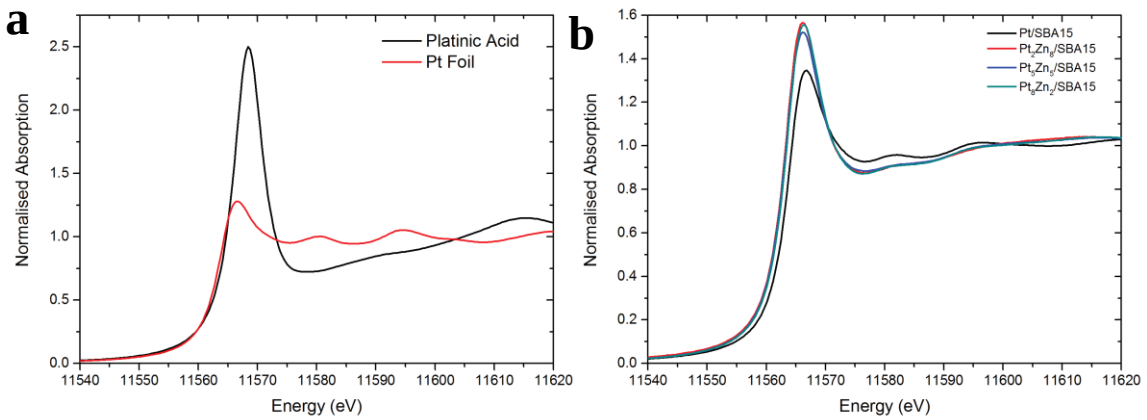


Figure 5.17. a) Pt L_3-edge XANES profiles of two standard materials, platinic acid (PtO) and metallic Pt. b) Measured spectrum of Pt(SBA-15) and the three PtZn(SBA-15) samples.

^{29}Si Nuclear magnetic resonance (NMR) was used to further distinguish the local structure of the samples and examine the speciation of the Si atoms. The data was collected and processed in

collaboration with Ben Griffith, Warwick University. Figure 5.18 shows the three different types of Si speciation, with either 0, 1 or 2 bonds to the adatom R (Zn or H). On increasing this coordination to Zn or H, the chemical shift decreases.

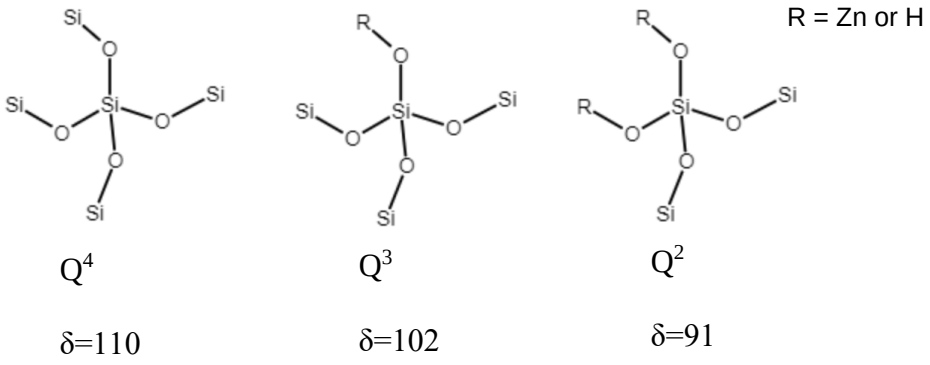


Figure 5.18. Schematic to show the Si speciation and corresponding chemical shift values. Increasing the coordination to R (Zn or H) leads to a decrease in chemical shift value.

The ^{1}H NMR data can also be used to understand the changes in the nature of the H network. Isolated surface silanol Si−OH species with no nearby ^{1}H species to promote H-bonding can be seen at resonances in the range of δ=0.6-1.6 ppm. Where these species do have H-bonding and are close to non-bridging O components, the chemical shift increases to δ=3.5 ppm. Finally, physisorbed H_2O is seen at resonances in the range of δ=5.0-6.0 ppm.

Figure 5.19 shows the deconvoluted and simulated spectra of the ^{29}Si and ^{1}H magic angle spinning (MAS) NMR for each PtZn(SBA-15) catalyst sample and the pure SBA-15 support. The fitted ^{29}Si values are found in Table 5.2, which shows the Si speciation percentages. As expected for the pure SBA-15 sample, the network is dominated by Q^4 units comprising 84% of the total Si speciation. The Zn(SBA-15) sample shows an 18% increase in Q^3 species in comparison to the native SBA-15 system. Hence, the Zn^{2+} cation causes significant network modification and an increase in the formation of non-bridging O bonds (Si=O···Zn). This is concordant with previous studies of Zn incorporation into glass formulations, which have demonstrated that Zn exhibits both network forming and network modifying characteristics.[23–25]

The corresponding ^{1}H MAS NMR data also shows large changes to the nature of the H network on addition of Zn to the SBA-15. The native SBA-15 system exhibits well resolved isolated silanol resonances in the range δ=0.6-1.6 ppm, indicating no nearby H-bonding. However the Zn(SBA-15) system shows broader resonances at δ=3.7 ppm, suggesting a more strongly H-bonded system. Zn incorporation has increased the population of non-bridging Si=O···Zn species, thus driving the majority of the OH species into a H-bonded network with the non-bridging O species. The large increase in the proportion of Q^3 Si species, together with the decrease in surface silanol species and the increase in H-bonding to the non-bridging O-Zn, suggests that the Zn incorporation is not confined to the SBA-15 surface but substitutes deeper into the bulk wall structure.

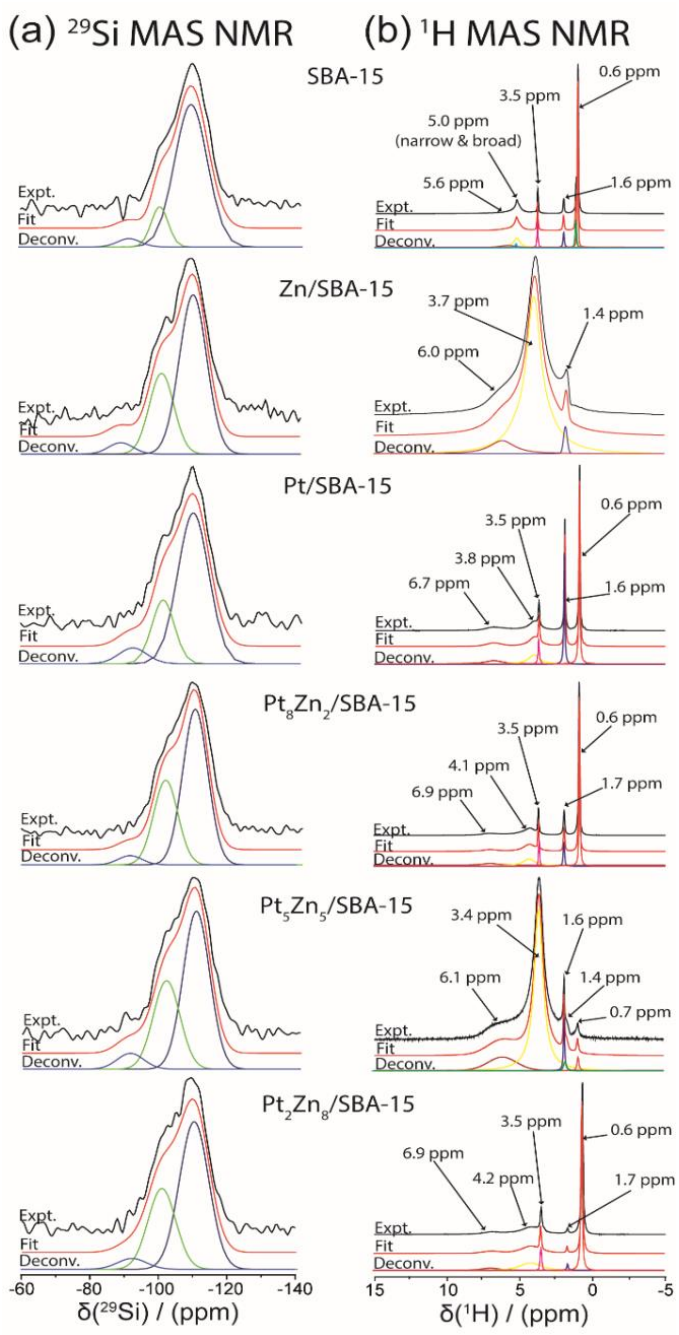


Figure 5.19. ^{29}Si and ^{1}H NMR deconvoluted and simulated spectra for the pure SBA-15 support and each PtZn(SBA-15) catalyst.

The wettability of the Zn modified SBA-15 surface is also higher, as evidenced by the greater intensity of the H_2O resonance at δ=6.0 ppm which suggests a higher affinity for physisorbed H_2O. The higher Zn content samples, such as Zn(SBA-15) and Pt_5Zn_5(SBA-15), display broad resonances at δ=3.4-3.6 ppm and δ=5.0-6.0 ppm, which are attributed to water clusters.[26] This shows that the Zn modified surfaces have a higher affinity for water than the hydrophobic Pt

modified surfaces. The Pt_2Zn_8(SBA-15) is expected to display similar affinity for water, although this sample had been extensively dried before the measurement.

Table 5.2. ^{29}Si MAS NMR data with speciation percentage identified for each sample and for the pure SBA-15 support.

Sample	Q^2		Q^3		Q^4	
	δ_{iso} (ppm)	I(% ±3)	δ_{iso} (ppm)	I(% ±3)	δ_{iso} (ppm)	I(% ±3)
SBA-15	−91.1	4	−102.5	12	−111.2	84
Zn(SBA-15)	−89.6	4	−101.6	30	−110.8	66
Pt(SBA-15)	−92.3	7	−101.8	22	−110.2	71
Pt_8Zn_2(SBA-15)	−91.6	4	−101.9	33	−110.4	63
Pt_5Zn_5(SBA-15)	−91.2	6	−101.6	34	−110.1	60
Pt_2Zn_8(SBA-15)	−92.3	5	−101.0	32	−110.4	63

The incorporation of Pt to form the Pt(SBA-15) system induces a very different response from the SBA-15 surface when compared with the incorporation of Zn. The ^{29}Si MAS NMR data suggests that the introduction of Pt causes modest network modification, as shown by the 10% increase in Q^3 resonances. Again the ^{1}H data shows some evidence of H-bonded silanol species from the broader δ=3.8 ppm resonance, but this contribution is much smaller than that observed in the Zn(SBA-15) system. This suggests that most of the network modification induced by Pt incorporation is confined to the surface and that the majority of Q^3 species involve Si-O-Pt linkages, which tether Pt nanoparticle formation to the SBA-15 surface.

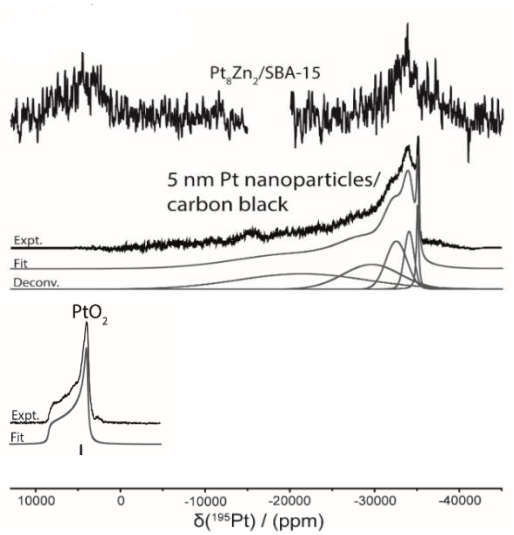


Figure 5.20. ^{195}Pt NMR spectra for Pt_8Zn_2(SBA-15) sample at the top. Deconvoluted and simulated reference spectra of Pt (middle) and PtO_2 (bottom).

The ^{195}Pt static NMR data from the Pt_8Zn_2(SBA-15) system corroborates the XAS, TEM and APT findings that demonstrate that Pt nanoparticles and PtO_2 are present in this sample. The deconvoluted spectra shown in Figure 5.20 can be matched with the reference sample patterns, indicating that both Pt and PtO_2 are present. From the intensities measured in this ^{195}Pt static NMR data, it can be observed that comparable amounts of diamagnetic PtO_2 accompany the Pt nanoparticle formation, while the oxide is likely found on the exterior of the Pt nanoparticles.

5.6 Formic acid decomposition

5.6.1 Liquid phase formic acid decomposition

The liquid phase formic acid decomposition reaction was selected as a probe reaction to investigate the catalytic activity and the effect of introducing the secondary metal on the surface active site. The liquid phase formic acid decomposition is known to be particularly susceptible to electronic and geometric changes in the Pt surface and the activity can be quickly measured through the assessment of residual acid strength using acid-base titrations. Reaction conditions were modified

from those reported in literature[27] in order to ascertain formic acid conversion at atmospheric pressure.

The desired amount of catalyst was dispersed in 0.1M formic acid and the mixture was stirred at 25 °C for 20 minutes. In addition to these tests, a series of stability tests were performed to determine catalytic activity after 60 minutes. Tests were also performed on the whole series of Zn containing species, in order to investigate how metal composition affected results. Finally two Ni catalysts, synthesised by two different routes, were tested to investigate the effect of the synthesis method on the catalysis.

Figure 5.21 shows conversion rates of the liquid phase formic acid decomposition reaction for the Pt, PtAg, PtNi and PtZn in the first 20 minutes of the reaction. The PtAg(SBA-15) catalyst shows a lower activity than the monometallic Pt(SBA15), whereas the PtZn(SBA-15) and PtNi(SBA-15) both show higher activities. These changes can be attributed to the electronic and structural change in the Pt surface as a result of the close contact with the secondary metals.

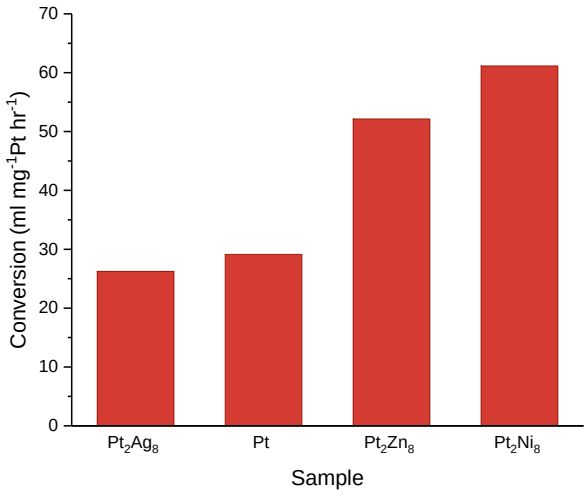


Figure 5.21. Conversion rates of the silica supported catalysts for the liquid phase formic acid decomposition reaction in the first 20 minutes.

As summarised in Table 5.3, all three catalysts have an electronic promotion effect due to the influence of the secondary metal on the Pt. Ag (4.26 eV), Zn (4.33 eV) and Ni (5.01 eV) all have lower work functions than Pt (6.35 eV), which means that the secondary metals all donate electron density towards the Pt. This leads to a down-shift in the d-band and therefore a weaker binding of reagents to the metal surface, as discussed in Section 1.3.1. All three samples with a secondary metal show this ligand effect, causing weakening of the reactant-surface bond and increased reactivity. Pt has a close to optimal binding strength and so the rate limiting step can depend on the reaction conditions. As discussed previously in Section 4.6, these tests were performed under conditions with a very high concentration of formic acid, which means adsorption is facile. In this case desorption is likely to be the rate limiting step and so, when adding a secondary metal, weakening of the product binding increases the overall reactivity. This electronic promotion partially explains the higher rate of conversion for PtZn(SBA-15) and PtNi(SBA-15), but does not account for the lower conversion for PtAg(SBA-15).

The average sample lattice parameters can also be seen in Table 5.3, showing that the PtAg(SBA-15) has an expanded lattice compared to the monometallic Pt(SBA-15). The average lattice parameters for PtZn(SBA-15) and PtNi(SBA-15) are both smaller than the Pt(SBA-15) monometallic lattice. In both the PtZn and PtNi, a compressive strain is seen in the Pt layer due to the smaller lattice parameter of the secondary metals (Zn=2.664 Å, Ni=3.524 Å) than Pt (3.924 Å). However in PtAg, a tensile strain emerges due to the larger lattice parameter of Ag (4.085 Å). For the cases under compressive strain, PtNi and PtZn, the d-orbital overlap is increased leading to a broadening of the d-band, as discussed in Chapter 1. This results in a down-shift of the d-band centre and a weaker binding of the products on the catalyst surface, which is the reason for the enhanced catalytic activity. In the case of PtAg, a tensile strain leads to the reduced overlap of the d-orbitals and an up-shift of the d-band centre, which increases the binding strength of the products and hence decreases the catalytic activity.

Overall, the combination of the increased electron density and compressive strain seen in PtZn and PtNi results in downshifted d-band centres and increased reactivity of the catalyst. However the effects for PtAg are contradictory, with the ligand effect causing a downshifted d-band centre and the tensile strain leading to an upshifted d-band centre. These effects broadly cancel each other out, which is evidenced by the similar rates of conversion seen in the formic acid decomposition reaction for both the Pt and PtAg samples. However the structural effect seems to be slightly more powerful, resulting in a marginally decreased activity for the PtAg catalyst.

Table 5.3. Summary of catalyst conversion rate, lattice parameter (as calculated from XRD) and the difference in work function of Pt and the secondary metal.

Sample	Conversion (ml $mg^{-1}Pt\ hr^{-1}$)	Average lattice parameter-XRD (Å)	Work function difference (eV)
PtAg(SBA-15)	26.2	4.006	2.09
Pt(SBA-15)	29.1	3.919	N/A
PtZn(SBA-15)	52.1	3.898	2.02
PtNi(SBA-15)	61.1	3.916	1.34

In comparison with the PVP samples tested in Chapter 4, the PtZn(SBA-15) sample showed the greatest enhancement in activity. In addition, the lattice contraction and electronic donation led to further characterisation and activity testing of this series of catalysts. The atomic ratios of Pt to Zn tested were 1:0, 8:2, 5:5 and 2:8. Figure 5.22 shows the full series of results for the Pt, Pt_8Zn_2, Pt_5Zn_5 and Pt_8Zn_2 samples. It can be seen that, on initial addition of Zn, the activity decreases in comparison to the monometallic Pt catalyst. However with continual addition of Zn the activity steadily increases, finally reaching the enhanced activity of the Pt_2Zn_8 composition shown above.

The WAXS results shown in Section 5.5.3 suggest that, on addition of any quantity of Zn, a lattice contraction occurs and so the enhancement of reactivity would be expected for all samples. However, it is thought that the small contraction from the addition of small quantities of Zn may not be enough to enhance the formate binding. Where Zn addition is minimal, it is likely that the majority of the Zn binds to the silica walls rather than to the Pt and thus has less of an effect on the Pt lattice, both electronically and structurally.

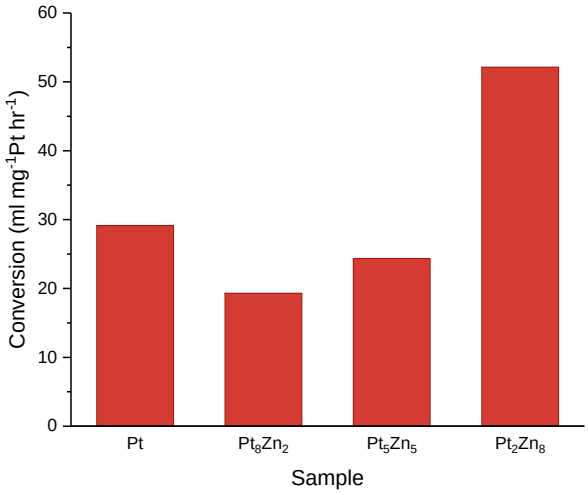


Figure 5.22. Conversion rates of the liquid phase formic acid decomposition reaction with the PtZn series of catalysts after reaction for 20 minutes.

The catalysts were also tested with a longer reaction time of 60 minutes to assess deactivation or induction periods. As shown in Figure 5.23, the Pt(SBA-15) sample has a slightly lower average conversion rate for the 60 minute test than the 20 minute test, indicating that slight deactivation is seen over the course of the reaction. Similarly, the PtZn(SBA-15) sample also appears to undergo deactivation, which is more severe than the Pt sample. This could be due to metal segregation and thus the loss of the activity enhancement from the secondary metal. Other deactivation routes are also possible including CO poisoning, the extent of which is unknown due to insufficient data on product selectivity.

Interestingly the PtNi(SBA-15) sample shows a higher conversion rate for the 60 minute test than the 20 minute test, indicating that there is an induction period between the start of the reaction and the point at which the maximum conversion rate is reached. This could be due to the high distribution of Ni across the support, as shown in the EDX point analysis discussed in Section 5.5.2. The reducing environment of formic acid may lead to further reduction of the Ni species around the Pt and increase the reactivity of the Pt. It is seen that the compression of the Pt lattice parameter is not as large as expected through contact with Ni, so the reducing environment may lead to higher metal interfaces and enhance this contraction. *In-situ* characterisation, such as XAS, could be used in the future to confirm these changes.

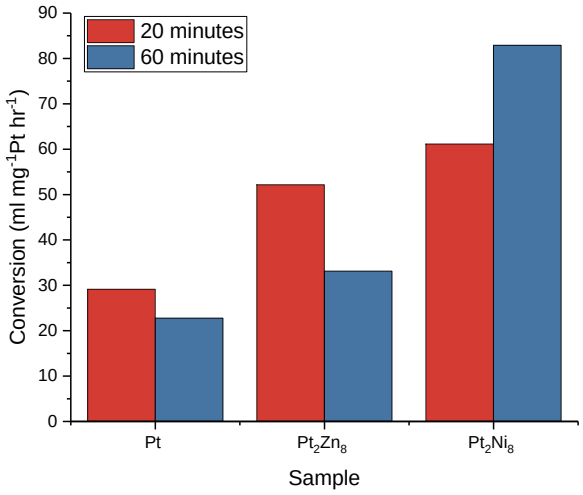


Figure 5.23. Conversion rates of liquid phase formic acid decomposition reaction with three catalysts after 20 minutes (red) and 60 minutes (blue).

The final liquid phase formic acid decomposition test was performed to compare two PtNi(SBA-15) catalysts that were prepared in slightly different manners. The normal method of preparation with combined impregnation and reduction of both metals was compared with a stepwise sample, which underwent a two-stage impregnation and reduction of the Ni then Pt. Figure 5.24 shows that both samples performed very similarly with excellent conversion rates. There is a slight difference

in the activity of the catalysts, with the stepwise synthesis method showing the slightly higher activity. This dependence on the synthesis route is further investigated in Chapter 6.

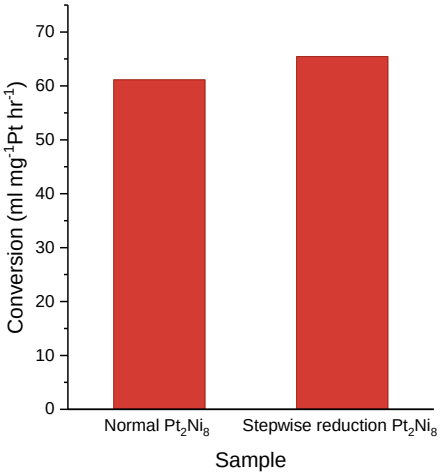


Figure 5.24. Conversion rates of liquid phase formic acid decomposition reaction with two PtNi(SBA-15) catalysts, one prepared with combined impregnation and reduction of both metals and the other with a two-stage impregnation and reduction of the metals.

5.6.2 *In-situ* XAS with gas phase formic acid decomposition

Further investigation into the PtZn(SBA-15) structure and deactivation was studied using the *in-situ* gas phase formic acid decomposition reaction and monitored with XAS. The samples were pressed into a pellet and loaded into a reaction cell, as shown in Figure 5.25. A vapour of formic acid was flowed into the cell with a flow rate of 0.18 ml/s for a total of 1.5 hours. Initial and final XANES spectra were compared and EXAFS fitting was performed for multiple points along the reaction timeline.

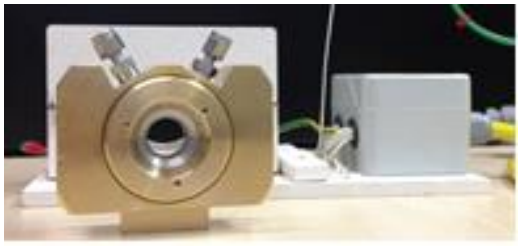


Figure 5.25. Reaction cell used for in-situ XAS with the gas phase formic acid decomposition reaction at Diamond Light Source beamline B18.

The Pt nanoparticles were investigated with the Pt L_3-edge, as discussed in Section 5.5.3. The initial PtZn(SBA-15) catalyst series showed mainly metallic Pt, with a small PtO component at the surface. Figure 5.26 shows the reference and initial spectra, as well as the final XANES spectrum. The predominant phase in the final XANES spectrum is clearly the metallic Pt phase, showing that the formic acid environment aids the reduction of the oxidic shell to Pt metal.

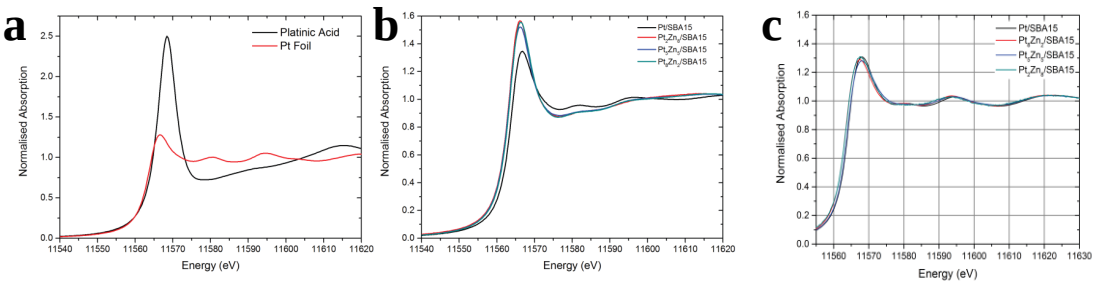


Figure 5.26. Pt L_3-edge XANES spectra. a) Reference patterns for PtO (platinic acid) and Pt metal. b) Initial XANES spectra of PtZn(SBA-15) series. c) Final XANES spectra of PtZn(SBA-15) series after exposure to formic acid vapour.

Time resolved EXAFS for the Pt(SBA-15) sample was studied to further understand this reduction, and to investigate the effect on nanoparticle diameter and on Pt-Pt bond distance. Figure 5.27 shows the extracted data. It can be seen that the conversion from oxidic Pt to metallic Pt is completed in 30 minutes, which is in the same time regime as the increase in bond length. However there is a continual increase in Pt nanoparticle diameter, even after the conversion to metallic Pt is complete. This indicates that there is a small amount of agglomeration of the Pt particles in the silica channels, caused by the limited interaction between Pt and the silica in the reducing formic acid environment.

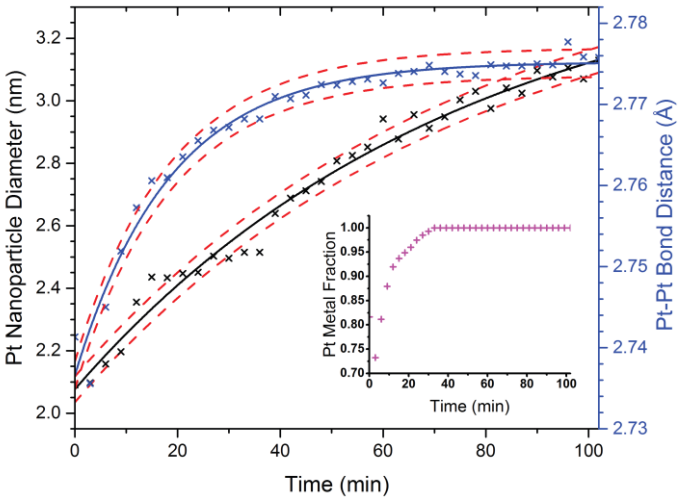


Figure 5.27. Graph showing the extracted nanoparticle diameter (black) and Pt-Pt bond distance (blue), compared to the relative metallic Pt fraction (as shown in the inset plot).

Tracking the conversion of the Zn species in the sample was also performed with XAS. The Zn K-edge was monitored and the initial and final states compared in the XANES spectra. As discussed in Section 5.5.3, the initial PtZn(SBA-15) catalyst series showed isolate Zn tetrahedron species with no long-range Zn bonding. Figure 5.28a shows the spectra of Zn(SBA-15) both before and after formic acid exposure. These can be compared to the reference patterns in Figure 5.28b, which show the proposed initial structure in red and the Zn formate dihydrate in black. The final spectrum after the Zn(SBA-15) reaction with formic acid shows similarities with the reference Zn formate dihydrate species, however there are some differences. The final sample white line intensity is greater than the reference and there is a broadening and dampening of the peak at 9685 eV. Both of these changes could be due to the nanoparticulate size of the species, which means there are more defects that affect the XANES region.

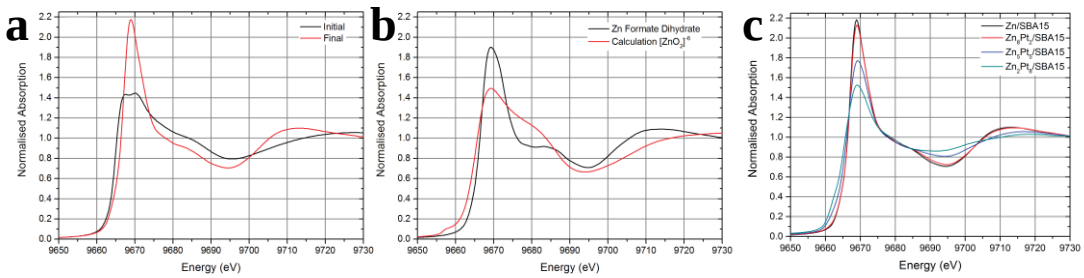


Figure 5.28. Zn K-edge XANES spectra. a) Comparison of initial and final states for Zn(SBA-15). b) Reference Zn formate dihydrate spectrum(black) and initial calculate isolated tetrahedron (red). c) Final XANES spectra of PtZn(SBA-15) series.

Figure 5.28a&b shows again the Zn(SBA-15) sample data and the reference spectra whilst the catalyst series of results can be seen in Figure 5.28c. This shows all the samples moving towards the Zn formate dihydrate structure. There is a substantial drop in the white line intensity on increasing the Pt content, which indicates a multi-phase component in the XANES and suggests more PtZn bimetallic structures. On increasing the Pt content, the number of Pt nanoparticles increases and so there is more contact between the Pt nanoparticle and the Zn bound to the walls. This means there are fewer Zn sites which are uncapped and are susceptible to leaching.

The conversion of the Zn silicate type isolated tetrahedron structure to the Zn formate dihydrate was monitored using EXAFS. Figure 5.29 shows the conversion of the silicate over the course of the reaction. The Zn(SBA-15) underwent a two-step complete conversion, whereas the Pt containing samples showed the same two-step conversion with the exception of a portion which did not convert to the formate species. The two-step conversion is thought to be due to the formation of two Zn silicate sites which are susceptible to conversion to the formate species, with the initial conversion of a less stable Zn site followed by conversion of a more stable Zn site.

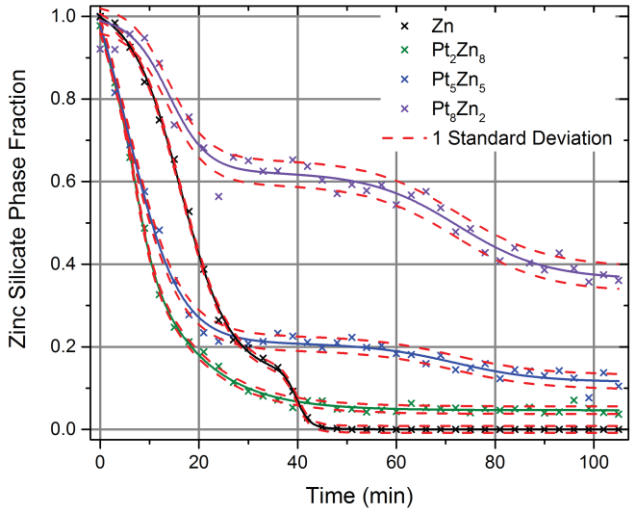


Figure 5.29. Conversion profile of Zn silicate to Zn formate phase for each sample.

On increasing the Zn content, the less stable site is preferred. This could be due to increased deposition into the silica network, rather than on the surface of the silica support. On increasing the Zn content, the proportion of Zn sites which are not converted decreases. This suggests that there is capping of Zn with Pt, which further stabilises the Zn silicate site and leads to resistance to conversion to Zn formate.

5.7 Conclusion

This chapter focussed on the synthesis and characterisation of silica supported bimetallic nanoparticles. The aim was to synthesise Pt bimetallic nanoparticles which have a large metal-metal interface inside the channels of SBA-15, a mesoporous silica, in order to maximise the structural and electronic effects found when introducing a secondary metal. The liquid phase formic acid decomposition reaction was selected as a probe reaction, in order to identify changes at the catalytically active surface of the Pt due to the susceptibility of this reaction to structural and electronic changes in the catalyst.

It was found that impregnating the metals into the SBA-15 channels was possible under gentle heating conditions. TEM and secondary electron imaging confirmed that the metals were indeed inside the channels and not on the surface. All samples were synthesised and thoroughly characterised with XRD, TEM and XAS. A summary of the particle sizes and lattice parameters can be seen in Table 5.4.

Table 5.4. Summary table of sample particle sizes and lattice parameters.

Sample	**Particle size (nm)**		**Lattice parameter (Å)**
	XRD	TEM	XRD
Pt(SBA-15)	4.9	3.2	3.919
PtAg(SBA-15)	3.2	2.5	4.006
PtNi(SBA-15)	5.0	2.1	3.916
PtZn(SBA-15)	2.6	4.2	3.898

Fine control of the metal-metal interface, however, was not facile. Both Zn and Ni interacted strongly with the silica support and therefore formed small clusters or isolated atoms, rather than nanoparticles cores for the Pt to coat. EDX point analysis showed that Ni was present across the support, as well as in the nanoparticles. Zn dispersion was confirmed with APT, XAS and WAXS, which showed no extended Zn structures. TPR confirmed that some Zn species which are adjacent to Pt species are reduced to the metallic state, leading to a Pt-Zn bimetallic component.

Liquid phase formic acid decomposition reactions showed that PtNi and PtZn have enhanced catalytic activity compared to Pt, whereas PtAg showed decreased activity. This was attributed mainly to the structural effect, where Zn and Ni have smaller lattices than Pt and so a contraction in the Pt lattice is seen. This leads to a decrease in the d-band centre and increased overlap with the bidentate formate intermediate. Additionally, the secondary metals also donate electron density

to the Pt in the bimetallic species, leading to a further decrease in d-band centre and enhanced activity.

The atomic ratio of the bimetallics was found to be important in the activity of the catalysts, with the Pt_2Zn_8(SBA-15) catalyst outperforming its Pt_8Zn_2(SBA-15) counterpart. This is thought to be due to the increased Pt-Zn contact in the Pt_2Zn_8(SBA-15) catalyst. Furthermore, the synthesis route was monitored through comparing a PtNi(SBA-15) co-reduction catalyst, prepared in the usual single step impregnation and reduction method, with a PtNi(SBA-15) stepwise catalyst, prepared through impregnation and reduction of Ni prior to the impregnation and reduction of Pt. It was found that the stepwise catalyst had a slightly higher activity, although they were comparable. The synthesis method will be further discussed in Chapter 6.

Time dependent studies were also performed, with Pt, PtZn and PtNi catalysts tested over 20 and 60 minutes. Both Pt and PtZn catalysts were seen to show small quantities of deactivation, with the PtNi catalyst showing an enhancement in rate after 60 minutes. It is thought that this could be due to an induction period, where the Ni is further reduced and forms a closer contact with the Pt, leading to a decrease in lattice parameter and enhanced activity.

The PtZn system was further investigated with *in-situ* XAS, in order to monitor the active structure and decomposition process. It was found that the initial catalyst consisted mainly of Pt nanoparticles coated with a small oxidic surface layer and highly dispersed isolated Zn species on the silica surface. After formic acid treatment, the PtO component was reduced to form Pt metal and the Zn silicate was converted to Zn formate. It is likely that the PtO component is the active component for the formic acid decomposition and so, under the reducing formate environment, the catalyst undergoes deactivation. The Zn silicate phase is converted to Zn formate in a two-step reaction with a fraction of the silicate remaining, indicating three Zn sites. It is thought that the two Zn sites which are leached to form the formate are bound on the silica surface with different

methods, so one is more susceptible to leaching. The third site which is resistant to leaching is thought to be responsible for the Pt-Zn bimetallic component.

These gas phase *in-situ* XAS studies are interesting in themselves, however it cannot be assumed that the same processes occur in liquid phase catalysis. There are likely to be differences in the formate concentration and so surface coverage, as well as an effect from the dramatic change in amount of water in the system. These variances can affect the catalytic nature as well as effect of the reaction on the structure of the catalyst. These gas phase studies have provided useful information into the catalyst structures, however the changes in reactivity are not necessarily transferable to the liquid phase system.

Synthesis of novel and interesting catalysts has been achieved, although the formic acid decomposition reaction appears to be inducing a change in the metal structure. Chapter 6 will further investigate the synthesis routes and how these affect reactivity. It will also involve testing of the catalysts with the oxygen reduction reaction, which is a commercially valuable process.

1.9 References

1 J. Gabaldon, M. Bore and A. Datye, *Top. Catal.*, 2007, **44**, 253–262.

2 K. S. W. Sing, D. H. Everett, R. A. W. Haul, L. Moscou, R. A. Pierotti, J. Rouquerol and T. Siemieniewska, *Pure Appl. Chem.*, 1985, **57**, 603–619.

3 D. Zhao, *Science (80-.).*, 1998, **279**, 548–552.

4 D. Zhao, Q. Huo, J. Feng, B. F. Chmelka and G. D. Stucky, *J. Am. Chem. Soc.*, 1998, **120**, 6024–6036.

5 D. M. Ford, E. E. Simanek and D. F. Shantz, *Nanotechnology*, , DOI:10.1088/0957-4484/16/7/022.

6 F. S. Xiao, *Top. Catal.*, 2005, **35**, 9–24.

7 A. J. Vizcaíno, A. Carrero and J. A. Calles, 2006, 1–12.

8 Y. Qiao, N. Said, M. Rauser, K. Yan, F. Qin, N. Theyssen and W. Leitner, *Green Chem.*, 2017, **19**, 977–986.

9 J. Czaplinska, I. Sobczak and M. Ziolek, *J. Phys. Chem. C*, 2014, **118**, 12796–12810.

10 M. Zhao, T. L. Church and A. T. Harris, *Appl. Catal. B Environ.*, 2011, **101**, 522–530.

11 J. Fan, X. Jiang, H. Min, D. Li, X. Ran, L. Zou, Y. Sun, W. Li, J. Yang, W. Teng, G. Li and D. Zhao, *J. Mater. Chem. A*, 2014, **2**, 10654–10661.

12 V. Chaudhary, *Int. J. Sci. Eng. Res.*, 2016, **7**, 1743–1748.

13 Y. Kathiraser, J. Ashok and S. Kawi, *Catal. Sci. Technol.*, 2016, **6**, 4327–4336.

14 M. M.-J. Li, L. Ye, J. Zheng, H. Fang, A. Kroner, Y. Yuan and S. C. E. Tsang, *Chem. Commun.*, 2016, **52**, 2569–2572.

15 J. Zhou, X. Duan, L. Ye, J. Zheng, M. M.-J. Li, S. C. E. Tsang and Y. Yuan, *Appl. Catal. A Gen.*, 2015, **505**, 344–353.

16 E. Pippel, S. A. Nepijko and J. Woltersdorf, *Phys. Status Solidi*, 1980, **61**, 469.

17 W. H. Qi and M. P. Wang, *J. Nanoparticle Res.*, 2005, **7**, 51–57.

18 B. Mei, A. Becerikli, A. Pougin, D. Heeskens, I. Sinev, W. Grünert, M. Muhler and J. Strunk, *J. Phys. Chem. C*, 2012, **116**, 14318–14327.

19 D. R. Short, A. N. Mansour, J. W. Cook, D. E. Sayers and J. R. Katzer, *J. Catal.*, 1983, **82**, 299–312.

20 A. N. Mansour, J. W. Cook and D. E. Sayers, *J. Phys. Chem.*, 1984, **88**, 2330–2334.

21 N. Ichikuni and Y. Iwasawa, *Catal. Letters*, 1993, **20**, 87–95.

22 F. W. Lytle, P. S. P. Wei, R. B. Greegor, G. H. Via and J. H. Sinfelt, *J. Chem. Phys.*, 1979, **70**, 4849–4855.

23 Y. Xiang, J. Du, L. B. Skinner, C. J. Benmore, A. W. Wren, D. J. Boyd and M. R. Towler, *RSC Adv.*, 2013, **3**, 5966–5978.

24 A. B. Rosenthal and S. H. Garofalini, *J. Am. Ceram. Soc.*, 2005, **70**, 821–826.

25 D. A. McKeown, I. S. Muller, A. C. Buechele and I. L. Pegg, *J. Non. Cryst. Solids*, 2000, **261**, 155–162.

26 S. Jones, S. Fairclough, M. Gordon-Brown, W. Zheng, A. Kolpin, B. Pang, W. Kuo, J. Smith and E. Tsang, *Chem. Commun.*, 2015, **51**, 46–49.

Chapter 6

Tailored platinum nickel nanoparticle catalysts

6.1 Background 141
6.2 Objectives 143
6.3 Experimental details 143
6.4 Characterisation of platinum nickel nanoparticles 144
6.4.1 Pt_1Ni_3 catalysts 144
6.4.2 Pt_1Ni_1 catalysts 156
6.5 SBA-15 wall effect 163
6.6 Oxygen reduction reaction 165
6.7 Conclusion 171
6.8 References 174

6.1 Background

A Pt catalyst is used for the Oxygen Reduction Reaction (ORR) at the cathode of traditional fuel cells. However, despite the use of the catalyst, the rate of reaction remains slow and the fuel cells are not economically viable due to the high cost of the Pt catalyst.[1,2] Recent research has been focussed on finding an alternative to the Pt catalyst, through the use of different metals or alloying to increase the Pt activity and decrease the cost.[3–5] Of these approaches, it has been found that the catalysts which contain Pt continue to have the highest activity for the reaction.[6,7] The Sabatier principle and volcano plot discussed in Chapter 1 explain that the oxygen and hydroxide bonds to a pure Pt surface are too strong and the optimal catalyst would have a slightly weaker surface-reagent bond.[8] Calculations show that, when alloying Pt with transition metals such as Ni, Co, Fe and Cr, electron density is transferred towards the Pt, leading to a down-shift in the d-band centre and weaker Pt-O binding.[9] This can increase the efficiency of the Pt as well as decreasing the overall catalyst cost.[10]

Recently, a large amount of research has been performed on tailoring these alloys to form the optimal catalyst for ORR. One method to improve the activity of the alloy catalysts is to tailor the surface facets. A 9-fold increase in activity has been observed when using the Pt{111} surface in comparison with the commercial catalyst. This has led to development of shape tailored catalysts and the octahedral morphology which favours the {111} surface.[11] Through combining this surface control and alloying with secondary metals, large increases have been observed in the activities reported. One active Pt_3Ni{111} surface showed an ORR activity 10 times higher than the Pt{111} surface and therefore a total 90-fold increase compared with the commercial Pt/C catalyst tested.[5,11–13] However, with high loadings of Pt, the cost efficiency is not greatly improved and it is expected that catalysts with both higher activities and lower Pt compositions are possible.

Creating Pt shell materials increases cost efficiency, as a large proportion of the Pt is at catalytically active surface sites.[14] There have been some theoretical investigations performed which investigate Pt-shell materials, which have a core of a secondary metal and a high concentration of Pt on the surface of the particle, as presented in detail in Chapter 1.[15] In summary, this increases cost efficiency due to the large proportion of the Pt at a catalytically active surface site. The catalytic activity has been modelled for a range of core-shell type catalysts and it has been found that materials containing a Pt or Pd shell are expected to have a high activity for ORR. Fe core - Pt shell materials and Ni core - Pt shell materials are expected to have a good catalytic activity.[15] Some experimental investigations into core-shell materials for ORR have been reported, one example of which is a Co core - Pt shell catalyst showing an activity 9 times greater than the commercial Pt catalyst.[16–18]

In Chapter 5, the use of SBA-15 as a structural directing agent was introduced. Through taking advantage of the strong interaction of Zn with the SBA-15 walls, a preference for highly dispersed surface coverage was developed for the PtZn system. The interaction of Ni with the silica walls is very interesting, as the bond energies of Ni-Ni and Ni-O are in a similar region. This leads to dispersion of Ni across the silica support and the facile formation of Ni particles in the channels, allowing various morphologies to be synthesised under slightly different conditions. The PtNi system synthesised with SBA-15 as a structure directing support is also of interest for development of a cost efficient ORR catalyst.

ORR catalysts are often deposited on a carbon support to maintain their small size and promote their electrical conductivity.[19,20] The catalysts synthesised in this chapter are initially synthesised in SBA-15, in order to control the growth and maintain directed alloy morphologies. After the particles are synthesised, they are removed from the SBA-15 and deposited on carbon before testing and characterisation. This allows electrical conductivity and maintains their morphologies, giving high ORR activities.

6.2 Objectives

The aim of this chapter is to investigate how the synthesis method and wall effect of SBA-15 can be manipulated to form highly active catalysts for industrially important reactions. As discussed in Section 6.1, on alloying Pt and Ni an increase in ORR activity is seen. A high activity can be extracted through manipulating the particles to form an intimate contact between the two metals, while maintaining a high quantity of Pt on the electrochemical surface. The investigation into the synthesis of the non-thermodynamically favoured alloy morphology is also interesting. This chapter aims to utilise the wall effect of the SBA-15 to form different alloy morphologies and to understand how this affects the activity of ORR. Catalyst characterisation and investigation of the synthesis mechanism are used to understand how the wall effect can be used to manipulate different syntheses. This work aims to identify which catalysts are most active for ORR and demonstrate that the support can have a strong effect on both the final material and the synthesis.

6.3 Experimental details

Detailed discussion of the synthesis method is provided in Chapter 3. In summary, PtNi particles are initially synthesised in the mesoporous silica SBA-15 using an incipient wetness impregnation technique. Controlled calcination temperature ramp and reduction were employed to maintain the delicate nanoparticle structures. PtNi(SBA-15) particles were then combined with Vulcan carbon and soaked in NaOH to slowly remove the silica and the resulting powder was washed in water to remove all silicate material. The wall effect was monitored through adjusting the initial synthesis of PtNi in SBA-15. Three different synthesis routes were investigated: stepwise (Ni then Pt), reverse-stepwise (Pt then Ni) and co-reduction. The stepwise samples were impregnated with one metal ion and reduced, before the impregnation of the second ion and further reduction. The co-reduction catalyst was formed through impregnation of both metals together, followed by one

single reduction. All materials were treated in the same manner for carbon addition and silica removal.

Thorough discussion of the ORR testing is provided in Chapter 3. All samples were tested for ORR activity in collaboration with Simantini Nayak, Vincent Group, University of Oxford.

6.4 Characterisation of platinum nickel nanoparticles

Catalysts of two different metal compositions and three different synthesis methods were produced, characterised and tested using ORR. The first composition, Pt_1Ni_3, was synthesised in three ways: stepwise (Ni first), co-reduction and reverse-stepwise (Pt first). The second composition, Pt_1Ni_1, was synthesised in two ways: stepwise (Ni first) and co-reduction. A comparison of the five catalysts was undertaken with various techniques including XRD, TEM, APT and XAS.

6.4.1 Pt_1Ni_3 catalysts

Characterisation of the Pt_1Ni_3 catalysts was studied using XRD and TEM and showed interesting behaviour of the stepwise and co-reduction catalysts, although the reverse-stepwise catalyst was less interesting. APT and EDX mapping was used to further characterise the stepwise and co-reduction catalysts.

Figure 6.1 shows an XRD profile for the Pt_1Ni_3 stepwise catalyst, along with the reference patterns for Pt, Ni and the PtNi alloy shown at the bottom in yellow, green and purple respectively. The observed profile contains peaks attributed to Pt, Ni and the PtNi alloy, with no additional PtO_x peaks seen.

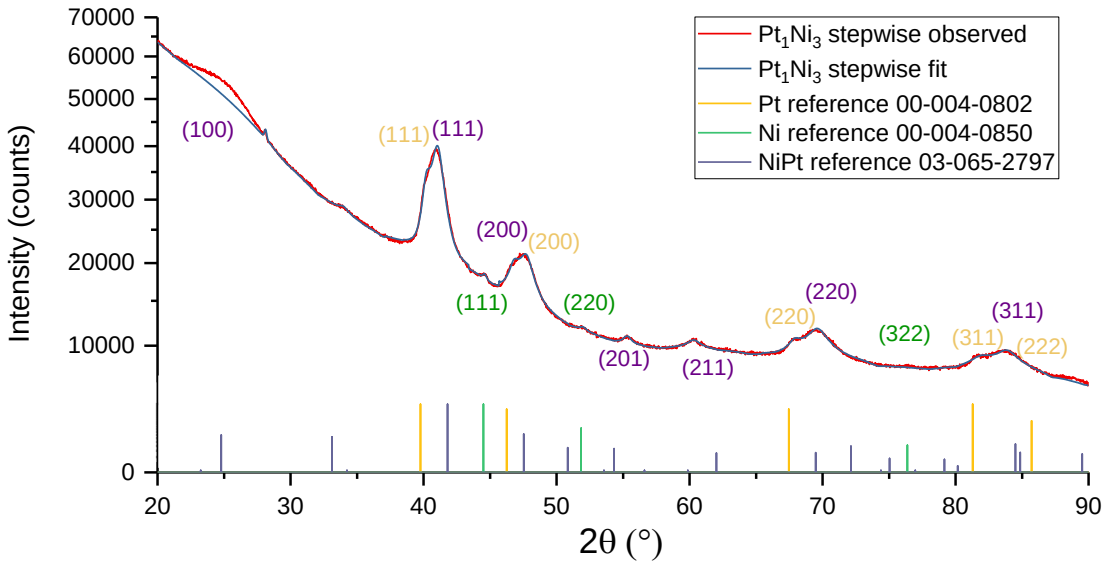


Figure 6.1. XRD profile for the Pt_1Ni_3 stepwise catalyst with the observed profile shown in red and the fitted profile in blue. Reference stick patterns are shown at the bottom for Pt (yellow), Ni (green) and NiPt alloy (purple).

The Pt and PtNi peaks often overlapped, so peak fitting was performed in order to calculate the FWHM and thus the crystallite size of both species. The Pt size was calculated from the (111), (200), (220) and (311) reflections. The PtNi size was also calculated from the (111), (200), (220) and (311) reflections as well as the (201) and (211) reflections. The crystallite diameters were calculated to be 9.1 nm for Pt and 8.1 nm for PtNi. The Ni peaks were too low in intensity to generate a reliable FWHM and so their crystallite size was not calculated. The Pt peaks show a slight shift to a higher position 2θ, which indicates a small contraction in the lattice parameter. The calculated lattice parameter for the Pt species in the Pt_1Ni_3 stepwise catalyst is 3.896 Å, which is smaller than the bulk Pt lattice of 3.924 Å.

The XRD profile for the Pt_1Ni_3 stepwise catalyst can be compared with the profile for the Pt_1Ni_3 co-reduction catalyst, shown in Figure 6.2. The profile shape is similar, with the Pt_1Ni_3 co-reduction curve showing the same reflection peaks as the Pt_1Ni_3 stepwise catalyst, however the peak intensities are very different. The Pt_1Ni_3 co-reduction curve shows a lower intensity for Pt and PtNi peaks and a higher intensity for Ni peaks. This suggests that the alloy type is different, as the Pt_1Ni_3 stepwise catalyst indicates Ni decoration on the surface of Pt particles whereas the

Pt_1Ni_3 co-reduction catalyst indicates a Pt shell on a Ni core. Both catalysts contain areas of alloyed PtNi and large interfaces between the two metals.

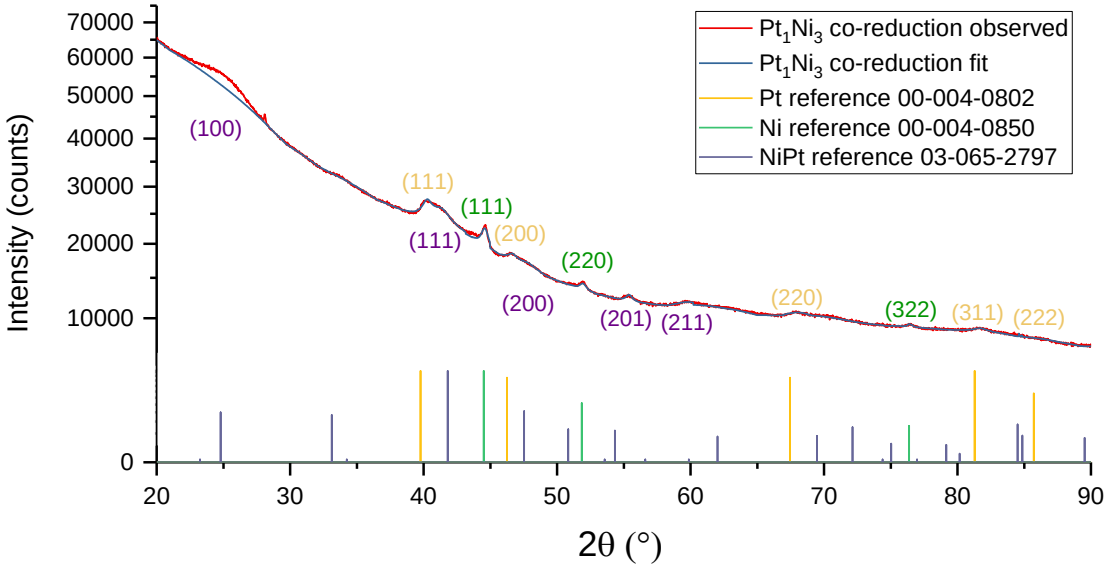


Figure 6.2. XRD profile for the Pt_1Ni_3 co-reduction catalyst with the observed profile shown in red and the fitted profile in blue. Reference stick patterns are shown at the bottom for Pt (yellow), Ni (green) and NiPt alloy (purple).

Again, the Pt and PtNi peaks are overlapped and so peak fitting was used for calculation of crystallite size. The peaks of all three species were fitted and crystallite sizes calculated using the same peaks for Pt and PtNi as before and the (111), (220) and (322) reflections for Ni. The Pt and PtNi crystallite diameters were found to be 9.1 nm and 6.8 nm respectively, similar to those calculated for Pt_1Ni_3 stepwise catalyst. The Ni crystallite size was found to be considerably larger at 21.7 nm. As for the Pt_1Ni_3 stepwise catalyst, this Pt_1Ni_3 co-reduction catalyst shows a contraction of Pt lattice, from 3.924 Å expected for the bulk material to 3.902 Å. The Ni lattice is largely unperturbed with a measured lattice parameter of 3.523 Å, while the lattice parameter for the bulk material is 3.524 Å.

The PtNi lattice is tetragonal and so the calculation of this lattice parameter from the XRD profile is not facile. However, in both the Pt_1Ni_3 stepwise and Pt_1Ni_3 co-reduction catalysts the reflections manifest at a slightly lower angle than expected and so a small lattice expansion may be occurring.

TEM was further used to understand particle size, morphology and distribution across the support. Figure 6.3 shows TEM images of both Pt_1Ni_3 stepwise and Pt_1Ni_3 co-reduction catalyst samples. Both samples show dark metal particles distributed across the carbon support. The particles in the Pt_1Ni_3 stepwise catalyst have an average diameter of 5.1 nm (standard deviation of 1.6 nm), which is larger than the co-reduction average of 2.7 nm (standard deviation of 1.9 nm). However, the Pt_1Ni_3 co-reduction catalyst sample shows more aggregated particles than the stepwise sample. The impact of the Pt particle size on the ORR has been previously investigated and it was concluded that the optimal particle size is around 4.5 nm.[21] The particles synthesised are within this region and so are expected to perform well for ORR.

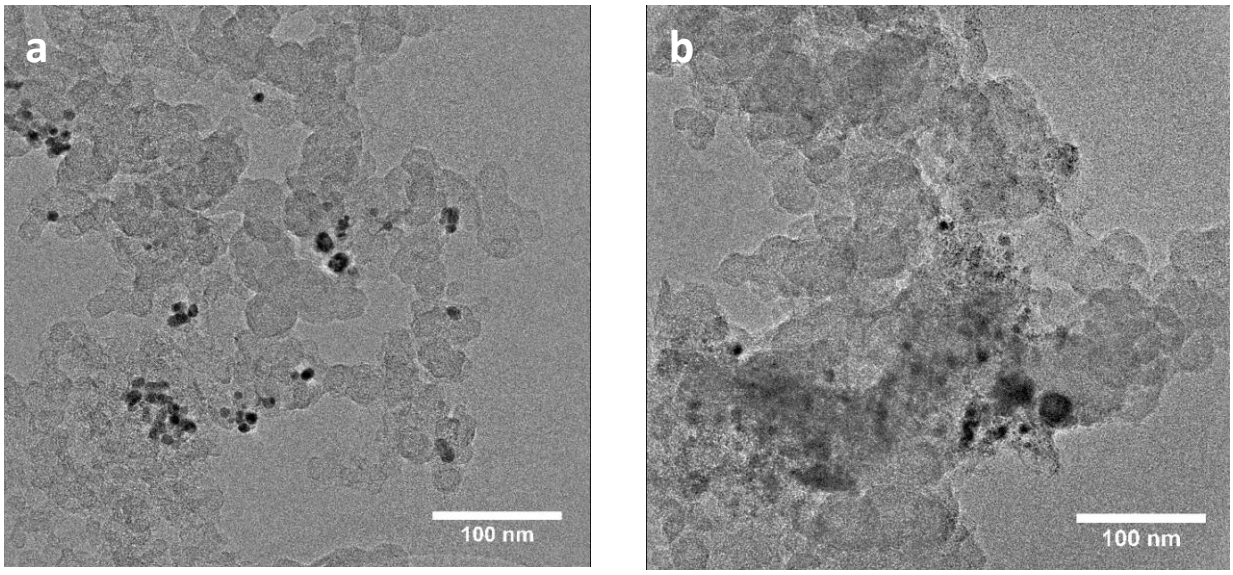


Figure 6.3. TEM images showing homogeneity across the support and size distribution of both a) Pt_1Ni_3 stepwise and b) Pt_1Ni_3 co-reduction samples.

The difference in sizes of these two Pt_1Ni_3 catalysts is highlighted by the size distribution histogram shown in Figure 6.4, where the stepwise sample is shown in red and the co-reduction sample is shown in black. Each sample distribution was collated from measurements of 100 particles.

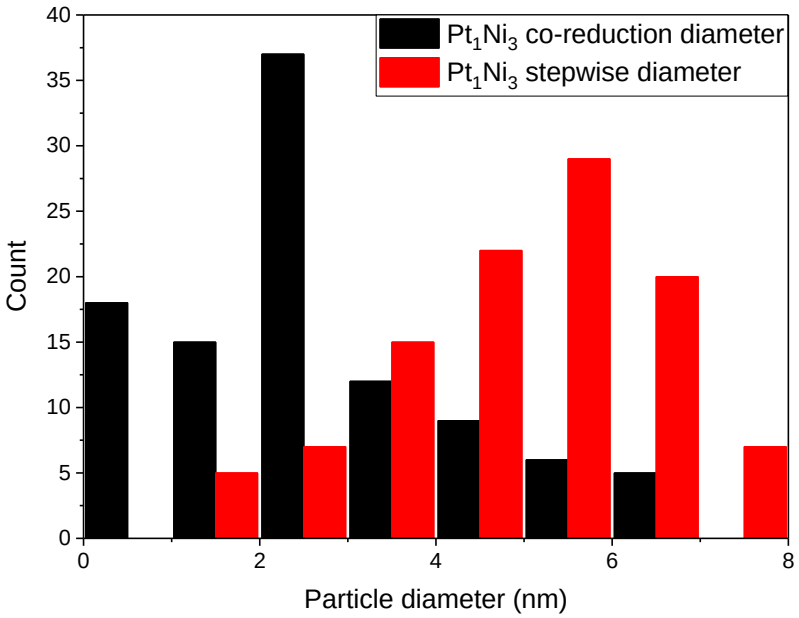


Figure 6.4. Size distribution histogram showing Pt_1Ni_3 stepwise (red) and Pt_1Ni_3 co-reduction (black) samples.

TEM characterisation has concluded that the catalyst samples contain small metal particles, with diameters less than 8 nm and a narrow size distribution. XRD has shown that each sample contains Pt and PtNi alloy and that the Pt_1Ni_3 co-reduction sample also contains crystalline Ni, although further investigation is needed to understand the bimetallic morphology.

High resolution STEM and EDX mapping was used to further understand the particle morphology and the interface between the metals, as shown in Figure 6.5 for the Pt_1Ni_3 stepwise catalyst sample. Two contrasting particle morphologies were seen in the sample. The majority of the sample shows a mixed alloy phase as shown in Figure 6.5a&b, where the Pt and Ni are both present in the particles. Additionally, there are some areas where NiO_x coats the carbon support and Pt particles are present on the surface of the Ni coating, as shown in Figure 6.5c-f.

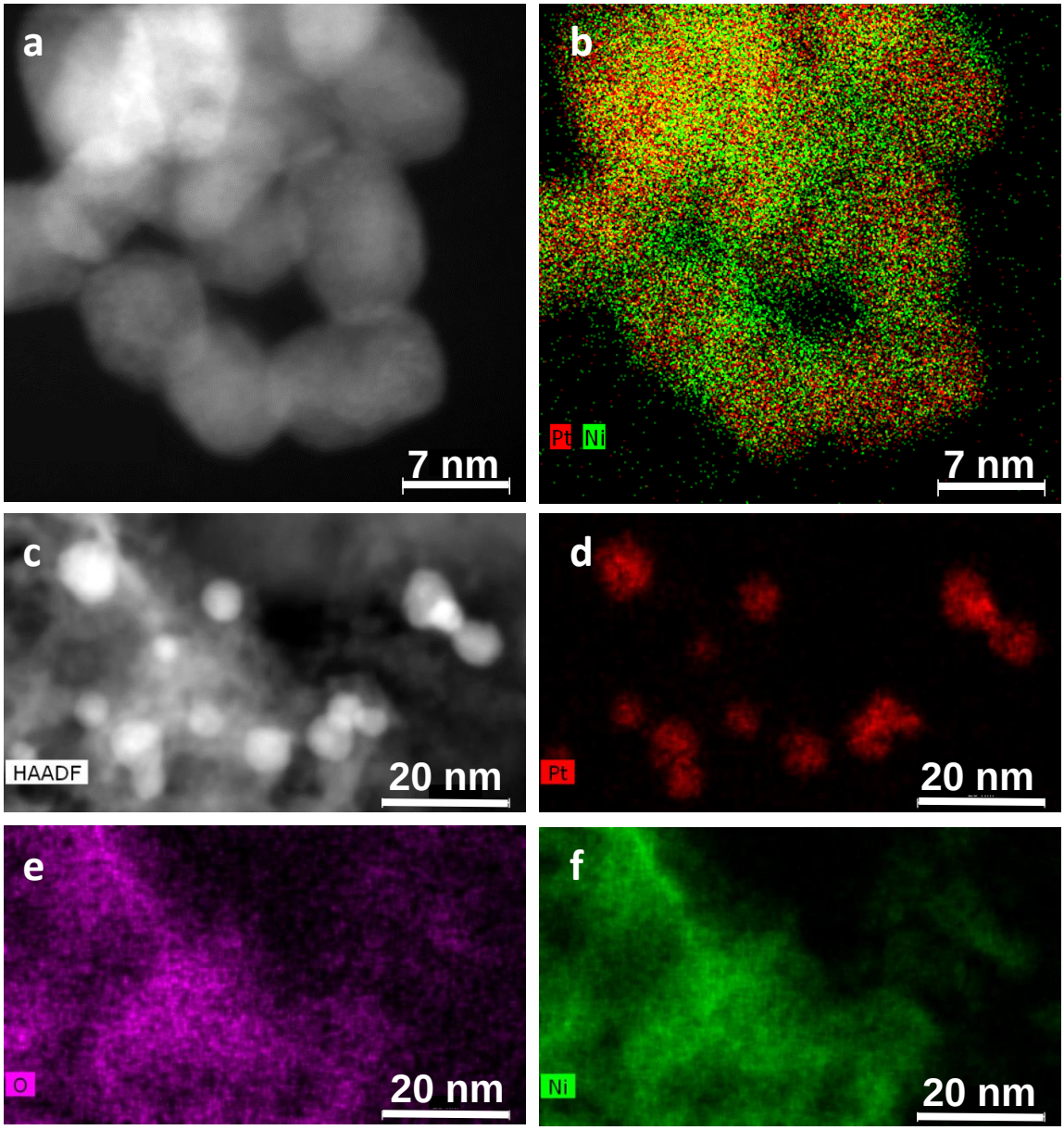


Figure 6.5. STEM & EDX images showing Pt_1Ni_3 stepwise samples. Pt is shown in red, Ni in green and O in purple. Figures a&b show an area of alloyed PtNi and figures c-f show an area of NiO_x coating the carbon support with Pt particles on the surface.

The areas indicated in Figure 6.5c-f show that Ni coating the carbon support is in an oxidic state, with Pt particles found at the surface of this structure. This indicates that there is a high dispersion of Ni across the silica walls, which is then dispersed across the carbon support on dissolution of the silica. The areas of alloy indicate that not all the Ni is reduced on the silica walls before the addition of Pt, with some Ni^{2+} species remaining stable in the channels. On addition of Pt and the

second reduction step, these Ni^{2+} species are now reduced due to the hydrogen spillover effect causing a resulting alloy-like morphology.

Figure 6.6 shows STEM and EDX mapping for the Pt_1Ni_3 co-reduction catalyst sample. The morphology is not easily distinguished from these maps, however it is thought that there are areas of mixed PtNi alloy as for the stepwise sample. There are also thought to be some areas of Pt surface enrichment, as can be seen from the overlay in Figure 6.6c.

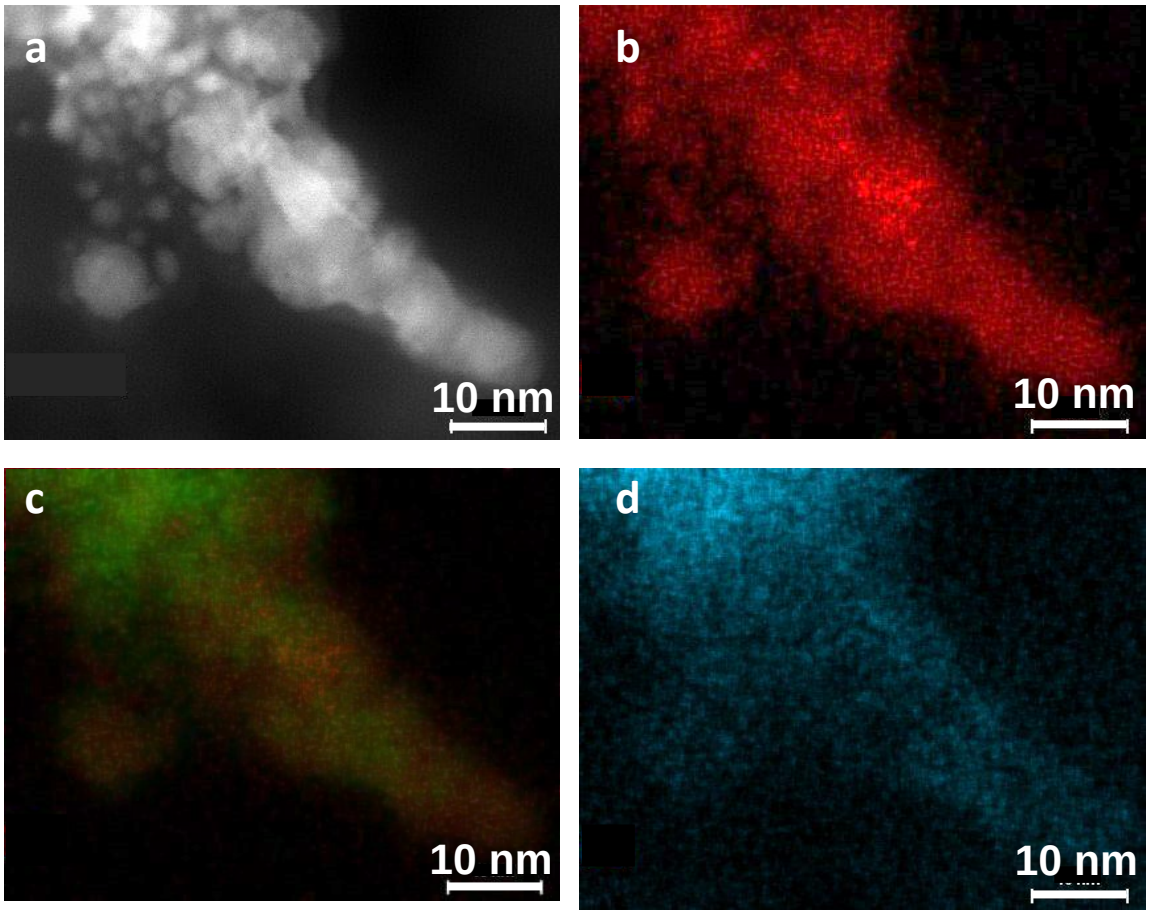


Figure 6.6. STEM/EDX images showing Pt_1Ni_3 co-reduction samples. Pt is shown in red, Ni in green and O in blue. a) HAADF STEM image, b-d) EDX maps of the same area, with Pt shown in red, Ni shown in green and O shown in blue. Note that c) shows an overlay of both Pt and Ni.

Atom probe tomography was also used to further investigate the bimetallic morphologies in these two samples. The Pt_1Ni_3 stepwise sample reconstruction is shown in Figure 6.7, with the Pt atoms shown in red and the Ni in green. It can be seen that the Pt forms particles which are supported on the Ni. The Ni and C peaks recorded in the mass spectrum are overlapping meaning deconvolution

is difficult, so the green areas could also include the C support. Around the Pt particles is a Ni-rich alloyed support, which is likely to be bound to the C support. It is also alloyed with the Pt which corroborates to the TEM analysis.

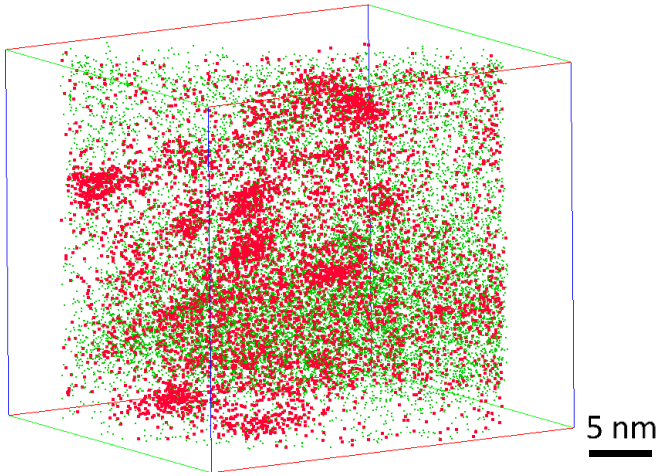


Figure 6.7. APT reconstruction of the Pt_1Ni_3/C stepwise sample showing Pt in red and Ni (or C) in green.

The Pt_1Ni_3 co-reduction sample was also studied and the reconstruction is shown in Figure 6.8, again showing Pt in red and Ni (or C) in green. There were two different phases found in this sample, with areas of the PtNi alloy shown in Figure 6.8a and areas of core-shell particles shown in Figures 6.8b&c. The reconstruction of the alloyed areas shows a range of Ni-rich alloying stoichiometries, with Pt content from 1-30%. However the alloy phases are thought to be supported on the C support, which is also detected as Ni, so the Pt:Ni ratio is thought to be higher than described by the figure. In addition to the alloyed phases described, Ni core - Pt shell type particles were also found. Pt deposition across the surface of the Ni particles was observed, but a complete Pt shell is not seen as the Ni surface below remained uncovered in places.

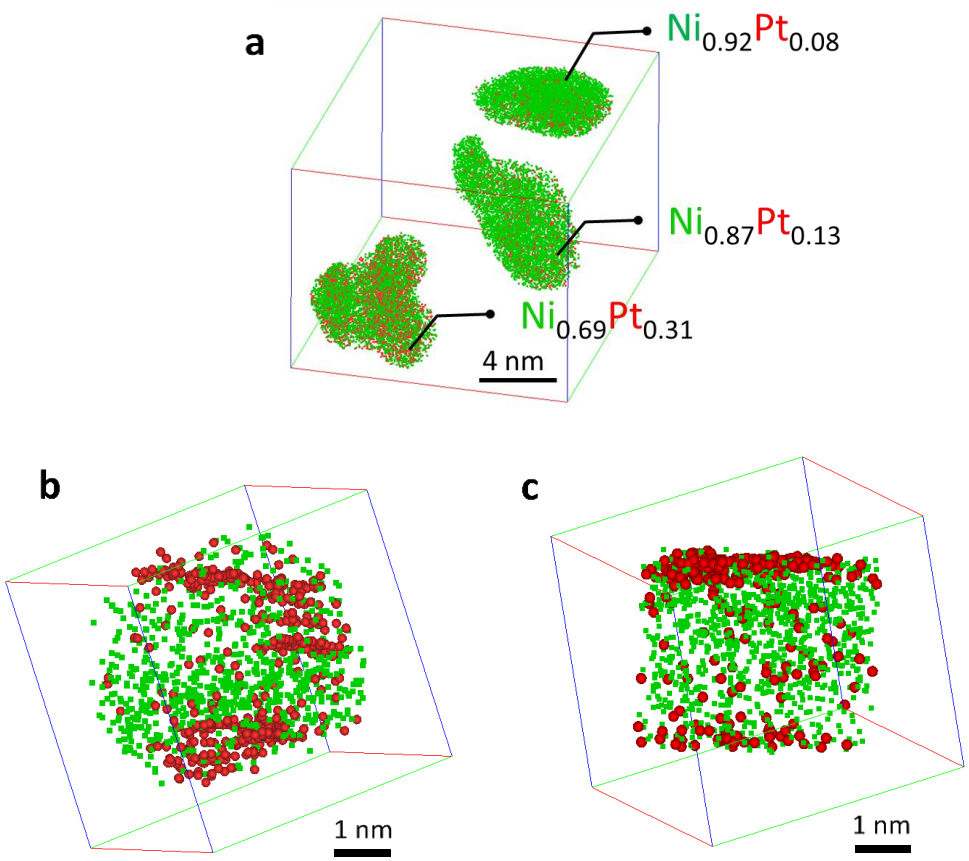


Figure 6.8. APT reconstruction of Pt_1Ni_3/C co-reduction sample showing Pt in red and Ni (or C) in green. a) shows areas of PtNi alloy and b&c) show areas of core-shell particles.

X-ray absorption was also used to understand the local structure of the materials, as shown by the EXAFS fitting spectra in Figure 6.9 and data in Table 6.1. The Pt_1Ni_3 co-reduction sample has a low Pt-Pt coordination number of 0.9 and a high Pt-Ni coordination number of 3.3, which indicate that the Pt is well dispersed around the Ni. The high Ni-Ni and Ni-O coordination numbers suggest that there are both Ni particle cores and NiO species. This supports the results shown from HR-TEM and APT, suggesting the presence of both Ni core - Pt shell particles and mixed alloys. The bulk Pt smallest radial distance is 2.775 Å, which is slightly larger than the radial distances shown in the Pt-Pt scattering path with EXAFS fitting. This indicates a small lattice contraction in this sample due to the introduction of a secondary metal.

Table 6.1. Table showing the EXAFS scattering paths and the corresponding distance, coordination number, Debye-Waller factor and energy difference for both Pt_1Ni_3 co-reduction and stepwise samples. Error is given in brackets as distance $x10^{-2}$ and Debye-Waller factor $x10^{-3}$.

Sample	Scattering path	Radial distance (Å)	Coordination Number	Debye-Waller Factor	Energy Difference (eV)
Co-reduction	Pt-C	2.02 (1)	1.7 ± 0.1	0.003 (1)	2.4
	Pt-Ni	2.56 (1)	3.3 ± 0.3	0.013 (1)	
	Pt-Pt	2.68 (1)	0.9 ± 0.1	0.007 (1)	
	Ni-O	2.06 (1)	5.9 ± 0.3	0.007 (1)	-2.7
	Ni-Ni	3.06 (1)	6.5 ± 0.4	0.014 (1)	
Stepwise	Pt-C	2.08 (1)	1.8 ± 0.2	0.015 (2)	3.6
	Pt-Ni	2.58 (1)	1.9 ± 0.2	0.009 (1)	
	Pt-Pt	2.68 (1)	5.0 ± 0.4	0.010 (1)	
	Ni-O	2.06 (1)	6.3 ± 0.1	0.008 (1)	-3.7
	Ni-Ni(1)	3.09 (1)	4.5 ± 0.4	0.014 (1)	
	Ni-Ni(2)	3.54 (3)	1.6 ± 0.4	0.015 (1)	

As with the Pt_1Ni_3 co-reduction samples, the stepwise sample also shows a decrease in Pt-Pt bond length which indicates an interaction between the Pt and Ni. However, the coordination numbers indicate a different morphology. The considerably higher Pt-Pt coordination number of 5.0 indicates that there are areas of Pt-rich species in this sample, rather than a thin deposition of Pt on Ni particles. The Ni-Ni coordination number remains high but is split over two Ni bond lengths which are both larger than expected, indicating the presence of Ni/NiO_x particles. The smaller Pt-Ni coordination number of 1.9 indicates that some Pt-Ni interaction remains, which could correspond to the Pt clusters sat on Ni/NiO particles.

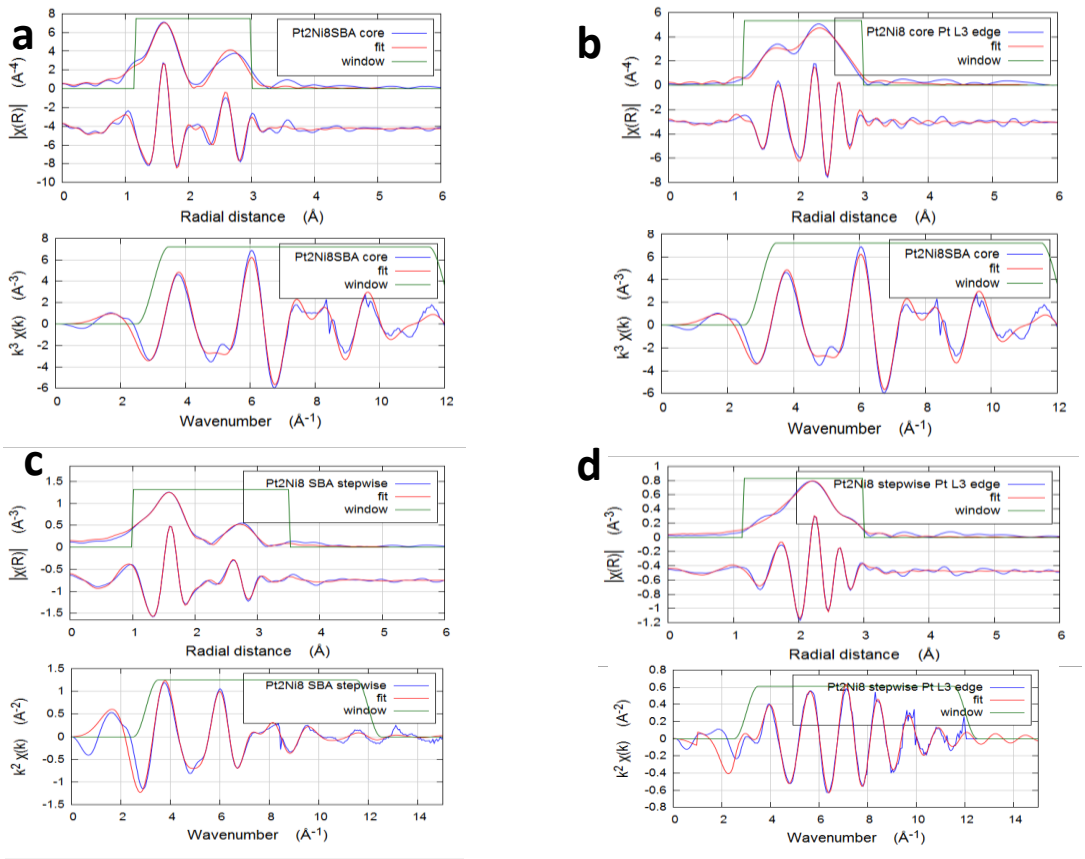


Figure 6.9. EXAFS fitting spectra for both Pt_1Ni_3 co-reduction and stepwise samples. a) Ni K-edge for co-reduction sample. b) Pt L_3-edge for co-reduction sample. c) Ni K-edge for stepwise sample. d) Pt L_3-edge for stepwise sample.

Both the APT and XAS results support the proposed morphology from HR-TEM and XRD. These all indicate that, although both samples contain some mixed alloy species, a large proportion of Pt in each sample is found in the differing morphologies. The Pt_1Ni_3 stepwise sample contains small Pt particles on NiO/C, whereas the co-reduction sample contains a Pt shell on a Ni core.

6.4.1.1 Pt_1Ni_3 reverse-stepwise synthesis

One final synthesis route was investigated by reversing the two-step synthesis. A Pt impregnation and reduction step was performed, followed by a Ni impregnation and reduction step. As with the other samples, the nanoparticles were then deposited on Vulcan C and the SBA-15 was removed. This reverse-stepwise sample was also characterised by XRD and TEM to understand the composition, crystallinity and particle size.

A typical XRD profile for the Pt_1Ni_3 reverse-stepwise catalyst is shown in Figure 6.10, with the observed profile shown in red, the fitted profile in blue and the reference stick patterns for Pt (yellow), Ni (green) and NiPt (purple) at the bottom. Five sharp peaks are seen at the reflections indicative of Pt, with the peaks assigned as the (111), (200), (220), (311) and (222) reflections. There are also two smaller peaks between 55 and 60 ° 2θ which are assigned to a small PtNi phase. It is thought that the other reflections expected from this phase are hidden beneath the much larger Pt peaks. The Pt lattice parameter was calculated to be 3.916 Å which is slightly smaller than the bulk Pt lattice parameter of 3.924 Å and indicates a small interaction when incorporating the Ni. This is supported by the small PtNi peaks observed, which indicate a small Ni interaction with the Pt nanoparticles. The Pt peaks are particularly sharp and the FWHM was used to calculate a crystallite diameter of 20.4 nm, which is significantly larger than the two previous samples investigated. This indicates that there is substantial agglomeration in the particles after the removal of SBA-15. The peaks from the small PtNi component can also be fitted and the crystallite diameter was calculated to be 7.2 nm. This small component could be due to deposits of Ni on the surface of the Pt particles.

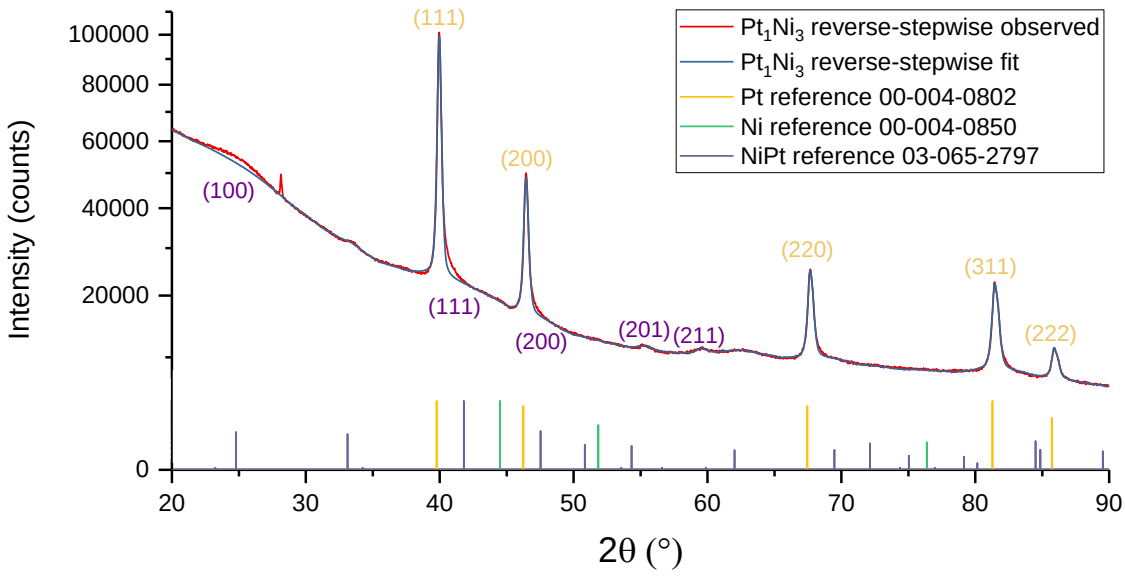


Figure 6.10. XRD profile for the Pt_1Ni_3 reverse-stepwise catalyst with the observed profile shown in red and the fitted profile in blue. Reference stick patterns are shown at the bottom for Pt (yellow), Ni (green) and NiPt alloy (purple).

TEM was also used to investigate the particle size and distribution across the support. Figure 6.11 shows a representative TEM image of the Pt_1Ni_3 reverse-stepwise sample, along with a size distribution histogram and clearly shows that these particles are much larger than the stepwise and co-reduction samples discussed above. The average diameter was calculated to be 15.5 nm (standard deviation of 10.6 nm) and the wide distribution is shown by the histogram. The average diameter calculated from TEM imaging was smaller than that from XRD, which is likely to be due to the larger error in measurement of TEM images and the avoidance of measuring aggregated particles. It can be seen that some large particles between 35 and 50 nm were measured which are likely to be present due to aggregation. In addition, the particles were often not spherical which skews the measurements and XRD calculations.

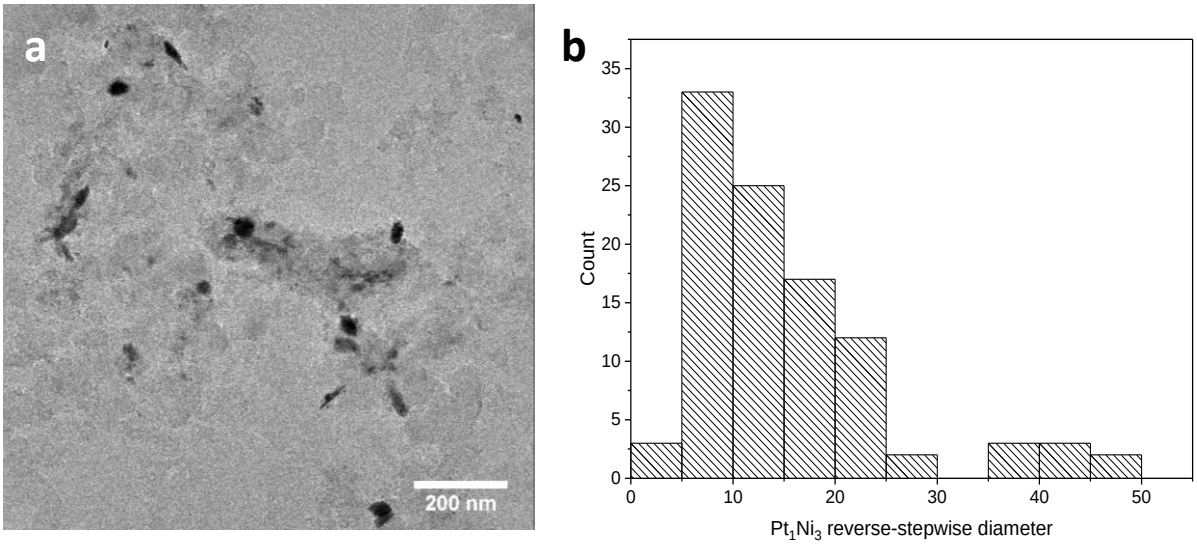


Figure 6.11. a) TEM image showing homogeneity across the support and b) size distribution histogram of the Pt_1Ni_3/C reverse-stepwise sample.

Both characterisation methods have shown that the Pt_1Ni_3 reverse-stepwise sample contains large Pt particles supported on the C, with some PtNi interaction. The large particle size leads to a low Pt surface area and so this sample is expected to show a much lower activity. Additionally, the very small component of PtNi indicates that only a small portion of the Pt is alloyed and as such the majority of the Pt will not benefit from this interaction.

6.4.2 Pt_1Ni_1 catalysts

A second series of catalysts was synthesised in order to investigate the effect of metal loading using a ratio of Pt_1Ni_1 instead of the previous Pt_1Ni_3 ratio. These samples were synthesised with the stepwise and co-reduction methods as discussed above. The reverse-stepwise method was not tested at this composition, as it was thought that changing the Pt content would not stop the large Pt crystallites produced with this method. TEM and XRD were used to analyse the composition, crystalline phases, particle size and dispersions of the catalysts.

A typical XRD profile for the Pt_1Ni_1 stepwise sample is shown in Figure 6.12, along with the reference patterns for Pt, Ni and the PtNi alloy shown at the bottom in yellow, green and purple respectively. Five distinct Pt peaks can be seen and assigned to the (111), (200), (220), (311) and (222) reflections. Additionally, the (111) and (200) peaks from a PtNi phase can be seen, and an additional broad (100) peak also occurs at 25 ° 2θ.

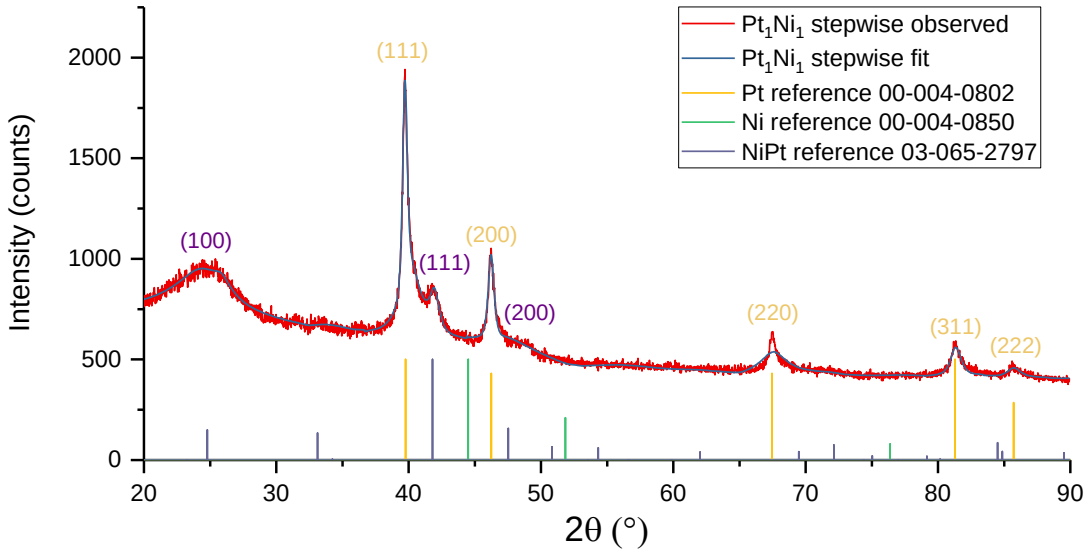


Figure 6.12. XRD profile for the Pt_1Ni_1 stepwise catalyst with the observed profile shown in red and the fitted profile in blue. Reference stick patterns are shown at the bottom for Pt (yellow), Ni (green) and NiPt alloy (purple).

The Pt lattice parameter was calculated to be 3.924 Å, which is the same as the bulk Pt lattice parameter indicating a limited Pt-Ni interaction in the majority of the Pt. The Pt (111), (200), (311)

and (222) peaks were fitted to find the FWHM and calculate the crystallite size. This gave a Pt crystallite diameter of 15.4 nm, which is larger than the analogous Pt_1Ni_3 stepwise sample due to the increased Pt content. It has been reported that the addition of a secondary metal reduces the agglomeration of PGMs,[22] which supports the evidence that under these Pt-rich conditions the agglomeration appears to be more enhanced. The PtNi (111) and (200) peaks were also fitted and a PtNi crystallite diameter was calculated to be 4.3 nm. The PtNi phase is thought to be at the surface of the Pt nanoparticles.

XRD of the Pt_1Ni_1 co-reduction sample, shown in Figure 6.13, also shows the clear Pt peaks assigned as the (111), (200), (220), (311) and (222) reflections. Additionally there are some small peaks visible for the PtNi phase, assigned as the broad (100) reflection and the (201) reflection. The other PtNi reflections are thought to be concealed beneath the Pt peaks.

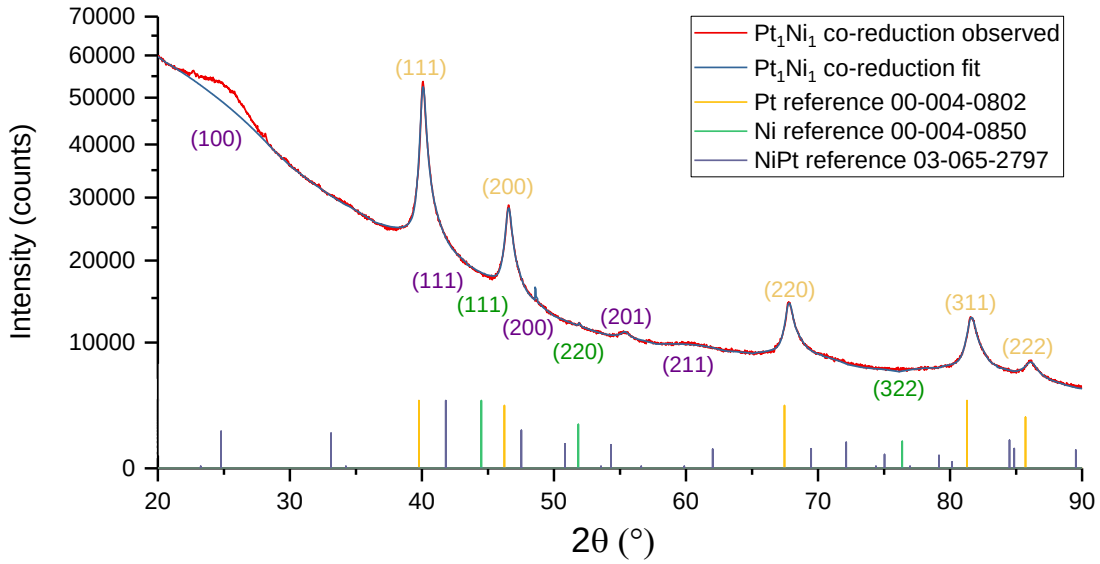


Figure 6.13. XRD profile for the Pt_1Ni_1 co-reduction catalyst with the observed profile shown in red and the fitted profile in blue. Reference stick patterns are shown at the bottom for Pt (yellow), Ni (green) and NiPt alloy (purple).

The Pt lattice parameter is calculated to be 3.910 Å, which is slightly smaller than the bulk Pt lattice parameter of 3.924 Å indicating that there is a slight lattice contraction in the Pt species on alloying with Ni. The Pt (111), (200), (220), (311) and (222) reflections were fitted and the FWHM

was used to calculate a crystallite diameter of 13.1 nm. As with the Pt_1Ni_1 stepwise sample, this Pt_1Ni_1 co-reduction sample is more aggregated than its Pt_1Ni_3 counterpart. The (201) reflection from the PtNi phase was also fitted and was used to calculate an average crystallite diameter of 9.7 nm.

In addition to XRD, TEM was also used to monitor particle size as well as dispersion across the support. Figure 6.14 shows a representative TEM image from both the Pt_1Ni_1/C samples, with the stepwise sample shown in Figure 6.13a and the co-reduction sample shown in Figure 6.13b. Both samples show well distributed particles across the support, although the co-reduction sample shows some very large, aggregated particles.

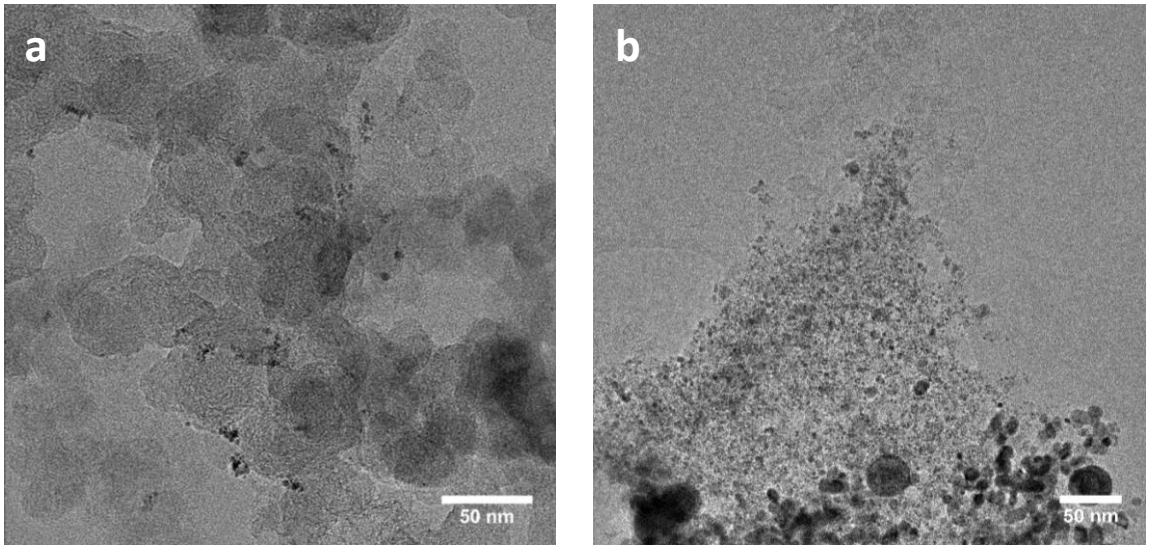


Figure 6.14. TEM images showing size distribution and homogeneity across the support of Pt_1Ni_1/C both a) stepwise and b) co-reduction samples.

The mean particle diameter was found to be 3.6 nm (standard deviation of 2.4 nm) for the stepwise sample and 6.3 nm (standard deviation of 6.2 nm) for the co-reduction sample. Both mean particle sizes are considerably smaller than the crystallite sizes found from XRD, which suggests that there are larger areas of aggregation in other areas of the sample not seen in TEM. The size distribution histogram shown in Figure 6.15 clearly shows that the co-reduction sample (black) has a greater variance than the stepwise sample (red). Particles with a diameter larger than 8 nm are present in

the co-reduction sample, indicating that severe aggregation occurs after removal of the SBA-15 channels which had been restricting the particle size to below 8 nm. This co-reduction sample may be more susceptible to aggregation due to the smaller PtNi phase, as the introduction of a secondary metal is expected to decrease the aggregation[22].

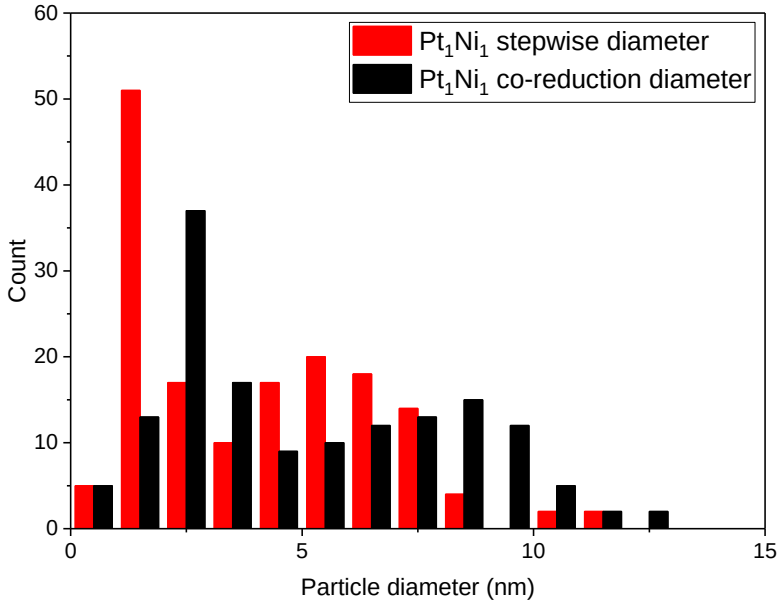


Figure 6.15. Size distribution histogram showing Pt_1Ni_1 both stepwise (red) and co-reduction (black). Samples size of 160 particles for both samples. Note that 6 outliers were observed for the co-reduction sample with diameters of 15-40 nm.

Both samples show a bimodal size distribution, with maxima at 2 nm and 6 nm for the stepwise sample and at 3 nm and 8 nm for the co-reduction sample. This could indicate that there are two particle phases present, with the smaller one likely to be the PtNi phase and the larger the Pt phase.

6.5 SBA-15 wall effect

The characterisations above have highlighted how changes in metal composition and synthesis route can affect the formation of nanoparticles inside the SBA-15 channels. This indicates that the channels of the SBA-15 not only restrict the particle growth to the channel width, but also have a structural directing impact. The PtZn system was extensively studied in Chapter 5 and it was suggested that the Zn had a strong interaction with the SBA-15 walls, which led to the high

dispersion of Zn atoms across the support. This chapter has explored the effect of the interaction between the walls and the Pt and the Ni species under various compositions and synthesis methods. The Ni appears to be highly dispersed across the SBA-15 walls in a similar manner to the Zn sample, whereas Pt favours the formation of particles in the channels.

TEM can be used after the first Ni reduction step in the stepwise samples, in order to assess the particle growth at this stage in the synthesis. Figure 6.16 shows a TEM image of the Ni(SBA-15) sample prior to Pt impregnation. The channels appear to contain no large particles, with a limited number of very small particles (< 2 nm) visible. The Ni is expected to interact strongly with the silica walls and therefore form a coating on the channel walls rather than aggregate to form large Ni particles in the channels.

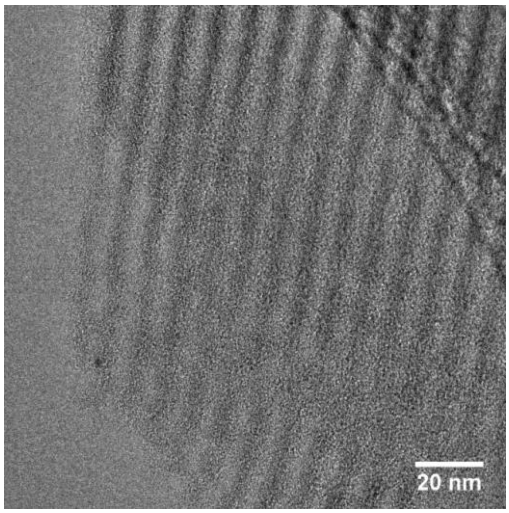


Figure 6.16. TEM image showing the Ni(SBA-15) sample prior to impregnation of Pt. SBA-15 channels do not appear to contain large Ni particles.

It is thought that after Ni impregnation but before reduction, some Ni species interact with the surface of the SBA-15 walls. However, at higher loadings, the wall surface becomes saturated and some Ni remains unsupported in the channels. Temperature programmed reduction (TPR) was used to analyse the reduction temperatures of the Ni species impregnated in the SBA-15. Two metal loadings were tested, 10 wt.% Ni and 2 wt.% Ni, both of which are similar to those used in the catalyst samples. The TPR profile is shown in Figure 6.17, with the 10 wt.% Ni in red and the

2 wt.% Ni in blue. In both samples, a reduction peak at 400 °C can be seen. In addition to this peak, the 10 wt.% Ni sample has an additional reduction peak at 500 °C, which does not appear in the 2 wt.% sample. This indicates that there are two Ni precursor species in the 10 wt.% sample, while only the one which is most susceptible to reduction is present in the 2 wt.% sample. This supports the theory that Ni ions interact with the SBA-15 walls on impregnation, causing high dispersion across the interior walls of the support. On addition of 10 wt.% Ni, the walls become saturated so some Ni remains unsupported in the channels. It is thought that this unsupported Ni is more resistant to reduction. The typical reduction temperature used in the synthesis was 400 °C, which means that the Ni on the walls is reduced while the Ni in the channels is not.

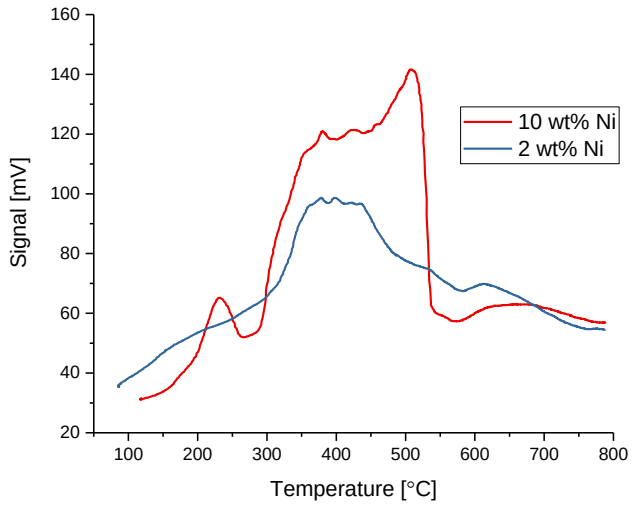


Figure 6.17. TPR profile of 10 wt.% Ni(SBA-15) in red and 2 wt.% Ni(SBA-15) in blue.

On addition of Pt to the system, the hydrogen spillover effect means that reduction can occur at a lower temperature and all the Ni species will be reduced at 400 °C. A further TPR was performed to confirm this using a sample containing 10 wt.% PtNi and the profile is shown in Figure 6.18. Two reduction peaks can be seen at 200 °C and 250 °C, which indicates that both of the Ni reduction peaks are shifted to lower reduction temperatures when Pt is present.

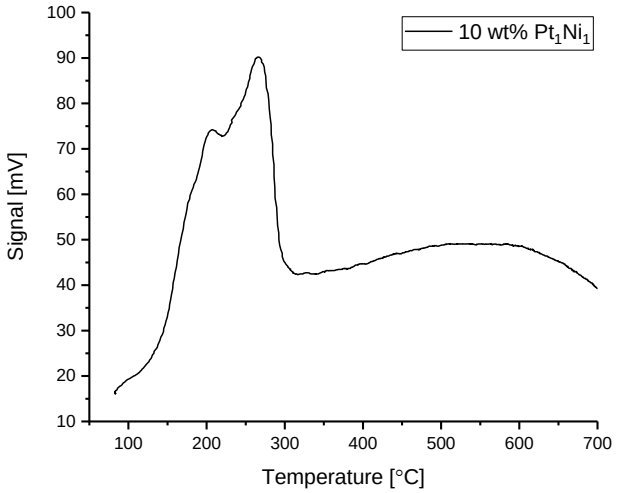


Figure 6.18. TPR profile showing the reduction of 10 wt.% PtNi(SBA-15).

TPR has shown that the Ni binds to the silica walls as it has a strong interaction with the walls, leading to highly dispersed Ni across the walls. The Pt preferentially forms nanoparticles inside the channels as it has a weak interaction with the walls. This weak interaction allows resistance to aggregation but is not so strong that it leads to high dispersion across the support. It is thought that the surface silanol groups may chelate to the Ni^{2+} more preferentially than the Pt^{2+} due to the smaller ionic radius of Ni^{2+}.[23]

The differences in structure of the three Pt_1Ni_3/C and two Pt_1Ni_1/C samples show that both the metal composition and synthesis route affect the structural directing impact which the walls have on the nanoparticle formation. The proposed synthesis mechanisms of the Pt_1Ni_3/C samples are described in the schematic in Figure 6.19. In the stepwise sample, where Ni is deposited first, a thin and well dispersed Ni layer is formed across the surface of the SBA-15 walls, while some Ni^{2+} ions remain in the channels. On impregnation and reduction of Pt, the hydrogen spillover effect leads to the reduction of the remaining Ni^{2+} ions in the channels, resulting in an area of high contact between the Ni and Pt. The fact that this sample is predominantly formed of Pt particles with Ni

deposits on the surface indicates that the Pt reduces to form individual particles, inducing the reduction of remaining Ni^{2+} ions at its surface.

However the co-reduction sample has well mixed precursor ions prior to reduction, which leads to the simultaneous reduction of the metals. In the Pt_1Ni_3 co-reduction sample, the high Ni composition leads to the thermodynamically favourable Ni core - Pt shell morphology as a result of the lower surface energy of Pt. The Pt_1Ni_3 reverse-stepwise sample shows large Pt particles with a small quantity of Pt-Ni interaction. It is thought that the initial Pt reduction forms large Pt particles which are then coated with Ni during the second reduction step.

The Pt_1Ni_1 samples have been less extensively characterised due to the higher Pt:Ni ratio, however postulations on the structures and mechanisms are presented. The stepwise Pt_1Ni_1 sample is thought to behave in a similar manner to its stepwise Pt_1Ni_3 counterpart. It proceeds via the deposition of a Ni layer, followed by Pt particle deposition and the remaining Ni^{2+} reduction. The Pt_1Ni_1 co-reduction sample appears to behave differently to its Pt_1Ni_3 counterpart. In this sample the concentration of Pt is too high to form the Ni core - Pt shell as before. The high Pt concentration instead leads to the formation of Pt particles which have Ni deposits on the surface. This study confirms that the SBA-15 wall effect can be used to tailor the morphology of bimetallic metal nanoparticles. However, it also highlights the dependence of the resultant particle morphology on both composition and synthesis route.

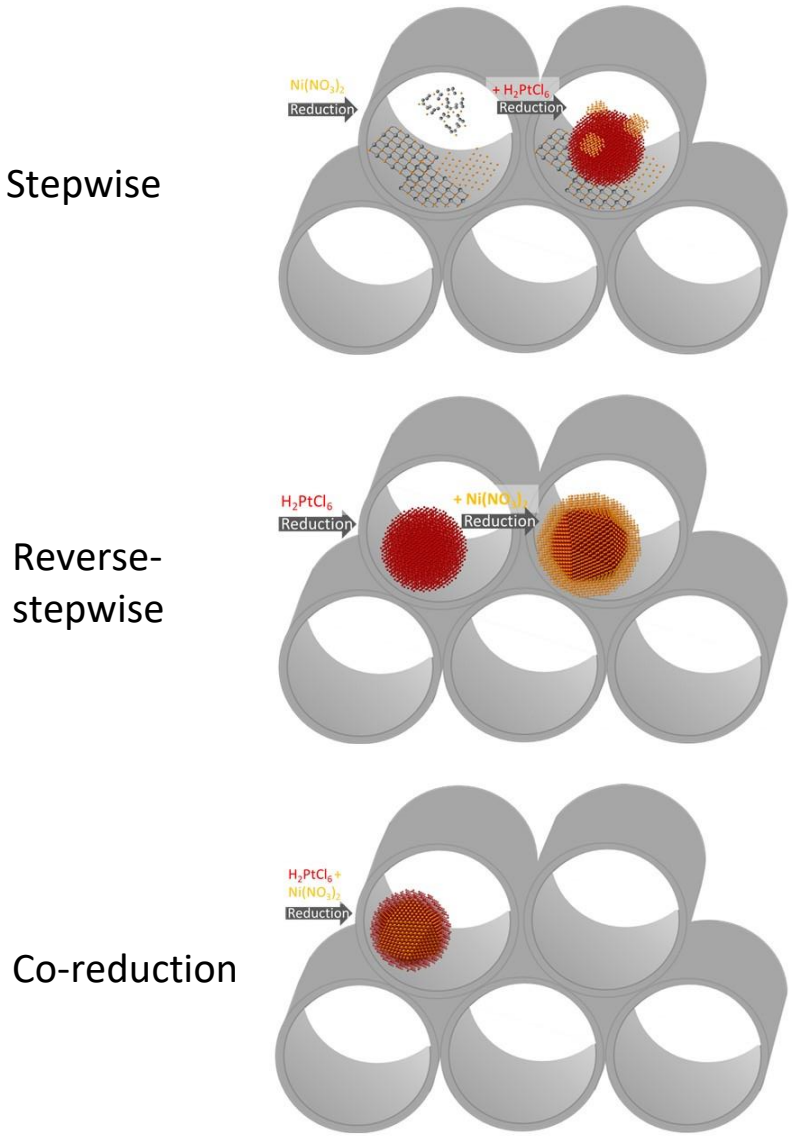


Figure 6.19. Schematic proposal of the synthesis mechanism when utilising the SBA-15 wall effect and varying the synthesis route.

6.6 Oxygen reduction reaction

The efficiencies of the synthesised catalysts were tested using the oxygen reduction reaction (ORR), which has previously been discussed as a reaction in need of catalyst development. The reaction is typically performed at the cathode of a fuel cell, although the slow commercial Pt catalyst is one of the issues causing fuel cells to be economically inviable. The binding of O and OH to the surface of Pt is stronger than the predicted optimum bond strength and so a decrease in these bonding strengths will improve the catalytic activity.[15]

The catalytic activity was measured by performing rotating disk electrode (RDE) experiments as described in Chapter 3. In summary, cyclic voltammetry (CV) measurements under O_2 and Ar environments were used to determine the Pt electrochemical surface area. This was followed by linear sweep voltammetry (LSV) measurements with a scan rate of 5 mVs^{-1} to measure the activities of the catalysts. All experimental measurements were performed in collaboration with Fang Niu and Simantini Nayak (Vincent Group, Oxford).

The metallic composition of each catalyst was determined with inductively coupled plasma mass spectrometry (ICP-MS) at the Max-Planck-Institut für Eisenforschung. Knowing the exact fraction of Pt in each sample is necessary to accurately calculate the Pt mass activities. The atomic compositions are shown in Table 6.2 and it can be seen that the experimental results match the calculated values of stoichiometry for each catalyst, as the results are within 2 at.% error. The only exception to this is the reverse-stepwise catalyst which has a lower Pt composition than expected. This is thought to be due to experimental error leading to partial loss of the Pt during the first reduction step.

Table 6.2. Table showing ICP results for each catalyst compared to calculated stoichiometries.

Sample	Experimental values		Calculated values	
	at.% Pt	**at.% Ni**	**at.% Pt**	**at.% Ni**
Pt_1Ni_3 stepwise	25.60	74.40	25	75
Pt_1Ni_3 co-reduction	22.98	77.03	25	75
Pt_1Ni_3 reverse-stepwise	18.97	81.04	25	75
Pt_1Ni_1 stepwise	48.78	51.22	50	50

Initial CV graphs were collected in order to calculate the electrochemical surface area of Pt in each sample. Figure 6.20 shows the CV plots for each synthesised sample as well as the commercial Pt

catalyst. The H desorption peaks were fitted to calculate of the surface area of Pt available for electrochemical reactions.

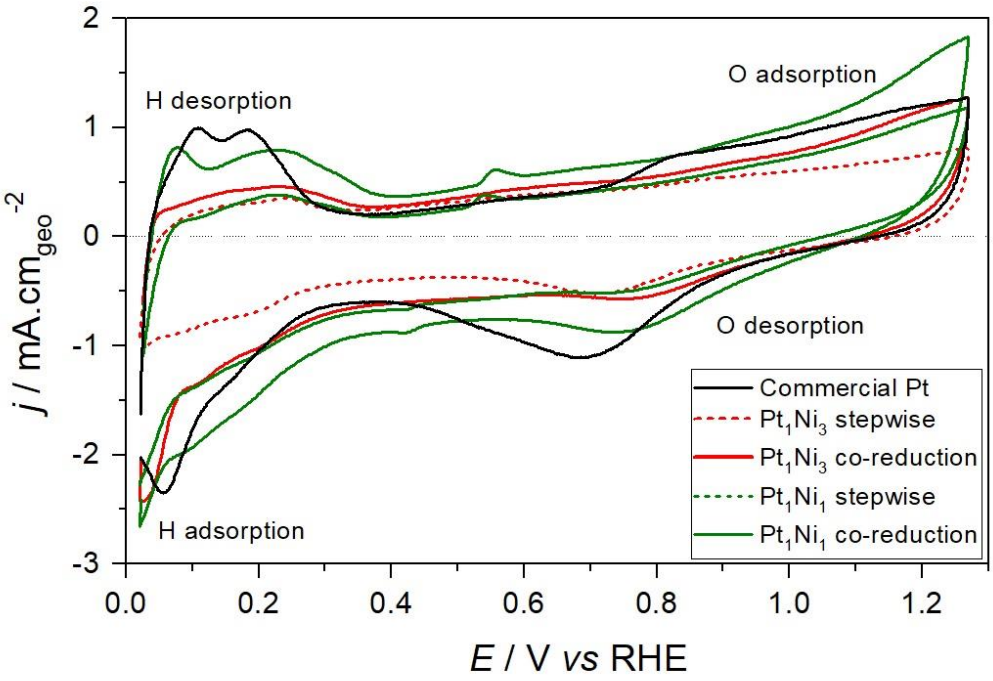


Figure 6.20. Cyclic voltammograms of the four catalyst species along with the commercial Pt reference sample. Electrochemical surface area was calculated from the area of the H desorption peak.

The results of surface area measurements are shown in Table 6.3 below, as well as the results of the calculations into the mass of Pt on the electrode which are calculated according to the ICP results. Exact composition data was not obtained for the Pt_1Ni_1 co-reduction, so the mass was calculated using the analogous stepwise sample data and is shown in italic.

Table 6.3. Catalytic mass and electrochemical surface area of each sample. Pt_1Ni_1 co-reduction mass value is estimated from the ICP results of the Pt_1Ni_1 stepwise sample and so is shown in italic in this table.

	Pt mass (µg cm^{-2})	**Pt electrode surface area (cm^2)**
Pt_1Ni_3 stepwise	21	1.25
Pt_1Ni_3 co-reduction	19.9	2.01
Pt_1Ni_1 stepwise	30.4	1.54
Pt_1Ni_1 co-reduction	*30.4*	2.45
Commercial Pt	40	2.37

The catalytic activity was measured by performing Linear Sweep Voltammetry (LSV) on each catalyst. Figure 6.21 shows the LSV plots for the five synthesised catalysts studied as well as the commercial catalyst. These LSV plots can give an initial indication of the catalytic activity, which is higher for catalysts with a higher half wave potential, defined as the potential at which the current is reduced by half. However, this data is not fully reliable as it is not normalised for Pt mass or electrochemical surface area. It can be seen from these voltammograms that the Pt_1Ni_3 reverse-stepwise, shown in grey, has very poor activity and so no mass or surface area measurements were analysed for this sample.

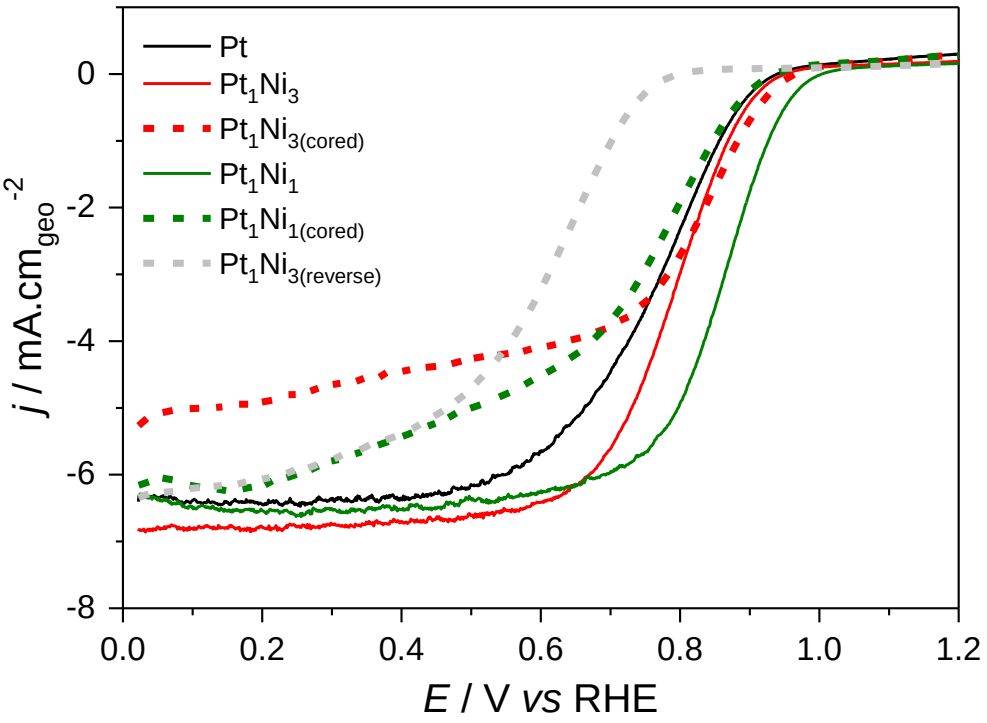


Figure 6.21. LSV plots of the whole series of catalysts as well as the Pt commercial catalyst.

In order to compare the catalytic ability, the mass activity or specific activity must be calculated. These are the activity measurements normalised to either the amount of Pt in the sample or the surface area respectively using Table 6.3. Each synthesised catalyst sample has a lower Pt mass than the commercial catalyst and the Pt_1Ni_3 and Pt_1Ni_1 co-reduction samples have a higher Pt surface area. This could lead to more active and cost efficient catalysts.

Throughout this work, the activities selected to compare the catalysts were taken at a potential of 0.9 V to give a representative analysis of the data. Figure 6.22 shows two bar graphs, displaying mass activity and specific activity. There is a general trend for mass activity that Pt_1Ni_1 stepwise > Pt_1Ni_3 co-reduction > Pt_1Ni_3 stepwise > Pt_1Ni_1 co-reduction > commercial Pt. This is generally replicated as expected in the specific activity bar graph, however the Pt_1Ni_3 stepwise catalyst has a higher specific activity than expected. This is due to the low surface area of this sample, which means there is a higher activity per active site.

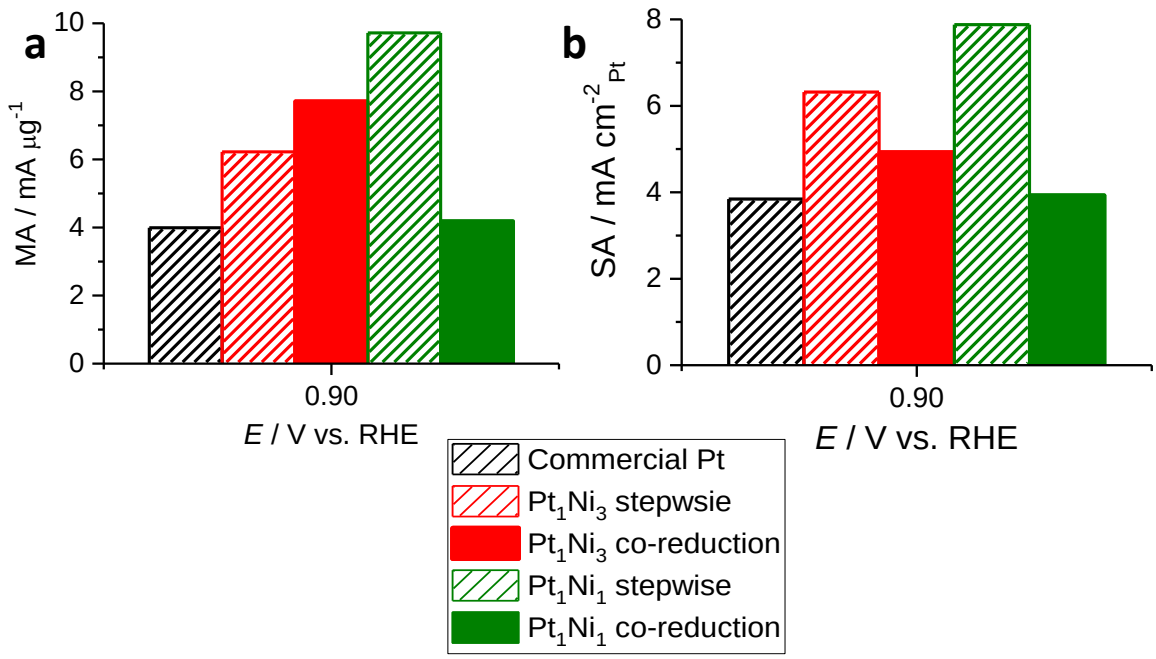


Figure 6.22. a) Mass activity and b) Surface area activity bar charts for four synthesised catalyst samples and the commercial Pt reference catalyst.

The trend of activity appears to depend both on the stoichiometry and the sample preparation order. The Pt_1Ni_1 composition performs best when produced following the stepwise synthesis route, whereas the Pt_3Ni_1 composition performs best following the co-reduction synthesis route. This is consistent with the changes in structure as a result of those factors as discussed in Section 6.4. The Pt_1Ni_1 stepwise and Pt_1Ni_3 co-reduction samples have the highest activities for ORR at 2-2.5 times the activity of the commercial catalyst. These samples both contain a high Pt surface area, but also a high degree of Pt-Ni contact. The Pt_1Ni_1 stepwise sample is thought to form Pt particles with some Ni clusters decorating the surface and the Pt_1Ni_3 co-reduction has shown Ni core - Pt shell formation as well as a mixed alloy phase.

The Pt_1Ni_3 stepwise sample showed a higher specific activity than the mass activity, which indicates a low surface area of Pt in this sample. This can be associated to the formation of Pt particles on the NiO coated C support, which envelops the Pt particles. This causes a lower Pt surface area and a large proportion of Pt in the particle core. The Pt_1Ni_1 co-reduction and Pt_1Ni_3 reverse-stepwise samples show low activity, similar to the commercial Pt catalyst, which is

thought to be due to the formation of larger Pt particles with no significant Pt-Ni interface. This means that there is a large proportion of inactive core Pt, reducing cost efficiency. There is also no electronic promotion from the Ni, resulting in stronger reagent binding and inferior activity.

6.7 Conclusion

The work in this chapter has been focussed on the further investigation and utilisation of the SBA-15 wall effect. The results of Chapter 5 demonstrated a strong interaction between Zn and the silica walls, which led to a structural directing effect and caused an unconventional Pt-Zn morphology. The aims of this chapter were to investigate the implications of the wall effect on the PtNi system and to manipulate these catalysts in order to optimise the ORR reaction.

Two different compositions of PtNi were synthesised, Pt_1Ni_1 and Pt_3Ni_1, under three different preparation methods: stepwise, co-reduction and reverse-stepwise. All five samples resulted in different catalyst morphologies, identified through techniques including XRD, HR-TEM and APT. The differences in particle size and Pt lattice parameter are summarised in Table 6.4.

Table 6.4. Summary table of sample particle sizes and lattice parameters.

Sample	**Particle size (nm)**		**Lattice parameter (Å)**
	XRD	TEM	XRD
Pt_1Ni_3 stepwise	9.1	5.1	3.896
Pt_1Ni_3 co-reduction	6.8	2.7	3.902
Pt_1Ni_3 reverse-stepwise	20.4	15.5	3.916
Pt_1Ni_1 stepwise	15.4	3.6	3.924
Pt_1Ni_1 co-reduction	13.1	6.3	3.910

The higher Pt to Ni ratio of Pt_3Ni_1 led to larger Pt particles, with the stepwise method creating a high Ni-Pt contact but the co-reduction method showing a poor Ni-Pt contact. In the stepwise

sample it is thought that the strong Ni-silica interaction leads to highly dispersed Ni on the channel walls before Pt is added. Following the addition of Pt and the second reduction step, there is close contact between the Ni and the Pt. In the co-reduction sample, however, the high Pt concentration leads to large Pt particles which have limited contact with the Ni particles at their surface.

The Pt_1Ni_3 stepwise sample showed similar behaviour to the Pt_1Ni_1 co-reduction sample, with Pt particles supported on a NiO/C support. The Pt_1Ni_3 co-reduction sample showed Ni core - Pt shell species, along with some areas of mixed alloy. This is thought to be due to the simultaneous reduction of Pt and Ni, resulting from the hydrogen spillover effect which aids Ni^{2+} reduction. Where the Ni concentration is high enough, it forms a core particle and the Pt coats its surface. In some regions, the reduction is too fast, or the composition does not allow the formation of the thermodynamically favoured Ni core - Pt shell morphology, resulting in the mixed alloy species. The Pt_1Ni_3 reverse-stepwise catalyst formed large Pt particles with little interaction with Ni and poor catalytic activity.

The interaction of Ni with the silica walls is dependent on the concentration of Ni in the system and on the other species present. In a pure Ni sample TPR shows that two different Ni species are present in the channels prior to reduction, one of which is supported in the SBA-15 walls and the other remains in the channels. These species have different reduction potentials, meaning the species in the channels reduce at a higher temperature, which is only accessible when Pt is present. Through allowing the Ni species to be reduced at two different temperatures, a greater variation in Pt-Ni contact was possible.

The catalysts were tested using the ORR reaction, with the aim of producing a catalyst with a lower Pt content and higher activity, in order to improve the cost efficiency. All the stepwise and co-reduction catalysts out-performed the commercial Pt catalyst, whereas the reverse-stepwise catalyst performed worse due to large Pt particles with no Ni-Pt contact. The Pt_1Ni_1 co-reduction

catalyst did not perform significantly better than the commercial Pt catalyst, also due to the large Pt particles with limited Ni-Pt contact.

The Pt_1Ni_1 stepwise catalyst consistently performed the best, at 2.5 times the activity of the commercial Pt reference catalyst. This is thought to be due to the small Pt nanoparticles and the high Pt-Ni contact. Clear analysis of this morphology is unknown and further characterisation of this system is required in the future. Whilst this catalyst performs the best, the Pt content remains high and so more investigation was performed into the Pt_1Ni_3 systems in order to improve the cost efficiency.

The Pt_1Ni_3 stepwise and co-reduction catalysts performed similarly. The co-reduction sample showed a higher mass activity, whereas the stepwise sample showed a higher specific activity which is expected to be due to its lower electrochemical surface area. The stepwise sample showed higher quantities of mixed alloy and Pt particles supported by a NiO/C composite. This indicates that the Pt-NiO interface is useful for enhancing the Pt activity, although the loss in Pt surface area leads to reduced activity.

The Pt_1Ni_3 co-reduction sample showed both Ni core - Pt shell and mixed alloy species. The core-shell species allowed a high Pt-Ni contact whilst maintaining the high Pt surface area from the Pt shell. The mixed alloy is present in both the stepwise and co-reduction samples, so the differences are attributed to the core-shell species in the co-reduction sample and the Pt particles supported on the NiO/C in the stepwise sample.

Overall this series of catalysts shows enhanced activity in comparison to the commercial Pt catalyst. However further improvements could be made through separation of the mixed alloy from the core-shell and Pt/NiO/C composites and through identification of the most active phase. The use of the SBA-15 wall effect to tailor the catalyst morphology has been shown to be effective,

although further synthetic modification is needed to restrict the various forms of bimetallic nanoparticles produced in one sample.

6.8 References

1 J. Stacy, Y. N. Regmi, B. Leonard and M. Fan, *Renew. Sustain. Energy Rev.*, 2017, **69**, 401–414.

2 M. Shao, Q. Chang, J.-P. Dodelet and R. Chenitz, *Chem. Rev.*, 2016, **116**, 3594–3657.

3 J. Greeley, I. E. L. Stephens, A. S. Bondarenko, T. P. Johansson, H. A. Hansen, T. F. Jaramillo, J. Rossmeisl, I. Chorkendorff and J. K. Nørskov, *Nat. Chem.*, 2009, **1**, 552.

4 R. Yang, J. Leisch, P. Strasser and M. F. Toney, *Chem. Mater.*, 2010, **22**, 4712–4720.

5 C. Cui, L. Gan, H.-H. Li, S.-H. Yu, M. Heggen and P. Strasser, *Nano Lett.*, 2012, **12**, 5885–5889.

6 C. Zhang, X. Shen, Y. Pan and Z. Peng, *Front. Energy*, 2017, **11**, 268–285.

7 C. Song and J. Zhang, *PEM Fuel Cell Electrocatalysts and Catalyst Layers: Fundamentals and Applications*, Springer London, London, 2008.

8 J. K. Nørskov, J. Rossmeisl, A. Logadottir, L. Lindqvist, J. R. Kitchin, T. Bligaard and H. Jónsson, *J. Phys. Chem. B*, 2004, **108**, 17886–17892.

9 K. Jiang, H.-X. Zhang, S. Zou and W.-B. Cai, *Phys. Chem. Chem. Phys.*, 2014, **16**, 20360–20376.

10 S. Koh and P. Strasser, *J. Am. Chem. Soc.*, 2007, **129**, 12624–12625.

11 V. R. Stamenkovic, B. Fowler, B. S. Mun, G. Wang, P. N. Ross, C. A. Lucas and N. M. Marković, *Science*, 2007, **315**, 493 LP-497.

12 N. S. Porter, H. Wu, Z. Quan and J. Fang, *Acc. Chem. Res.*, 2013, **46**, 1867–1877.

13 S.-I. Choi, S. Xie, M. Shao, J. H. Odell, N. Lu, H.-C. Peng, L. Protsailo, S. Guerrero, J. Park, X. Xia, J. Wang, M. J. Kim and Y. Xia, *Nano Lett.*, 2013, **13**, 3420–3425.

14 S. P. Lin, K. W. Wang, C. W. Liu, H. S. Chen and J. H. Wang, *J. Phys. Chem. C*, 2015, **119**, 15224–15231.

15 B. Corona, M. Howard, L. Zhang and G. Henkelman, *J. Chem. Phys.*, 2016, **145**, 244708.

16 P. Strasser, S. Koh, T. Anniyev, J. Greeley, K. More, C. Yu, Z. Liu, S. Kaya, D. Nordlund, H. Ogasawara, M. F. Toney and A. Nilsson, *Nat. Chem.*, 2010, **2**, 454–460.

17 D. Wang, H. L. Xin, R. Hovden, H. Wang, Y. Yu, D. A. Muller, F. J. DiSalvo and H. D. Abruña, *Nat. Mater.*, 2012, **12**, 81.

18 J. Zhang, *PEM fuel cell electrocatalysts and catalyst layers : fundamentals and applications*, Springer, London, 2008.

19 S. C. Roy, A. W. Harding, A. E. Russell and K. M. Thomas, *J. Electrochem. Soc.* , 1997, **144**, 2323–2328.

20 E. Auer, A. Freund, J. Pietsch and T. Tacke, *Appl. Catal. A Gen.*, 1998, **173**, 259–271.

21 C. Wang, D. van der Vliet, K.-C. Chang, H. You, D. Strmcnik, J. A. Schlueter, N. M. Markovic and V. R. Stamenkovic, *J. Phys. Chem. C*, 2009, **113**, 19365–19368.

22 J. Czaplinska, I. Sobczak and M. Ziolek, *J. Phys. Chem. C*, 2014, **118**, 12796–12810.

23 Weast, *CRC handbook of chemistry and physics*, Cleveland, Ohio : CRC Press, Cleveland, Ohio, 52nd edn., 1972.

Chapter 7

Conclusions and Future Perspectives

7.1 Conclusions 177
7.2 Future Perspectives 178

7.1 Conclusions

Throughout this thesis the main aims of the research have been to synthesise bimetallic nanoparticles of defined morphology, in order to improve both cost efficiency and catalyst activity. The particle growth was controlled through the use of polymer or mesoporous supports and systematic metal deposition was employed to synthesize particles of directed morphology. Each series of catalysts was well characterised in order to determine the particle morphology and was tested with the formic acid decomposition reaction in order to understand the changes in the active surface sites.

The first series of materials, synthesized through polymer stabilisation, showed small amounts of aggregation of the seed particles, the extent of which was dependent on the secondary metal. In addition, although Pt deposition was successful, the surface was not a smooth layer but rather the Pt formed small clusters on the surfaces. The formic acid decomposition reaction showed that the addition of a secondary metal improved the activity of the catalyst because the secondary metal donates electron density towards the Pt, causing an increased activity. The PtNi species shows an enhanced activity which is thought to be due to the geometric effect from the Pt lattice contraction discussed in Chapter 1. These activity enhancements indicated that by improving the interface a further increase in activity may be seen.

Particle aggregation and poor metal-metal interfaces were the biggest downfalls to the polymer supported synthesis method and so the second series of catalysts was synthesized inside the silica channels of the well-structured SBA-15. This led to finer control of particle size and an investigation into the effect of the silica wall on the particle morphology. Particle size was successfully controlled through impregnation at low concentrations and through gentle heating conditions for the reduction step. However, control of the metal interface was more complex and was dependent on the interaction of each individual metal with the silica wall surface. Zn was

found to be highly dispersed across the inner surface of the silica walls, with zinc ions found well distributed across the whole support. On the other hand, Pt showed a much weaker interaction with the walls, forming particles inside the channels. This series of catalysts, similarly to the polymer stabilised series, mainly showed enhanced formic acid decomposition activities due to electronic and geometric promotion effects. The exception to this was the PtAg catalyst, which showed a lower activity due to a negative geometric influence. The strong interaction between some metals and the silica walls is thought to be a useful tool for the synthesis of directed morphologies.

The wall effect was further investigated through modification of synthesis route and metal composition when synthesising catalysts for the oxygen reduction reaction. These catalysts show an increase in activity compared to the commercial Pt catalyst tested as a reference. Both characterisation results and activity differences, highlight the changes in morphology due to the synthesis route and the metal composition. A suggested mechanism is presented, allowing understanding of the synthesis process.

This thesis has provided a brief introduction to the manipulation of synthetic routes, in order to form designed nanoparticles, with 2 different synthetic routes investigated. Neither route provides a facile method for synthesis of non-thermodynamically-favoured predicted structures, although with slight changes in composition and synthetic parameters the control could be possible. The highly controlled particles show an enhancement in activity, which is expected to be due to the strong electronic and geometric modification at the metal interfaces.

7.2 Future Perspectives

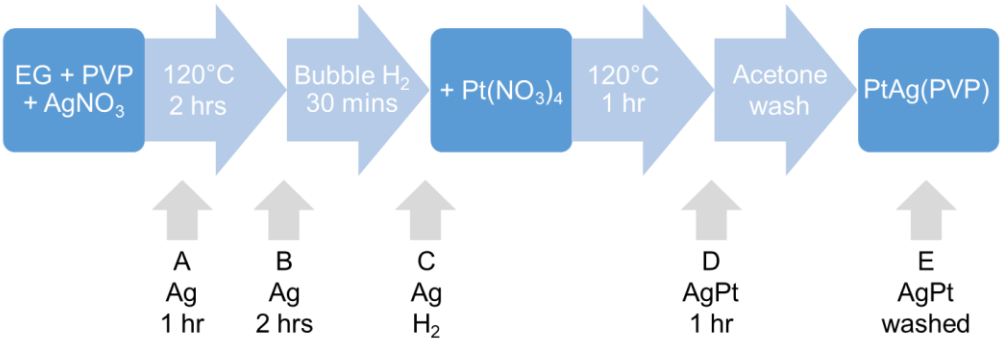
The research of this thesis offers a basis for the understanding of tailoring nanoparticle structures with specific metal interfaces. It is expected that further research into the modification of synthetic parameters and catalyst compositions, through using these results, will be beneficial for catalyst tailoring in many industrial processes. Through the use of machine learning and development of

intelligent design, it is thought that these synthetic methods may provide a foundation for a route to the synthesis of these novel and non-ideal structures.

APPENDICES

Appendix 1

Further Cryo-TEM study images of the PtAg(PVP) sample, as discussed in 4.5.1. Aliquots studied are labelled A-D as detailed in the following scheme:



Schematic to show stepwise synthesis method and cryo-TEM sampling points.

Sample A shows occasional large Ag particles with smaller Ag seed particles between them. The Ag seed movement can be examined through imaging a time-lapse below, with images taken every 5 seconds for 45 seconds.

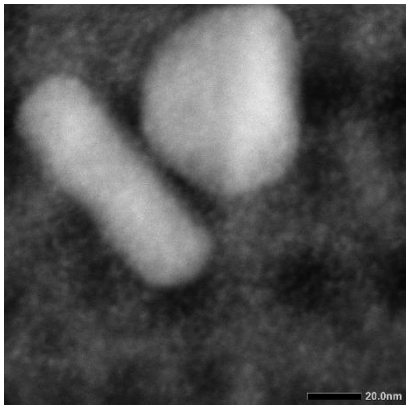
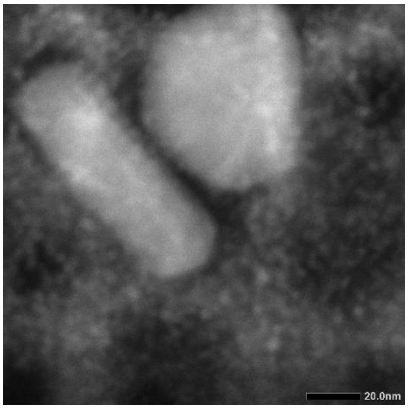
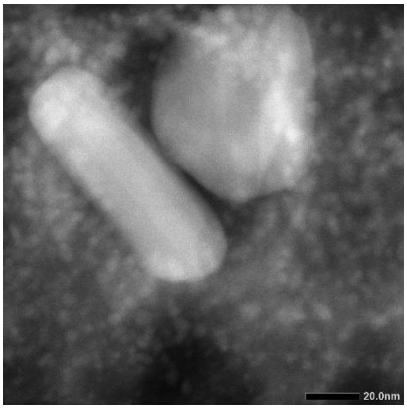
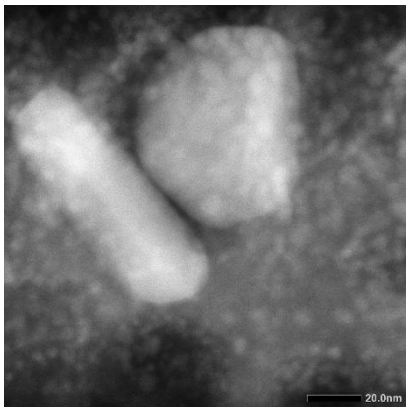
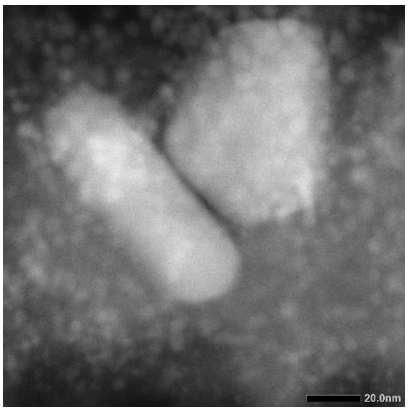
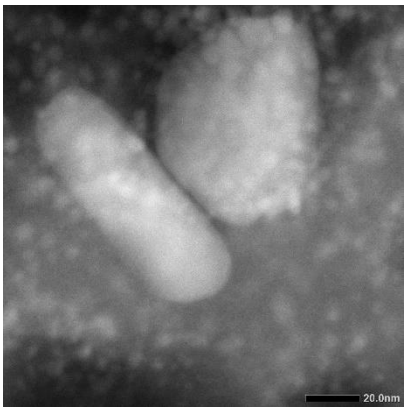
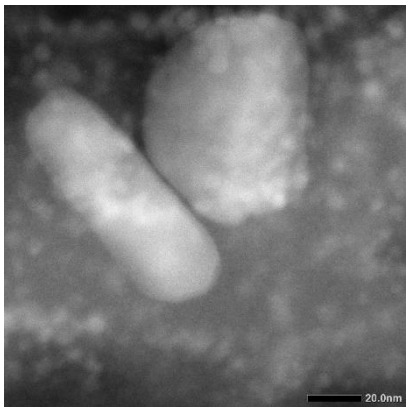
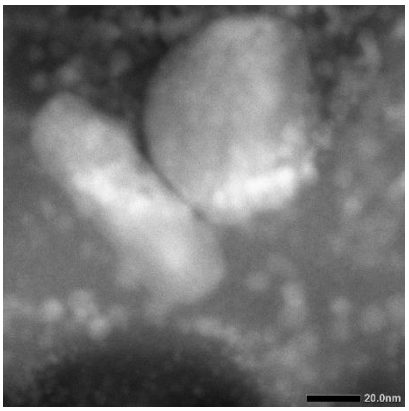
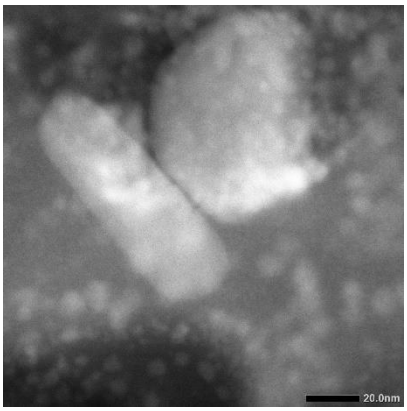
		
0 seconds	5 seconds	10 seconds
		
15 seconds	20 seconds	30 seconds
		
35 seconds	40 seconds	45 seconds

Figure A1.1. Dark field time-lapse of PtAg(PVP) at sample point A, with one image taken every 5 seconds for 45 seconds. Ag seeds can be seen to aggregate and move towards the larger Ag particles.

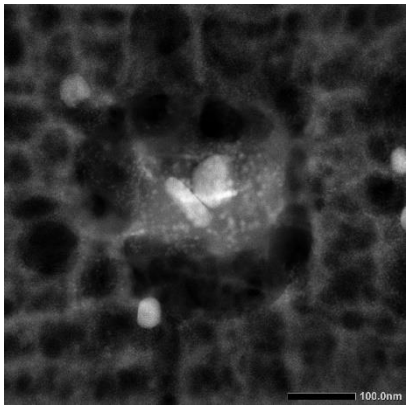
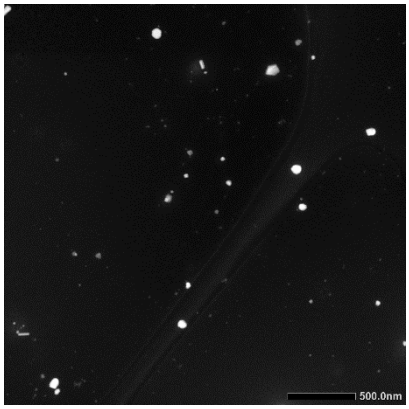
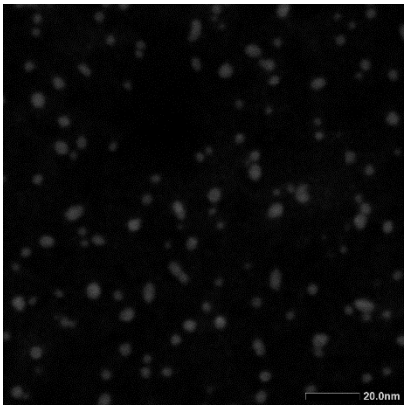
		
Post time-lapse, shows area of beam damage and particle agglomeration.	Frequent large Ag particles 20-50 nm	Many small Ag seeds around 5nm between large particles

Figure A1.2. Three dark field images of PtAg(PVP) at sample point A. The first shows the beam damage to the sample after the time-lapse above, the empty area around the large particles shows the areas which the seed particles have moved from. The middle image shows the frequent large Ag particles across the sample. The final image shows the smaller seed particles of around 5 nm dominating the reaction mixture.

Sample point B shows some growth in the larger Ag particles and more agglomeration of the seed particles.

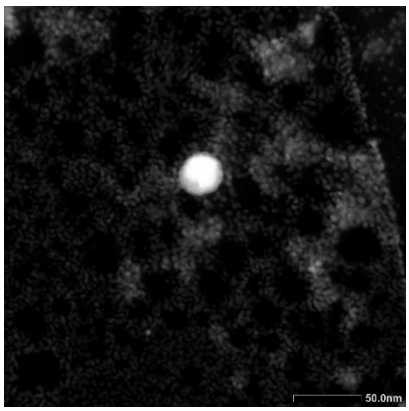
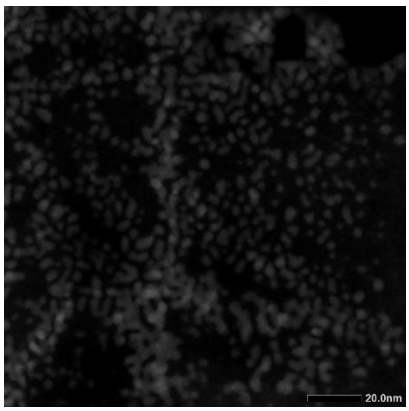
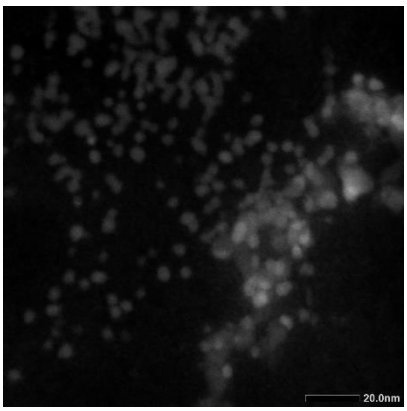
		
Large particles around 50 nm remain, with small seeds throughout.	Many small particles remaining around 5 nm.	Areas of agglomeration of the smaller particles in the PVP.

Figure A1.3. Three dark field images of PtAg(PVP) at sample point B. The image on the left shows the large particles around 50 nm remain in the sample, with the smaller seed particles throughout the sample. The middle

image shows the seed particles are still throughout the PVP, although some are more agglomerated as seen in the third image.

Sample point C was taken after the H_2 bubbling and shows no change in the particle sizes, although more dispersion throughout the solvent is seen rather than the agglomeration exhibited in sample B. Seed growth is seen under the electron beam similar to sample A & B.

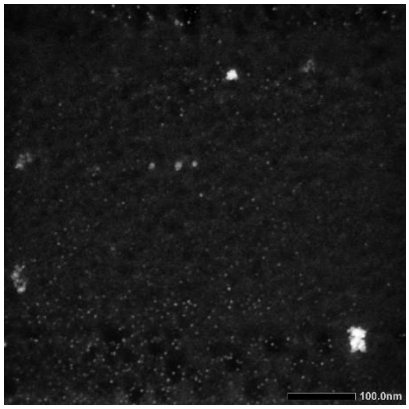
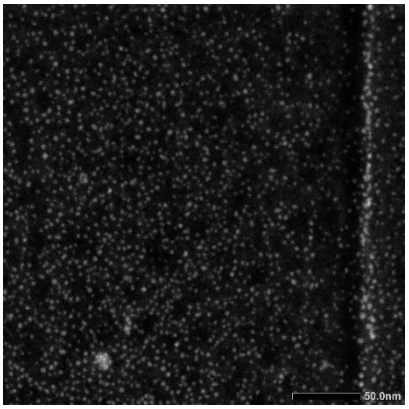
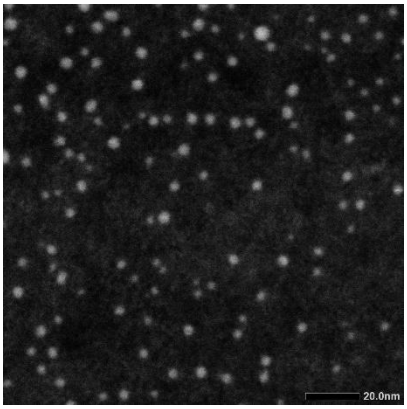
		
Large particles remain with the seeds between them.	High dispersion of the smaller particle across the sample	Seed particles agglomerate after movement is allowed under electron beam.

Figure A1.4. Three dark field images of PtAg(PVP) at sample point C. The first image shows that the particle sizes have remained the same after H_2 bubbling, with some large particles and many smaller seeds. The middle image shows that the seeds are well dispersed throughout the sample and the agglomeration has diminished. The final image shows the increase in seed size after the electron beam was held on the area for 30 seconds. The seed particles are fluidized and grow, likely through an Ostwald ripening process.

Sample D was taken after Pt addition and reduction for 60 minutes.

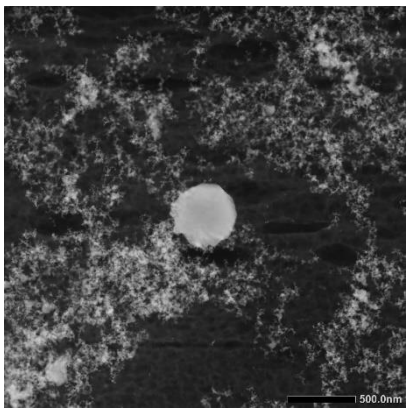
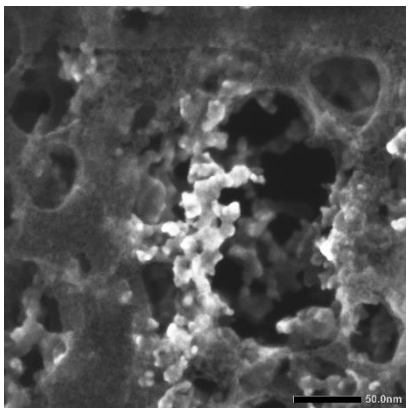
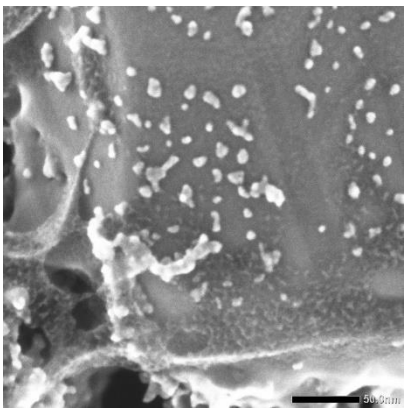
		
Large particles remain with highly aggregated web of smaller particles around.	Chain-like structures of smaller particles held in the PVP and frozen solvent.	Decoration of the larger particles with smaller particles

Figure A1.5. SEI images showing PtAg(PVP) at sample point D. The first image shows that the particle sizes have remained the same, with some large particles and many smaller seeds. The middle image shows chain-like structures of the smaller particles. The final image shows the decoration of smaller particles on the surface of the larger particles.

Appendix 2

The XRD patterns shown in this chapter have shown a high background between the 2θ angles of 20-35 °. This can be attributed to the SBA-15 structure, as shown by the blank support SBA-15 XRD profile shown below in Figure A2.1.

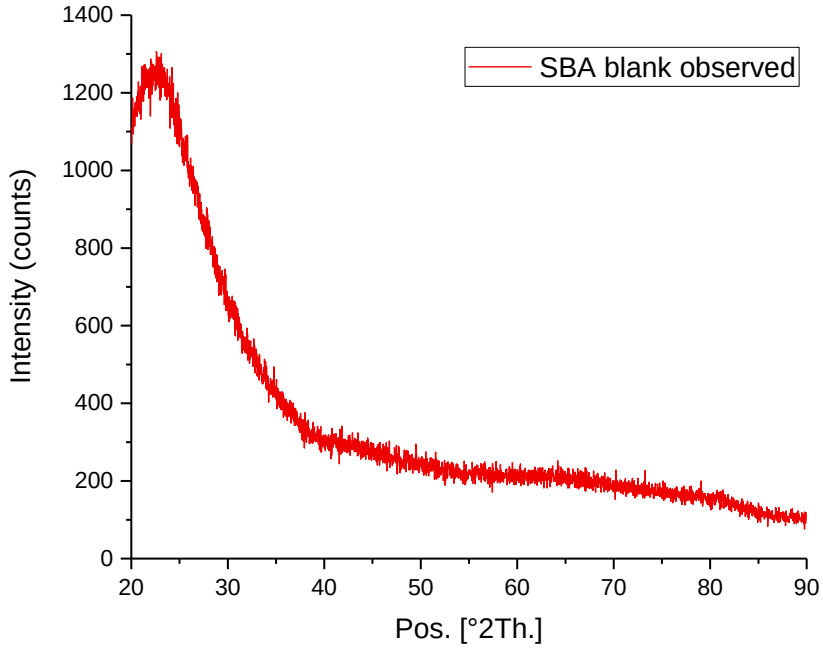


Figure A2.1. Blank SBA-15 XRD profile showing high background between 20-35 °2θ

In the main text each bimetallic sample was analysed with TEM and the main ratio for each sample was Pt_2X_8(SBA-15). In addition to this ratio, for the Zn sample, a further series of samples was synthesised and teste for formic acid decomposition. Below, Figure 31-34 show the TEM, and in some samples EDX characterisation, results for these samples.

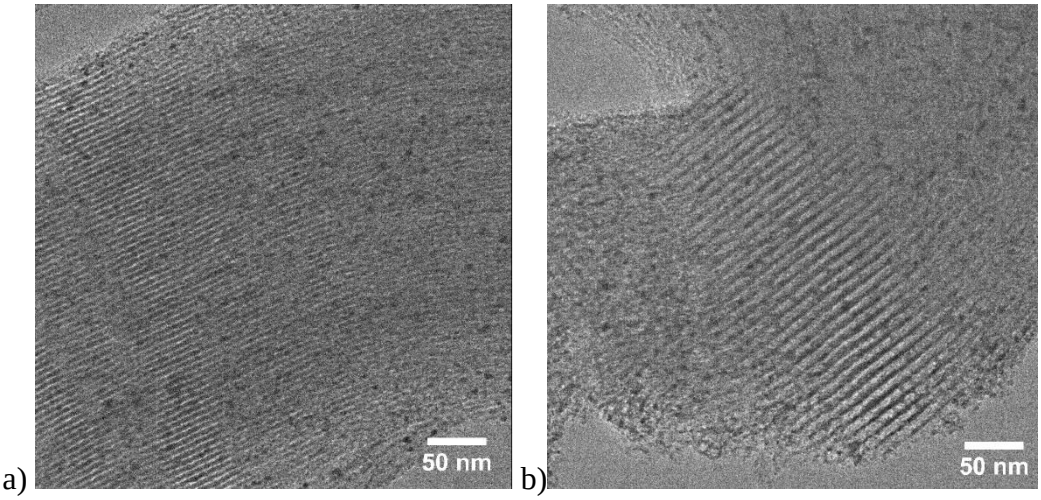


Figure A2.2 a&b) TEM images showing Pt_5Zn_5(SBA-15). Average diameter of the particles was measured to be 3.2 nm (± 2.3 nm, n=105).

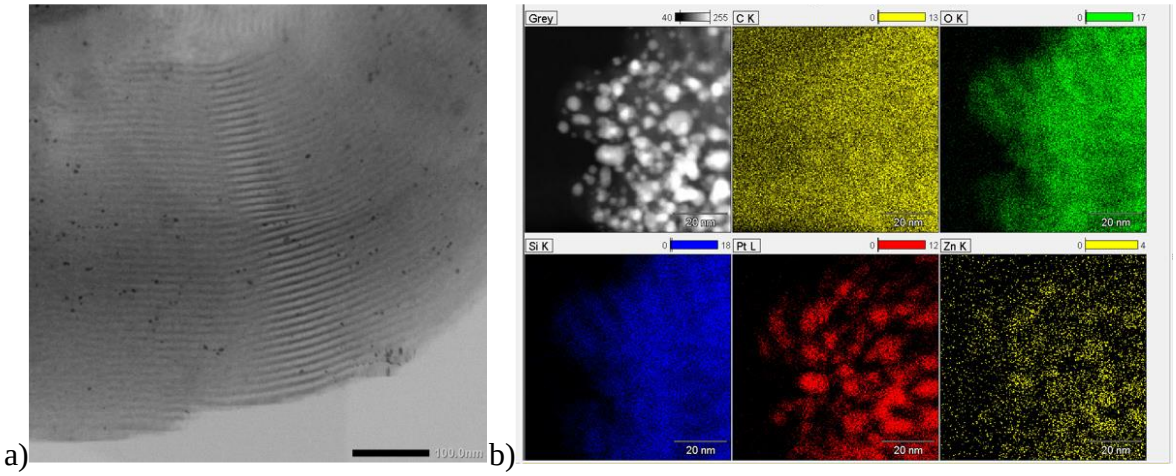
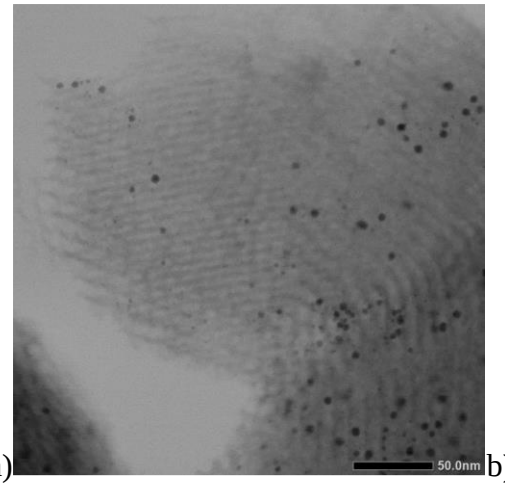


Figure A2.3. a) TEM image of Pt_8Zn_2(SBA-15). b) EDX maps indicating Pt in red and Zn in yellow, along with C (bright yellow), O (green) and Si (blue). The mean diameter of the particles is 3.1 nm (± 1.5 nm, n=150).

a) 

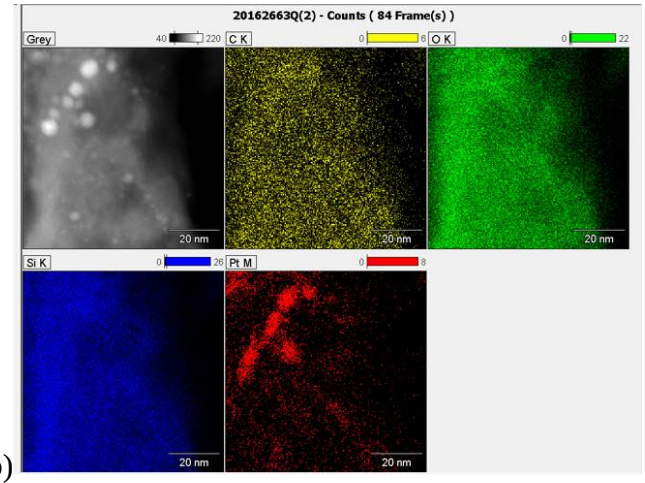
b) 

Figure A2.4. a) TEM image of Pt(SBA-15). b) EDX maps indicating Pt in red, along with C (yellow), O (green) and Si (blue). The mean particle diameter is 3.2 nm (± 2.2 nm, n=101).

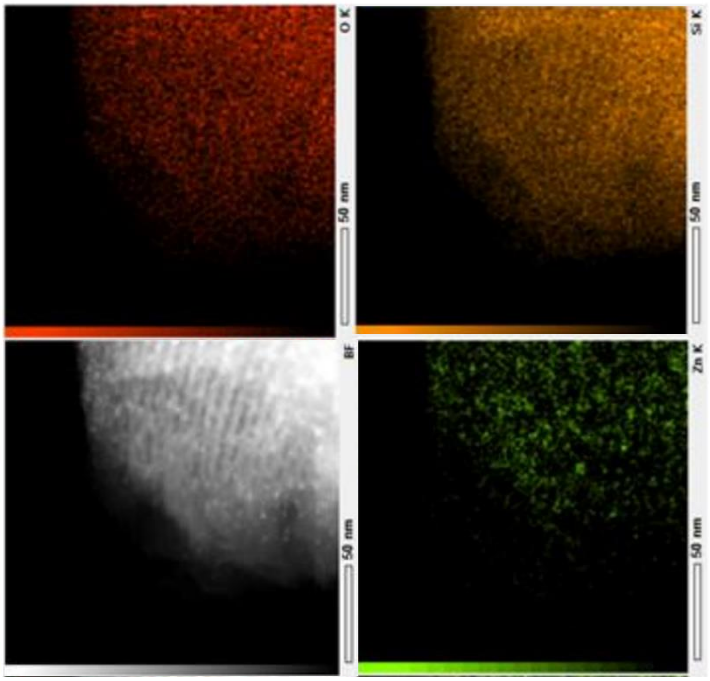


Figure A2.5. TEM and EDX mapping of Zn(SBA-15) showing Zn in green, along with O in red and Si in orange.